Impact Damage Behaviour of Lightweight Materials

Kedar Pandya

Department of Engineering

University of Cambridge

This dissertation is submitted for the degree of

Doctor of Philosophy

St. John's College   December 2017

To my loving parents, my pillars of strength, for always being there for me …

To my dear Rishika, my life partner and companion, for her love and motivation …

Declaration

I hereby declare that except where specific reference is made to the work of others, the contents of this dissertation are original and have not been submitted in whole or in part for consideration for any other degree or qualification in this, or any other University. This dissertation is the result of my own work and includes nothing which is the outcome of work done in collaboration, except where specifically indicated in the text. This dissertation contains less than 65,000 words (approximately 47,829 words) including appendices, bibliography, footnotes, tables and equations and has less than 150 figures.

Kedar Pandya

December 2017

Acknowledgements

Abstract

Impact damage resistance is an essential requirement of lightweight structural components for high-performance applications. The aim of this thesis is to study the impact damage and perforation behaviour of lightweight materials including thin aluminium alloy plates and carbon fibre reinforced epoxy composites. The focus of this investigation is on the stress state and strain rate dependence of failure, and the effect of microstructural modifications on indentation and impact response.

The thesis is divided into three parts. In the first part (Chapter 2) the impact response of thin monolithic ductile aluminium alloy plates is investigated. Impact perforation experiments are performed using different projectile nose shapes to span a wide range of stress states at the onset of ductile fracture. Impact perforation behaviour, ballistic limit velocity, energy absorption capability and sensitivity to projectile tip geometry are evaluated. Modes of deformation and failure during impact are assessed experimentally. It is shown that modelling the stress state and strain rate dependence of plasticity and failure is crucial to accurately predict ductile fracture initiation in thin metal plates.

In the second part (Chapters 3 and 4), the stress state and strain rate dependent yield and failure behaviour of epoxy resin is investigated. An iterative numerical-experimental approach is shown to be essential to develop a material model capable of predicting the failure behaviour of epoxy for a wide range of stress triaxialities across different regimes of failure. The influence of microstructural modifications in epoxy, through two different toughening strategies, on its failure behaviour is investigated. The effect of increasing the applied strain rate on the stress state dependent response of epoxy is investigated to provide an insight into the impact damage resistance of carbon fibre reinforced epoxy composites.

In the third part (Chapter 5), experimental studies are conducted on the quasi-static indentation and impact perforation response of plain weave carbon fibre reinforced epoxy composites to investigate the effect of toughening the epoxy matrix to improve resistance to indentation and impact. The nose shape sensitivity of failure initiation in carbon/epoxy composite targets is assessed by considering indenters with different tip geometries.

Conclusions and suggestions for future work are presented in Chapter 6.

x

Contents

List of Figures

List of Tables

Chapter 1　Introduction

1.1　Motivation

Impact loading is one of the important loading conditions that structures undergo during their service life. Hence, resistance to impact perforation is an essential requirement of structural components for both conventional and high-performance applications. Protection against impact damage is a critical issue in the design of ballistic grade armour, shock and impact absorbers, and development of high-grade aerospace, marine, automotive and civil structures. Typical instances of medium to high velocity impact include bird strikes and impact of runway debris/hailstones on aircraft during takeoff/landing, impact of space debris on satellites/space vehicles, accidental blade impact in aircraft engines, road traffic accidents, discharge of small and medium calibre bullets, and impact of blast fragments on marine structures and military vehicles. Ballistic impact is a localized high velocity impact onto a target caused by a propelling source, generally of low mass and high velocity. Ballistic impacts can result in partial or complete perforation of the target depending on the projectile mass, velocity and shape. In order to ensure the safety of lightweight structures against perforation by high velocity projectiles, a clear and complete understanding of impact damage initiation and evolution in lightweight materials is essential.

Development of novel lightweight materials with superior mechanical properties such as high specific stiffness, high specific strength, high fracture toughness, corrosion resistance and increased fatigue life has been the focus of modern research. Lightweight materials and structures have had a significant impact on the aerospace, defence and automotive industries over the past few decades. These lightweight structures are generally susceptible to impact loading. Thus, for their effective use in industrial applications, enhancement of their impact

resistance, in turn, their energy absorption capability is essential. Various lightweight materials have been employed for protection against impact loads including light alloys (e.g. Al, Mg and Ti alloys) (Gupta et al., 2008; Iqbal et al., 2010), polymer matrix composites with fibres made of carbon, glass, aramid (Kevlar, Twaron) or ultra-high molecular weight polyethylene (Spectra, Dyneema) and polymers such as epoxy, polyester or polyethylene (Cheeseman and Bogetti, 2003; Pandya et al., 2013), polymers (e.g. polycarbonate) (Wright et al., 1993) and ceramics (e.g. Al-SiC) (Beissel et al., 2012). Recent advances at enhancing the protective capability of structural components include use of hybrid composites (Hazell and Appleby-Thomas, 2009; Muhi et al., 2009; Pandya et al., 2013, 2011), development of sandwich structures with foam core (Hosur et al., 2008; Hou et al., 2010; Ivañez et al., 2011) or honeycomb core (Buitrago et al., 2010; Feli and Namdari Pour, 2012), use of fibre-metal laminates (Chen et al., 2013; Hoo Fatt et al., 2003; Seyed Yaghoubi and Liaw, 2013), incorporation of shear thickening fluids (Lee et al., 2003; Petel et al., 2013), use of natural fibre composites (Wambua et al., 2007), development of multi-layered structures (Mohagheghian et al., 2017a, 2016; Naik et al., 2012) and adoption of various toughening strategies for polymers (Laurenzi et al., 2013; Mohagheghian et al., 2011; Pandya et al., 2012; Pandya and Naik, 2015a, 2015b; Zamani et al., 2012) and polymer matrix composites (Pandya et al., 2012; Rahman et al., 2013; Tehrani et al., 2013).

Three major factors play a role in understanding the damage behaviour of lightweight structures; material type, micro-structure and loading case. Two classes of materials, which have emerged as innovative, effective and economical lightweight materials used extensively in the aerospace, defence and automotive sectors, are aluminium alloys and carbon fibre reinforced epoxy (CFRE) composites. Wrought aluminium alloys emerged as novel high-performance materials in the late 1920s, replacing conventional alternatives like steel due to their high specific strength and ease of manufacture. Apparent disadvantages of aluminium alloys such as low yield strength, susceptibility to stress corrosion cracking and exfoliation corrosion were overcome by the early 1970s due to the development of innovative heat-treated and/or age hardened high-strength alloys with significant improvements in their resistance to fatigue and corrosion. The parallel development of high strength and high stiffness carbon fibres led to a substantial growth in the manufacture of CFRPs for high-technology aerospace, automotive, civil and sports applications. High-grade

2

thermosetting epoxy resins generally outperform other polymer matrices in terms of their mechanical properties, dimensional stability, resistance to environmental degradation, processing ease and long service life, which leads to their almost exclusive use as the matrix component in CFRPs. Today, the consumption of CFRE composites is driven by the aerospace industry (Boeing, 2006; EADS Report, 2006) and turbine blades for wind power generation (Watson and Serrano, 2010). For instance, the airframe and primary structure of state of the art commercial aircraft comprises of at least 50% CFRP and 20% Al alloys by weight (e.g. Airbus A350 (EADS Report, 2006) and Boeing 787 Dreamliner (Boeing, 2006)). However, epoxy resin is known to be brittle, and is susceptible to crack initiation and propagation during indentation and impact (Bandyopadhyay, 1990; Garg and Mai, 1988). Impact damage tolerance is a critical factor in the design and development of CFRE composites, and depends on the failure properties of the epoxy matrix (Asp et al., 1996a, 1996b, 1995).

An effective strategy of increasing the protective capability of epoxy-based composites is to enhance the fracture toughness of epoxy resin by the addition of various toughening agents like liquid rubber, thermoplastics, rigid particles and core-shell particles (Bain et al., 2016; Becu et al., 1997; Carolan et al., 2016; Day et al., 2001; Gurusideswar and Velmurugan, 2014; Lin and Shieh, 1998; Liu et al., 2016; Sue, 1992; Thitsartarn et al., 2015). Recently, the use of nanoscale fillers such as carbon black, nanoclay, nanosilica, alumina nanoparticles, graphene nanoplatelets and carbon nanotubes (CNTs) to enhance the energy absorption capability of epoxy polymers has been considered (Argento et al., 2011; Hao et al., 2011; Naik et al., 2014a, 2014b; Pandya and Naik, 2015b; Sun et al., 2009). By dispersing nanofillers into various fibre and matrix systems, it is possible to manufacture epoxy nanocomposites (Yamamoto et al., 2009). The effect of incorporation of nanofillers into epoxy and epoxy based composites on their mechanical properties has been studied (Coleman et al., 2006a, 2006b; Sun et al., 2009; Thostenson et al., 2001). Generally, it is observed that the mechanical properties of nanocomposites are superior to those without nanoparticle reinforcement. Further, the addition of nanofillers does not lead to significant weight penalty. There is a need to understand the influence of microstructural modifications on the mechanical properties of epoxy resin to evaluate the effectiveness of various toughening strategies in improving the ballistic impact characteristics of CFRE composites.

3

Numerical modelling is an essential tool for the efficient design and optimisation of structures. However, modelling the response of lightweight materials to complex loading cases such as indentation and impact is challenging. Factors affecting the response of materials to ballistic impact loading include material type, geometry and boundary conditions of the target as well as the size, nose shape and kinetic energy of the projectile. Previous investigations have demonstrated that the projectile nose shape (or "effective nose shape") has a significant influence on the ballistic impact resistance of thin ductile metal plates and CFRE composite targets, since the projectile tip geometry determines the stress state and strain distribution within the impacted target plate (Ben-Dor et al., 2002; Liu and Stronge, 2000; Mohagheghian et al., 2017a, 2017b, 2016; Palomby and Stronge, 1988; Ulven et al., 2003; Wen, 2000). Researchers are working towards developing better numerical models capable of accurately predicting the response of lightweight materials to complex loading conditions such as impact, to understand their failure behaviour over a wide range of stress states and strain rates (Bai and Wierzbicki, 2009, 2008a; Bao and Wierzbicki, 2004; Fiedler et al., 2001).

1.2   Thesis objectives

The objective of this research work is to investigate the impact damage and perforation behaviour of thin ductile monolithic aluminium alloy plates and carbon fibre reinforced epoxy composites. The following research questions are addressed:

1. How is the impact energy absorption and perforation resistance of thin ductile aluminium alloy plates influenced by the projectile nose shape? Which numerical model best predicts ductile fracture during impact perforation over a wide range of stress states?

2. How can we systematically probe and model phenomenologically the stress state dependent yield and failure response of epoxy resin? How do microstructural modifications in epoxy resin through different toughening strategies influence its quasi-static and high strain rate mechanical behaviour?

3. How are the quasi-static and impact characteristics of carbon fibre reinforced epoxy composites influenced by microstructural modifications within the epoxy matrix? How do carbon/epoxy composites compare with aluminium alloys in terms of perforation resistance during indentation and impact? Is the quasi-static indentation response of composite targets influenced by the indenter tip geometry?

1.3 Thesis outline

In Chapter 2, the impact perforation response of thin ductile monolithic aluminium alloy plates is investigated. The effect of varying the projectile nose shape on the impact response is considered. Different numerical models are used to predict stress state dependent ductile fracture during impact and the effect of strain rate sensitivity of aluminium alloy on the suitability of these models is explored.

In Chapter 3, the stress state dependent quasi-static yield and failure behavior of filled epoxy is systematically characterized. The phenomenological material model developed is applied to the more complex loading case of indentation. Filled epoxy is considered in this chapter to provide an insight into the deformation and damage response of the more complex carbon fibre reinforced epoxy composites under impact loading.

In Chapter 4, the effect of strain rate and two different toughening strategies on the initial yield and failure behaviour of epoxy resin is investigated. Addition of core-shell particles and reaction induced phase separation are the two toughening strategies considered.

In Chapter 5, experimental studies are conducted on the quasi-static indentation and ballistic impact perforation behaviour of plain weave carbon/epoxy composites to investigate the effect of toughening the epoxy matrix. Quasi-static edge-clamped indentation studies are performed on carbon fibre reinforced epoxy composites using indenters with different tip geometries to assess the nose shape sensitivity of failure initiation in composite plates. The energy absorbed during quasi-static and impact perforation for the composites are compared with the corresponding values for thin aluminium alloy target plates investigated in Chapter 2.

Finally, in Chapter 6, conclusions are drawn and recommendations are made for future studies.

1.4 Impact perforation behaviour of ductile monolithic metal plates

The impact perforation behaviour of monolithic metallic plates is of interest to researchers and engineers alike for a wide variety of applications. The ballistic impact perforation regime can be divided into three velocity ranges; sub-ordnance velocities (25-500 m/s), ordnance velocities (500-1300 m/s) and ultra-ordnance velocities (1300-3000 m/s) (Backman and Goldsmith, 1978). The scope of this review is restricted to ballistic impact on flat target plates at sub-ordnance velocities, with normal impact of the projectile onto the target.

Backman and Goldsmith (1978) classified metallic target plates as thin, intermediate, thick and semi-infinite depending on the influence of the distal surface on the penetration process. Plates can be considered thin when the loading and strain distribution can be considered independent of target thickness. Further, the impact response of targets under projectile impact can be divided into non-perforation and perforation regimes. In the non-perforation regime, the projectile is either reflected or stopped by the target plate. When the incident velocity of the projectile is increased, a limit is reached at which the kinetic energy of the projectile becomes sufficiently large to cause failure of the target plate and allow the projectile to pass through. This limit is normally called the ballistic limit of the target plate. Ballistic limit velocity is defined as the average of equal number of highest partial penetration velocities and lowest complete penetration velocities of a specific projectile and target combination, which occur within a specified velocity range. In other words, ballistic limit velocity defines incident projectile impact velocity at which there is 50% probability of partial penetration and 50% probability of complete perforation. Although the ballistic limit is a statistical measure for the impact resistance of the target, in general terms the ballistic limit is understood as the minimum incident projectile velocity for which perforation of the target takes place (Corbett et al., 1996). Metallic targets undergo fracture

under impact loading through various failure mechanisms depending on several factors such as ductility, thickness, hardness and susceptibility to shear plugging, illustrated in Figure 1.1 (Yungwirth, 2006).

Studies are available in literature on various aspects of ballistic impact response of ductile metal target plates such as penetration/perforation behaviour, damage and failure modes, empirical modelling of impact, evaluation of ballistic limit velocity and energy absorption capability, and parametric studies including effect of projectile mass and projectile nose shape sensitivity. This review summarizes ballistic impact studies on thin ductile monolithic metal plates in the sub-ordnance velocity range.

In case of thin monolithic metal plates, the incident kinetic energy of a projectile during ballistic impact in the non-perforation regime is dissipated primarily through plastic deformation of the target. Two types of plastic deformation which take place are bulging and dishing (Backman and Goldsmith, 1978). Bulging refers to local plastic deformation of the target in direct contact with the projectile. Plastic deformation of the target taking place around the impact zone is known as dishing. For high incident projectile velocities, well above the ballistic limit, bulging is the dominant deformation mechanism while at lower incident velocities, up to the ballistic limit, considerable dishing is observed within the target. Dishing can be induced by bending, membrane stretching or a combination of both. The amount of dishing occurring before perforation of the target is dependent on the projectile nose shape (Backman and Goldsmith, 1978).

Perforation of thin ductile monolithic metal plates is dependent on the nose shape of the projectile. Damage and energy absorbing mechanisms and consequently the ballistic limit of thin ductile metal target plates can be varied significantly by using different projectile tip geometries. The most commonly observed perforation mechanisms for blunt, hemispherical, conical and ogival projectiles are summarised in Figure 1.2 (Mohagheghian, 2013).
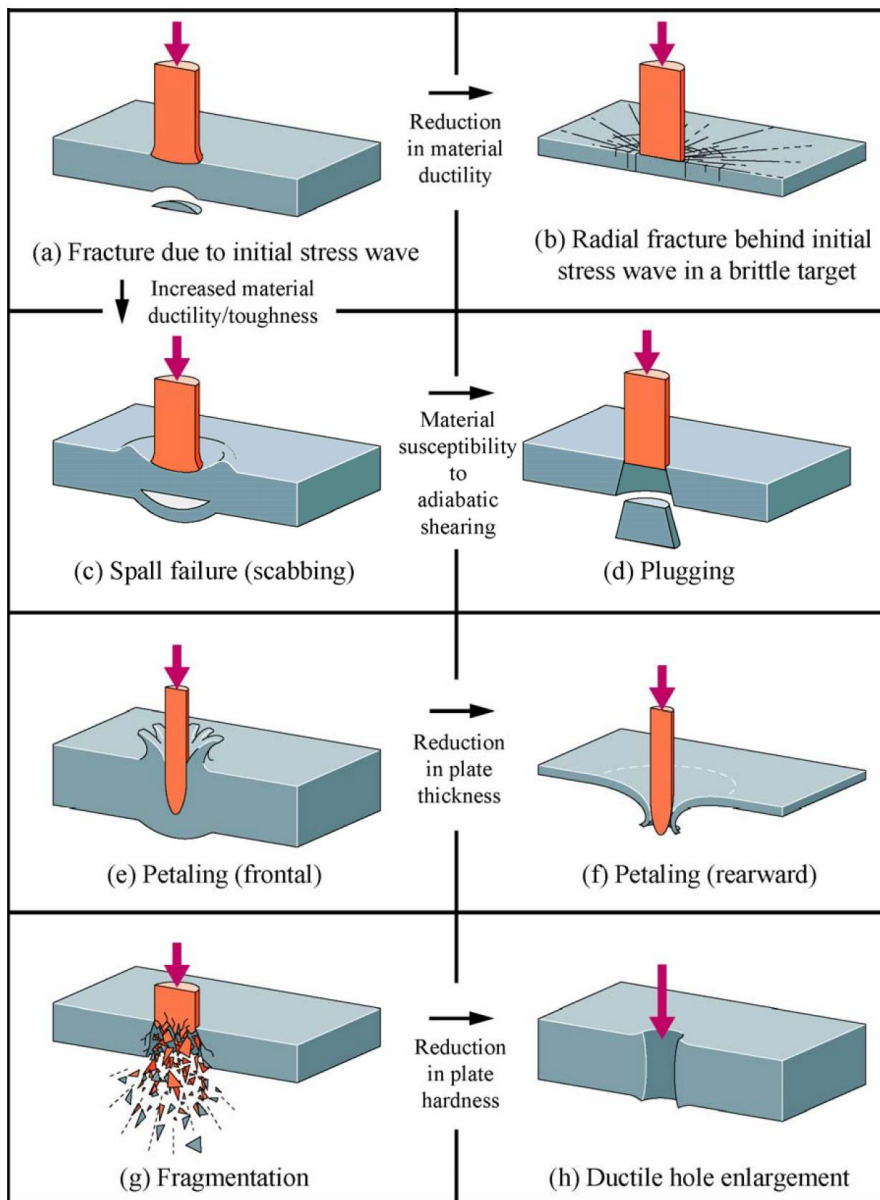
Figure 1.1 Dependence of perforation mechanisms on various parameters (reproduced from Yungwirth, 2006).
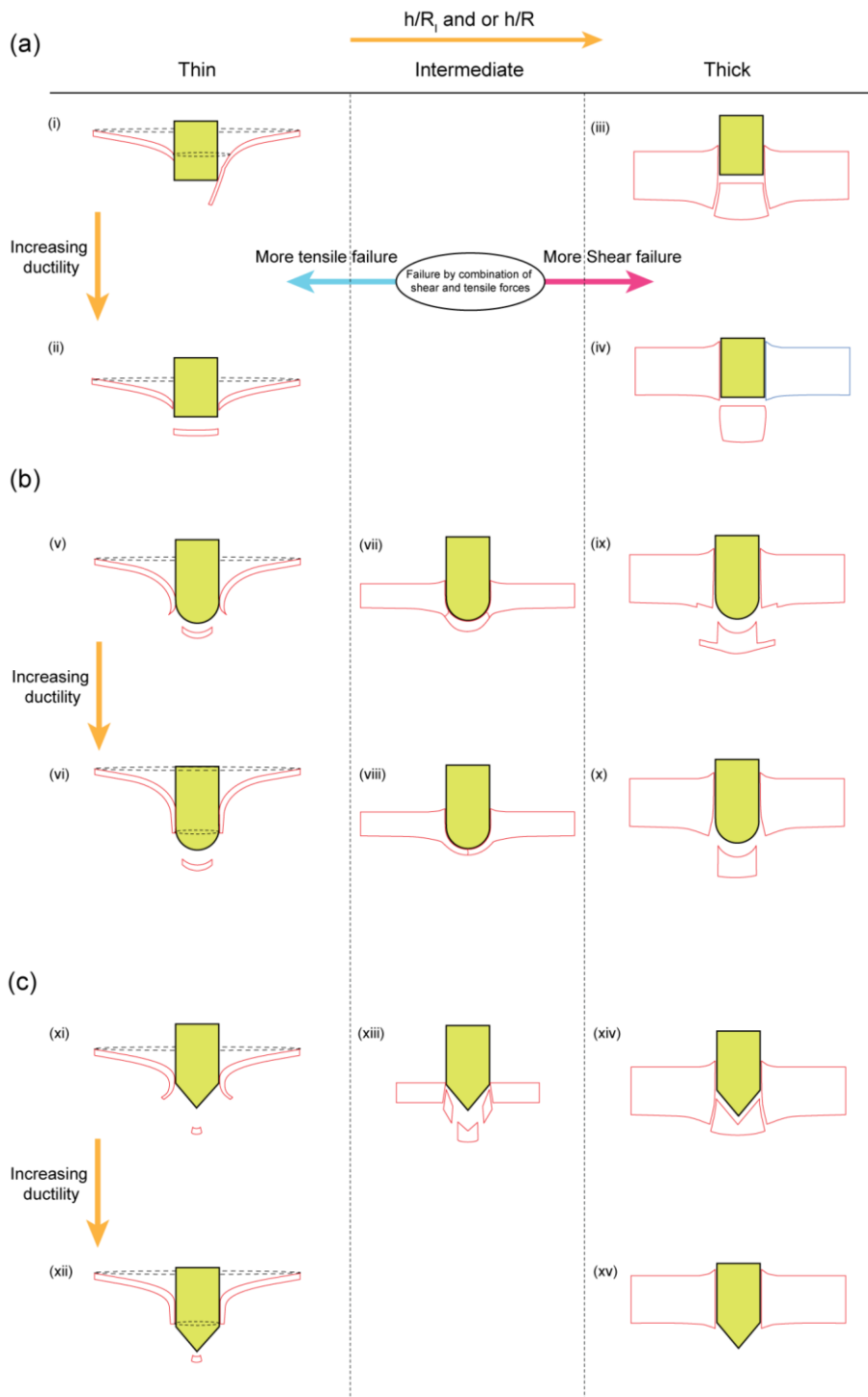
Figure 1.2 Failure mechanisms reported in literature for ductile metal target plates impacted by (a) flat, (b) hemispherical and (c) conical projectiles, based on studies by Backman and Goldsmith (1978), Crouch et al. (1990) and Leppin and Woodward (1986) (reproduced from Mohagheghian, 2013).

For a flat-ended, cylindrical projectile with sharp corner edges, the major failure mechanism is shear plugging (Figure 1.2a). Shear plugging is a type of shear failure of plates subjected to high localized forces. This type of failure takes place at the periphery of the flat projectile. Immediately upon ballistic impact, the contact force between the projectile and the target results in through-thickness shear stress within the target around the periphery of the projectile. The projectile therefore first elastically and then plastically indents the target. After this initial indentation reaches a critical depth, a crack is formed under the edge of the projectile. This crack propagates through the thickness of the target, forming a plug of nearly the same diameter as the projectile. Subsequently, the plug formed is ejected from the back face of the target. Corran et al. (1983) and Borvik et al. (2003) studied the effect of target plate thickness on the ballistic performance of metal plates struck by flat-ended, cylindrical projectiles. They reported that, beyond a critical plate thickness, the rate of increase of perforation energy with plate thickness decreases. They attributed this transition to the gradual change from global deformation observed in thin targets to localized shear deformation for thick plates (Figure 1.2a). Palomby and Stronge (1988) and Liu and Stronge (2000) observed discing in thin metal targets impacted by blunt projectiles at incident projectile velocities near the ballistic limit. They attributed the failure mode to a combination of shear and tensile forces, depending on the ductility of the material. In some cases, the shear plug formed was seen to rotate around a plastic hinge without detachment allowing the projectile to pass through the target (Crouch et al., 1990; Langseth and Larsen, 1994; Liu and Stronge, 2000).

In the case of spherical or hemispherical projectiles, the target is observed to deform uniformly in the absence of stress concentrations (Figure 1.2b). As a result, the impacted target experiences greater stretching thus absorbing more energy. Failure of the target takes place due to necking at a radius smaller than that of the projectile. The radius at which necking occurs is determined by the friction between the target and projectile and development of biaxial strains within the target (Atkins et al., 1998). While necking occurs close to the centre of the target plate for lower values of friction, by increasing the friction the location moves toward the edge of contact. Friction was found to affect the strain distribution as well as stress state of the material under the projectile (Lee et al., 2004). Necking failure under the projectile is followed by formation of a mode I crack which

propagates along a circular path within the necking region. A cap, with a radius smaller than the projectile radius, is detached from the plate. This failure mode is known as discing (Atkins et al. 1998). Since the hole formed in the target is smaller than the diameter of the projectile, the hole needs to expand to let the projectile pass through. This can take place through ductile hole enlargement in ductile metals or through formation of radial cracks in metals without sufficient ductility. In the latter case, the projectile passes through by petal formation and bending at the back face of the target.

The failure mechanism for a spherical projectile can change by increasing the target thickness or increasing the impact velocity (Figure 1.2b). Numerical results of Teng and Wierzbicki (2005) on thin long metal beams suggested that while tensile failure occurs close to the ballistic limit for spherical projectiles, by increasing the impact velocity the failure mode changes to shear dominated failure. Ductile hole enlargement, plugging and scabbing (Backman and Goldsmith, 1978) are possible failure mechanisms for intermediate and thick ductile targets impacted by spherical/hemispherical projectiles.

Petal formation and bending is the main damage mechanism of thin targets impacted by conical projectiles (Figure 1.2c). Like spherical/hemispherical projectiles, a small cap can form at the tip of the projectile. The size of the cap, which is considerably smaller than that formed by a spherical/hemispherical projectile, was reported to increase with increasing thickness of the target (Leppin and Woodward, 1986). Following cap detachment, a star shaped crack is formed on the back face of the target. As the projectile perforates the target further, the cracks propagate and form petals. Subsequently, petal bending occurs along with dishing on the back face. By increasing the thickness of the plate or cone angle of the projectile perforation can also occur by shear plugging.

The kinetic energy of a conical projectile is absorbed through a combination of different failure mechanisms including dishing, crack propagation and petal bending. However, the contribution of crack propagation is negligible compared to the other mechanisms (Landkof and Goldsmith, 1985). When dishing occurs in the target plate prior to fracture initiation, the energy absorbed through petal bending can be substantially greater compared to the case when petal bending initiates with minimal dishing (Wierzbicki, 1999). The energy absorbed by the target depends on the size of the ejected cap initially created by the projectile

(Landkof and Goldsmith, 1985). The number of petals is another important factor which affects energy absorption by petal bending. The number of petals, which determines the size and shape of the petal (Landkof and Goldsmith, 1985; Wierzbicki, 1999), depends on the nose angle and the ductility of the target material (Atkins et al., 1998). Experimental studies (Atkins et al., 1998; Ghosh and Travis, 1979; Kpenyigba et al., 2013) indicate a decreasing trend in the number of petals with increasing cone angle. Calculating the number of petals is difficult, since some small cracks may form that fail to propagate (Atkins et al., 1998). Petals may be classified as primary and secondary based on the size of cracks (Kpenyigba et al., 2013).

1.4.1 Transition between failure modes

The failure mode of ductile metal plates depends on a range of factors such as thickness, susceptibility to adiabatic shearing and anisotropy of the target as well as nose shape, deformability and impact velocity of the projectile. In order to study the projectile nose shape sensitivity of the impact damage behaviour of metals, Palomby and Stronge (1988) performed impact experiments on thin-walled mild steel tubes using flat, intermediate and hemispherical projectiles. They showed a transition in the dominant failure mechanism, from shear plugging at the periphery of the contact zone for flat projectiles to discing, characterized by dishing and localized radial necking outside the contact region, in case of hemispherical projectiles. The transition between different failure mechanisms has also been studied by other authors by systematically varying the nose shape of a rigid projectile, by changing either the frontal nose radius/tip radius (Corran et al., 1983), the chamfer size/corner radius (Iqbal et al., 2010), or the cone angle/apex angle of the projectile (Ghosh and Travis, 1979; Kpenyigba et al., 2013; Leppin and Woodward, 1986; Vijayan et al., 2016).

To understand the effect of nose radius on the failure mode, Corran et al. (1983) conducted a series of impact tests on thin mild steel targets using projectiles with different frontal nose radii ranging from infinity (blunt projectile) to the projectile radius (hemispherical projectile). They observed a transition in failure mode from shear plugging for frontal nose radii exceeding 12 mm to tensile tearing for smaller frontal nose radii (9.5 and 6.25 mm).

Their results show an optimum in the impact perforation energy corresponding to the radius for which the transition occurs from shear plugging to tensile failure. A similar change in the failure mode was also observed by Teng and Wierzbicki (2005). Their numerical results suggest that while shear plugging occurs under a flat-ended projectile, introducing a larger corner radius gradually changes the failure mode to tensile failure.

Iqbal et al. (2010) numerically investigated the effect of changing the projectile nose shape on the ballistic limit and failure modes of thin aluminium target plates. They changed the projectile nose shape from blunt to hemispherical and ogival by introducing different corner radii R_C to the edge of a projectile of radius R_I. While $R_C = 0$ corresponds to a blunt projectile, $R_C = R_I$ represents a hemispherical projectile. $R_C > R_I$ represents different ogive nosed projectiles. They reported that the ballistic limit increases as the projectile tip geometry is changed from blunt to hemispherical and then significantly decreases for ogive nosed projectiles.

Liu and Stronge (2000) illustrated a change in failure mode during impact, for a given projectile nose shape, if a more deformable projectile were used. An increase in the projectile deformability led to a corresponding increase in the projectile diameter and tip radius upon impact. For flat projectiles with higher strength/lower deformability, the dominant failure mode during impact was observed to be shear plugging. Conversely, for flat projectiles with lower strength/higher deformability, the target failed through tensile tearing upon impact, a failure mode characteristic of hemispherical projectiles, accompanied by an increase in ballistic limit. The increase in ballistic limit for softer projectiles was attributed to more dishing in the target plate, with the larger effective projectile tip radius upon impact leading to a reduction in the induced shear strains.

For polymer-metal bilayer plates perforated by a blunt indenter, Mohagheghian et al. (2017a) concluded that an optimum thickness of the frontal polymer layer exists for which the energy absorption per unit mass is maximum. A clear correlation was found between this optimum and a transition in the failure mode of the metallic backing layer. A gradual transition from shear plugging failure to tensile failure was observed on increasing the thickness of the frontal polymer layer. This behaviour is similar to the transition from shear dominated failure to tensile failure of thin metal plates as the projectile nose shape is varied

from blunt to hemispherical (Corran et al., 1983; Iqbal et al., 2010; Palomby and Stronge, 1988). In general, the stress state and plastic strain distribution in thin ductile metal targets is significantly affected by the local curvature in the plate imposed by the projectile. This significantly influences the energy absorbing capability of the target, an important parameter in ballistic impact studies, by changing the dominant failure mechanisms. It can be clearly seen from the literature that the projectile nose shape (or effective nose shape) has a significant influence on the ballistic impact resistance of thin ductile metal plates, since the projectile tip geometry determines the stress state and strain distribution within the impacted target plate.

1.4.2 Stress state dependence of fracture in ductile materials

Predicting ductile fracture at different states of stress has been of interest in many research fields, especially in impact mechanics. As shown by Corran et al. (1983), predicting impact energy absorption requires the transition from shear plugging to tensile failure to be captured accurately. The classical J2 theory of metal plasticity assumes that the effects of hydrostatic pressure and the third stress invariant of the stress tensor on plastic flow stress are negligible. Ductile fracture is a local phenomenon occurring by nucleation, growth and coalescence of micro-voids leading to macroscopic cracks. Fracture initiation is preceded by large plastic deformation with considerable stress and strain gradients around the point of fracture. As a result, the infinitesimal J2 theory of plasticity is not accurate enough.

The effect of hydrostatic pressure on the growth of voids is well known and is considered in several constitutive models by introducing the stress triaxiality parameter η, which is defined as the ratio of hydrostatic pressure to the equivalent stress. A monolithic exponential decay in the ductility of materials with increasing stress triaxiality has been established in previous investigations (Johnson and Cook, 1985; Rice and Tracey, 1969).

Recently, it has been identified by several researchers that while failure models including only stress triaxiality, such as the Johnson-Cook model and Gurson model, work well at high triaxialities, they fail to capture localization and fracture at low triaxiality, shear dominated deformation such as shear plugging failure due to projectile impact, cropping of sheet metal or dynamic shear off (Nahshon and Hutchinson, 2008). Experimental results of Bao and

Wierzbicki (2004) showed that at low and negative stress triaxialities, the experimental data deviates from the well-known exponential model. They used a combination of tensile tests on notched specimens, upsetting tests and combined shear and tension tests and found three different branches in the response as shown in Figure 1.3. For high stress triaxialities, the data obtained by axisymmetric specimens fit very well to the normal exponential form obtained for void growth. However, at the lower stress triaxialities, the monotonic behaviour is not valid any more. Bao and Wierzbicki (2004) suggested that the type of failure changed at low and negative stress triaxialities to shear failure. The insufficiency of accounting only for stress triaxiality in fracture models has also been noted by other authors (Barsoum and Faleskog, 2007; Gao and Kim, 2006; Gruben et al., 2012).
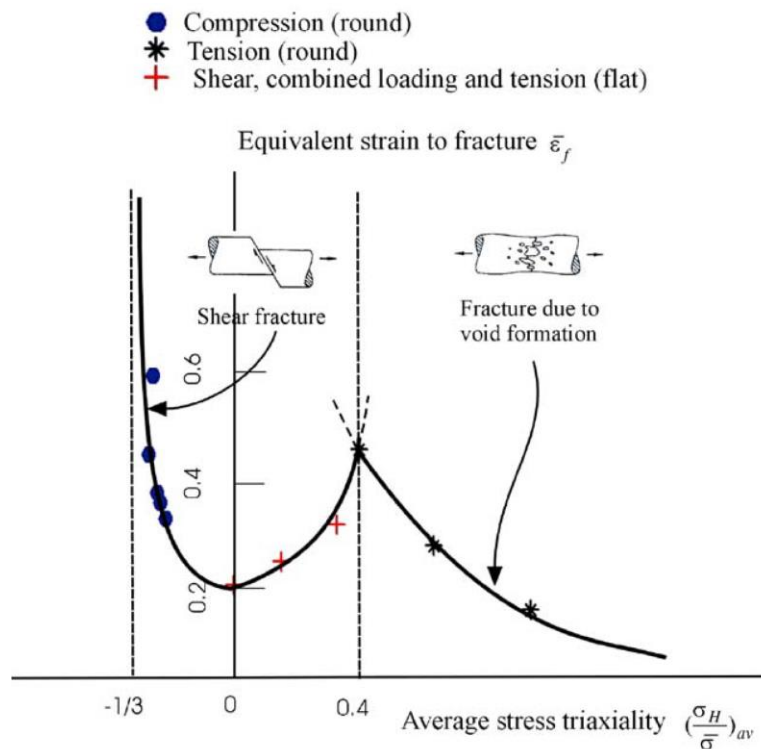
Figure 1.3 Three different branches obtained for ductile fracture at different levels of stress triaxialities (reproduced from Bao and Wierzbicki (2004)).

Teng and Wierzbicki (2006) evaluated the suitability of six fracture models to predict the ballistic impact response of thin aluminium and steel target plates by comparing their numerical results with experimental data available in literature. The candidate failure models selected were the Johnson-Cook (Johnson and Cook, 1985), Bao-Wierzbicki (Bao and Wierzbicki, 2004; Wierzbicki et al., 2005), modified Cockcroft-Latham, Wilkins, maximum shear stress and constant failure strain criteria. They concluded that the stress state dependent Johnson-Cook and Bao-Wierzbicki failure models can predict the experimentally observed fracture patterns and residual velocities. Several attempts have been made to predict the ballistic impact response of thin ductile metal plates using phenomenological models such as the Johnson-Cook model (Gupta et al., 2008, 2007, 2006; Iqbal et al., 2010; Kpenyigba et al., 2013), shear energy based failure criterion (Raguraman et al., 2010), Rusinek-Klepaczko model (Kpenyigba et al., 2015) and the modified Mohr-Coulomb (MMC) model proposed by Bai and Wierzbicki (2009) (Gilioli et al., 2015; Mohagheghian et al., 2017b).

Wierzbicki et al. (2005) and Xue (2007) proposed that the fracture strain values obtained by axisymmetric tensile tests at different stress triaxialities gives an upper limit for ductile fracture. They suggested that experimental data lies between the two bounds corresponding to axisymmetric and plane strain conditions (Figure 1.4). The difference between these two limits is due to sensitivity of ductile fracture to the Lode angle.

Wierzbicki et al. (2005) and Bai and Wierzbicki (2008) assumed that the reduction of the material ductility with decreasing normalised third invariant of stress (Lode angle parameter) has an elliptical form for a particular value of stress triaxiality (Figure 1.5a). As a result, a 3D surface mapping the dependence of equivalent strain at failure on stress triaxiality and Lode angle parameter was obtained as shown in Figure 1.5b.
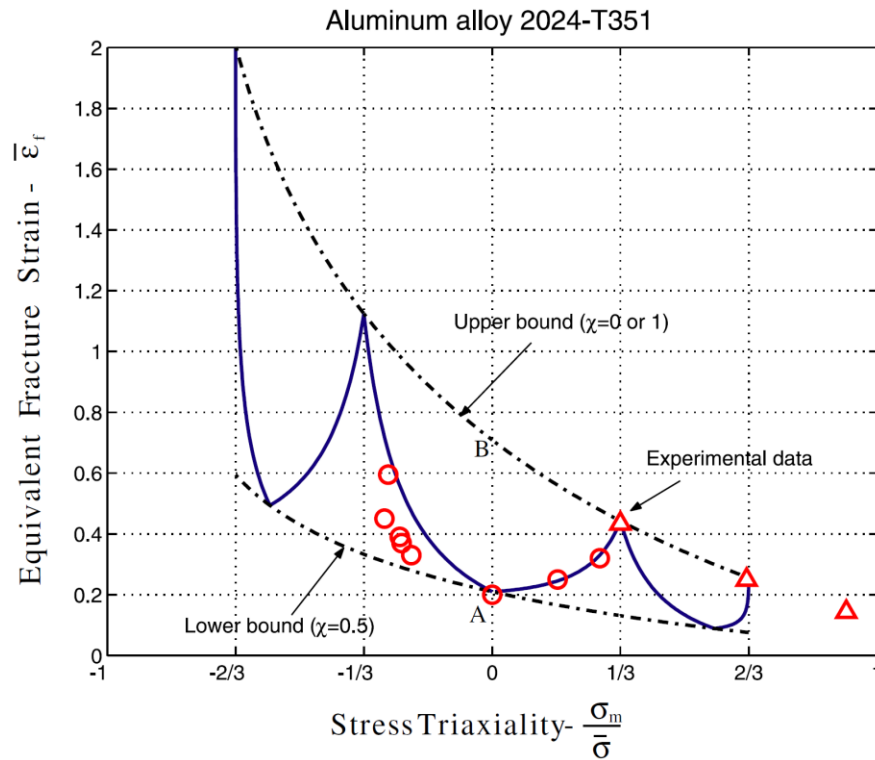
Figure 1.4 Upper and lower bounds for ductile fracture corresponding to axisymmetric and plane strain conditions (reproduced from Xue (2007)).

Bai and Wierzbicki (2009) developed a new fracture model based on the Mohr-Coulomb (MC) fracture criteria. By transforming the MC fracture model from stress space to strain space and considering a general form of hardening rule which depends on both hydrostatic pressure and Lode angle, they proposed a modified Mohr-Coulomb (MMC) criterion. A 2D form of the MMC fracture model considering plane stress conditions was applied by Luo and Wierzbicki (2010) and Li et al. (2010) to analyse the metal forming processes of stretch bending and deep drawing of Advanced High Strength Steels (AHSS).

Recently, modifications have been made in existing failure models to include the dependence of ductile fracture on the Lode angle such as the Gurson model (Nahshon and Hutchinson, 2008), Cockcroft-Latham and Rice-Tracey models (Gruben et al., 2012).

(a)

(b)
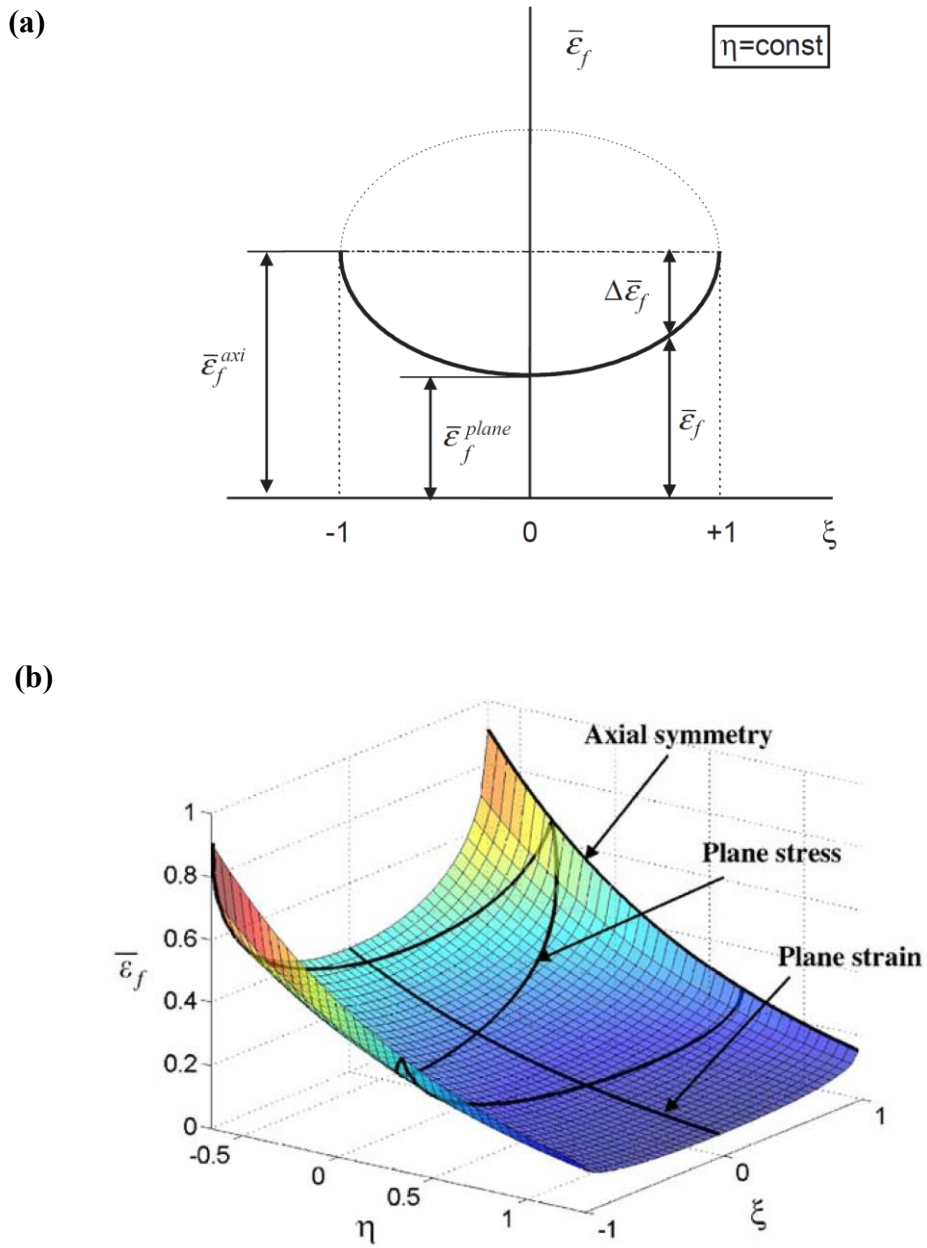
Figure 1.5 (a) Elliptical form for variation of failure strain with Lode angle parameter, and (b) 3D failure surface considering both stress triaxiality and Lode angle parameter dependence (reproduced from Wierzbicki et al. (2005)).

1.5   Failure behaviour of epoxy

High-grade epoxy resins have been used in several high-performance industrial applications, especially as the matrix component in fibre-reinforced composites. Their high specific strength, high specific stiffness, high glass transition temperature and processing ease lead to their almost exclusive use in the manufacture of carbon fibre reinforced polymer (CFRP) composites for aerospace applications (Boeing, 2006; EADS Report, 2006). However, epoxy resin is known to be brittle, and is susceptible to crack initiation and propagation during indentation and impact loading (Bandyopadhyay, 1990; Garg and Mai, 1988). Resistance to impact damage is a critical issue in the development of CFRPs, and depends on the failure properties of the epoxy matrix (Asp et al., 1996a, 1996b, 1995). An effective strategy for increasing the impact damage tolerance of epoxy-based composites is to enhance the fracture toughness of the epoxy resin (Gurusideswar and Velmurugan, 2014; Pandya and Naik, 2016). Studies on the effectiveness of various toughening strategies to enhance the damage tolerance of epoxy are summarized in the following section.

1.5.1 Summary of different toughening strategies

Toughened epoxies are a rapidly developing class of materials for use in modern applications due to their synergistic properties derived from several components, offering unique mechanical, electrical, optical and thermal properties. The enhancement of mechanical properties is due to the large reactive surface area per unit volume of the fillers, interaction of epoxy resin with the fillers and state of dispersion. The mechanical properties of toughened epoxies have been extensively studied including stiffness, toughness, hardness, scratch resistance, damping, creep characterization, high strain rate response, plate impact behaviour and ballistic impact behaviour. Various additives have been used for toughening of epoxy including liquid rubber, thermoplastics, rigid particles, and core-shell particles (Carolan et al., 2016; Day et al., 2001; Lin and Shieh, 1998; Liu et al., 2016; Thitsartarn et al., 2015). Studies indicate an enhancement in fracture energy (Carolan et al., 2016; Sue, 1992; Thitsartarn et al., 2015) and impact resistance (Laurenzi et al., 2013; Naik et al., 2014a, 2014b; Pandya et al., 2012; Pandya and Naik, 2015a, 2015b; Tehrani et al., 2013)

through additional damage mechanisms, when the epoxy resin is toughened with polymeric or particulate additives (Bandyopadhyay, 1990). However, it has been reported that the addition of toughening agents may also lead to a decrease in the failure strength, modulus, and glass transition temperature of epoxy, while increasing its viscosity (Bain et al., 2016; Becu et al., 1997).

Recently, the mechanical response of a variety of epoxy nanocomposites has been investigated to assess the effect of incorporation of nanofillers into the resin. The nanofillers used are alumina/titania nanoparticles (Naik et al. 2014a; Song et al. 2009; Wetzel et al. 2003; Wetzel et al. 2006), nanoclay (Akbari and Bagheri, 2007; Ye et al., 2007), nanosilica (Battistella et al., 2008; Chen et al., 2008; Deng and Ye, 2006; Dittanet and Pearson, 2012; Guo and Li, 2007; Johnsen et al., 2007; Roy et al., 2013; Sun et al., 2011; Wang et al., 2013; Yao et al., 2005, 2008; Zamanian et al., 2013; Zhang et al., 2008), single-walled carbon nanotubes (Fereidoon et al., 2013; Hu et al., 2014; Martinez-Rubi et al., 2011; Shadlou et al., 2013) and multi-walled carbon nanotubes (Ayatollahi et al. 2011; Glaskova et al. 2013; Hsieh et al. 2011; Naik et al. 2014b; Singh et al. 2013; Zhang et al. 2008; Tehrani et al. 2011). Other important aspects including toughening and fracture mechanisms, strain rate response, fatigue properties, energy absorption capability and interphase characterization of nanofilled epoxy have been studied (Gómez-del Río et al., 2014; Mirjalili and Hubert, 2010; Srivastava and Koratkar, 2010; Sun et al., 2009; M Zappalorto et al., 2011; Michele Zappalorto et al., 2011; Zhao and Schiraldi, 2005). There are limited studies on the ballistic impact response of toughened epoxy without fibre reinforcement (Pandya et al. 2012a).

1.5.2 Stress state dependence of failure

Understanding the stress state sensitivity of plasticity and damage is particularly important for complex load cases such as quasi-static and impact indentation (Mohagheghian et al., 2017a, 2017b, 2016, 2015). While there have been several recent studies on the stress state dependent yield and failure behaviour of ductile metals (Bai and Wierzbicki, 2009, 2008a; Bao and Wierzbicki, 2004; Beese et al., 2010), there have been relatively few comparable studies for epoxy resins (Fiedler et al., 2001; Ghorbel, 2008; Kody and Lesser, 1999, 1997; Lesser and Kody, 1997; Morelle et al., 2017; Morin et al., 2010). The yield and failure of

ductile metals depends on all three stress invariants; stress triaxiality, von Mises stress and Lode parameter. It is well established that epoxies exhibit hydrostatic stress dependent yield and failure behaviour. In addition, epoxy polymers exhibit rate and temperature-dependent behaviour with non-linear responses during loading and unloading. It is observed that the mechanical behaviour of epoxy is different in tensile, compressive and shear loading. Several yield and failure criteria have been used for epoxy in literature including modified von Mises (Kody and Lesser, 1999, 1997; Lesser and Kody, 1997), modified Tresca and modified Coulomb criteria. Christensen's yield criterion, Mohr's parabolic criterion (Fiedler et al., 2001) and modified Drucker-Prager criterion (Morelle et al., 2017; Werner and Daniel, 2014) have also been applied to capture the stress-strain behaviour of epoxy over a wide range of stress triaxialities. Equivalent strain-based (Morin et al., 2010) and critical dilatational energy-based (Asp et al., 1996a, 1996b) approaches have also been proposed to account for pressure dependent mechanical behaviour. Ghorbel (2008) developed a generalized yield criterion for polymers, based on the parabolic form of the Drucker-Prager criterion, which includes dependence on the first invariant of the stress tensor (stress triaxiality) as well as the second and third invariants of the deviatoric part of the stress tensor. A good agreement was obtained between the predictions and experimental data for different polymers under various states of stress.

Asp et al. (1995) studied the triaxial tensile response of epoxies to explain the low transverse failure strain of epoxy based composites in terms of the stress state in the epoxy matrix. In subsequent investigations (Asp et al., 1996a, 1996b), a pressure dependent critical dilatational strain energy density criterion was used to predict the stress state dependent yield behaviour of epoxy. Two modes of failure, ductile and brittle, were observed depending on the loading conditions. Brittle failure, observed predominantly in the tensile regime, was attributed to crack initiation arising from micro-cavitation. Lesser and Kody (1997) reviewed the existing yield and failure criteria for predicting the effect of stress state for epoxy. A modified von Mises yield criterion, with hydrostatic stress dependence, was proposed to adequately predict the response of epoxy in states of stress ranging from uniaxial compression to biaxial tension. Further studies (Kody and Lesser, 1999, 1997) elucidated the effect of crosslinking, glass transition temperature, and the addition of CTBN rubber particles on the state of stress at yield and failure in epoxy.

Fiedler et al. (2001) characterized the quasi-static yield and failure criteria for a Bisphenol-A type of epoxy resin, commonly used as a matrix for CFRPs. The results of uniaxial tensile, uniaxial compression and torsion tests on epoxy specimens were fitted to the pressure-dependent Mohr's parabolic criterion. Morin et al. (2010) suggested an equivalent strain-based failure criterion with hydrostatic stress and strain rate dependence which was found to be essential to correctly predict the experimental tensile, notched tensile and shear response of epoxy. Werner and Daniel (2014) proposed an elastic-viscoplastic constitutive model formulated in strain space, and based on a modified Drucker-Prager criterion. This was developed to model the mechanical response of a high-strength epoxy commonly used in carbon fibre composites. The predicted response matched well with the experimental compression and shear behaviour.

Chevalier et al. (2016) used a micromechanics-based approach to develop a brittle failure criterion for highly crosslinked epoxies, in terms of a local critical value of maximum principal stress at the tip of internal defects. The brittle failure criterion provided accurate predictions of failure initiation over a wide range of stress triaxialities, from uniaxial compression to notched tensile response. Morelle et al. (2017) used a pressure dependent Drucker-Prager model to predict the stress-strain response of RTM6 epoxy resin under different loading conditions including uniaxial compression, uniaxial tension, notched tension, shear, and torsion. Fractographic analysis indicated a competition between shear yielding and maximum principal stress driven brittle failure.

1.5.3 Strain rate dependence of failure

Polymers are known to have a strong strain rate sensitivity compared to metals. In order to obtain the high strain rate and ballistic impact response of fibre reinforced epoxy composites, an understanding of the strain rate dependence of yield and failure of the epoxy matrix is essential. The dependence of the constitutive response and damage mechanisms during fracture of thermosetting polymers on strain rate has been studied (Dalmas et al. 2013; Mulliken and Boyce 2006b; Ravi-Chandar 1998). Extensive research is available in literature on the high strain rate and impact behaviour of epoxy. A representative survey is presented in this section.

Miwa et al. (1995) investigated the strain rate and temperature dependence of shear yield strength and shear strength of epoxy resin, with a view to improving its fracture toughness. It had been previously established that shear bands formed in epoxy resin played a major role in determining fracture toughness. Further, shear strength at the fibre-matrix interphase in epoxy matrix based FRPs had been observed to contribute to fracture toughness. In their work, Miwa et al. (1995) observed that shear yield strength and ultimate shear strength of epoxy resin increased as the logarithm of the applied strain rate in the strain rate range of 10^{-2} to 10^2 /s. Also, they found that time-temperature superposition was valid for the shear properties considered. Tay et al. (1995) obtained an empirical strain rate dependent constitutive relationship for neat epoxy resin and glass fibre reinforced epoxy under compressive loading for a strain rate range of 10^{-4} to 10^3 /s. They observed a significant increase in the dynamic modulus with an increase in strain rate. Further, the stress-strain response was observed to be a function of both the strain rate and the stress state in the range of parameters considered.

The mechanical behaviour of epoxy resin under a variety of stress states was investigated by Liang and Liechti (1996). They performed experiments under uniaxial tensile, plane strain compressive, simple shear and biaxial loading to obtain the stress localization response of epoxy. Stress localization in the form of shear bands was observed. The onset of shear banding was seen to be delayed by higher strain rates, while promoted by tensile stresses. Trojanowski et al. (1997) studied the high strain rate thermomechanical behaviour of epoxy under compressive loading using a SHPB apparatus at a strain rate of 2500 /s. They used a fast response infrared radiometer to compute the surface temperature of the epoxy specimen. A significant increase in surface temperature of up to 50°C was observed. The rate of increase in surface temperature was proposed to be directly proportional to the amount of input energy stored as internal energy within the specimen.

Strain rate and temperature dependence of compressive yield strength of epoxy resin was investigated by Mayr et al. (1998) and Cook et al. (1998). Due to their highly cross-linked network structure, resulting in high glass transition temperatures, epoxy resins tend to be more brittle with lower fracture toughness compared to other thermosetting and thermoplastic polymers. The most common damage mechanisms in epoxies due to stress

localization are shear yielding/shear banding, microcracking and crazing, with shear yielding being a key failure mechanism. Mayr et al. (1998) and Cook et al. (1998) studied the effect of strain rate and temperature on the shear yielding mode of damage in epoxies. The yield strength was observed to decrease with an increase in temperature for the range of strain rates considered. Chen and Zhou (1998) studied the uniaxial compressive response of epoxy over a strain rate range of 10^{-4} to 10^3 /s. The compressive strength of epoxy was observed to increase with increasing strain rate until adiabatic heating offset strain rate hardening. Constitutive models predicting the compressive high strain rate response of epoxy resin were presented by Chen and Zhou (1998) and Lu et al. (2001).

Hou et al. (2000) carried out quasi-static and high strain rate torsion tests to understand the mechanical response of epoxy under pure shear loading. Chen et al. (2002) determined the high strain rate behaviour of epoxy under uniaxial tensile and compressive loading. The dynamic stress-strain behaviour under tension was observed to differ significantly from the dynamic compressive response. Also, the dynamic compressive strength of epoxy was found to be significantly higher than its quasi-static compressive strength. Hu et al. (2003) and Xia et al. (2003) investigated the mechanical response of epoxy under multiaxial loading. The viscoelastic behaviour, influence of hydrostatic stress and effect of loading path on stress-state response of epoxy was investigated over a range of strain rates.

Kanchanomai et al. (2005) studied the effect of loading rate on damage and fracture mechanisms of epoxy resin over a loading rate range of 10^{-1} to 10^3 mm/min. The fracture strain under three-point bending was observed to decrease with increasing loading rate. Plastic deformation modes such as formation of shear lips, stretched zone, crazes, and crack blunting were found to be the dominating fracture mechanisms at low loading rates, while brittle fracture modes dominated at high loading rates. Jordan et al. (2008) investigated the compressive behaviour of epoxy over a strain rate range of 10^{-3} to 10^4 /s. An approximately bilinear dependence of yield stress on strain rate was observed which was captured using a one-dimensional Mulliken-Boyce model. Garg et al. (2008) studied the temperature rise in epoxy during high strain rate deformation using a high-speed infrared photovoltaic detector. Strain rates greater than 1000 /s were achieved using a SHPB apparatus, while specimen temperature was measured as a function of strain. A comparison of energy storage versus

dissipative mechanisms showed that the energy storage mechanism in epoxy is independent of strain rate. Littell et al. (2008) evaluated the stress-strain behaviour of epoxy resin under tension, compression and shear loading over a quasi-static strain rate range of 10^{-5} to 10^{-1} /s and over temperatures ranging from room temperature to 80°C. They observed significant strain rate and temperature dependence in the material response.

High strain rate properties of epoxy resin were evaluated under shear (Naik et al., 2010) and compressive loading (Naik et al., 2011). Further, effect of radial constraint on the high strain rate compressive response of epoxy was obtained by Pothnis et al. (2012). These studies (Naik et al., 2011, 2010; Pothnis et al., 2012) reported a significant increase in shear strength and compressive strength of epoxy with an increase in strain rate. Pothnis et al. (2012) observed an increase in compressive strength of epoxy specimens in the presence of radial constraint compared to the case with no radial constraint. Bardella and Belleri (2011) performed uniaxial compression tests on epoxy to evaluate its strain rate dependence in the quasi-static strain rate range of 10^{-6} to 10^{-3} /s. They reported a linear relationship between epoxy yield strength and logarithm of the strain rate in the strain rate range considered. They also observed a mild volumetric instability within the viscoelastic range, allowed by the free lateral expansion of the epoxy specimen. Li and Strachan (2011) used molecular dynamics (MD) to characterize the thermomechanical response of epoxy. They showed that atomistic simulation is capable of capturing mechanical behaviour of thermosetting polymers including role of polymerization degree, thermal history, strain rate and dependence on glass transition temperature. Knorr et al. (2012) investigated the effect of glass transition temperature on the ballistic impact response of epoxy. They demonstrated that glass transition temperature is a dominant factor influencing the ballistic performance of epoxy resins.

1.5.4 Damage mechanisms

Damage mechanisms of epoxy resin include shear yielding, microcracking, crazing, crack tip blunting, shear plugging and formation of ring and radial cracks. Additional damage mechanisms due to toughening of epoxy under quasi-static loading (Chen et al. 2008; Dittanet and Pearson 2012; Johnsen et al. 2007; Zappalorto et al. 2011a; Zhang et al. 2008)

include particle debonding/void formation, plastic void growth and matrix shear banding. The major energy absorbing mechanism is the plastic deformation of epoxy resin. Plastic deformation blunts the crack tip reducing the local stress concentration and allows the material to support higher loads before failure. In some cases, crazing takes place. In case of nanoparticle reinforced epoxy, additional damage mechanisms (Gojny et al., 2005; Mirjalili and Hubert, 2010; Tang et al., 2011) are nanoparticle rupture, bridging, crack deflection, 'sword-in-sheath' mechanism caused by failure of outermost layer in case of MWCNTs and reduction in spherulite size. Some of the possible damage and fracture mechanisms are illustrated in Figure 1.6.
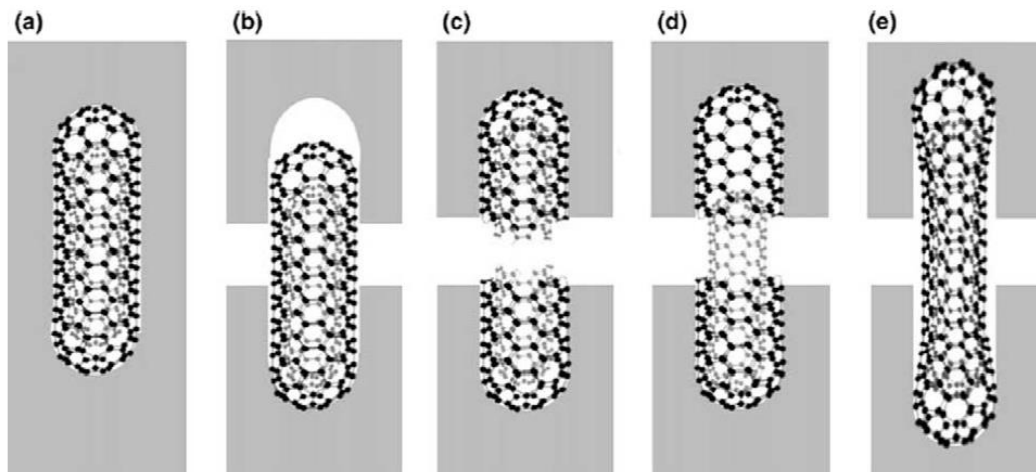
Figure 1.6 Schematic description of possible fracture mechanisms of carbon nanotubes (CNTs), (a) initial state of the CNT, (b) pull-out caused by CNT/matrix debonding, (c) rupture of CNT, (d) telescopic pull-out, (e) bridging and partial debonding of the interface (reproduced from Sun et al. (2009)).

1.6 Impact behaviour of fibre reinforced epoxy composites

Ballistic impact behaviour of fibre reinforced composites has generated considerable interest among researchers and structural engineers alike over the past few decades (Alcock et al., 2008; Cheeseman and Bogetti, 2003; Chen et al., 2014; Duan et al., 2005; Gama and Gillespie Jr, 2011; Gower et al., 2008; Ha-Minh et al., 2013; Mohan and Velu, 2014; Silva et al., 2005). Several analytical and experimental studies are available in literature on the

impact response of epoxy-based composites. Naik et al. (2005, 2006) and Naik and Shrirao (2004) presented an analytical model for the ballistic impact behaviour of epoxy matrix composites. They considered conical deformation and kinetic energy carried by the moving cone in their formulation. The ballistic impact response of thick woven fabric composites was investigated by Naik and Doshi (2005, 2008). The method developed was based on in-plane and through-the-thickness wave propagation and energy balance. Shear plugging was considered in their formulation. Udatha et al. (2012) studied ballistic impact resistance of 3D woven composites. Gama and Gillespie (2008) developed a quasi-static penetration model based on quasi-static punch shear tests.

The behaviour of fibre reinforced epoxy composites under ballistic impact loading depends on the thickness of the target. The analytical formulations presented in the above-mentioned studies are applicable to only specific materials and ranges of thickness. Pandya et al. (2014) presented a generalized analytical formulation of ballistic impact behaviour of 2D woven fabric composites impacted by a rigid cylindrical projectile. The formulation presented, valid for a wide range of laminate thicknesses, considered both shear plugging and tensile failure during conical deformation on the back face of the target.

Experimental studies on various aspects of ballistic impact behaviour of epoxy-based composites such as effect of target thickness, form of reinforcement of the target, damage initiation and evolution due to impact loading, post-impact mechanical behaviour, impact penetration/perforation and stress wave attenuation are available in literature (Abu Talib et al. 2012; Caprino et al. 2007; Haijun et al. 2013; Larsson 1997; López-Puente et al. 2008; Pandya et al. 2012a; Pandya et al. 2012b; Pandya et al. 2013; Sevkat et al. 2009; Shaktivesh et al. 2013; Ulven et al. 2003; Wu et al. 2008). Since the test conditions and the target materials are different in the above-mentioned studies, the corresponding results cannot be directly compared. Numerical studies on ballistic impact behaviour of epoxy-based composites have also been carried out (Gu and Xu 2004; Gu and Li 2005; Haque et al. 2012; López-Puente et al. 2008; Lulu et al. 2013; Sevkat et al. 2009).

There are limited studies on the ballistic impact behaviour of fibre reinforced composites with toughened epoxy matrices (Laurenzi et al., 2013; Pandya et al., 2012; Pol et al., 2012; Rahman et al., 2013; Tehrani et al., 2013). Pol et al. (2012) performed experiments to

understand the effect of adding nanoclay particles to epoxy on the ballistic impact response of woven fabric E-glass/epoxy composites. Pandya et al. (2012) investigated the effect of multi-walled carbon nanotube dispersion in the epoxy matrix on the ballistic impact behaviour of unidirectional E-glass/epoxy. Laurenzi et al. (2013) studied the high velocity response of multi-walled carbon nanotube dispersed Kevlar-29/epoxy. Rahman et al. (2013) carried out experimental investigations on the ballistic impact resistance of carbon nanotube dispersed E-glass/epoxy. Tehrani et al. (2013) investigated the effect of carbon nanotube dispersion on the ballistic impact behaviour of carbon/epoxy composites. These studies reported an enhancement in ballistic impact resistance of fibre reinforced composites with filled epoxy matrices on addition of toughening particles.

Understanding stress state dependence of failure for carbon fibre reinforced epoxy composites is essential to accurately predict their quasi-static and high strain rate perforation response for a wide range of projectile nose shapes. While there are several analytical studies on the ballistic impact behavior of fibre reinforced composites (Caprino et al., 2007; Cheeseman and Bogetti, 2003; López-Puente et al., 2007; Mohan and Velu, 2014; Morye et al., 2000; Naik et al., 2012, 2006, 2005; Pandya et al., 2015; Rajagopal and Naik, 2014; Shaktivesh et al., 2013), there are only a few investigations on projectile nose shape sensitivity of failure initiation in carbon fibre reinforced epoxy composites during ballistic impact (Ben-Dor et al., 2002; Ulven et al., 2003; Wen, 2000).

1.6.1 Damage mechanisms during impact

During ballistic impact, the kinetic energy of the projectile is absorbed by the fibre reinforced epoxy composite target through various damage and energy absorbing mechanisms (Pandya et al. 2014; Shaktivesh et al. 2013; Udatha et al. 2012) such as compression of the target directly below the projectile, compression in the region surrounding the impacted zone, shear plugging of the target, stretching and tensile failure of yarns / layers in the region consisting of primary yarns, tensile deformation in the region consisting of secondary yarns, conical deformation and bulge formation on the back face of the target, delamination, matrix cracking, friction between the projectile and the target and heat generation.

Additional damage mechanisms of toughened epoxy-based composites (Alhazov and Zussman, 2012; Gao et al., 2011; Kinloch et al., 2007; Tsai and Cheng, 2008) include cohesive failure in matrix and interphase regions, adhesive failure at fibre surface, crack path deflection, and fibre bridging and pull-out.

1.7   Summary

As can be seen from the literature, it is apparent that there are limited studies on the impact perforation response of lightweight materials, including thin aluminium alloys and carbon fibre reinforced epoxy composites. These materials have great potential to be used for impact energy absorption. Several attempts have been made to predict the perforation response of thin ductile metal plates using phenomenological models. Previous attempts at modelling ductile fracture during impact considered a limited range of projectile nose shapes. There is a need to accurately predict the onset of ductile fracture in thin ductile metals for a wide range of stress states at higher strain rate loads such as impact.

Thermosetting epoxy resins have been investigated under quasi-static and high strain rate regimes. However, there is clear lack of knowledge regarding modelling the plasticity and failure behavior of epoxies for a wide range of stress states and strain rates. Understanding the stress state sensitivity of plasticity and damage is particularly important for complex load cases such as quasi-static and impact indentation. While there have been several recent studies on the stress state dependent yield and failure behaviour of ductile metals, there have been relatively few comparable studies for epoxy resins. It is well established that epoxies exhibit hydrostatic stress dependent yield and failure behaviour. In addition, epoxy polymers exhibit strain rate and temperature dependent behaviour with non-linear responses during loading and unloading.

While there are several analytical studies on the ballistic impact behavior of fibre reinforced composites, there are only a few investigations on projectile nose shape sensitivity of failure initiation in carbon fibre reinforced epoxy composites during ballistic impact. There is a need to systematically characterize the quasi-static and impact perforation behavior of carbon fibre reinforced epoxy composites for different indenter/projectile tip geometries to

accurately predict their ballistic impact characteristics over a wide range of stress states and strain rates.

In the current investigation, the impact perforation response of thin ductile aluminium alloy plates will be investigated by rigid projectiles of different nose shapes in the sub-ordnance velocity range to span a wide range of stress states. Next, the stress state and strain rate dependent plasticity and failure behavior of epoxy is systematically characterized and modelled phenomenologically. The influence of microstructural modifications in epoxy through two different toughening strategies on the material response is investigated. Finally, experimental studies are performed on the quasi-static indentation and ballistic impact perforation response of carbon fibre reinforced epoxy composites.

Chapter 2   Impact response of thin aluminium alloy plates

2.1   Introduction

In this chapter, the projectile nose shape sensitivity for the impact damage behaviour of thin aluminium alloy plates will be studied. Numerical and experimental investigations are performed on the ballistic impact response of 1 mm thick aluminium alloy 6082-T4 plates. Penetration/perforation behaviour, ballistic limit velocity, energy absorption capability and sensitivity to projectile nose shape are evaluated. Modes of deformation, damage and failure during ballistic impact are assessed experimentally. This study develops further the research work carried out by Mohagheghian et al. on the quasi-static indentation response of thin aluminium alloy plates (Mohagheghian, 2013; Mohagheghian et al., 2017b). Specifically, it aims to provide an understanding of the influence of strain rate on the stress state sensitivity at failure. By starting with a material system that is relatively well understood, albeit at low rates of strain, this study provides a convenient benchmark and point of departure for subsequent studies of epoxy and fibre reinforced epoxy under indentation loading (Chapters 3-5).

The impact perforation response of thin-walled lightweight structural components made of ductile metals or alloys depends on the projectile nose shape. The mechanics of penetration of plates and shells by projectiles has been extensively studied (Backman and Goldsmith, 1978; Corbett et al., 1996). The deformation and failure mechanisms during sub-ordnance impact of thin metal plates and shells are determined to a large extent by the projectile tip geometry (Corran et al., 1983; Iqbal et al., 2016; Leppin and Woodward, 1986; Levy and

Goldsmith, 1984). Previous experimental impact studies have been performed on thin ductile metal target plates using flat, hemispherical, conical and ogival projectile nose shapes to study the perforation resistance and failure mechanisms associated with each projectile tip geometry (Corran et al., 1983; Gupta et al., 2008, 2007, 2006; Iqbal et al., 2010; Kpenyigba et al., 2015, 2013; Levy and Goldsmith, 1984; Palomby and Stronge, 1988; Raguraman et al., 2010; Rodríguez-Millán et al., 2014). Resistance to impact perforation was found to be highest for hemispherical projectiles, corresponding to the maximum energy dissipated during impact (Corran et al., 1983; Gupta et al., 2007; Kpenyigba et al., 2015, 2013; Rodríguez-Millán et al., 2014). The dominant impact energy absorbing modes for flat, hemispherical and conical/ogival projectile nose shapes were shear plugging, tensile tearing, and petal formation and bending, respectively. The mechanism of petal formation and bending during impact of conical and ogival projectiles has been studied extensively though experimental and analytical investigations (Crouch et al., 1990; Ghosh and Travis, 1979; Gupta et al., 2016; Landkof and Goldsmith, 1985; Leppin and Woodward, 1986; Vijayan et al., 2016; Wierzbicki, 1999). Palomby and Stronge (1988) performed impact experiments on thin-walled mild steel tubes using flat, intermediate and hemispherical projectiles. They showed a transition in the dominant failure mechanism, from shear plugging at the periphery of the contact zone for flat projectiles to discing, characterized by dishing and localized radial necking outside the contact region, in case of hemispherical projectiles. The transition between different failure mechanisms has also been studied by other authors by systematically varying the nose shape of a rigid projectile, by changing either the frontal nose radius/tip radius (Corran et al., 1983), the chamfer size/corner radius (Iqbal et al., 2010), or the cone angle/apex angle of the projectile (Ghosh and Travis, 1979; Kpenyigba et al., 2013; Leppin and Woodward, 1986; Vijayan et al., 2016). Additional studies on the impact perforation of thin ductile metal plates include effect of layering/configuration (Gupta et al., 2008, 2016; Iqbal et al., 2012; Iqbal and Gupta, 2011), oblique impact (Awerbuch and Bodner, 1977; Gupta et al., 2017, 2016), effect of target thickness (Abdulhamid et al., 2013; Gupta et al., 2007; Iqbal and Gupta, 2011; Leppin and Woodward, 1986; Senthil et al., 2016; Teng and Wierzbicki, 2005), effect of target span (Iqbal et al., 2015, 2012; Liu and Stronge, 2000; Senthil et al., 2016), double-nosed projectile impact

(Gupta et al., 2017; Iqbal et al., 2013; Kpenyigba et al., 2015), effect of boundary conditions (Tiwari et al., 2014) and effect of anisotropy (Seidt et al., 2013).

It can be clearly seen from previous studies (Corran et al., 1983b; Iqbal et al., 2010; Liu and Stronge, 2000; Mohagheghian et al., 2017a; Palomby and Stronge, 1988) that the projectile nose shape (or "effective nose shape") has a significant influence on the ballistic impact resistance of thin ductile metal plates, since the projectile tip geometry determines the stress state and strain distribution within the impacted target plate. Therefore, there is a need to have a stress state dependent material model capable of predicting the ballistic impact damage behaviour for a wide range of projectile nose shapes. Previous attempts at modelling ductile fracture during impact considered a limited range of projectile nose shapes. Mohagheghian et al. (2017b) demonstrated the elements of the constitutive model necessary for predicting failure for a wide range of indenter nose shapes (from blunt to hemispherical), but for quasi-static edge-clamped perforation loading. There remains uncertainty regarding the effects of strain rate on the conclusions of that study.

The aim of this study is to investigate the projectile nose shape sensitivity for the sub-ordnance impact perforation of a 1 mm thick plate of aluminium alloy 6082-T4. The nose shape of the rigid projectile is systematically varied from flat to hemispherical in two ways, either by introducing different corner radii (R_c) or by changing the frontal nose radii (R_f). These two series of tip geometries provide a wide range of stress states and deformations at the onset of failure in the target. This work bridges the gap between the quasi-static indentation (Mohagheghian, 2013; Mohagheghian et al., 2017b) and high strain rate response of thin aluminium alloy plates to illustrate the sensitivity of state of stress to ballistic impact damage initiation and evolution in thin ductile metal plates. Penetration/perforation behaviour, ballistic limit velocity, energy absorption capability and sensitivity to projectile nose shape are evaluated. Modes of deformation, damage and failure during ballistic impact are assessed experimentally. Next, we consider numerical modelling to predict ductile fracture during impact perforation over a wide range of stress states and assess the suitability of different failure criteria. The role of strain rate sensitivity of aluminium alloy 6082-T4 on the suitability of these failure criteria is evaluated. The finite element simulation results are compared with the experimental ballistic impact data. Finally,

the importance of considering stress state dependent failure models to predict ductile failure during ballistic impact is discussed.

In this investigation, firstly characterization of the quasi-static yield response and calibration of the MMC failure model for AA 6082-T4 by Mohagheghian et al. (2017b) is discussed briefly in section 2.2 and presented in detail in Appendix A. The quasi-static stress state dependent material model developed was then validated by performing quasi-static edge-clamped indentation experiments (Mohagheghian et al., 2017b), described in section 2.3. A summary of the quasi-static perforation test results and development of the FE model used in the numerical analysis is presented. Section 2.4 presents the ballistic impact perforation experiments carried out in the current work. The dependence of the location of failure in the target plate and critical velocities during impact on the projectile nose shape are discussed. Finally, the experimental ballistic impact results are compared with FE in section 2.5. Two candidate ductile failure models, Johnson-Cook and MMC are compared. The numerical model is refined to include strain rate dependent plasticity and failure (section 2.6). The role of strain rate sensitivity of AA 6082-T4 on the suitability of the failure models in predicting the ballistic impact response is evaluated. The projectile nose shape sensitivity, and in turn, the stress state dependence of failure during impact perforation is assessed (section 2.7).

2.2   Quasi-static characterisation data

The quasi-static characterisation methodology of AA 6082-T4 presented by Mohagheghian et al. (2017b) is summarised in Appendix A. The material properties obtained by Mohagheghian et al. (2017b) and used in the present study are given in this section.

Mohagheghian et al. (2017b) measured the anisotropy of AA 6082-T4 sheets by performing quasi-static tensile tests (ASTM Standard E8/E8M) on dog-bone specimens machined with orientations parallel, perpendicular and at 45° to the rolling direction (Appendix A). The values of R_{11}, R_{22}, R_{33} and R_{12} for AA 6082-T4, obtained from Lankford's r values and used to define the Hill yield surface are presented in Table 2.1.

Table 2.1 Measured anisotropy constants for AA 6082-T4 used to define the Hill anisotropic yield surface (Mohagheghian, 2013; Mohagheghian et al., 2017b).

R_{11}	R_{22}	R_{33}	R_{12}	R_{13}	R_{23}
1	1.01	0.876	1.01	1	1

The post-necking strain hardening behaviour was assumed to follow a power law relationship at large plastic strains. The power law relationship is given in Appendix A and the coefficients are given in Table 2.2.

Table 2.2 Coefficients of power law isotropic hardening for AA 6082-T4 (Mohagheghian et al., 2017b).

A	n	ε_0
480	0.0027	0.19

Mohagheghian et al. (2017b) used the MMC model to predict ductile fracture during quasi-static perforation of thin aluminium alloy plates. Details of the MMC model and the failure characterisation methodology is presented in Appendix A. The fracture conditions for the dog-bone and notched specimens are presented in Table 2.3.

Table 2.3 Fracture conditions for dog-bone and notched specimens (Mohagheghian et al., 2017b).

Test	$\bar{\varepsilon}_f$	η_{avg}	$\bar{\theta}_{avg}$
Tensile (dog-bone)	0.63	0.398	0.856
Tensile (notched)	0.50	0.507	0.451

2.3 Quasi-static edge-clamped indentation experiments

Mohagheghian et al. (2017b) performed quasi-static edge-clamped indentation experiments on monolithic AA 6082-T4 plates of 1 mm thickness with different indenter nose shapes to validate the plasticity and failure models calibrated (Appendix A). The quasi-static indentation results from that study are briefly summarized in this section. The nose shape of the indenter was changed from flat to hemispherical by varying either the corner radii or frontal nose radii to span a wide range of stress states, strain distributions and failure modes. A schematic of the indentation test setup used by Mohagheghian et al. (2017b) is shown in Figure 2.1. The test specimens consisted of flat plates with a circular target area of inner diameter 100 mm fully clamped around the edge by a circular steel ring. Twelve M4 bolts were used to fasten the clamping ring through clearance holes in the test specimen (a square plate 130 mm x 130 mm) to a supporting plate. The indentation experiments were conducted using an Instron screw driven machine. Indenters with a diameter of 12.5 mm and different nose shapes were mounted to the load cell on the crosshead of the machine. The tests were carried out at a crosshead speed of 1 mm/min. The indenters were machined from mild steel, and underwent no plastic deformation during the edge-clamped indentation experiments. The force and displacement were obtained from the load cell and crosshead displacement, respectively. The tests were performed until initiation of failure in the plate.

In the first series of edge-clamped indentation experiments, indenters with five different corner radii (R_c), 0 (flat), 1.5, 3, 4.5 and 6.25 (hemispherical) mm were used as shown in Figure 2.2a. Quasi-static force-displacement curves were obtained. It was observed that an increase in corner radius led to an increase in indenter displacement at failure initiation accompanied by a reduction in the slope of the curve. The energy absorbed up to failure (E_A) during quasi-static indentation was obtained from the area under the force-displacement curve. For the second set of indentation experiments, the nose shape of the indenter was gradually changed from flat to hemispherical by decreasing the frontal nose radius (R_f) from infinity (flat) to 6.25 mm (hemispherical) as illustrated in Figure 2.2b.
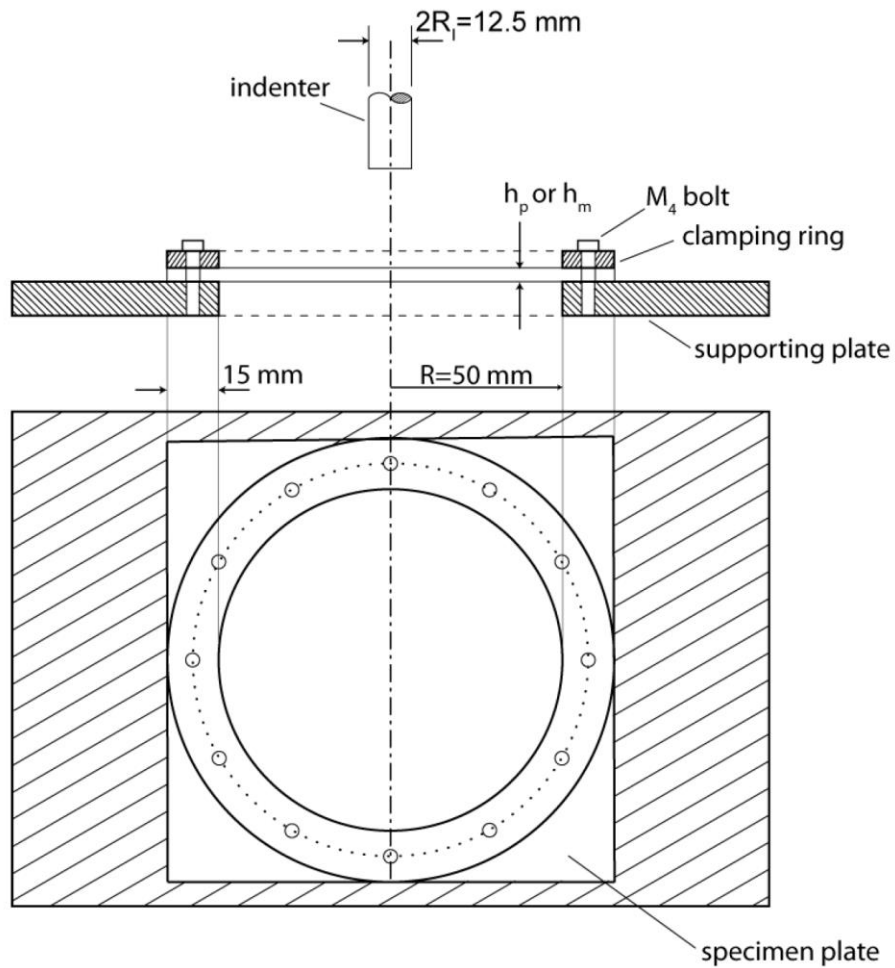
Figure 2.1 Schematic of test setup for quasi-static edge-clamped indentation experiments (Mohagheghian et al., 2017b).

Indenters with intermediate values of R_f, 7.5, 9, 12 and 30 mm were also used. Experimental force-displacement curves were obtained. The slope of the curve gradually decreased as the projectile tip geometry was changed from flat to hemispherical, similar to the case of varying indenter corner radii. However, the peak force and displacement at failure initiation both reached a maximum for R_f equal to 9 mm, with an optimum value of E_A for that indenter nose shape. Inspection of failed plates indicated a transition in failure mode, from shear plugging to tensile failure, at R_f equal to 9 mm.
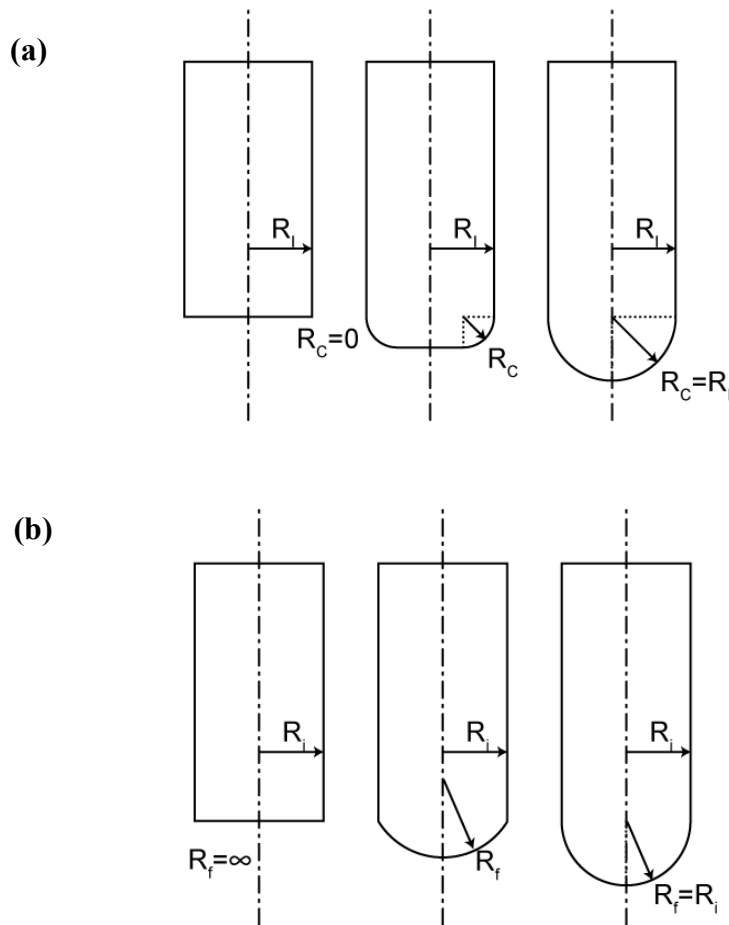
Figure 2.2 Transition from a flat to a hemispherical indenter by (a) changing the corner radius (R_c) and (b) changing the frontal nose radius (R_f) (Mohagheghian et al., 2017b).

2.3.1 Comparison of FE with experiments

Mohagheghian et al. (2017b) developed a 2D axisymmetric model to predict the quasi-static perforation response of thin AA 6082-T4 plates. Details of the model development are presented in Appendix A. The comparison between experimental and numerical results for energy absorbed up to failure initiation E_A is shown in Figures 2.3a and 2.3b for indenters with different corner (R_c') and frontal nose radii (κ_f'), respectively. Non-dimensional parameters R_c' and κ_f' are defined as:

$$R_c' = R_c/R_I$$

$$\kappa_f' = R_I/R_f \tag{2.1}$$

where, R_c and R_f denote the indenter corner radius and frontal nose radius, respectively. R_I is the indenter diameter (equal to 6.25 mm). $R_c' = \kappa_f' = 0$ for a flat indenter and $R_c' = \kappa_f' = 1$ in case of a hemispherical indenter.

A good agreement between experimental results and numerical predictions using the MMC failure model can be seen for both series of indenter shapes. In all cases, the predicted slopes of the force-displacement curves closely matched the experiments. The point of failure in the plate during indentation was successfully captured by the FE simulations except for indenters with sharper edges (close to the flat indenter nose shape).

For indenters with different corner radii (R_c') (Figure 2.3a), the MMC failure model gives an accurate prediction of E_A. To assess the importance of incorporating stress state dependence in the failure model, FE simulations were repeated with a simpler constant failure strain criterion independent of stress state. A constant fracture strain criterion with $\bar{\varepsilon}_f = 0.63$ (obtained from uniaxial tensile dog-bone experiments) was considered. It can be observed from Figure 2.3a that the comparison indicates a poor agreement with the experimental results in terms of E_A. Although the MMC failure model slightly underpredicts the energy absorption for hemispherical and flat indenters, a much closer overall match with the experiment is observed. These quasi-static edge-clamped indentation FE results reinforce that a single failure strain is incapable of predicting fracture for different indenter corner radii. There is a need to use stress state dependent failure models to accurately predict the nose shape sensitivity of the quasi-static indentation response of thin ductile metal plates.
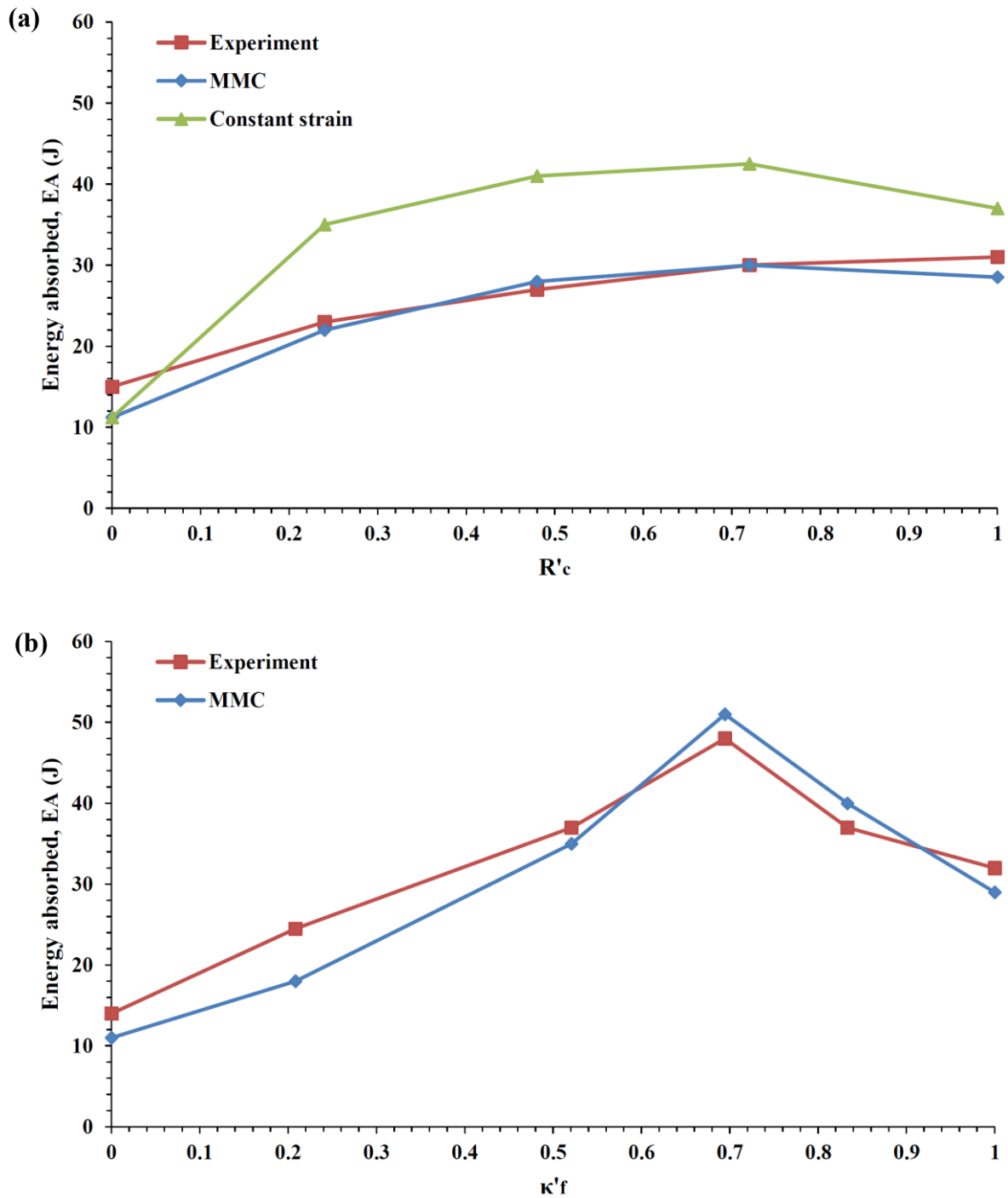
Figure 2.3 Comparison between experimental and numerical values for energy absorbed (E_A) by 1 mm thick AA 6082-T4 plates during quasi-static edge-clamped indentation for indenters with (a) different corner radii (R_c') and (b) different frontal nose radii (κ_f'). (Mohagheghian et al., 2017b).

Mohagheghian et al. (2017b) showed that for all corner radii except the flat indenter, the stress triaxiality at the critical point remains almost constant throughout deformation. Fracture initiated from the back surface of the plate in these cases. In contrast, for the flat indenter, the critical material point was located under the indenter edge on the contact surface and experienced large negative values of η because of the high contact pressure. For a hemispherical indenter, the stress state at onset of failure at the critical material point was close to an equi-biaxial stress state ($\eta = 2/3$ and $\bar{\theta} = -1$). By decreasing the corner radius, the average value of $\bar{\theta}$ reduced. For small corner radii, $\bar{\theta}$ was close to zero indicating plane strain conditions at the critical point. These results indicate the importance of accounting for the Lode angle in the failure model, since the Lode angle parameter emerged as the most important variable for the critical material point for the different indenter nose shapes (except flat). If a failure model were to only include dependency on the stress triaxiality (e.g. Johnson-Cook failure model), the FE results would indicate failure initiation in the plate at approximately the same plastic strain for all indenter nose shapes (except flat), and would thus be unable to reproduce the experimental data.

For variation in the frontal nose radius (κ_f'), comparison between E_A obtained from experiments and FE simulations is shown in Figure 2.3b. A good agreement can be seen across the full range of indenter nose shapes. A peak in E_A is seen at $R_f = 9\ mm$, which corresponds to a transition in the failure mode of failure, and is revealed clearly by the FE simulations. This transition in the failure mode agrees with the observation of Corran et al. (1983), who also reported a maximum in energy absorption for a 1.3 mm thick steel plate.

For $R_f < 9\ mm$, the damage was widely distributed below the indenter and failure initiated from the back surface. Tensile failure occurred in these cases. The location of failure moved from near the edge of the indenter to near to the centre of the plate as the frontal nose radius was reduced. However, for $R_f > 9\ mm$, near the point of failure, damage localised in a narrow band under the edge of the indenter, where failure occurred. The plates underwent failure by the mechanism of shear plugging.

The largest discrepancy between experimental and numerical results were for $R_f > 12\ mm$. Mohagheghian et al. (2017b) attributed this to premature failure in the FE simulations due

to inaccuracies in the calibrated MMC failure strain locus in stress space for shear dominated stress states, which lie away from the two experimental points used to fit the surface (uniaxial tensile and notched tensile). These points were well separated in Lode angle space, but close in terms of stress triaxiality. For the FE material model to perform better under negative stress triaxialities, Mohagheghian et al. (2017b) identified the need for additional calibration data points with low stress triaxialities.

2.4 Impact perforation experiments

We now assess how the numerical model developed by Mohagheghian et al. (2017b) (Appendix A) is affected by increasing the strain rate, by considering ballistic impact perforation of the thin aluminium alloy plate.

2.4.1 Impact test setup

The test specimens used in the present study consist of flat monolithic aluminium alloy plates (AA 6082-T4) of 1 mm thickness with a circular target area of diameter 100 mm fully clamped around the edge. The clamping arrangement for the ballistic impact experiments is identical to the quasi-static indentation test setup (Figure 2.1). Projectiles with diameter 12.5 mm and mass 20.2 g were machined from mild steel. Ballistic impact experiments were carried out with the full range of projectile nose shapes (Figure 2.2). It should be noted that despite the difference in nose shape all projectiles were designed to have the same mass. No plastic deformation of the projectile was observed during any of the impact experiments.

The projectiles were fired using a single stage gas gun with a barrel of internal diameter 12.7 mm. The specimen supporting plate was mounted to a steel frame and oriented normal to the barrel, so that the projectile impacted at 90° to the target. A high-speed camera (Vision Research Phantom V12) oriented perpendicular to the flight of the projectile was used to record the motion of the projectile during its interaction with the target. The projectile was designed with a tail of diameter 5 mm, in which reference grooves were machined, so that the high-speed camera could continue to track the projectile motion throughout its interaction with the target, even when the clamping frame obscured the projectile tip. The

high-speed images therefore provided measurements of both the impact velocity V_i and the residual velocity V_r. Positive velocity was defined in the direction of initial impact. Negative V_r therefore indicates reflection of the projectile, and a positive V_r indicates complete perforation of the target plate. Laser velocity gauges mounted at the barrel exit were used to verify the impact velocity obtained from the high-speed photography, and showed good agreement.

2.4.2 Experimental results

2.4.2.1 Critical impact velocities

A measure of the ballistic limit for each projectile nose shape was obtained by plotting V_r against V_i for several impact experiments. At least six impact experiments were performed for each projectile nose shape. A curve was fitted through all data points with $V_r > 0$. The intersection of this curve with the residual velocity axis is defined as the upper ballistic limit (UBL). Similarly, a curve was fitted through all data points with $V_r < 0$. The intersection of this curve with the residual velocity axis is defined as the lower ballistic limit (LBL). A plot of V_r against V_i for ballistic impact on a AA 6082-T4 target plate by a projectile with different corner radii is shown in Figure 2.4. The energy absorbed by the target (E_A) is calculated as:

$$E_A = \frac{1}{2} m_p (V_i^2 - V_r^2)$$
(2.2)

2.4.2.2 Failure characteristics

Figure 2.5 illustrates the transition in failure mode during ballistic impact perforation of thin aluminium alloy plates with variation in projectile corner radius. Figures 2.5a, 2.5b and 2.5c depict numerical predictions of damage distribution within the thin target plate (left), and photographs of back faces of target plates completely perforated by projectiles (right) with corner radii of 1.5, 3 and 4.5 mm, respectively. The transition from shear plugging dominated failure in case of blunt projectiles to predominantly tensile tearing in case of

hemispherical projectiles is clearly observed. A similar trend is observed in case of variation in the projectile frontal nose radius. From Figure 2.5, it is clearly seen that discing takes place for all three values of R_c considered (Atkins et al., 1998). Discing is attributed to a combination of shear and tensile forces, depending on the ductility of the material. Formation of a cap takes place, with a radius smaller than the projectile radius, for each value of R_c considered. Rotation of the cap formed during ballistic impact around a plastic hinge without complete detachment is observed (Crouch et al., 1990; Langseth and Larsen, 1994; Liu and Stronge, 2000). The radius of the plug formed decreases with an increase in projectile corner radius, indicating a shift in the location of the critical material point at failure initiation towards the centre of the back face of the target.
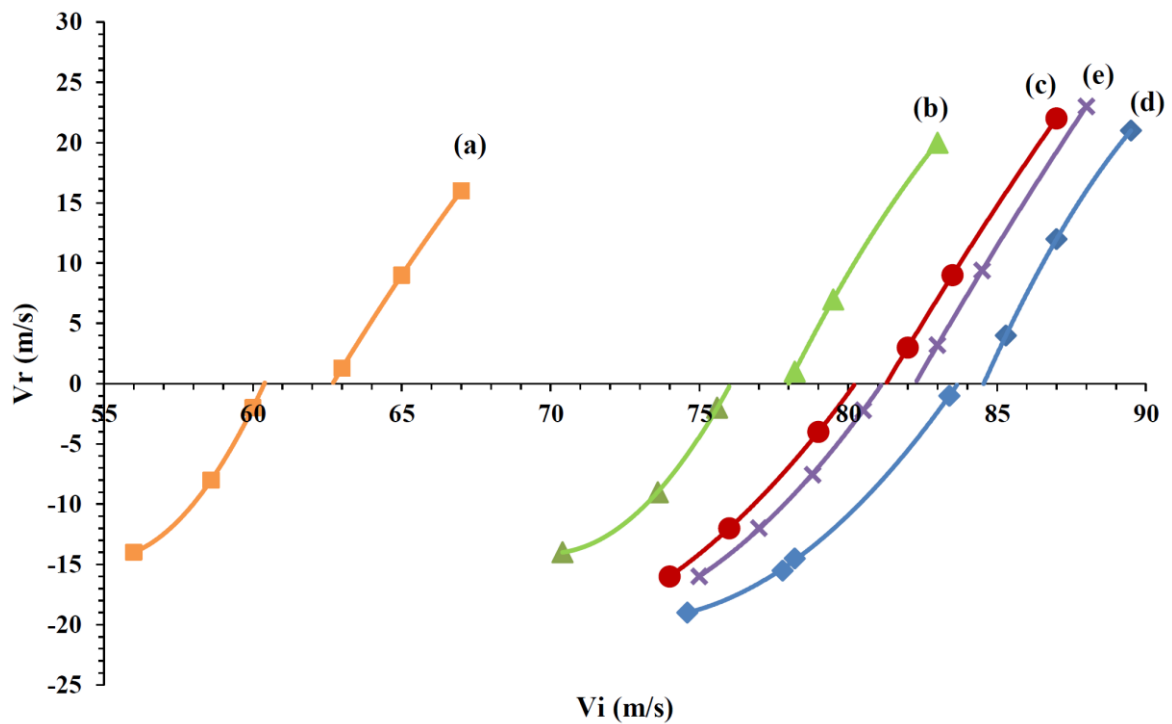
Figure 2.4 Residual velocity (V_r) versus incident velocity (V_i) for ballistic impact on AA 6082-T4 target by a projectile with corner radius of (a) $R_c = 0$ mm (flat), (b) $R_c = 1.5$ mm, (c) $R_c = 3$ mm, (d) $R_c = 4.5$ mm, and (e) $R_c = 6.25$ mm (hemispherical).
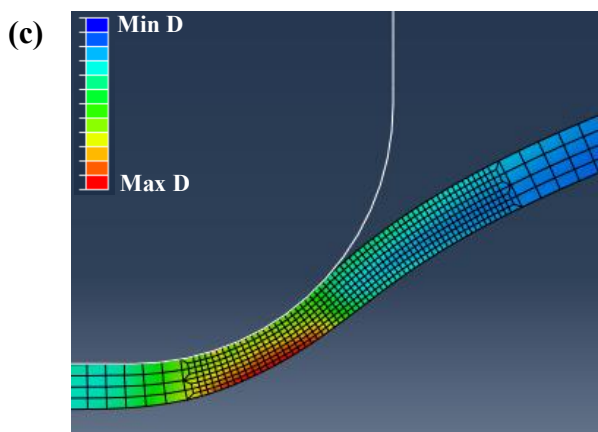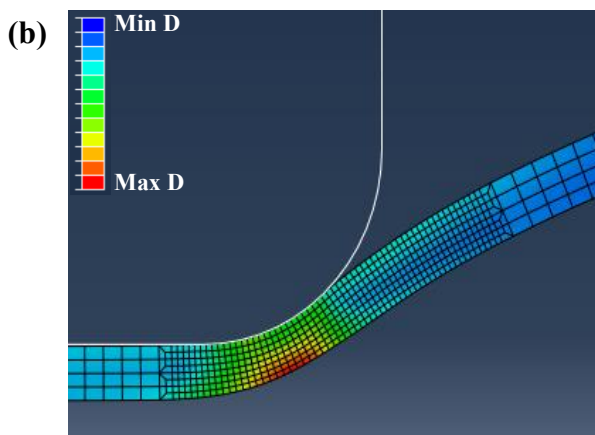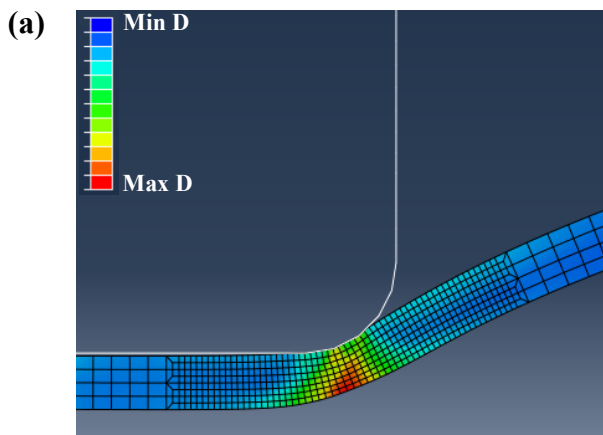
Figure 2.5 Transition in failure modes during impact perforation of thin AA 6082-T4 target with variation in projectile corner radius, numerical results based on MMC failure model (left) and experimental results (right), (a) $R_c = 1.5$ mm, (b) $R_c = 3.0$ mm, (c) $R_c = 4.5$ mm.

Radial crack formation is observed to gradually increase with an increase in the projectile corner radius. For R_c = 1.5 mm (Figure 2.5a), micro-cracks are seen on the back face of the target around the periphery of the exiting projectile. For R_c = 4.5 mm (Figure 2.5c), significant radial crack formation and propagation is observed. These experimentally observed damage patterns during impact are consistent with the quasi-static perforation results obtained by Mohagheghian et al. (2017b).

2.5 Impact perforation model

2.5.1 Initial FE model

The initial FE model used to predict the impact perforation of AA 6082-T4 is the 2D axisymmetric model described in Appendix A. Mass scaling used by Mohagheghian et al. (2017b) to facilitate quasi-static edge-clamped indentation simulations in Abaqus/Explicit is removed for ballistic impact calculations. In the first iteration, strain rate sensitivity of the plasticity was omitted. Plate fracture during impact is modelled by implementing the MMC failure criterion, and failure is considered to occur when damage initiation ($D = 1$) takes place at any location in the target plate (Bao and Wierzbicki, 2004). The MMC failure locus in stress space is implemented in Abaqus in tabular form. Element deletion after failure is considered.

It should be noted that damage in the target plate is restricted to ring cracking in the axisymmetric model. Other tensile failure modes such as radial cracking and petal formation and bending are not captured by the FE model.

Ballistic impact perforation behaviour of the thin monolithic metal target plate is investigated numerically by varying the incident velocity of the projectile (assumed to be rigid in the model) and obtaining values of residual velocity of the projectile and energy absorbed by the target. Deformation and damage behaviour during ballistic impact were noted. In order to assess the effect of state of stress on ductile fracture during ballistic impact, numerical predictions of two types of failure models are considered; the MMC failure model which takes into account the effect of hydrostatic stress and Lode angle, and a simpler

constant failure strain criterion with $\overline{\varepsilon}_f = 0.63$ independent of stress state (obtained from quasi-static uniaxial tensile tests on dog-bone specimens) (Mohagheghian et al., 2017b). It should be noted that both failure criteria are assumed to be independent of the strain rate in the first iteration. This assumption will be interrogated subsequently.

Figures 2.6a and 2.6b show numerical predictions of energy absorbed (E_A) during ballistic impact perforation using MMC failure model for projectiles with different corner and frontal nose radii, respectively. FE results for E_A during impact perforation using constant failure strain model for projectiles with different corner and frontal nose radii are given in Figures 2.7a and 2.7b, respectively for comparison.

As shown in Figures 2.6 and 2.7, four distinct stages of penetration / perforation are observed in the numerical predictions. It should be noted that the projectile impact velocity was increased in increments of 2 m/s to span the four stages of penetration, and further numerical studies were carried out to obtain the critical velocities with an accuracy of 0.2 m/s. The initial damage velocity is defined as the minimum incident projectile velocity for which the damage indicator D equals unity (MMC failure model) or the effective failure strain reaches a value of 0.63 (constant failure strain model) at any material point within the target plate. Failure initiation takes place at this stage, which gradually propagates through the thickness of the target on increasing the incident velocity. The complete damage velocity is defined as the minimum incident projectile velocity at which damage propagates through the entire thickness of the target. At higher incident projectile velocities, complete perforation of the thin metal target takes place. The minimum incident projectile velocity at which the projectile residual velocity is zero is defined as the lower ballistic limit (LBL). Similarly, the maximum incident projectile velocity for which the projectile residual velocity is zero is denoted as the upper ballistic limit (UBL). The upper ballistic limit corresponds to an incident projectile velocity for which the projectile leaves the back face of the target with zero velocity. It is reiterated that in the 2D axisymmetric FE model used in the present simulations, other failure modes besides ring cracking such as radial crack formation, petal formation and petal bending are excluded.

47

Based on Figures 2.6 and 2.7, it is observed that the energy absorbed by the metal target for all four stages of penetration/perforation is significantly influenced by the nose shape of the projectile. It is observed that in case of both, variation in R_c and R_f, the energy absorbed by the target at the ballistic limit (both upper and lower) is maximum for a projectile nose shape intermediate between flat and hemispherical. Both failure models indicate that there exists an 'optimum' projectile nose shape for which energy absorbed by the thin metal target under ballistic impact is maximised.

It is interesting to note that a sharper peak in energy absorbed by the target under ballistic impact is obtained for projectiles with variation in R_f compared to projectiles with variation in R_c, irrespective of the failure model used. In the present study, the global maximum energy absorbed by the metal target is for the case of the projectile with $R_f = 9\ mm$ (Figures 2.6b and 2.7b), and is found to be significantly greater than the energy absorbed by the target when impacted by a hemispherical projectile. This is similar to the case of quasi-static edge-clamped indentation investigated by Mohagheghian et al. (2017b).

For the case of increasing R_c, the MMC failure model (Figure 2.6a) predicts a steady decrease in the ballistic limit range (BLR), defined as the difference in energies absorbed by the target at upper and lower ballistic limits, with the transition from flat to hemispherical projectile tip geometry. This corresponds to a shift in the dominant failure mechanism from shear plugging in case of flat projectiles to predominantly tensile tearing for hemispherical projectiles. A similar trend is observed for variation in R_f (Figure 2.6b). In contrast, the constant failure strain model does not display a gradual trend in BLR values for both sets of projectile tip geometries.

A comparison of the failure models used in the numerical study shows that the constant failure strain model consistently predicts a higher energy absorption capability of the target compared to the MMC failure model for the different projectile nose shapes considered in the present study (Figures 2.6 and 2.7). This is expected since the constant failure strain model, which uses the effective failure strain of the target material under uniaxial tension, is near the upper limit for effective plastic strain at failure for positive values of stress triaxiality.

2.5.2 Comparison with experiment

Comparison between experimental results and numerical values based on MMC failure model is shown in Figures 2.8a and 2.8b for projectiles with different corner and frontal nose radii, respectively. Similarly, comparison between experimental results and numerical values based on constant failure strain model is shown in Figures 2.9a and 2.9b for projectiles with different corner and frontal nose radii, respectively. It may be noted that only the lower and upper ballistic limits can be obtained experimentally. Ductile fracture is a local phenomenon occurring by nucleation, growth and coalescence of micro-voids leading to macroscopic cracks. Thus, it is difficult to experimentally determine the incident projectile velocities corresponding to initial and complete damage within the target plate. The upper ballistic limit is obtained by fitting the experimental data using the Recht-Ipson model for perforation of thin targets (Recht and Ipson, 1963) for positive residual velocities. On the other hand, the lower ballistic limit is obtained by fitting the experimental data to a second-order polynomial least squares approximation, for negative residual velocities close to the ballistic limit.

Experimental data on the energy absorbed during ballistic impact of metal plates shows a similar trend to the results of the numerical simulations. From Figures 2.8 and 2.9, there is good agreement between experimental results and FE simulations based on the constant failure strain criterion for both series of indenter shapes, except near the flat projectile nose shape. On the other hand, it is observed from Figure 2.8 that the experimental results and FE simulations based on the MMC failure model exhibit poor agreement in terms of energy absorption. These results are in contradiction to the quasi-static edge-clamped indentation results obtained by Mohagheghian et al. (2017b) given in Figure 2.3. This indicates that there is a need to refine the plasticity and failure models to account for strain rate sensitivity of the material under consideration. There is a need to recalibrate the failure surface at higher strain rates to accurately model the ballistic impact perforation behaviour.

A comparison between the quasi-static edge-clamped indentation and ballistic impact response of thin monolithic AA 6082-T4 plates (Figures 2.3, 2.8 and 2.9) indicates a similar qualitative trend in terms of energy absorbed by the target plate with respect to

indenter/projectile nose shape, with the values of energy absorbed by the target plate during ballistic impact being significantly higher than those obtained during the indentation tests for the entire range of projectile nose shapes considered.

2.6   Model refinement

In order to refine the finite element model developed by Mohagheghian et al. (2017b) (Appendix A), we introduce strain rate dependence to the plasticity and ductile failure models in turn.

2.6.1 Strain rate dependent plasticity and failure

In the next iteration, the strain rate sensitivity of AA 6082-T4 is considered in the plasticity model. It should be noted that dependence of effective failure strain on strain rate is omitted in this iteration. Studies are available in literature on the uniaxial tensile stress-strain response of AA 6xxx and AA 7xxx aluminium alloys over a wide range of strain rates (Chen et al., 2009; El-Magd and Abouridouane, 2006; Lee and Kim, 2003; Lemanski et al., 2013; Nicholas, 1981; Pothnis et al., 2011; Staab and Gilat, 1991; Yibo et al., 2013; Zhou et al., 2013). Strain rate dependent plasticity for AA 6082-T4 considered in the present study is assumed to obey a Johnson-Cook type post-yield response given by:

$$\sigma_y = \sigma_{y_0}\left(1 + Bln\left(\frac{\dot{\varepsilon}_p}{\dot{\varepsilon}_0}\right)\right) \tag{2.3}$$

where, σ_{y_0} is the yield strength at the reference plastic strain rate $\dot{\varepsilon}_0$ ($\dot{\varepsilon}_0 = 5 \times 10^{-4}$ /s, the strain rate for quasi-static uniaxial tensile dog-bone tests discussed in Appendix A), $\dot{\varepsilon}_p$ is the plastic strain rate and B is a non-dimensional fitting parameter.

Based on a review of the available literature, the range of B is found to vary from 0.004-0.012 for AA 6xxx alloys (Chen et al., 2009; Lee and Kim, 2003; Lemanski et al., 2013; Nicholas, 1981; Yibo et al., 2013) and from 0.011-0.030 for AA 7xxx alloys (Chen et al., 2009; El-Magd and Abouridouane, 2006; Lee and Kim, 2003; Nicholas, 1981; Pothnis et

al., 2011), respectively. A least squares fit to the linear σ_y versus $ln\left(\frac{\dot{\varepsilon}_p}{\dot{\varepsilon}_0}\right)$ curve satisfactorily accounts for the strain rate sensitivity of the post-yield response. A representative value of $B = 0.01$ for AA 6082-T4 is selected for further numerical analysis. Strain rate dependent plasticity is implemented in the Abaqus FE model in tabular form.

Numerical calculations are performed using both the MMC and constant failure strain models with strain rate dependent plasticity to predict the energy absorbed during impact perforation of thin AA 6082-T4 target plates. The values of energy absorbed during ballistic impact increase by 10-20% for both failure models considered across the entire range of projectile nose shapes after the incorporation of the strain rate dependent post-yield response in the FE model. The constant failure strain model now overpredicts E_A for all projectile nose shapes considered. Although the MMC failure model still underpredicts E_A for projectiles close to the flat nose shape, it gives a more accurate prediction of E_A compared to the constant failure strain model across the entire range of projectile nose shapes. This highlights the importance of including strain rate dependence in the plasticity model to accurately predict high strain rate ductile fracture.
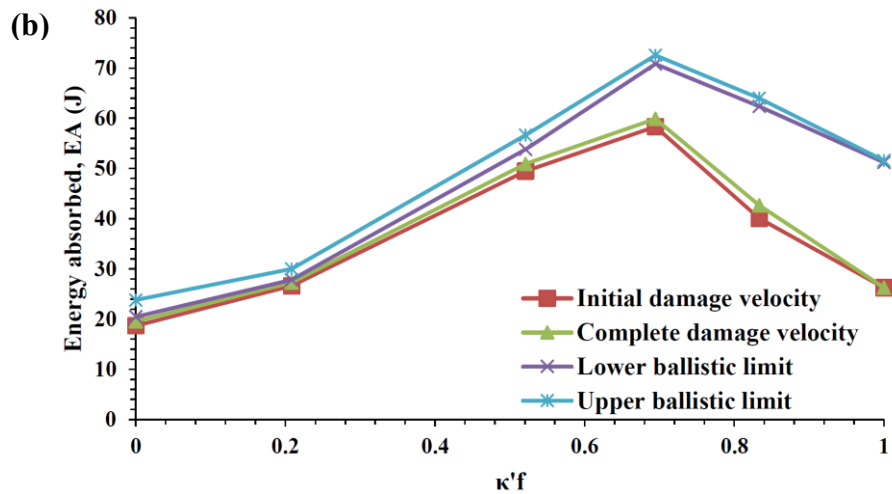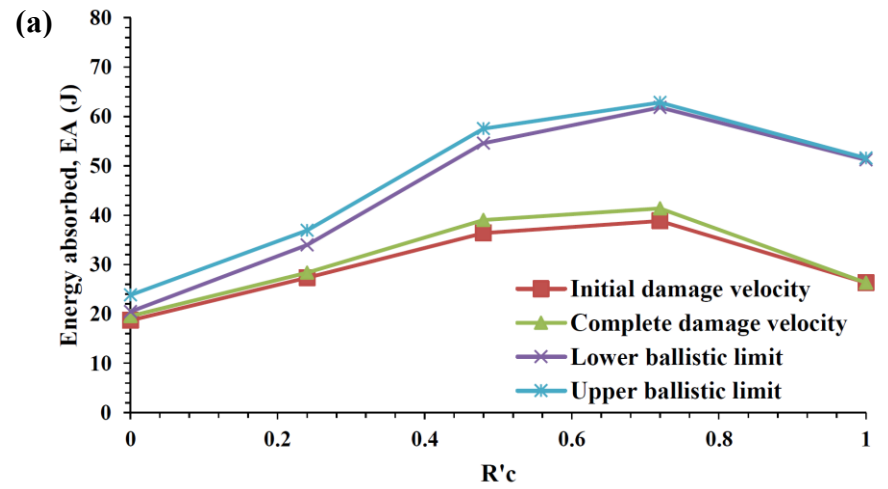
Figure 2.6 Numerical predictions of energy absorbed, E_A during ballistic impact perforation using MMC failure model for projectiles with (a) different corner radii, R'_c and (b) different frontal nose radii, κ'_f.
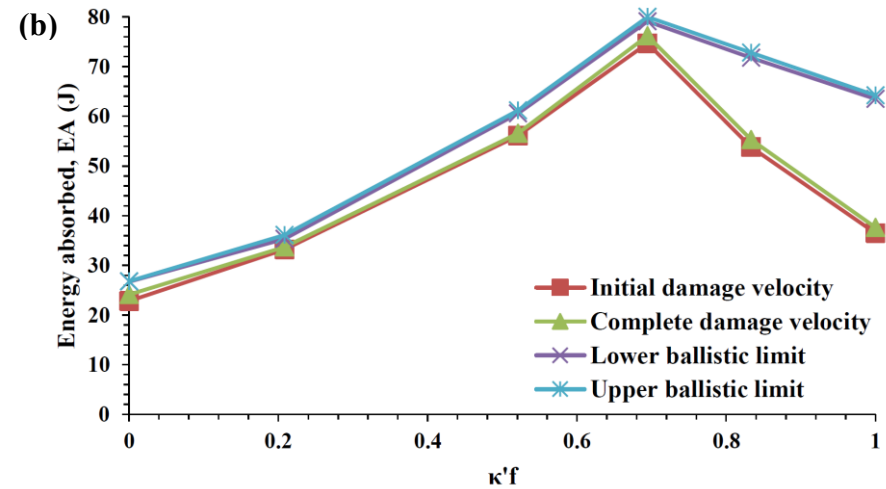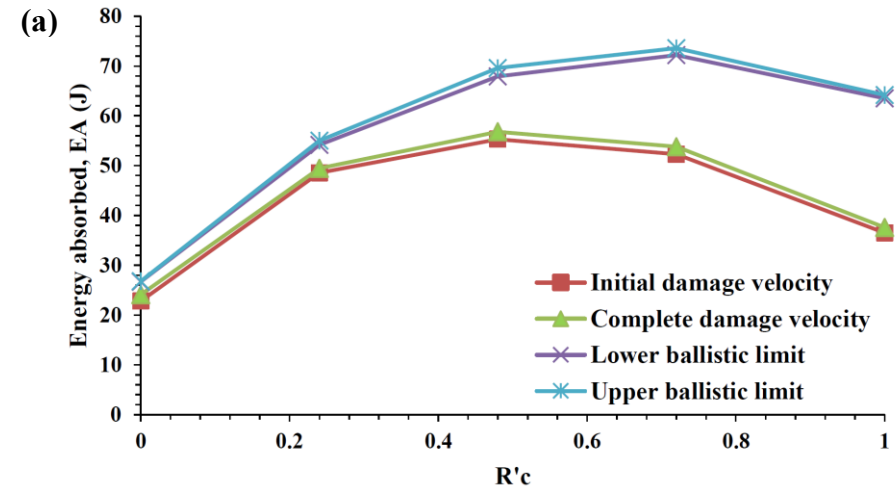
Figure 2.7 Numerical predictions of energy absorbed, E_A during ballistic impact perforation using constant failure strain model for projectiles with (a) different corner radii, R'_c and (b) different frontal nose radii, κ'_f.
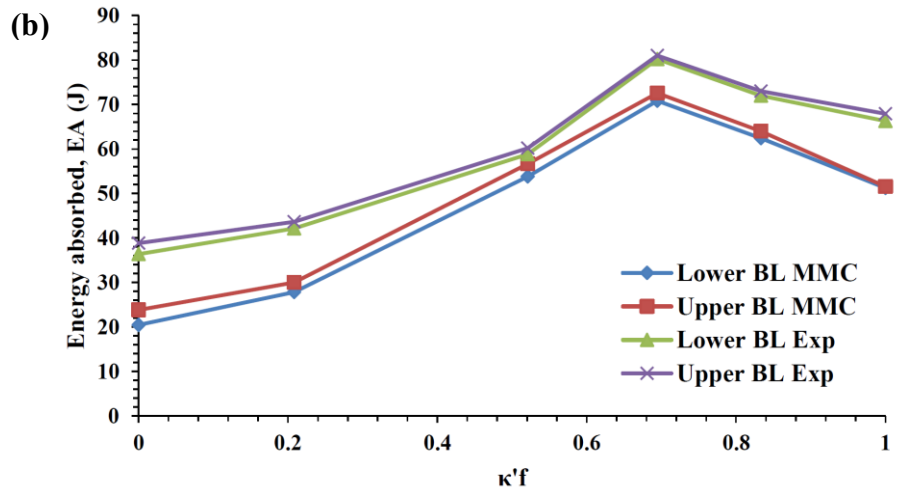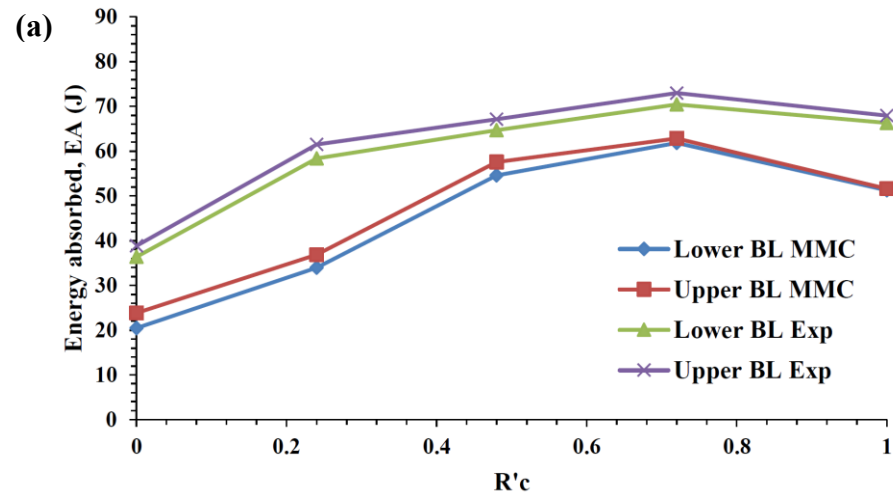
Figure 2.8 Comparison between experimental results and numerical values based on MMC failure model for E_A during impact for projectiles with (a) different corner radii, R'_c and (b) different frontal nose radii, κ'_f.
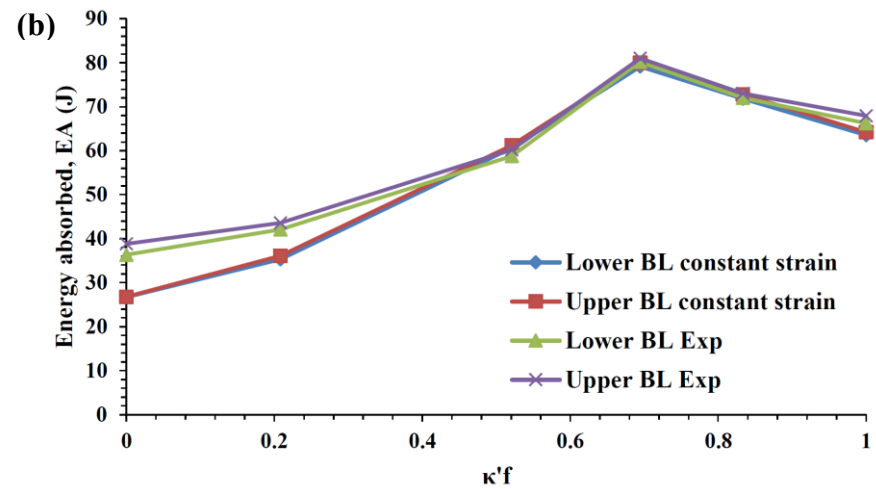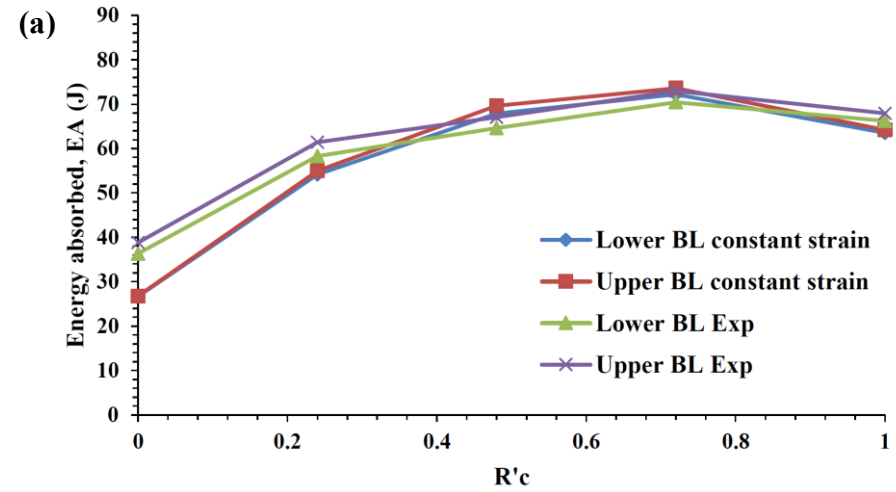
Figure 2.9 Comparison between experiments and FE based on constant failure strain model for E_A during impact for projectiles with (a) different corner radii, R'_c and (b) different frontal nose radii, κ'_f.

Next, the effect of introducing strain rate dependence to the failure strain criteria is investigated. A similar investigation is performed on the strain rate sensitivity of the effective failure strain of aluminium alloys. The strain rate dependence of the effective failure strain, $\overline{\varepsilon}_f$ in the MMC failure model (Equation A.4) is approximated to be of the Johnson-Cook type given by:

$$\overline{\varepsilon}_f = \overline{\varepsilon}_{f_0}\left(1 + D_4 ln\left(\frac{\dot{\varepsilon}_p}{\dot{\varepsilon}_0}\right)\right) \tag{2.4}$$

where, $\overline{\varepsilon}_{f_0}$ is the effective strain at ductile failure at the reference plastic strain rate $\dot{\varepsilon}_0$ ($\dot{\varepsilon}_0 = 5 \times 10^{-4}$ /s, the strain rate for quasi-static uniaxial tensile dog-bone tests discussed in section 2.2.1), $\dot{\varepsilon}_p$ is the plastic strain rate and D_4 is a non-dimensional fitting parameter.

A least squares fit to the linear $\overline{\varepsilon}_f$ versus $ln\left(\frac{\dot{\varepsilon}_p}{\dot{\varepsilon}_0}\right)$ plot satisfactorily accounts for the strain rate sensitivity of the effective failure strain for AA6082-T6, as shown by Zhou et al. (2013). A representative value of $D_4 = 0.007$ is selected for modelling the strain rate dependent ductile failure (Zhou et al., 2013) of AA 6082-T4 in further numerical calculations. The strain rate sensitivity of the MMC failure model is implemented in Abaqus in tabular form.

In the final iteration, numerical studies are repeated using both failure models under consideration, including strain rate sensitivity of both the post-yield response and effective failure strain. The numerically obtained values of energy absorbed by the target during impact across the range of projectile nose shapes in this iteration does not increase significantly (0.5-2%) compared to the first iteration. This indicates that the ballistic impact characteristics of AA 6082-T4 are insensitive to strain rate dependency of ductile failure.

2.6.2 Comparison of MMC and Johnson-Cook model

The need to include stress state dependence to predict ductile fracture has been thoroughly investigated (Bai and Wierzbicki, 2009, 2008; Bao and Wierzbicki, 2004; Mohagheghian et al., 2017b; Teng and Wierzbicki, 2006; Wierzbicki et al., 2005). The Johnson-Cook (JC) failure model (Johnson and Cook, 1985) proposes that effective plastic strain at onset of ductile failure depends only on the first and second invariants of the stress tensor while the

MMC failure model considers dependence of all three stress invariants in predicting ductile fracture in metals. Further numerical studies are performed on the impact response of thin AA6082-T4 targets considering both the MMC and JC failure models in order to investigate their suitability in predicting impact response. The JC failure model is regularly used in numerical studies to predict onset of ductile fracture. However, it is not clear how well the JC model predicts failure of ductile metals for a wide range of projectile nose shapes, without recalibration. The constant failure strain model is not considered in further investigations since it does not correctly capture the projectile nose shape sensitivity of the ballistic impact behaviour. A modified form of the JC failure model is considered, with the effective failure strain given by:

$$\overline{\varepsilon}_f = (D_2 e^{D_3 \eta}) \left(1 + D_4 ln \left(\frac{\dot{\varepsilon}_p}{\dot{\varepsilon}_0} \right) \right) \qquad (2.5)$$

where, η denotes stress triaxiality, $\dot{\varepsilon}_0 = 5\text{x}10^{-4}$ /s is the reference plastic strain rate, $\dot{\varepsilon}_p$ is the plastic strain rate and D_2, D_3 and D_4 are non-dimensional fitting parameters. Results from the two quasi-static characterisation tests; tensile dog-bone and notched experiments (Appendix A) presented in Table 2.3 are used to obtain the values of parameters D_2 and D_3. The values of D_2 and D_3 fitted to the characterisation results are 1.465 and -2.12, respectively. $D_4 = 0.007$ is used from section 2.5.2.1.

The quasi-static MMC and JC failure models considered in further calculations are shown in the stress triaxiality-Lode parameter space in Figure 2.10. The MMC model considers dependence of both stress triaxiality and Lode angle on ductile fracture while the JC model considers only hydrostatic stress dependence and is independent of the Lode angle.
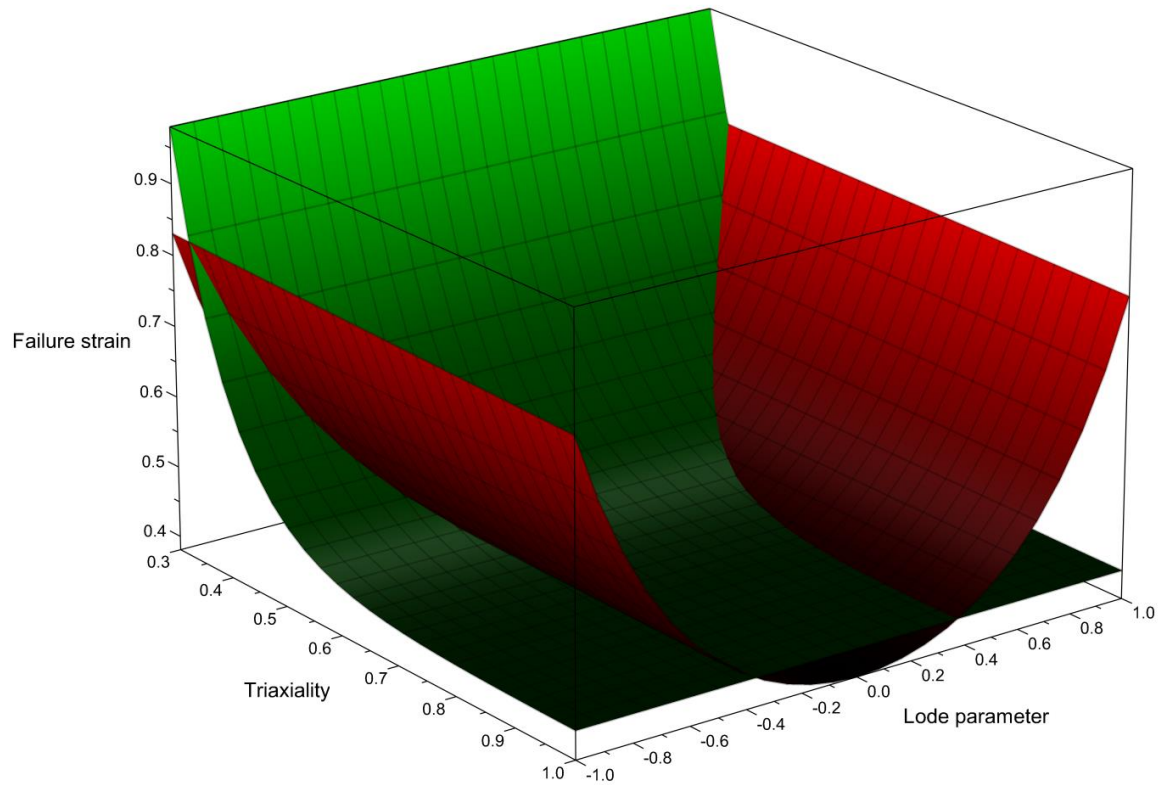
Figure 2.10 3D plots of stress state dependence of ductile failure strain for MMC (red) and JC (green) failure models.

Figures 2.11a and 2.11b show a comparison between experimental results and numerical predictions of E_A at upper ballistic limit based on the MMC and JC failure models for projectiles with different corner and frontal nose radii, respectively. It should be noted that the experimental values of E_A at upper ballistic limit are obtained by fitting the projectile impact velocity vs residual velocity curve using the Recht-Ipson model, for positive residual velocities. As a result, unique experimental values of E_A at upper ballistic limit are obtained for each projectile nose shape. Numerical results with and without strain rate dependent plasticity and failure are shown for both failure criteria for comparison. For the case of variation in projectile corner radius (Figure 2.11a), both the MMC and JC failure models without strain rate dependent plasticity and failure (QS) under-predict E_A for all corner radii considered, with the JC model providing a better overall match with the experimental results.

This is similar to the earlier observation from Figures 2.8a and 2.9a, which illustrate the constant failure strain model providing more accurate predictions of E_A compared to the MMC model. This reinforces the need to include strain rate sensitivity of yield and failure in the material model considered to avoid spurious predictions. From Figure 2.11a, the JC model with strain rate dependent plasticity and failure accurately predicts the experimental results for the flat and hemispherical projectile. However, the JC model overpredicts E_A for the intermediate corner radii. On the other hand, the inclusion of strain rate dependence in the plasticity and MMC failure model in the FE calculations successfully predicts the experimental results for corner radii near the hemispherical nose shape $(R_c \geq 3\,mm)$. However, there is a large discrepancy between the experimental and numerically obtained results for E_A based on the MMC model near projectile corner radii close to the flat nose shape $(R_c \leq 3\,mm)$.

For projectiles with different frontal nose radii (Figure 2.11b), the quasi-static (QS) JC model provides a superior overall match with the experiments than the QS MMC model, mimicking the trend observed in Figure 2.11a for projectiles with varying corner radii. The strain rate dependent JC model overpredicts the experimental results for all intermediate frontal nose radii between flat and hemispherical, while the strain rate dependent MMC failure model predicts E_A reasonably well for all projectile frontal nose radii except for $\kappa'_f = 0$ (flat nose shape).

2.7   Discussion: Projectile nose shape sensitivity and stress state dependence

Figure 2.12 shows a plot of average stress triaxiality versus average Lode angle parameter for the critical material point within the AA 6082-T4 target plate at the onset of ductile fracture during ballistic impact based on the strain rate dependent MMC and JC failure models for the entire range of projectile nose shapes considered. The MMC failure model accurately predicts the location and mode of failure observed experimentally for both series of projectile nose shapes. The JC failure model gives a good match with the experiments in

57

terms of location of failure within the target during impact perforation, except for projectiles with nose shapes close to flat.

For variation in projectile corner radius, FE calculations based on the MMC failure model indicate that, for all nose shapes except flat, the value of stress triaxiality remains largely constant (0.56-0.61) during impact damage initiation (Figure 2.12). Fracture initiates from the back surface of the target in these cases, similar to the case of quasi-static edge-clamped indentation investigated by Mohagheghian et al. (2017b). However, for the flat-nosed projectile, the critical material point is located at the periphery of the projectile on the contact surface and experiences a value of stress triaxiality $\eta = -0.26$ (Figure 2.12). Increasing the projectile corner radius across the range of nose shapes from flat to hemispherical leads to a steady decrease in the average value of Lode angle parameter from 0.16 to -0.45 (Figure 2.12). The JC failure model, independent of the Lode angle, predicts that stress triaxiality varies in a narrow range (0.55-0.64) at the critical failure point at onset of ductile fracture during impact for all projectile corner radii considered. Fracture is predicted to initiate from the back surface for all projectile nose shapes implying fracture through tensile tearing, with $\eta = 0.6$ for the flat projectile. This contrasts with the value of $\eta = -0.26$ predicted for the flat projectile based on the MMC model (Figure 2.12). Perforation experiments indicate failure of the thin AA 6082-T4 target plate impacted by a flat projectile through the mechanism of shear plugging. This experimental observation agrees better with the location of failure predicted by the MMC model than that predicted by the JC model. These results indicate that the JC model is unable to predict the projectile nose shape sensitivity of the location and mechanism of ductile fracture during impact perforation. These results also stress the importance of including Lode angle dependence in the failure model.
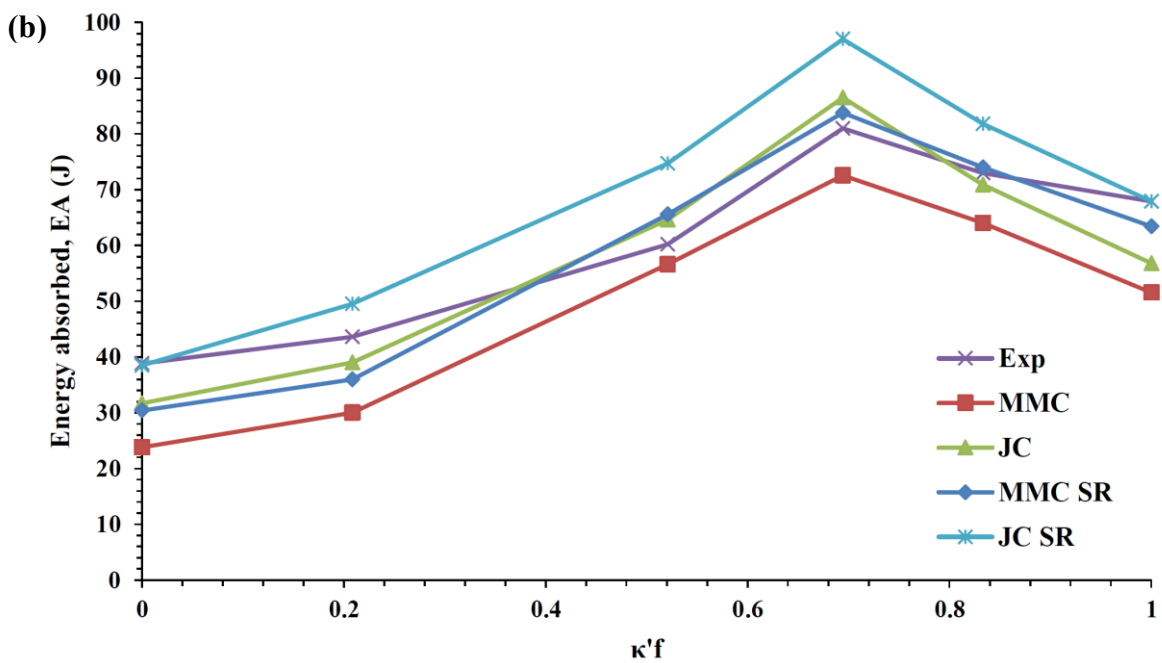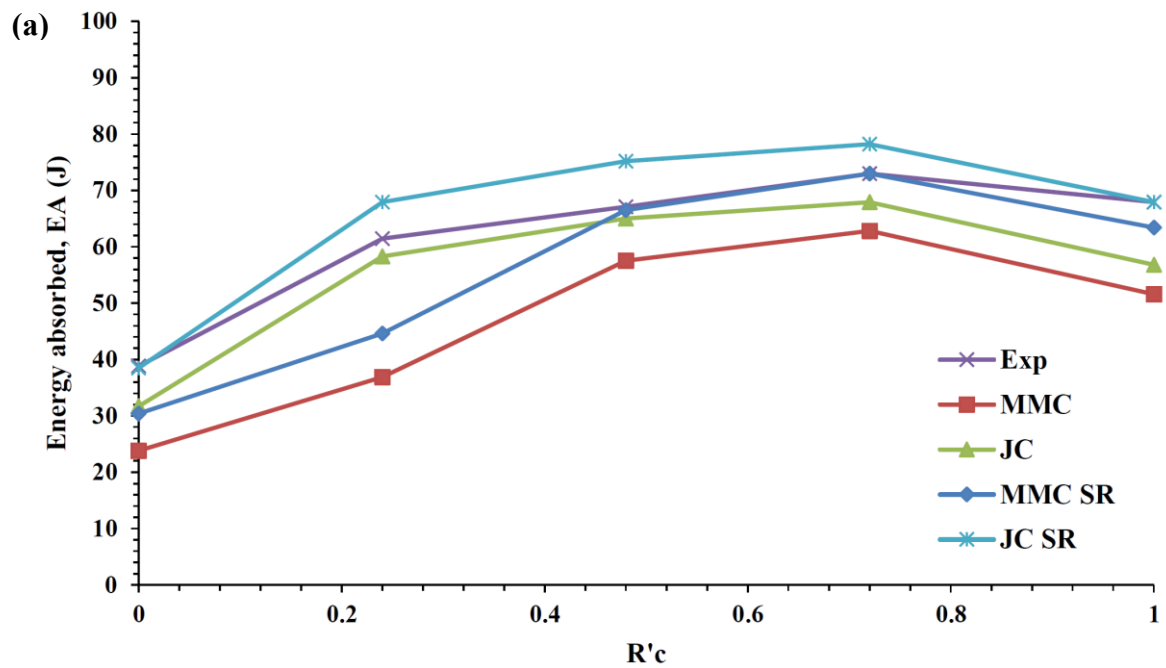
Figure 2.11 Comparison between experimental results and numerical values for energy absorbed at upper ballistic limit based on MMC and JC failure models with and without strain rate (SR) dependent plasticity and failure for projectiles with (a) different corner radii, R'_c and (b) different frontal nose radii, κ'_f.
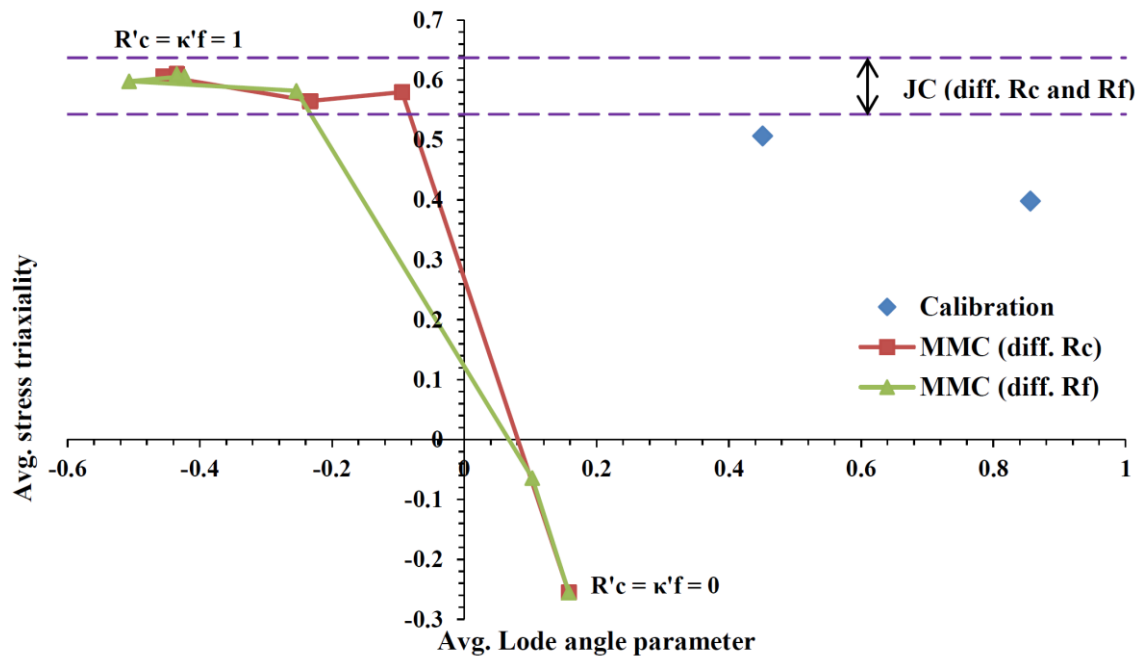
Figure 2.12 Average stress triaxiality versus average Lode angle parameter for the critical material point at onset of ductile fracture during impact based on MMC and JC failure models for projectiles with different corner radii, R'_c and different frontal nose radii, κ'_f.

In case of changing projectile frontal nose radius, the MMC failure model predicts stress triaxiality varying between 0.58-0.61 at the critical material point for $R_f \leq 12 \; mm$ at failure (Figure 2.12). For $R_f \geq 30 \; mm$ (close to flat projectile nose shape), the stress triaxiality is negative, ranging from -0.26 for the flat-nosed projectile to -0.06 for $R_f = 30 \; mm$. Decreasing the projectile frontal nose radius from flat to hemispherical leads to a steady decrease in the average value of Lode angle parameter from 0.16 to -0.50 (Figure 2.12). FE predictions based on the MMC model indicate a transition in the mechanism of failure, from shear plugging dominated fracture for $R_f \geq 30 \; mm$ to tensile tearing for $R_f \leq 12 \; mm$ during impact perforation of the target. This prediction matches reasonably well with the experimentally observed transition in failure mode at $R_f = 9 \; mm$. The JC failure model predicts a narrow band of stress triaxiality (0.55-0.63) across all projectile frontal nose radii. The JC model predicts tensile failure initiating at the back surface for all projectile nose

60

shapes and fails to effectively capture the transition in failure mode observed in the impact perforation experiments. Therefore, it can be concluded that the strain rate dependent MMC failure model is most suitable for predicting the ballistic impact perforation characteristics of thin ductile metal plates.

Discrepancies between experimental and numerical results for E_A using the MMC failure model for projectile nose shapes close to flat can be attributed to premature failure in the FE simulations arising from limited calibration tests used to define the MMC failure surface in stress space, an observation echoed by Mohagheghian et al. (2017b). There is a need to perform additional calibration tests at negative stress triaxialities to improve the accuracy of FE predictions for these cases.

2.8 Conclusions

Experimental and numerical investigations are performed on the ballistic impact behavior of a thin aluminium alloy 6082-T4 target. This study focuses on predicting the projectile nose shape sensitivity of the impact perforation characteristics including critical velocities, energy absorption capability, states of stress and deformation at onset of failure, and failure mechanisms. Two series of projectile tip geometries are considered to provide a wide range of loading distributions within the target at failure initiation. The suitability of different failure models is assessed to predict ductile fracture over the entire range of stress states by comparing FE calculations with experimental impact perforation results. The role of strain rate sensitivity of aluminium alloy on the suitability of these failure criteria is evaluated. The specific observations are:

- Four distinct stages of perforation are observed in the numerical predictions; initial damage, complete damage, lower ballistic limit and upper ballistic limit.
- Energy absorbed by the thin ductile metal target is significantly influenced by the nose shape of the projectile. Energy absorbed by the target is the highest for a projectile nose shape intermediate between flat and hemispherical. There exists an optimum projectile nose shape for which energy absorbed by the target is maximised.
- A sharper peak in energy absorbed by the target is obtained for projectiles with variation

in R_f compared to projectiles with variation in R_c. The global maximum energy absorbed by the target is for the case of the projectile with $R_f = 9mm$.

- There is a need to include strain rate dependent plasticity and failure in the FE material model to better predict the ballistic impact behaviour.

- Numerical predictions based on the modified Mohr-Coulomb and Johnson-Cook failure criteria are compared with experimental results to assess their suitability in predicting stress state dependent ductile fracture. The Johnson-Cook model cannot accurately predict the transition in failure mode of ductile fracture during impact perforation. Therefore, it can be concluded that of the different failure criteria considered, the strain rate dependent modified Mohr-Coulomb failure model is most suitable for predicting the ballistic impact perforation characteristics of thin ductile metal plates.

- Discrepancies between experimental and numerical results for E_A using the MMC failure model for projectile nose shapes close to flat can be attributed to premature failure in the FE simulations arising from limited calibration tests used to define the MMC failure surface in stress space. There is a need to perform additional calibration tests at negative stress triaxialities to improve the accuracy of FE predictions for these cases.

Chapter 3   Prediction of failure initiation in core-shell particle filled epoxy

3.1   Introduction

In this chapter, the quasi-static failure response of core-shell particle (CSP) filled epoxy resin will be studied. Epoxy toughened by the addition of CSPs is of practical interest as a matrix material in fibre-reinforced composites where impact damage tolerance is of particular concern. In this chapter, the stress state sensitivity of plasticity and failure in CSP filled epoxy is investigated, which is necessary to understand the indentation resistance of the material. This provides a necessary basis for understanding the influence of alternative toughening strategies and the strain rate on the epoxy response (Chapter 4), and subsequently the effect of the matrix toughening on the impact resistance of fibre-reinforced composites (Chapter 5).

In recent years, epoxy resins have been used in a wide variety of applications including structural adhesives, surface coatings, and as the matrix component in fibre-reinforced composites. High-grade epoxies possess several useful properties such as high specific strength, high specific stiffness, high glass transition temperature, excellent resistance to environmental degradation, dimensional stability, processing ease and long service life, leading to their almost exclusive use in the manufacture of carbon fibre reinforced polymer (CFRP) composites for aerospace applications. However, epoxy resin is known to be brittle, and is susceptible to crack initiation and propagation (Bandyopadhyay, 1990; Garg and Mai, 1988). Resistance to damage is a critical issue in the development of CFRPs, and depends on the failure properties of the epoxy matrix (Asp et al., 1996a, 1996b, 1995). An effective

strategy for increasing the impact damage tolerance of epoxy-based composites is to enhance the fracture toughness of the epoxy resin (Gurusideswar and Velmurugan, 2014; Pandya and Naik, 2016). Various additives have been used for toughening of epoxy including liquid rubber, thermoplastics, rigid particles, and core-shell particles (Carolan et al., 2016; Day et al., 2001; Lin and Shieh, 1998; Liu et al., 2016; Thitsartarn et al., 2015). Studies indicate an enhancement in fracture energy (Carolan et al., 2016; Sue, 1992; Thitsartarn et al., 2015) and impact resistance (Laurenzi et al., 2013; Naik et al., 2014a, 2014b; Pandya et al., 2012; Pandya and Naik, 2015a, 2015b; Tehrani et al., 2013) through additional damage mechanisms, when the epoxy resin is toughened with polymeric or particulate additives (Bandyopadhyay, 1990). However, it has been reported that the addition of toughening agents may also lead to a decrease in the failure strength, modulus, and glass transition temperature of epoxy, while increasing its viscosity (Bain et al., 2016; Becu et al., 1997).

Understanding the stress state sensitivity of plasticity and damage is particularly important for complex load cases such as quasi-static and impact indentation (Mohagheghian et al., 2017a, 2017b, 2016, 2015). While there have been several recent studies on the stress state dependent yield and failure behaviour of ductile metals (Bai and Wierzbicki, 2009, 2008; Bao and Wierzbicki, 2004; Beese et al., 2010), there have been relatively few comparable studies for epoxy resins. Several yield and failure criteria have been used for epoxy in literature including modified von Mises (Kody and Lesser, 1999, 1997; Lesser and Kody, 1997), modified Tresca and modified Coulomb criteria. Christensen's yield criterion, Mohr's parabolic criterion (Fiedler et al., 2001) and modified Drucker-Prager criterion (Morelle et al., 2017; Werner and Daniel, 2014) have also been applied to capture the stress-strain behaviour of epoxy over a wide range of stress triaxialities. Equivalent strain-based (Morin et al., 2010) and critical dilatational energy-based (Asp et al., 1996a, 1996b) approaches have also been proposed to account for pressure dependent mechanical behaviour. Ghorbel (2008) developed a generalized yield criterion for polymers, based on the parabolic form of the Drucker-Prager criterion, which includes dependence on the first invariant of the stress tensor (stress triaxiality) as well as the second and third invariants of the deviatoric part of the stress tensor. A good agreement was obtained between the predictions and experimental data for different polymers under various states of stress.

This study aims to systematically characterise and model phenomenologically the quasi-static stress state dependence of plasticity and failure of core-shell particle toughened epoxy DLS 1832-1. As discussed in the above studies, it is well established that there is a need to include hydrostatic stress (pressure) dependence to obtain the quasi-static initial yield and failure surface of epoxy. Furthermore, two types of failure, ductile and brittle, can be anticipated over a wide range of stress triaxialities. It is therefore crucial to identify the regimes of triaxiality in which each mode of failure is active. However, as discussed subsequently, there are no standard protocols for characterising unambiguously this stress state sensitivity for epoxies. For toughened epoxies, significant ductility can be expected across a wide range of triaxialities, which poses a further challenge. It will be shown that accurate modelling of conditions at failure is sensitive to the details of the strain hardening.
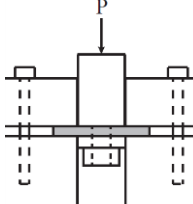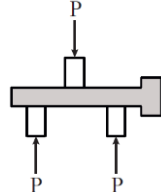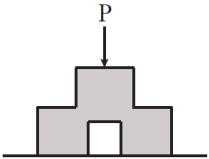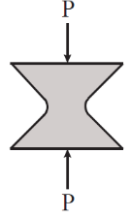
In section 3.2, current stress-state dependent constitutive models and experimental techniques are reviewed, for application to the toughened epoxy. It is shown that the properties of epoxy pose particular challenges for the accurate assessment of the stress state at the onset of yield and failure. Preliminary FE simulations indicate that identification of local states of stress at failure initiation, both within and in the vicinity of the gauge section, is essential to correctly capture the critical locations, as well as the type/regime of failure initiation. It is concluded that an iterative experimental and numerical approach is necessary. A systematic, iterative approach to model development allows us to identify how specific modelling approximations, such as pressure independent plasticity and different strain hardening models, influence the predictive accuracy. Quasi-static compression, tension and shear punch tests are carried out on toughened epoxy DLS 1832-1, to span a wide range of stress triaxialities (section 3.3). An iterative approach using finite element analysis in parallel with the obtained experimental results is used to obtain the stress state dependent quasi-static initial yield and failure surfaces for the filled epoxy (section 3.4). The material model thus developed is then applied to the more complex loading case of indentation. Quasi-static edge-clamped and back face supported indentation experiments are carried out with three different indenter nose shapes; flat, intermediate, and hemispherical. The experimental results are compared with FEA in order to validate the model (section 3.5).

3.2 Assessment of characterisation techniques

In this section, we employ finite element analysis to interrogate the suitability of candidate characterisation strategies for probing the stress state dependence of plasticity and failure for epoxies.

There exists no standard test protocol that allows the stress state dependence of the mechanical properties of polymers to be systematically probed. Conventional tensile dog-bones and compression disk specimens span a limited range of stress triaxiality, and therefore additional specimen geometries are sought to supplement these. Various specimen geometries have been developed to investigate the effect of stress triaxiality on the failure response of ductile metals. These include: the shear-compression specimen, shear-compression disk, hat-shaped specimen, double-shear specimen, shear punch specimen and butterfly specimen, as described by Dorogoy et al. (2011). Dorogoy et al. (2011) also describe specimen geometries for the specific investigation of stress triaxiality effects, including the circumferentially-notched tensile specimen, notched plane specimen, shear and plane-notched tensile specimen and a standard tensile specimen with transverse hydrostatic compression. Dorogoy et al. (2011) and Karp et al. (2013) proposed a shear-compression disk specimen that is particularly attractive for systematically probing the yield and failure properties of ductile metals under controlled stress triaxiality. This is sketched in Figure 3.1. They observed a good agreement with experimental results for steel and aluminium alloys using the Johnson-Cook failure criterion. A summary of different specimen types, their relative ease of manufacture, applicability to high strain rate (HSR) loading experiments, schematic of the test setup and range of stress triaxiality is given in Table 3.1. The shear-compression disk is chosen as a representative candidate specimen for the subsequent simulation studies in this section.

Table 3.1 Summary of different candidate specimen geometries (Dorogoy et al., 2011).

Candidate specimen geometry	Ease of manufacture	HSR applicability	Schematic of test setup	Stress triaxiality range
Shear-compression specimen	Moderate	No		Negative
Shear-compression disk	Moderate	Yes	Figure 3.1	Low negative to positive
Shear punch specimen	Easy	Yes		Negative
Double shear specimen	Easy	Yes		Low positive
Hat-shaped specimen	Moderate	No		Negative
Butterfly specimen	Difficult	Yes		Negative
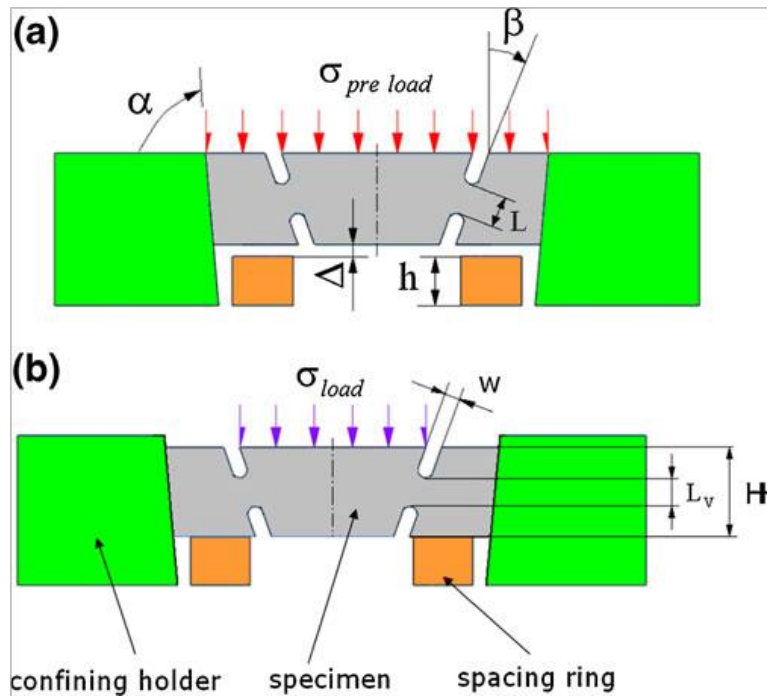
Figure 3.1 Experimental setup for quasi-static studies on shear-compression disk specimens, (a) pre-load stage (acting over entire width of specimen W_s), (b) main loading stage (acting over width of the test section W_t) (reproduced from Dorogoy et al. (2011)).

3.2.1 FE analysis of different candidate specimen geometries

In this section, we perform some preliminary finite element calculations in order to assess the suitability of both standard (compression disks, tensile dog-bones) and non-standard (the shear-compression disk) test specimens for characterizing epoxy. In particular, we aim to assess to what extent the nominal stress state in the gauge section is likely to give an accurate representation of conditions at failure. As described previously, epoxy can undergo a transition from a ductile to a brittle response over specific ranges of stress triaxiality. Understanding how this might affect the interpretation of the characterization experiments is essential. Furthermore, if large plastic strains are experienced before fracture, it is important to understand how this deformation alters the critical locations and apparent states of stress in the test specimens.

68

For the purposes of this initial assessment, an elastic-plastic constitutive model fitted to literature data for epoxy was used, as follows. The elastic properties used in the FEA are based on the uniaxial compression test data obtained by Fiedler et al. (2001). The density ρ = 1250 kg/m^3, Young's modulus E = 3.6 GPa and Poisson's ratio ν = 0.39. Isotropic linear elasticity is assumed for the elastic deformation. The strain hardening behavior was also based on the uniaxial compression test data (Fiedler et al., 2001) with compressive yield stress $\sigma_{y,c}$ = 117 MPa, compressive failure stress σ_f = 410 MPa and failure strain ε_f = 0.36. The hardening curve was implemented in the finite element package Abaqus/Standard in tabular form. The onset of yielding is assumed to obey Mohr's parabolic criterion, given by:

$$\sigma_v^2 + 3\sigma_h\left(\sigma_{y,c} - \sigma_{y,t}\right) - \sigma_{y,c}\sigma_{y,t} = 0 \tag{3.1}$$

where, σ_v is von Mises stress, σ_h is hydrostatic stress, and $\sigma_{y,c}$ and $\sigma_{y,t}$ are the compressive and tensile yield strengths, respectively. The value of $\sigma_{y,t}$ = 93 MPa was based on the uniaxial tensile test data obtained by Fiedler et al. (2001).

Initiation of failure within the specimen was also taken to follow Mohr's parabolic criterion. This was fitted to the quasi-static uniaxial compression and tensile properties obtained by Fiedler et al. (2001). The failure surface is given by (all values in MPa):

$$\sigma_v^2 + 382\sigma_h - 21150 = 0 \tag{3.2}$$

In the following FE calculations, element failure is not included in the model, but the above criterion is used to identify the time step and location at which failure is predicted to initiate.

A 2D axisymmetric model of the shear-compression disk was developed using the finite element package Abaqus/Standard. The geometry of the test specimen is given in Figure 3.1. The key dimensions are gauge length L = 2 mm, thickness H = 6 mm, notch width w = 1 mm, width of test section W_t = 12.45 mm and width of disk specimen W_s = 22.7 mm. Axisymmetric continuum elements (CAX4R) were used to discretize the shear-compression disk. Local mesh refinement was necessary in the gauge section. Quasi-static simulations were carried out at a loading rate of 0.12 mm/min, corresponding to a nominal strain rate of 10^{-3} /s, where we take the nominal strain ε_n to be defined as δ/L_v, where δ and L_v denote vertical displacement of the specimen and vertical length of the gauge section (Figure 3.1),

respectively. The nominal strain rate is defined as the applied loading rate divided by L_v. FE calculations were performed in order to assess the effect of friction between the specimen and the supports (by varying μ from 0 to 0.3), the effect of implementing a tie constraint between the specimen and the vertical support (i.e. sticking friction) and effect of variations in the notch angle β on the stress state during damage initiation.

The evolution of the damage indicator, given by Equation 3.2, within a shear-compression disk specimen with $\beta = 0°$ is shown in Figure 3.2a. It was observed that the damage pattern shown in Figure 3.2a is consistent across different values of notch angle β and coefficient of friction μ (including for sticking friction, i.e. a tie constraint). Damage is observed to occur first near the notch, where the value of hydrostatic stress is large and positive. This point is referred to subsequently as the critical point, and occurs in the same location for all combinations of β and μ. It is noted that the stress triaxiality is a maximum at that location. Figure 3.2b shows a plot of σ_v versus σ_h at the critical point (A) and the centre of the gauge section (B) for different values of β, when the failure criterion is first satisfied at that location. From Figure 3.2b, the values of σ_v and σ_h span a wide range at the gauge section. However, they fall in a much narrower range of 65-72 MPa and 38-44 MPa at the critical point, across the full range of notch angle β and coefficient of friction μ. This implies that the shear-compression disk specimen risks introducing ambiguity in identifying the stress state at failure if used to characterize epoxy, on account of this material's greater sensitivity to tensile stress triaxialities (and hence premature failure at the notch) versus ductile metals.

Further FE simulations were carried out on standard tensile dog-bone, notched tensile and compression disk specimens, to check that standard geometries are not similarly affected. FE simulations for the tensile dog-bone and notched tensile specimens were performed in 3D with the geometry discretized using solid elements. The geometry of the tensile dog-bone specimen was as per ASTM Standard D638-14 (Type V) while the geometry of the notched specimens was identical to those used by Beese et al. (2010). While the bottom surface of each type of tensile specimen was fully clamped, a displacement boundary condition was applied to the top surface to simulate the motion of the crosshead. A 2D axisymmetric model of the compression disk specimen with radius $r = 4$ mm and thickness $t = 4$ mm was developed in Abaqus/Standard. The lower edge of the compression disk was

fully clamped and a displacement boundary condition was applied to the top edge. The contact surfaces at the top and bottom of the compression disk specimen were considered to be frictionless ($\mu = 0$).

The observed evolution of the damage indicator (D) (Equation 3.2) for these types of specimens is shown in Figures 3.3 and 3.4. The corresponding plots of σ_v versus σ_h at damage initiation for the critical point (A) and the centre of the gauge section (B) are shown in Figure 3.5. It should be noted that the nominal strain ε_n is defined as $\delta/2r_n$ for the notched tensile specimen, where δ and r_n denote grip displacement and notch radius, respectively.

3.2.2 Discussion

Shear-compression disk specimens can be used to effectively control the state of stress at the centre of the gauge section of the specimen (B) at the onset of damage by varying β, and thus systematically span the failure envelope of epoxy. However, because of the material properties of epoxy, damage may first initiate at a critical point (A) away from the gauge section, at a state of stress that is almost independent of the parameter β. There is therefore a risk that the failure surface cannot be mapped reliably.

For traditional test specimen geometries (tensile dog-bone, compression disk, notched tensile specimen), although a critical point (A) also exists away from the gauge section (B), the state of stress at the onset of failure is similar at both points. Thus, the position on the failure surface can be more confidently determined.

Furthermore, test methods using these specimens are well-established and the specimens are easier to manufacture from plane sheets compared to the shear-compression disk specimens. They are also suitable for testing over a wide range of strain rates. However, the traditional test specimens do not offer the same versatility for systematically varying the state of stress at the centre of the gauge section (B) compared to the shear-compression disk specimens, allowing a more limited number of points on the failure envelope to be probed.
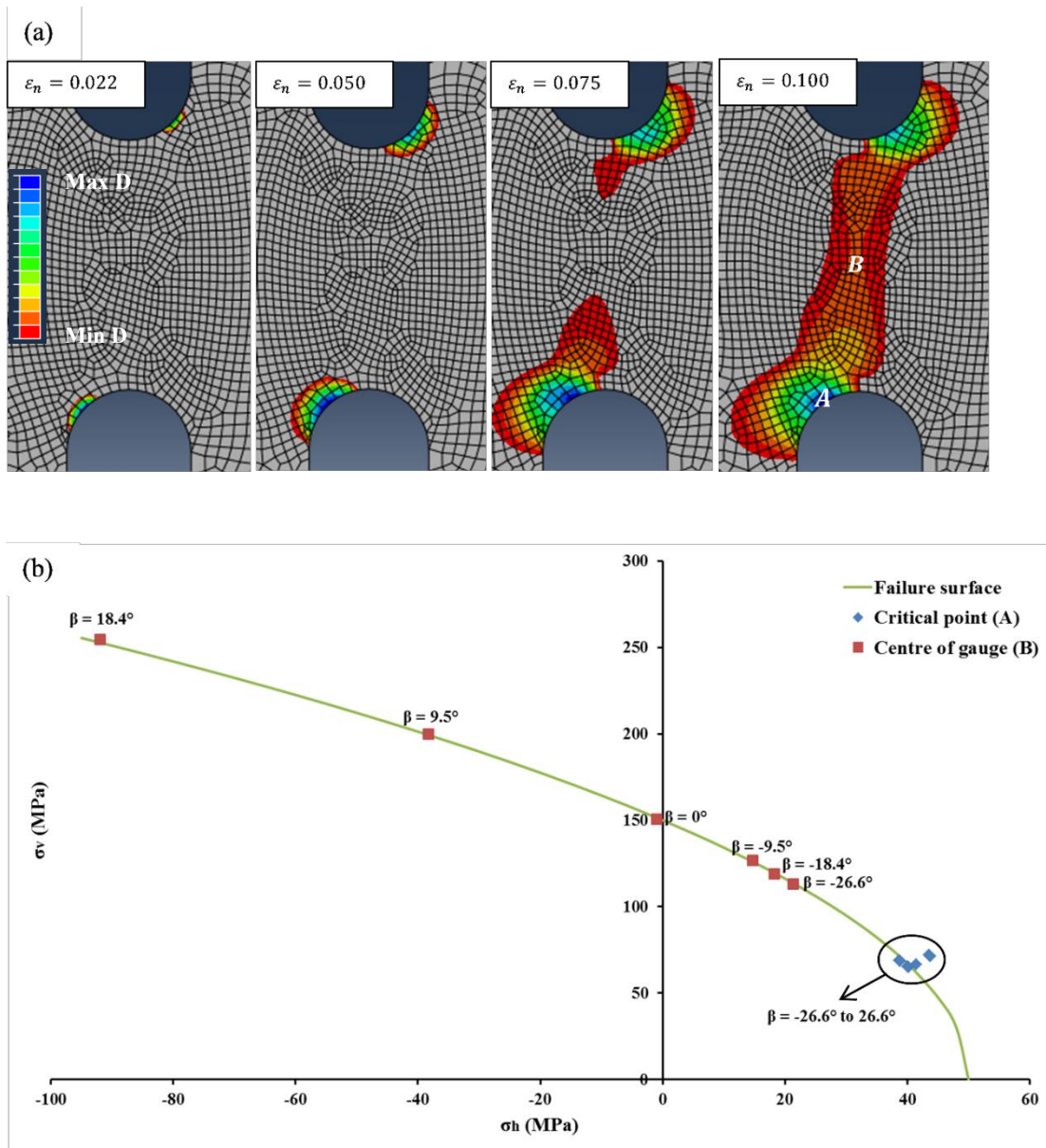
Figure 3.2 (a) Evolution of damage indicator with nominal strain in a shear-compression disk specimen ($\beta = 0°$), (b) Plot of σ_v versus σ_h at damage initiation for critical point (A) and centre of gauge (B).
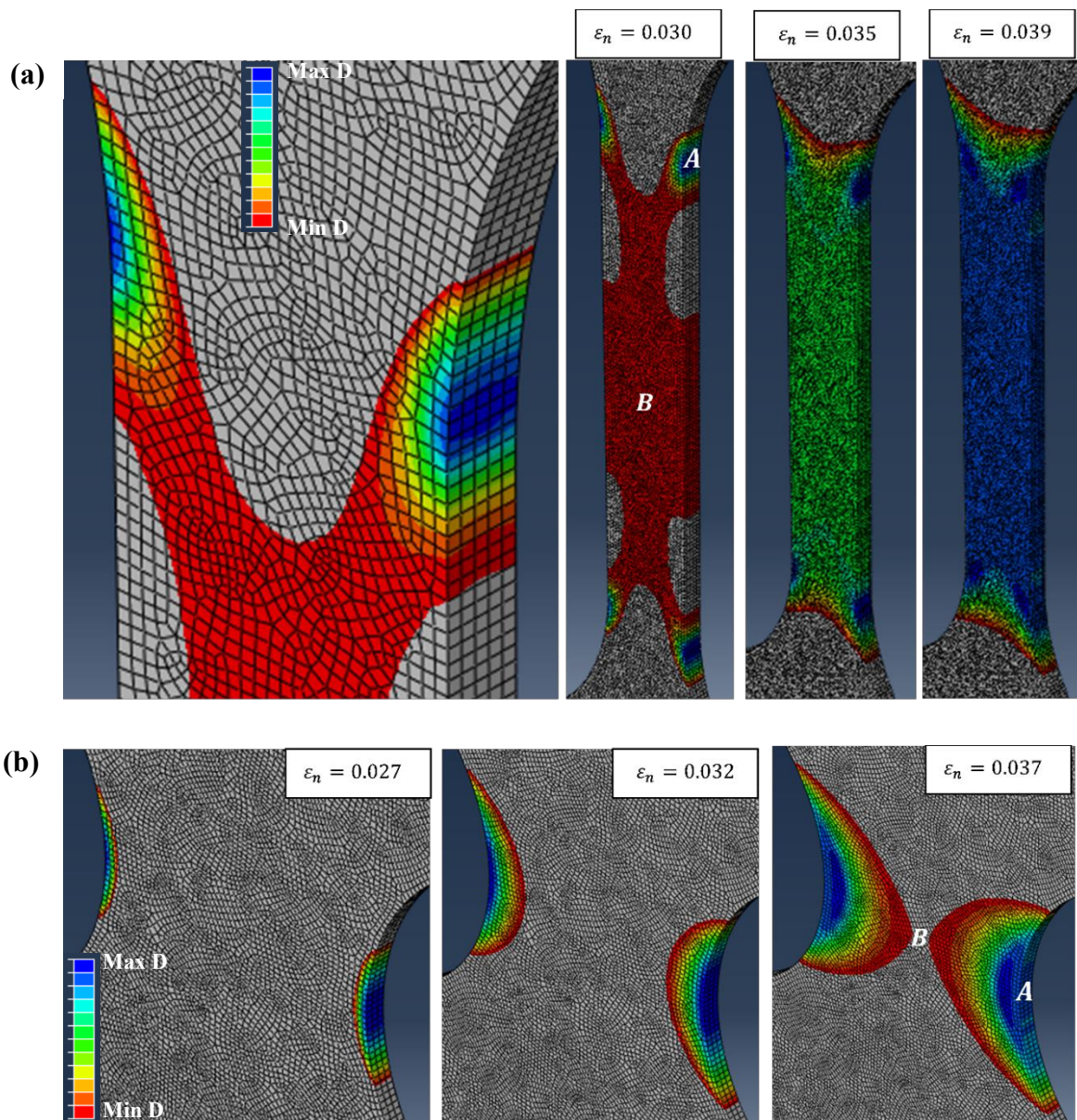
Figure 3.3 Evolution of damage indicator with nominal strain under tensile loading in; (a) dog-bone specimen and (b) notched specimen.
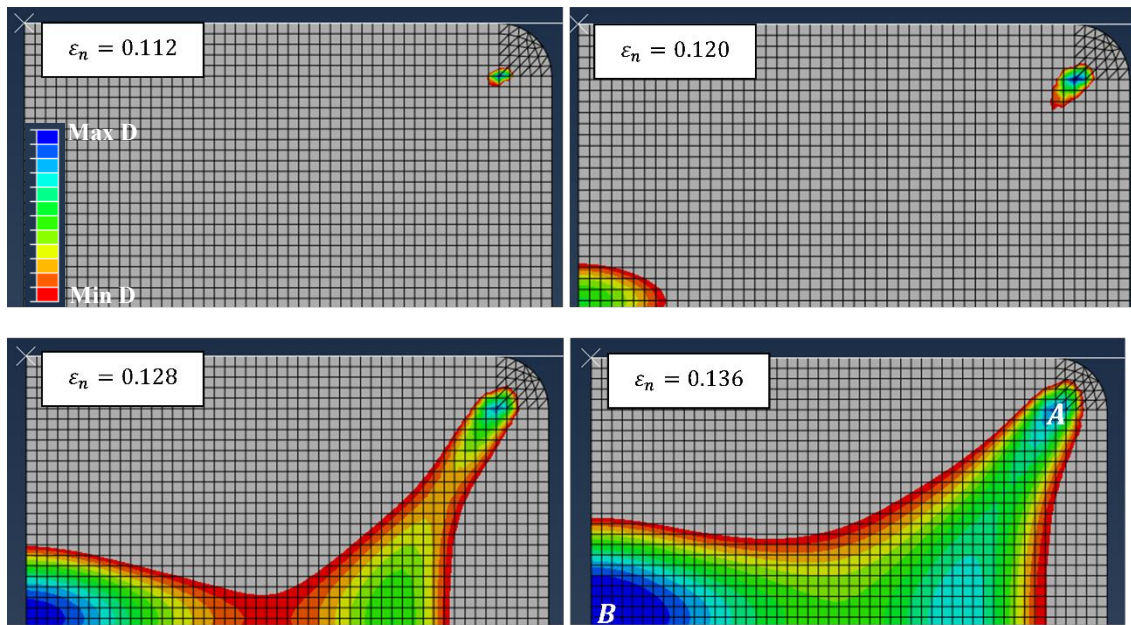
Figure 3.4 Evolution of damage indicator with nominal strain in a circular disk specimen under compressive loading.
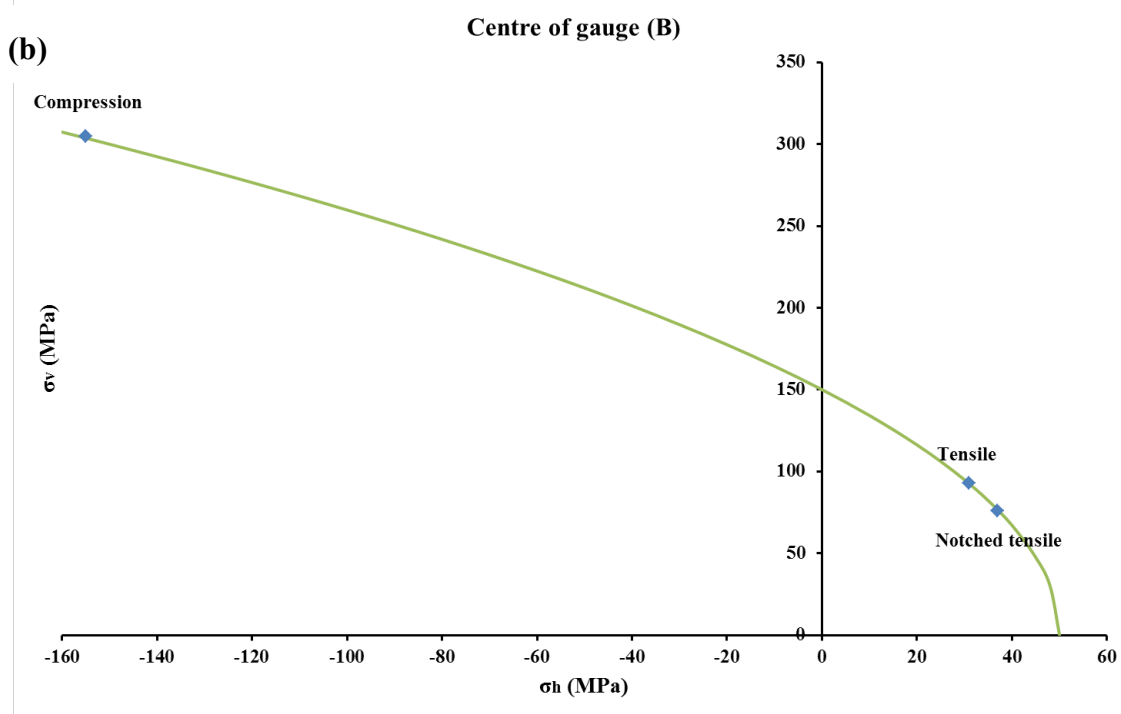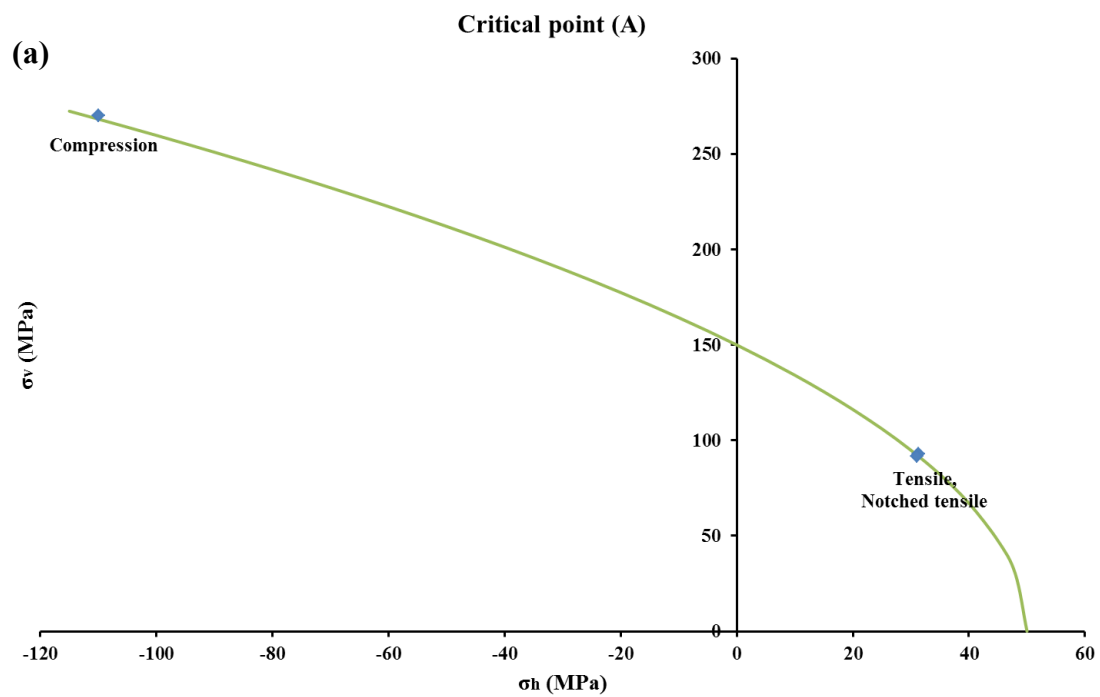
Figure 3.5 Plot of σ_v versus σ_h at damage initiation for (a) critical point (A) and (b) centre of gauge (B) for dog-bone, notched and circular disk specimens.

Based on the results of this preliminary study, traditional test specimen geometries, machined from cured epoxy sheets were selected to systematically probe the stress state dependence at failure initiation for epoxy. Furthermore, the preliminary study highlighted the benefits of using FEA in parallel with the experiments, to help identify critical states of stress. As will be shown subsequently, if the constitutive model is to be determined, an iterative numerical-experimental approach is necessary. In the following, three specimen geometries are considered to allow access to a reasonable range of stress states: a tensile dog-bone, a flat plate for shear punch testing and a circular disc for compression testing.

3.3 Quasi-static characterisation of CSP-toughened epoxy

Aero-grade epoxy DLS 1832-1 toughened by a weight fraction of approximately 10 wt% core-shell particles (outer diameter of 100 nm) was supplied by Hexcel Composites, UK. The epoxy was supplied in the form of square plates 130 mm x 130 mm, with a thickness of 4.05 (±0.1) mm. The density ρ of filled epoxy was measured to be 1250 kg/m^3 and the Poisson's ratio $v = 0.35$ was obtained from material data sheets for high-grade epoxies. The filled epoxy, assumed to be isotropic, was characterised using three tests: compression, tension, and shear punch. Repeat tests were conducted for each load case to obtain the variability in the material response.

3.3.1 Characterisation test setup

Disk-shaped specimens of diameter 8 mm and thickness 4.05 mm were machined from the square plates for the quasi-static compression tests. The compression tests were carried out using a screw-driven Instron test machine at a crosshead speed of 0.33 mm/min, corresponding to a nominal strain rate of approximately 1.36 x 10^{-3} /s. The compressive force was obtained from the load cell, and the compressive displacement was obtained from clip gauge readings to correct for crosshead compliance.

Quasi-static tensile tests were conducted on dog-bone specimens of the filled epoxy. The gauge section of the dog-bone specimens was of length 70 mm, width 10.5 mm and thickness 8.9 mm. The tensile tests were carried out on a screw-driven Instron test machine at a

crosshead speed of 5 mm/min, corresponding to a nominal strain rate of approximately 1.2 x 10^{-3} /s. The tensile force was obtained from the load cell, and the tensile displacement (extension) was obtained from the crosshead displacement, using a laser extensometer to correct for crosshead compliance.

Quasi-static shear punch tests were performed as per ASTM Standard D732-10. Schematic of the shear punch test fixture showing the punch, die, bolts and the specimen is presented in Figure 3.6. Square plate specimens of dimensions 50 mm x 50 mm, with a thickness of 4.05 mm were machined from the square plate samples for the shear punch tests. As with the compression tests, the shear punch tests were carried out using a screw-driven Instron test machine at a crosshead speed of 0.33 mm/min, corresponding to a nominal strain rate of approximately 1.36 x 10^{-3} /s. The force was obtained from the load cell, and the crosshead displacement obtained during the shear punch tests was corrected for crosshead compliance using the laser extensometer data from the compression tests.

3.3.2 Characterisation test results

Nominal stress-strain curves for quasi-static compressive, tensile and shear punch response of filled epoxy DLS 1832-1 are shown in Figure 3.7. Two experimental stress-strain curves are presented for each loading case, indicating good repeatability of the tests.

Figure 3.7a presents the quasi-static compression behaviour of filled epoxy. Each compressive nominal stress-strain curve indicates a linear elastic response up to yield, followed by non-linear strain hardening up to a local maximum value of nominal stress. This point of material instability is followed by strain softening up to a local minimum value of nominal stress, immediately then followed by strain hardening up to compressive failure. The quasi-static compressive yield strength and modulus of filled epoxy is obtained as 114 MPa and 2.56 GPa, respectively. The compressive failure strength is 616 MPa.

77
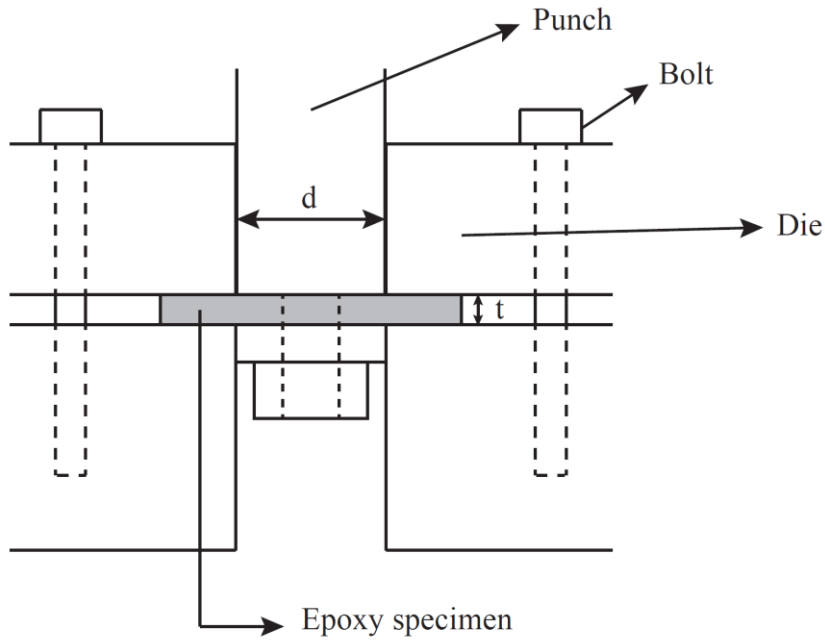
Figure 3.6 Schematic of quasi-static shear punch test setup.

The quasi-static tensile response of filled epoxy is given in Figure 3.7b. The tensile nominal stress-strain response is linear elastic up to yield, followed by a non-linear response up to failure. The quasi-static tensile yield strength and modulus is 76 MPa and 2.68 GPa, respectively. The tensile failure strength is 86 MPa.

Figure 3.7c presents the quasi-static shear punch response of filled epoxy. It should be noted that the nominal stress, $\sigma_{n,sp}$ and nominal strain, $\varepsilon_{n,sp}$ for shear punch loading is calculated as:

$$\sigma_{n,sp} = \frac{F}{\pi dt} \tag{3.3}$$

$$\varepsilon_{n,sp} = \frac{\delta}{t} \tag{3.4}$$

where, F, δ, d and t denote the punch force, punch displacement, punch diameter and specimen thickness, respectively.

The shear punch nominal stress-strain response is linear elastic up to yield, followed by a non-linear response up to brittle failure initiation, characterised by the presence of cracks at the periphery of the punch and a sudden drop in nominal stress. Brittle failure initiation is followed by a saw-tooth response at an approximately constant nominal stress value, indicating crack propagation within the shear punch specimen. This is followed by strain hardening up to final failure. The quasi-static shear punch yield strength and modulus is 58 MPa and 2.55 GPa, respectively. The shear punch failure strength, considered in the present study to be the nominal stress value at the point of brittle failure initiation, is 66 MPa. The observed characteristic saw-tooth response is the well-known type B crack growth behaviour in toughened epoxies, described by Garg and Mai (1988) as brittle unstable crack growth during which the crack proceeds in a stick-slip manner.

3.4 Model development

In this section, we develop a finite element model capable of predicting the response of the epoxy across a wide range of stress states. We employ an iterative strategy to develop the model, building up the complexity systematically, and comparing with the experimental data at each stage. This enables us to identify the significance of key modelling assumptions. This model will then be applied in section 3.5, to predict the more complex load case of indentation, for different plate support conditions and indenter geometries.

For the first iteration, it is assumed that (i) the elastic response is isotropic and linear, and (ii) plasticity is governed by the von Mises yield criterion (i.e. J2 plasticity) with isotropic hardening. We opt to fit the initial yield stress and strain hardening to the experimental results obtained in uniaxial compression (Figure 3.8). This stress state is convenient as it provides the largest strain to failure, and hence avoids the need for interpolation of the hardening curve. For consistency, we take the Young's modulus to be 2.56 GPa (the measured value in compression), and the Poisson's ratio to be 0.35. In the first iteration, we take the yield stress to be 114 MPa (Figure 3.7a). To avoid numerical instabilities arising from strain softening in the FE analysis, the compressive post-yield response is approximated by an exponential function as shown in Figure 3.8. The finite element model

is then used to predict the tensile and shear punch responses of the filled epoxy, and comparison is made with the experiments (Figure 3.9). It is found that the model gives a good prediction of the shear punch response. However, it significantly overestimates the yield strength in uniaxial tension (Figure 3.9a). It is therefore evident that there is a need to introduce hydrostatic stress dependence into the FE model.

In the second iteration, the pressure-dependent exponential Drucker-Prager (EDP) model is introduced to better represent the plastic response, given by:

$$a\sigma_v{}^b + \sigma_h - c = 0 \qquad\qquad (3.5)$$

where, a, b and c are constant fitting parameters. The constant $b = 2$ was assumed, assigning a parabolic shape to the initial yield surface. This enabled the yield surface to be fitted using two measurements of the yield stress. The value of constant $a = 0.009$ /MPa was obtained from the ratio of the compressive and tensile yield strengths.

The default flow potential eccentricity and zero dilation angle were selected to approximate associated flow (flow potential eccentricity and dilation angle are defined in Extended Drucker-Prager models, section 19.3.1 of the Abaqus Analysis User's Manual). The Abaqus FE analysis was carried out using both symmetric and unsymmetric solvers to ensure convergence in the obtained FE result. The exponential function used in Iteration 1 to represent the strain hardening response was also used in iteration 2 (Figure 3.8). In all subsequent FE calculations, the elastic response is modelled as described for iteration 1.

Comparing the FE results from iteration 2 with the experiments shows an improved prediction of the onset of yielding across all load cases. However, while the experimental tensile response showed post-yield strain hardening before failure, the FE model predicted post-yield strain softening (Figure 3.9a), as a result of strain localisation. Thus, it is apparent that the tensile response is sensitive to the assumed degree of strain hardening at small plastic strains.
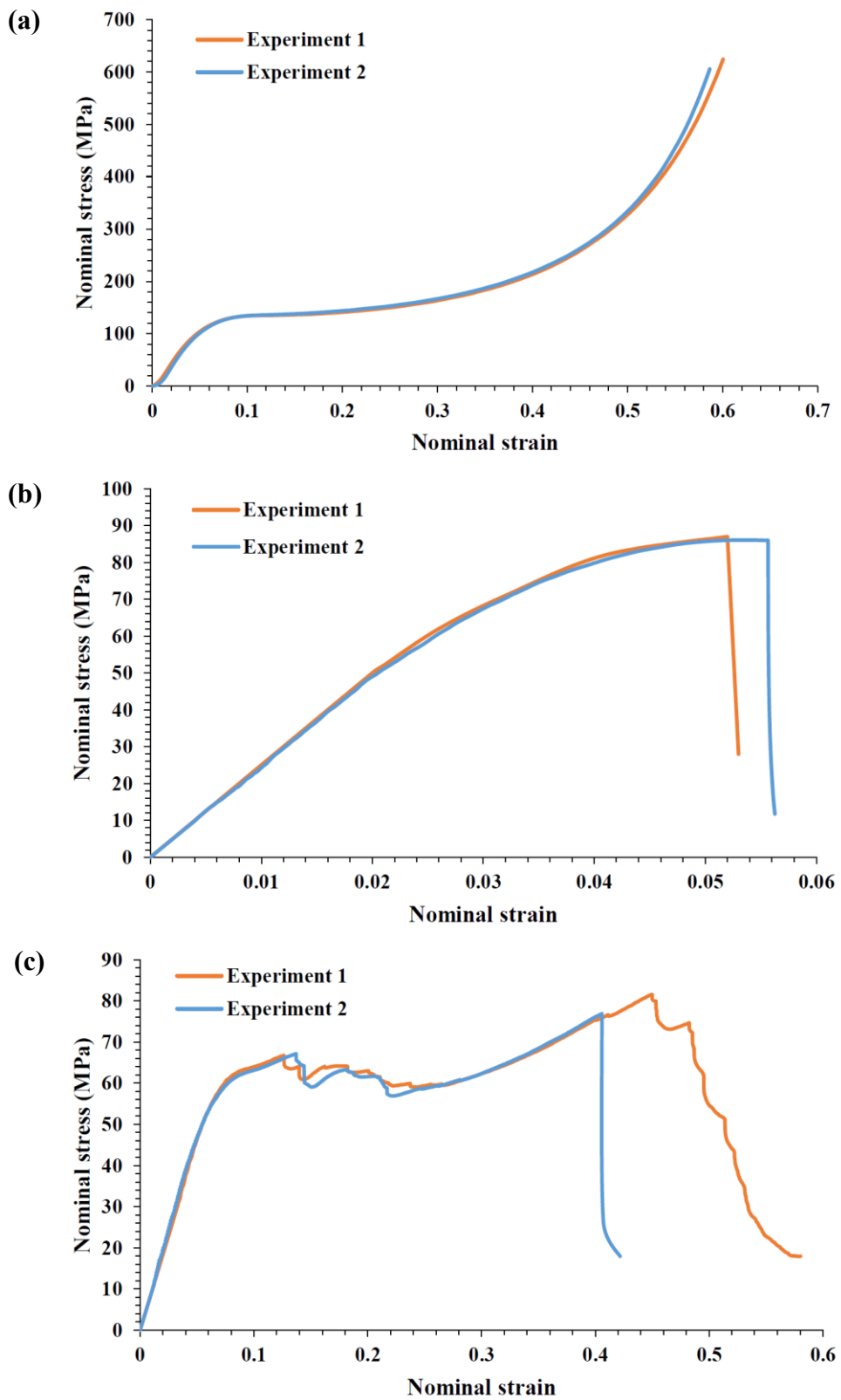
Figure 3.7 Experimental quasi-static response of filled epoxy DLS 1832-1; (a) compression, (b) tension, and (c) shear punch.
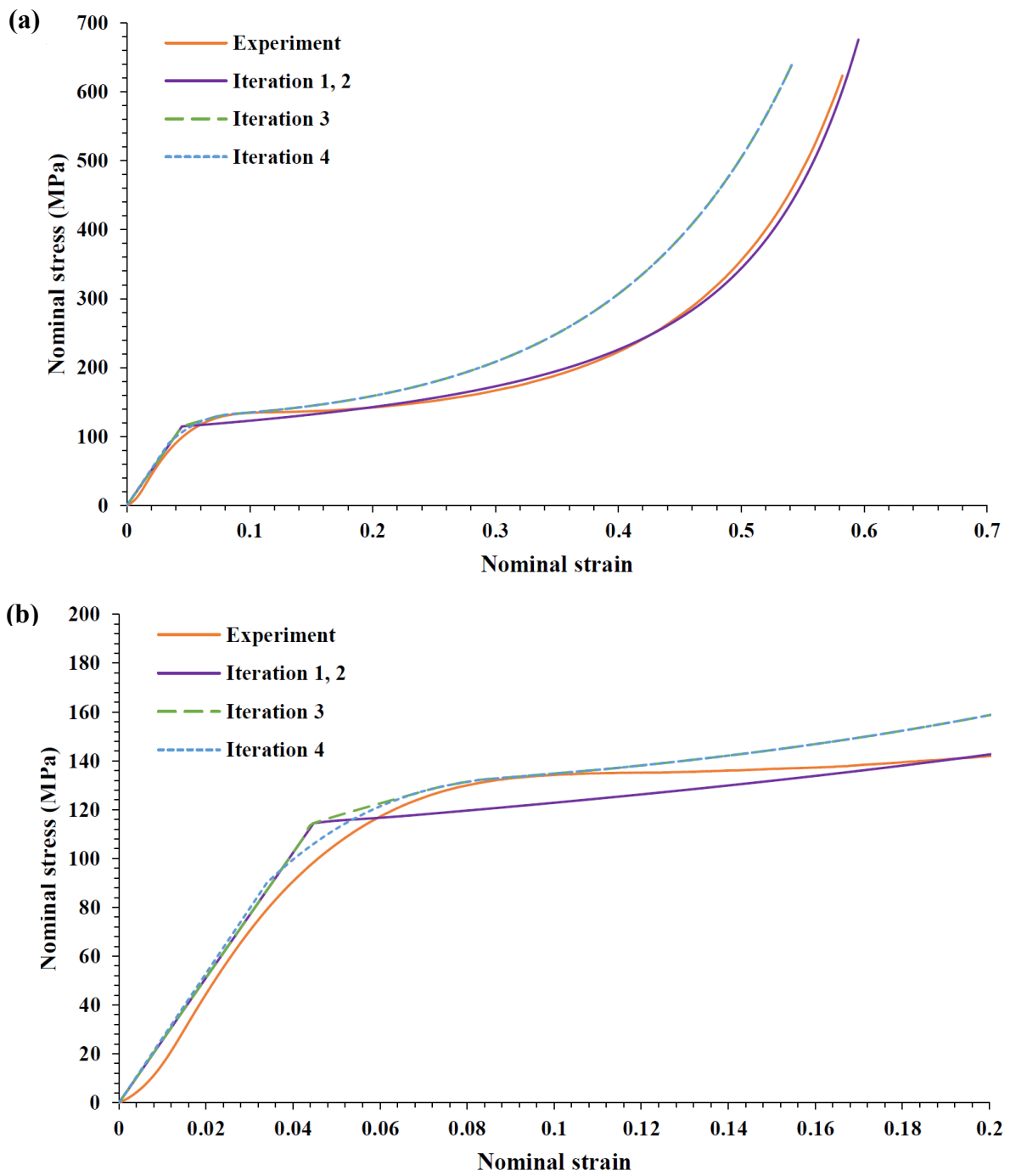
Figure 3.8 Finite element models based on quasi-static compression response of filled epoxy DLS 1832-1; (a) complete response, and (b) near yield point. Iterations 1-4 are defined in the main text.

In the third iteration of the model, the EDP yield criterion and yield strength was assumed to be identical to iteration 2, but the degree of strain hardening at small plastic strains was increased, to reflect the local maximum in the compressive strength seen in the uniaxial compression experiments (Figure 3.8). Beyond this local maximum, while the experiment showed strain softening, to avoid stability problems the subsequent strain hardening was approximated in the FE model by a monotonically increasing polynomial function, as shown in Figures 3.8a and 3.8b. The FE result for the quasi-static tensile response from Iteration 3 (Figure 3.9a) shows an improved prediction of the post-yield strain hardening. However, there remains a discrepancy with the experimental response.

In the final iteration (iteration 4), the compressive yield point and strain hardening response for the FE material model were considered to be variables, with the value of the EDP model parameter a adjusted accordingly. First, an initial yield point was taken to be a particular point on the compressive stress-strain curve. Next, the Young's modulus was adjusted to ensure the elastic strain at yield matched the strain recorded in the experiment. The strain hardening response was taken to match the compression experiment up to the local maximum in compressive stress (i.e. at the first onset of strain softening recorded in the experiments). Subsequent strain hardening was modelled using a monotonically increasing polynomial, as for iteration 3. This process was repeated for a wide range of choices for the initial yield point in compression. The final choice of parameters was taken as the best least squares fit to the uniaxial tension experiment. The revised compressive yield strength and modulus obtained after Iteration 4 were 90 MPa and 2.65 GPa, respectively (Figure 3.8). The revised value of parameter a was 0.025 /MPa. Figure 3.9a illustrates that there is a good match between the predicted FE result in Iteration 4 and the experimental quasi-static tensile response of filled epoxy. There is good agreement between the experimental shear punch response and the predicted FE result for all four iterations.

Using the EDP material model parameters derived using the method outlined above, the pressure dependent quasi-static initial yield surface is obtained for filled epoxy and is shown in Figure 3.10. The stress states at initial yield for the three loading cases are marked.

83
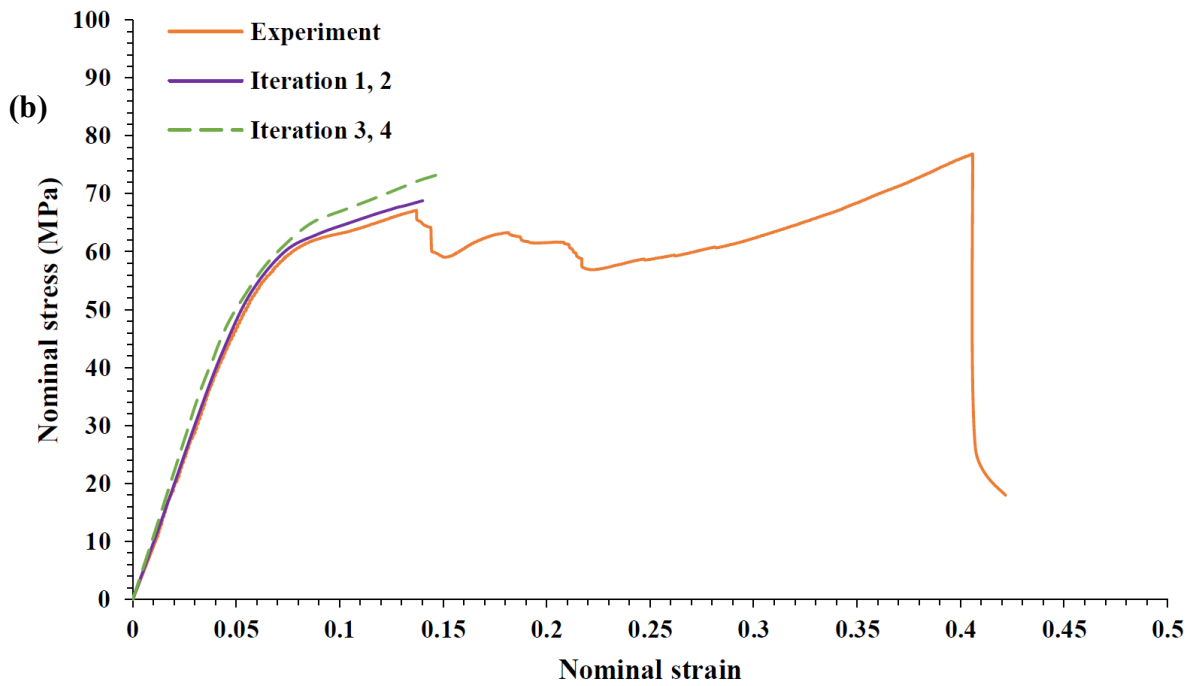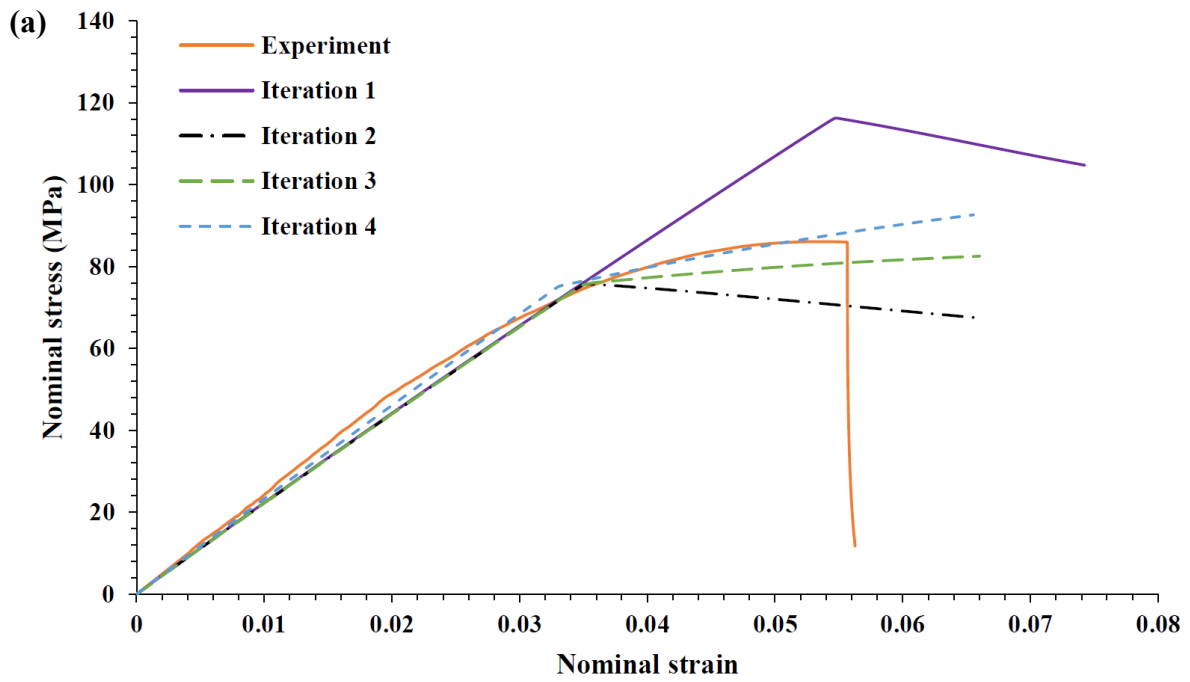
Figure 3.9 Comparison between experimental and numerical results for quasi-static response of filled epoxy DLS 1832-1; (a) tension, and (b) shear punch.
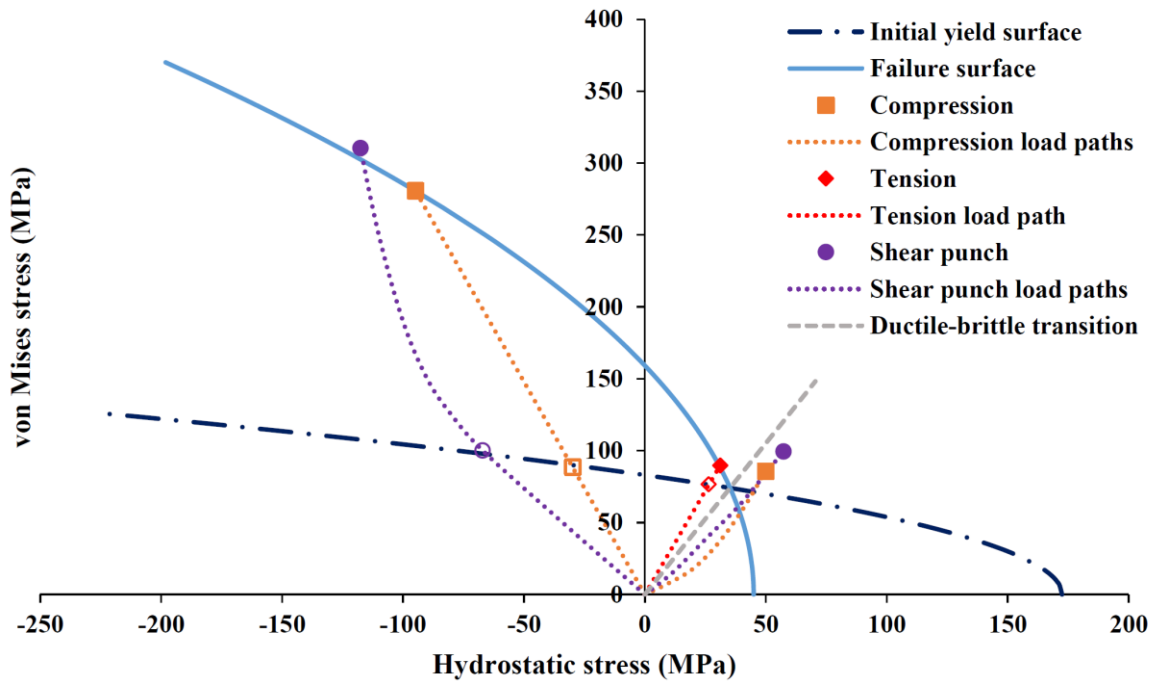
Figure 3.10 Quasi-static initial yield and failure surfaces for filled epoxy DLS 1832-1 with loading paths for critical material points, based on parabolic Drucker-Prager criterion, indicating transition from ductile to brittle regime. Note that open symbols indicate stress states at yield while closed symbols denote stress states at onset of failure.

3.4.1 Discussion

Stress triaxiality, η is defined as:

$$\eta = \frac{\sigma_h}{\sigma_v} \tag{3.6}$$

The nominal values of stress triaxiality at the centre of the gauge section for uniaxial compression, uniaxial tension and pure shear loading are -0.33, 0.33 and 0, respectively. At initial yield in the compression experiment, the FE model predicts that $\sigma_v = 88.4$ MPa, $\sigma_h = -29.6$ MPa, and $\eta = -0.33$, as expected. For the tensile experiment, the model predicts that

σ_v = 76.6 MPa, σ_h = 26.4 MPa, and η = 0.33. For the shear punch experiment, σ_v = 100.2 MPa, σ_h = -67.4 MPa, and η = -0.67, which is significantly different to the nominal value.

The FE analysis for the shear punch specimens indicates a complex stress state (including tensile, compressive and shear regimes) spanning a wide range of stress triaxialities within, and in the vicinity of, the gauge section. As noted above, the value of η at initial yield in the gauge section deviates from the nominal value for pure shear. The FE model indicates that initial yield within the shear punch specimen takes place at the top surface directly in contact with the punch, and not at the centre of the gauge section. This observation reinforces the need to run FE simulations in parallel with the observed experimental results to correctly identify critical initial yield and failure points within the test specimens. It is insufficient to assume that the experimentally measured yield stress will correspond to conditions in the gauge section at the nominal value of stress triaxiality.

3.4.2   Stress state at failure

The elastic-plastic constitutive model is now applied to predict the stress state at the onset of failure in the test specimens. Both the compression disk and tensile dog-bone specimens exhibit significant ductility before failure. Cracks are seen at the circumference of the failed compression disks on both the top and bottom surface. Photographs of the filled epoxy shear punch specimens indicating damage progression is shown in Figure 3.11. The shear punch specimens display an initial ductile response, followed by the initiation of radial cracks propagating outward from the periphery of the punch leading to fracture (Figure 3.11). Candidate locations of failure are identified for each loading case; centre of the gauge section for the tensile dog-bone, centre and edge of the compression disk specimen, and both the top and bottom surfaces for the shear punch specimen.

Next, comparing the compressive, tensile and shear punch experimental responses with the corresponding FE results, candidates for the critical points at failure, and their states of stress, are identified, as follows. Considering first the tensile test, the experiments clearly indicate that failure occurs within the gauge section. The FE model predicts a uniform state of stress in the gauge section throughout the tensile test, and so the stress state at failure can be identified unambiguously. This is listed in Table 3.2. Considering next the compression

test, it is assumed first that failure initiates in the centre of the disk, where the stress state is uniform. This assumption will be interrogated subsequently. The predicted stress state at failure is given in Table 3.2. These two data points are sufficient to fit a parabolic failure envelope in stress space, as shown in Figure 3.10. We take this envelope to represent a ductile failure criterion, with both tests demonstrating plastic straining prior to failure. The ductile failure surface intersects the initial yield surface at a critical stress triaxiality, η^* of 0.48. Two distinct regimes of failure are thus deduced, with a transition from ductile failure ($\eta < 0.48$) to brittle failure ($\eta > 0.48$) at the critical stress triaxiality.
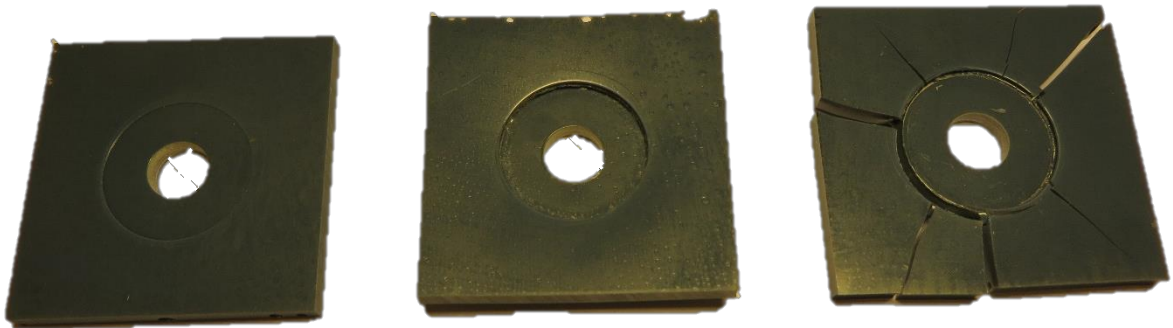
Figure 3.11 Photos of filled epoxy DLS 1832-1 shear punch specimens under quasi-static loading indicating damage progression.

The identification of these two regimes, brittle and ductile, prompts a re-examination of the compression test, where the stress state was non-uniform near the periphery. Specifically, regions of positive stress triaxiality are identified near the edge of the disk, which may be candidates for initiation of brittle failure. The predicted stress state at failure at the edge of the compression disk specimen is given in Table 3.2.

Finally, interrogation of the FE analysis for the shear punch experiment indicates two candidate locations for the onset of failure; one directly underneath the punch on the top surface of the specimen with negative stress triaxiality, and the other at the bottom surface of the specimen with positive stress triaxiality (Table 3.2). For the case of shear punch

loading, the state of stress at the critical failure point on the top surface of the specimen directly under the punch lies on the parabolic failure surface (Figure 3.10). Thus, for the ductile regime, the EDP model is found to predict both initial yield and failure initiation across the range of stress states. In the brittle failure regime, a maximum principal stress failure criterion with a weak dependence on Lode angle is proposed for predicting failure.

Table 3.2 Stress state at failure initiation obtained from FE simulations for candidate failure points.

Sr. No.	Loading case	Location of failure	σ_v (MPa)	σ_h (MPa)	η	Failure regime
1	Tension	Gauge section	89.7	31.1	0.35	Ductile
2	Compression	Centre of disk	280.6	-94.8	-0.34	Ductile
3	Compression	Edge of disk	85.7	50.0	0.58	Brittle
4	Shear punch	Top surface	310.5	-117.6	-0.38	Ductile
5	Shear punch	Bottom surface	99.4	57.3	0.58	Brittle

3.5 Quasi-static indentation: Nose shape sensitivity

Studies have been previously carried out on the indentation response of ductile metals to test the predictive capabilities of different plasticity and damage models (Mohagheghian et al., 2017a, 2017b, 2016). The stress state of the test specimen is complex, and varies in the vicinity of the indenter. Understanding damage initiation in epoxy under complex stress states induced by indentation loads may help support understanding of the role of the matrix in indentation damage tolerance of structural composites (covered later in thesis). Following Mohagheghian et al. (2017b), we will consider quasi-static indentation with a range of

indenter tip geometries to span a wide range of stress states in the epoxy specimen. Two plate supporting conditions will be considered: back face supported, and edge clamped, the latter introducing plate bending in combination with the indentation stresses.

3.5.1 Test configuration

Figure 3.12a presents a schematic of the variation in indenter nose shape by varying the frontal nose radius (R_f). Mild steel indenters of radius (R_i) 6.25 mm and three different nose shapes; flat ($R_f = \infty$), intermediate ($R_f = 9$ mm) and hemispherical ($R_f = R_i$) were used in the present study. Square plates of filled epoxy DLS 1832-1 of dimensions 130 mm x 130 mm were clamped using a circular steel ring of internal diameter 100 mm and thickness 5 mm. Twelve M4 bolts were used to fasten the clamping ring to a supporting steel plate through clearance holes. A schematic of the edge-clamped indentation test setup is shown in Figure 3.12b. For the back face supported indentation tests, a circular steel disk was fit inside the supporting steel plate to provide rigid backing as shown in the schematic (Figure 3.12c). The filled epoxy plates were of thickness ranging from 4.10-4.95 mm. The indenters were mounted to the load cell on the crosshead of the Instron test machine. The indentation tests were carried out at a crosshead speed of 0.33 mm/min, corresponding to a nominal strain rate range of approximately 1.11 x 10^{-3} to 1.34 x 10^{-3} /s. The force was obtained from the load cell, and the crosshead displacement obtained during the indentation tests was corrected for crosshead compliance using the laser extensometer data obtained from the compression tests. A minimum of four tests were carried out for each indenter nose shape to ensure good repeatability of the indentation response.

3.5.2 Edge-clamped indentation: Experimental results

The indenter force-displacement curves measured during the quasi-static edge-clamped indentation tests for the three different indenter nose shapes are presented in Figure 3.13. The curves show an approximately linear rise in indenter force with increasing indenter displacement, representing elastic plate bending. As the indenter starts to penetrate the epoxy plates, micro-cracks begin to form in the radial direction around the periphery of the indenter.

Further penetration is accompanied by the propagation of these cracks radially outward from the periphery of the projectile. At a certain critical indenter displacement, circumferential cracks originate on the top surface of the plate specimen at the distance up to which the radial cracks have thus far reached. These circumferential cracks quickly propagate and join up the radial cracks leading to fracture. A sharp load drop is observed at the onset of brittle fracture. In some cases, after the initial load drop, there is a secondary plateau in the indenter force-displacement plots, followed by a second sharp drop in indenter force. This represents a case when two sets of circumferential cracks originate and propagate, the first an incomplete circular crack at a smaller radius at a lower indenter displacement, and the second partial crack at a larger radius corresponding to displacement at final plate fracture. A large scatter is observed in the indentation response, both in terms of the initial slope of the force-displacement curve, and in the force at failure, for each indenter nose shape.

To account for the effect of variation in plate thickness, non-dimensional force (F^*) and displacement (δ^*) parameters were defined as:

$$F^* = \frac{F}{Et^2} \tag{3.7}$$

$$\delta^* = \frac{\delta t}{R^2} \tag{3.8}$$

where, F, δ, E, R and t denote indenter force, indenter displacement, Young's modulus, plate radius and plate thickness, respectively.

The analytical solution for displacement at the centre of a simply supported linear elastic plate under a central point load (Timoshenko and Woinowsky-Krieger, 1959) states that δ^* is a function of F^*. We deduce that such a relationship is applicable to the edge-clamped indentation case because the indenter force-displacement response is linear. The ratio of indenter diameter to plate diameter is sufficiently small to assume a point load case. Further, there is need to consider translation of the plate in the horizontal direction, constrained only by the vertical pins (similar to the simply supported boundary condition), as shown in subsequent simulation studies. The non-dimensional force-displacement response of filled epoxy under edge-clamped indentation loading for the different indenter nose shapes is

presented in Figure 3.14. It is observed that a consistent experimental quasi-static indentation response with significantly reduced scatter in the slope of the curve during loading is obtained after accounting for variations in plate thickness. There is, however, a significant scatter in the onset of fracture and post fracture response of epoxy depending on the initiation and propagation of brittle radial and circumferential cracks during perforation.

3.5.3 Edge-clamped indentation: Comparison with FE

Next, a finite element model of the indentation experiment was developed in order to interrogate the stress state in the plate at failure, and candidates for the critical location for failure initiation. It has been shown in previous investigations (Mohagheghian et al., 2017b) that boundary compliance can be significant. To account for the effect of boundary compliance on the predicted indentation response, a 3D quarter plate FE model was first simulated in Abaqus/Standard. The clamping conditions used in the experiments were simulated in detail. A quarter plate was modelled with symmetry boundary conditions applied along the symmetry planes. As well as the circular test area, the region of plate under the clamping ring and the retaining bolts were included. The retaining bolts were modelled as cylindrical rigid pins, discretized using discrete rigid elements (R3D4). Frictionless contact was defined between the retaining pins and the plate. The indenter was also modelled as rigid (discretized using element type R3D4). The plate was modelled using solid elements (C3DR). The mesh in regions of the plate close the indenter was refined to a typical element size of 0.42×0.42×0.25 mm (Mohagheghian, 2013). Hard, frictionless contacts in the clamping area were simulated by constraining only the vertical (i.e. out-of-plane) degrees of freedom at the surface of the plate in the clamping area to be zero. The nodes were free to translate in the horizontal plane, with pull constrained by the retaining pins. This condition represents the presence of a clamping ring with frictionless contact between it and the specimen plate (Mohagheghian, 2013).
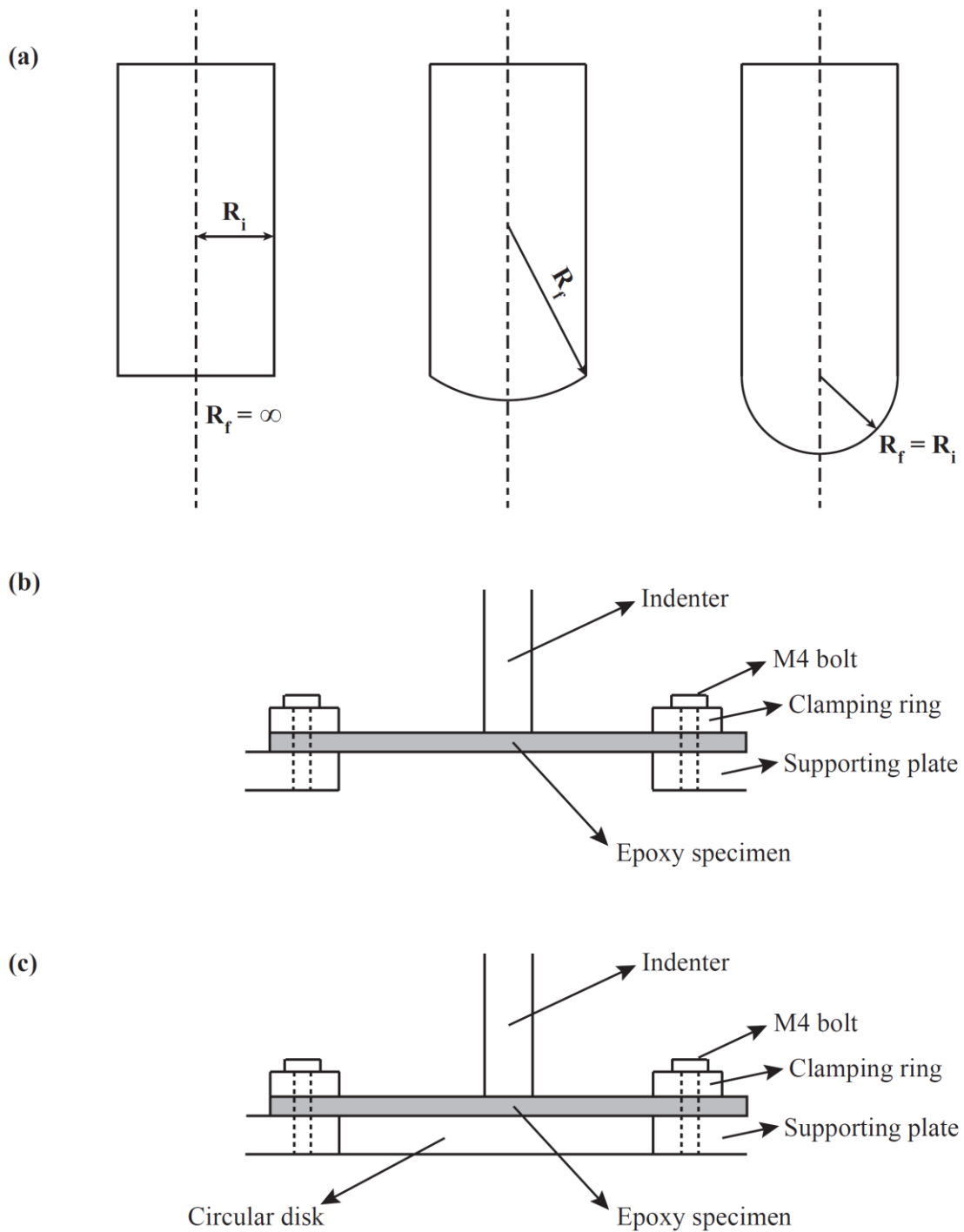
Figure 3.12 Schematic of (a) variation in projectile nose shape by changing the frontal nose radius, (b) edge-clamped indentation test setup, and (c) back face supported indentation test setup.

Based on the FE results from the 3D quarter plate model, a 2D axisymmetric model was developed, with axial and rotational springs included to represent the predicted boundary compliance. Axisymmetric continuum elements (CAX4R) were used to discretize the filled epoxy plate and the indenter was again modelled using rigid elements (RAX2). Most of the plate was meshed with ten elements through the thickness, with local mesh refinement under the indenter corner. A comparison of the FE result with the experimentally obtained indentation response of filled epoxy for the three different nose shapes is presented in Figure 3.14. A good agreement is obtained between the experimental results and the FE analysis using the material model developed. Careful consideration of the boundary compliance is found to be essential to accurately predict the quasi-static indentation response.

The edge-clamped indentation plate specimens undergo brittle failure for all three indenter nose shapes as seen in Figures 3.13 and 3.14. Comparing the experimental indentation response with the corresponding FE results, critical failure points are identified within the plate specimens. The location of failure for all indenter nose shapes was determined to be a point at the centre of the plate on the back face. It is observed that the state of stress at the critical point at failure initiation under quasi-static edge-clamped indentation is insensitive to the indenter nose shape. Failure initiation during indentation occurs in the brittle failure regime (Figures 3.13 and 3.14), with σ_v and σ_h ranging from 101-106 MPa and 68-73 MPa, respectively and at a constant stress triaxiality of $\eta = 0.67$. The value of stress triaxiality for edge-clamped indentation was found to be consistent with the theoretical value for equi-biaxial tensile loading.
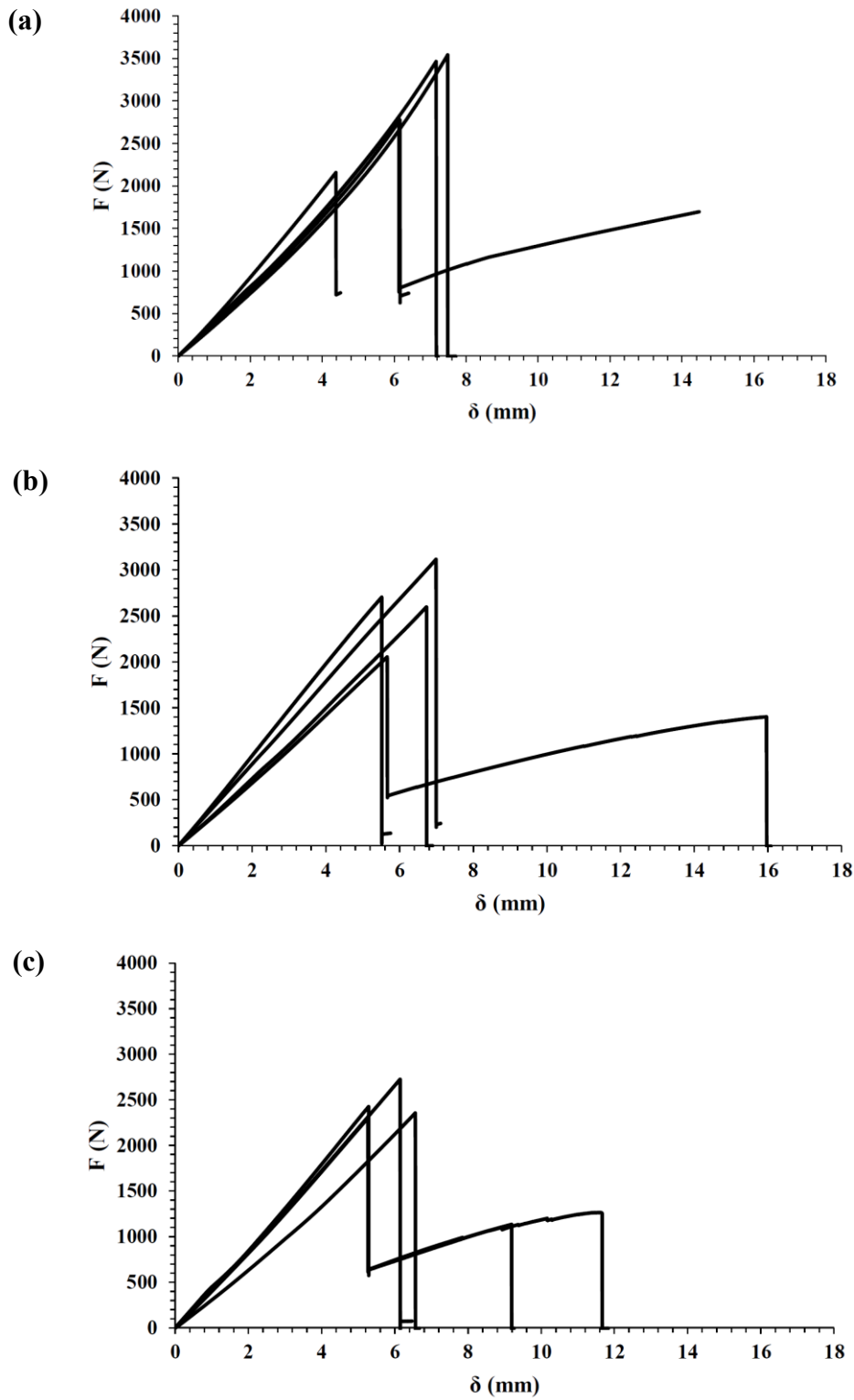
Figure 3.13 Quasi-static edge-clamped indentation response of filled epoxy DLS 1832-1, for different indenter nose shapes; (a) flat, (b) intermediate, and (c) hemispherical.
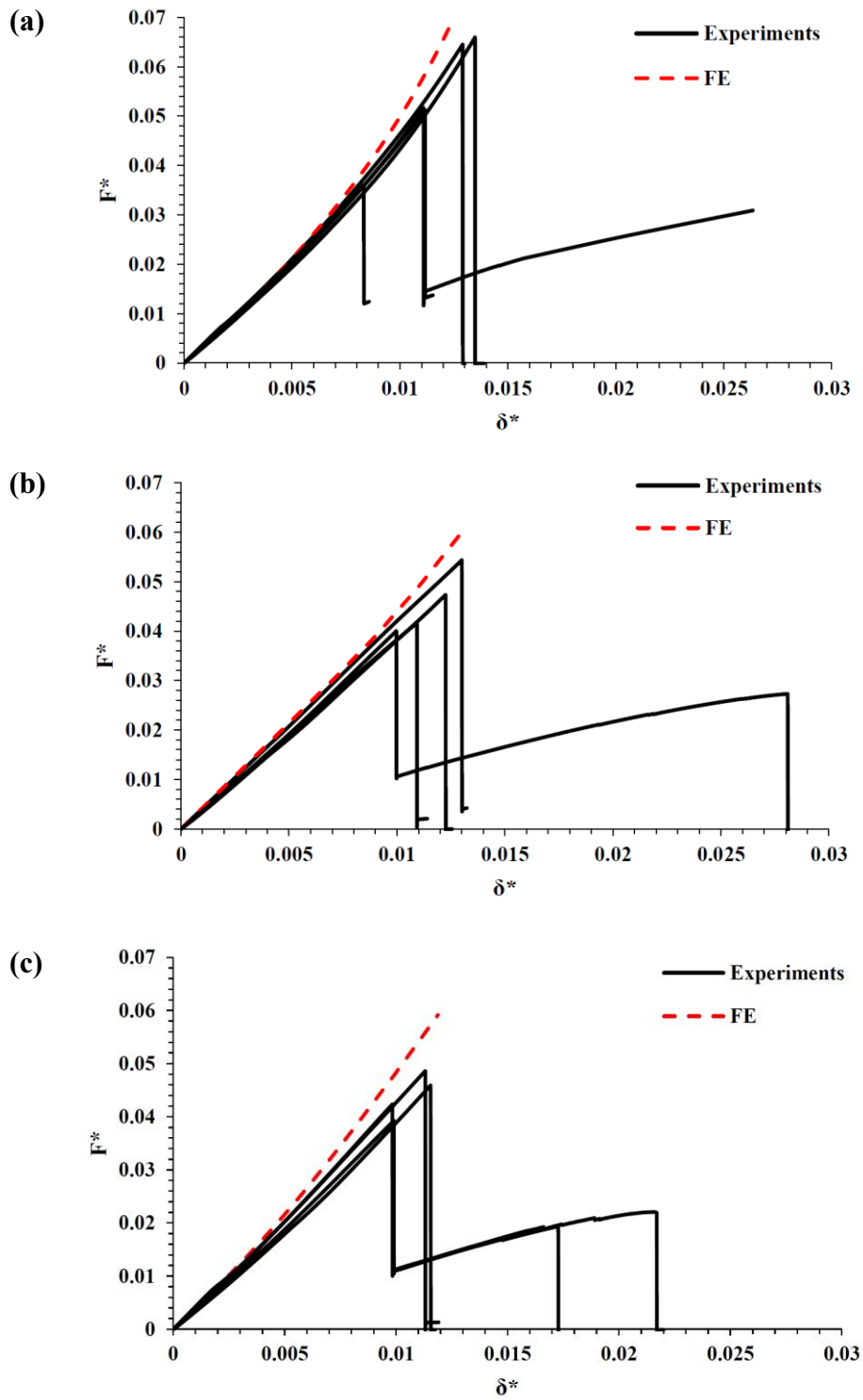
Figure 3.14 Comparison between experimental and numerical results for quasi-static edge-clamped indentation response of filled epoxy DLS 1832-1, for different indenter nose shapes; (a) flat, (b) intermediate, and (c) hemispherical.

3.5.4 Back face supported indentation: Experimental results and comparison with FE

The experimental force-displacement curves during quasi-static back face supported indentation tests for the three different indenter nose shapes are presented in Figure 3.15a. The epoxy plate specimens do not undergo failure up to the maximum cross head force of 30 kN for the different indenter tip geometries considered (Figure 3.15a). An examination of the plate specimens after unloading showed permanent deformation directly under the indenter, indicating ductile behaviour with elastic recovery on unloading.

The 2D axisymmetric model with boundary compliance from the previous section was used to predict the indentation response. However, for these calculations, the back face support was modelled by a rigid boundary at the lower surface of the plate. A good agreement is obtained between the experimental results and the FE analysis using the material model developed. It was observed that, in the range of plate thicknesses considered (4.10-4.95 mm), the back face supported force-displacement curves were insensitive to variations in plate thickness. This contrasts with the edge-clamped indentation predictions, which are dependent on plate thickness.

FE analysis was carried out up to a force of 100 kN to identify critical failure points within the plate specimens (Figure 3.15b). Two potential critical locations of failure, common for all three indenter nose shapes, were identified; one directly in contact with the indenter on the top surface (negative stress triaxiality) and the other near the edge of the indenter (not in contact) on the top surface (positive stress triaxiality).
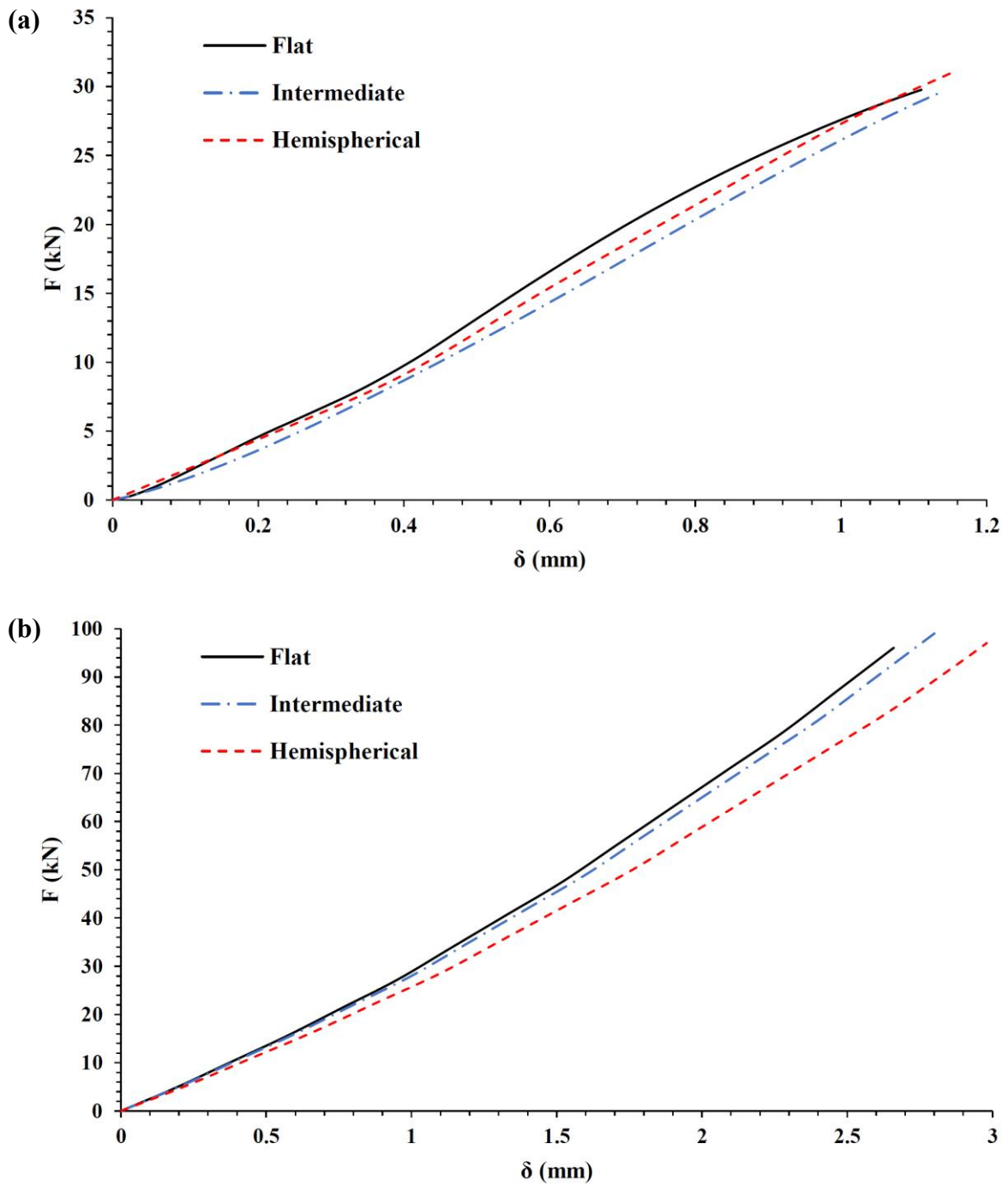
Figure 3.15 Quasi-static back face supported indentation response of filled epoxy DLS 1832-1, for different indenter nose shapes (a) Experimental results and (b) FE calculations.

3.6   Discussion: Brittle failure regime

Further analysis was conducted for the cases where failure occurred in the brittle regime, to see if a failure criterion can be deduced. A wide range of stress states and triaxialities were observed for candidate failure points. However, failure appears to occur at a common value of maximum principal tensile stress. The state of stress at the critical failure point for the different indenter nose shapes during edge-clamped indentation obtained from FE analysis is shown in Figure 3.16a along with the other candidate failure points in the brittle regime ($\eta > 0.48$) (Table 3.2). Figure 3.16b is a plot of the maximum principal stress at failure initiation at candidate failure points in the brittle failure regime for different loading cases including edge-clamped indentation (with flat, intermediate, and hemispherical indenter nose shapes), compression and shear punch. For the brittle failure regime, it can be concluded that a maximum principal stress failure criterion (principal stress at failure equal to 100 MPa) with a weak dependence on Lode angle can be effectively used to predict failure.

The stress triaxiality at the critical ductile failure point under quasi-static back face supported indentation loading was found to be $\eta < -1$. Therefore, based on the initial yield and failure surfaces for filled epoxy in the ductile regime (Figure 3.16a), it can be concluded that the plate specimen will not fail in a ductile manner up to a cross head force of 100 kN. The critical brittle failure point ($\eta > 0.48$) was localised to a small region throughout loading up to 100 kN for all three indenter nose shapes, with the value of maximum principal stress below 100 MPa. Hence, the absence of ductile or brittle failure in the experimentally obtained force-displacement curves (up to 30 kN) for quasi-static back face supported indentation corroborates the failure models developed for both regimes.

3.7   Conclusions

This chapter aims to systematically characterise and model phenomenologically the stress state dependent response of core-shell particle toughened epoxy DLS 1832-1 under quasi-static loading. Towards this, compression, tension and shear punch tests are carried out to

span a wide range of stress triaxialities. An iterative numerical-experimental approach is necessary to obtain the stress state dependent initial yield and failure surfaces for the filled epoxy. Quasi-static indentation tests with three different indenter nose shapes and two boundary conditions are performed to further probe the predicted regimes of response under more complex load cases. A good agreement is obtained between the experimental results and the FE analysis using the material model developed. Careful consideration of the boundary compliance and effect of variation in plate thickness is essential to accurately predict the quasi-static indentation response.

Two distinct regimes of failure are identified for filled epoxy, with a transition from ductile failure ($\eta < 0.48$) to brittle failure ($\eta > 0.48$) at a critical stress triaxiality. For the ductile regime, the pressure dependent exponential Drucker-Prager model is found to predict both initial yield and failure initiation across the range of stress states. In the brittle failure regime, a maximum principal stress failure criterion with a weak dependence on Lode angle is suitable for predicting failure.

Figure 3.16 (a) Quasi-static initial yield and failure surfaces for filled epoxy DLS 1832-1, with candidate failure points in the brittle regime, and (b) maximum principal stress at failure for candidate failure points in the brittle regime.

Chapter 4　Effect of strain rate and toughening strategies on failure initiation in epoxy

4.1　Introduction

In this chapter, the effect of strain rate and different toughening strategies on the initial yield and failure behaviour of epoxy resin will be studied, based on the quasi-static characterisation and modelling methodology for core-shell particle filled epoxy developed in Chapter 3. The effect of increasing the applied strain rate on the stress state dependent response of epoxy is investigated to provide an insight into the impact damage resistance of carbon fibre reinforced epoxy composites. Chapters 3 and 4 inform the follow up study on the impact perforation of carbon fibre reinforced epoxy composites (Chapter 5).

High grade thermosetting epoxy resins are used extensively in high performance applications such as aerospace composites due to their superior mechanical properties and high glass transition temperature, which results from their highly crosslinked molecular network structure. However, the corresponding lack of molecular mobility leads to a tendency towards brittleness, making epoxy resin susceptible to crack initiation and propagation (Bandyopadhyay, 1990; Garg and Mai, 1988; Mayr et al., 1998). In the region surrounding a crack tip in a polymer, buildup of stress concentration results in localized deformation by yielding, microcracking or crazing. It has been shown in previous studies that, if yielding can be enhanced in preference to crack propagation, then the fracture toughness of the polymer can be significantly increased (Mayr et al., 1998). Thus, yielding can be a key mechanism to control the toughness of epoxy resin. Hence, an effective strategy of enhancing the fracture toughness of epoxy would be to employ toughening strategies

which lower yield stresses without significantly compromising the failure strength, modulus, and glass transition temperature. Popular toughening strategies include incorporation of polymeric (e.g. liquid rubber) or particulate additives (e.g. core-shell particles, rigid particles) and reaction induced phase separation based toughening (Carolan et al., 2016; Day et al., 2001; Lin and Shieh, 1998; Liu et al., 2016; Sun et al., 2009; Thitsartarn et al., 2015). The possible damage and energy absorbing mechanisms of toughened epoxy include particle debonding, plastic void growth and matrix shear banding (Liang and Liechti, 1996; Naik et al., 2011; Pothnis et al., 2012; Sun et al., 2009).

Carbon fibre reinforced epoxy composites are replacing conventional lightweight metals and alloys in modern structural components. Resistance to impact perforation is an important design requirement of lightweight structures. Epoxy resin has been shown to have a strong strain rate sensitivity compared to metals. Understanding the strain rate sensitivity of epoxy is particularly important to provide an insight into the deformation and damage response of carbon fibre reinforced epoxy composites under higher strain rate loading conditions such as impact. The effectiveness of various toughening strategies to improve both the quasi-static and high strain rate mechanical properties of epoxy needs to be thoroughly investigated. The effect of strain rate on the compression, tensile and shear properties of highly crosslinked epoxy has been studied extensively (Chen et al., 2002; Chen and Zhou, 1998; Jordan et al., 2008; Kanchanomai et al., 2005; Miwa et al., 1995; Naik et al., 2011, 2010; Pothnis et al., 2012; Tay et al., 1995; Trojanowski et al., 1997). Empirical models and simple phenomenological approaches with a linear yield stress vs log(strain rate) approximation have been proposed to account for the strain rate sensitivity of epoxy resins (Chevalier et al., 2016; Miwa et al., 1995; Morelle et al., 2017; Morin et al., 2010; Tay et al., 1995; Werner and Daniel, 2014).

This study aims to investigate the effect of strain rate and two different toughening strategies on the pressure dependent initial yield and failure behaviour of epoxy. Specifically, we seek to determine the influence of both strain rate and microstructural modifications in epoxy on the shape and size of the initial yield and failure envelopes in stress space. Addition of core-shell particles and reaction induced phase separation are the two toughening strategies considered in this investigation. Four material types are characterised in this study; neat

epoxy DLS 1832-1 (hereafter referred to as unfilled epoxy), core-shell particle filled epoxy DLS 1832-1 (hereafter referred to as filled epoxy), neat epoxy 8552 (hereafter referred to as untoughened epoxy), and phase separation toughened epoxy 8552 (hereafter referred to as toughened epoxy). Quasi-static compression, tension and shear punch tests are carried out to span a wide range of stress triaxialities for each material type (section 4.2). The exponential Drucker-Prager (EDP) model developed in section 3.4 is used to obtain the pressure dependent quasi-static initial yield and failure surfaces for the four materials investigated (section 4.2). The effectiveness of the two toughening strategies is evaluated by comparing the quasi-static stress state dependent response of; filled vs unfilled epoxy, and toughened vs untoughened epoxy. The critical stress triaxialities are identified for each material type, denoting the extent of the ductile and brittle failure regimes.

Next, compression, tension and shear punch tests are carried out at higher strain rates (0.1-10 /s) for the filled and unfilled epoxy specimens to probe the strain rate sensitivity of the initial yield and failure surfaces (section 4.3). A linear fit of the experimental compressive yield strength vs log(strain rate) data is used to model the strain rate sensitivity of the initial yield surface. A strain rate dependent EDP model is thus obtained assuming no change in the overall shape of the parabolic initial yield surface. Candidate locations of failure are identified for the tensile and shear punch loading case at higher rates of strain. Next, comparing the tensile and shear punch experimental response at higher strain rates with the corresponding FE results, critical failure points are identified within the test specimens for each loading case. The state of stress at the location of failure initiation is obtained from FE analysis for both the filled and unfilled specimens. Thus, the strain rate dependent parabolic failure surface is obtained for the two materials (section 4.4). Importantly, from a resilient design perspective, the variation in the critical stress triaxiality for the brittle-ductile transition with both the applied strain rate and toughening strategy is observed. The experimental measurements are in good agreement with the strain rate dependent initial yield and failure criteria obtained.

4.2 Materials and quasi-static characterisation

Four types of materials were supplied by Hexcel Composites, UK in the form of square plates 130 mm x 130 mm:

(A) Aero-grade epoxy DLS 1832-1 of thickness 4.5 (±0.1) mm and density 1250 kg/m^3.

(B) Aero-grade epoxy DLS 1832-1 toughened by a weight fraction of approximately 10 wt% core-shell particles (outer diameter of 100 nm) of thickness 4.05 (±0.1) mm and density 1250 kg/m^3.

(C) Aero-grade epoxy 8552 of thickness 4.5 (±0.1) mm and density 1280 kg/m^3.

(D) Reaction induced phase separation toughened aero-grade epoxy 8552 of thickness 4.5 (±0.1) mm and density 1280 kg/m^3.

The Poisson's ratio $v = 0.35$ of all four epoxies was obtained from material data sheets for high-grade epoxies. The four materials, assumed to be isotropic, were characterised using three tests; compression, tension, and shear punch. Repeat tests were conducted for each load case to obtain the variability in the material response. The compression, tension and shear punch test setups are given in section 3.3. Quasi-static characterisation tests were carried out on a screw-driven Instron test machine at a strain rate of approximately 10^{-3} /s for each material type. The force was obtained from the load cell, and the crosshead displacement obtained was corrected for crosshead compliance for all three loading cases.

4.2.1 Effect of toughening strategies

4.2.1.1 Addition of core-shell particles

Nominal stress-strain curves for quasi-static compressive, tensile and shear punch response of filled and unfilled epoxy DLS 1832-1 are shown in Figure 4.1. Two experimental stress-strain curves are presented for each loading case, indicating good repeatability of the tests. Table 4.1 presents the quasi-static properties of filled and unfilled epoxy under three loading cases.

Figure 4.1a presents the quasi-static compression behaviour of filled and unfilled epoxy. Each compressive nominal stress-strain curve indicates a linear elastic response up to yield, followed by non-linear strain hardening up to a local maximum value of nominal stress. This point of material instability is followed by strain softening up to a local minimum value of nominal stress, immediately then followed by strain hardening up to compressive failure. The addition of 10% by weight core-shell particles to neat epoxy leads to a 26% decrease in compressive yield strength, 20% reduction in compressive modulus, 18% decrease in compressive failure strength, and 7% increase in the compressive failure strain.

The quasi-static tensile response of filled and unfilled epoxy is given in Figure 4.1b. The tensile nominal stress-strain curve of filled epoxy indicates ductile behaviour, with a linear elastic response up to yield, followed by a non-linear response up to failure. The corresponding plot for unfilled epoxy shows a linear elastic response up to failure, indicating brittle failure. The addition of 10% by weight core-shell particles to neat epoxy leads to a 18% decrease in tensile modulus, 95% increase in tensile failure strength, and 330% increase in failure strain.

The quasi-static elastic moduli for both filled and unfilled epoxy show little dependence on the loading condition and can be assumed to be constant (Table 4.1). The compressive and tensile yield strengths of filled epoxy are different, thereby indicating pressure dependent initial yield behaviour.

Figure 4.1c presents the quasi-static shear punch response of filled and unfilled epoxy. The nominal stress and nominal strain for shear punch loading are defined in Equations (3.3) and (3.4) in the previous chapter. The shear punch nominal stress-strain response of filled epoxy is linear elastic up to yield, followed by a non-linear response up to brittle failure initiation, characterised by the presence of cracks at the periphery of the punch and a sudden drop in nominal stress. Brittle failure initiation is followed by a saw-tooth response at an approximately constant nominal stress value, indicating crack propagation within the shear punch specimen. This is followed by strain hardening up to final failure. For the unfilled epoxy specimen, initial linear elastic response is followed by slight non-linear behaviour up to brittle failure initiation. Final failure soon follows brittle failure initiation, with only a marginal increase in the value of strain.

Table 4.1 Quasi-static compression, tension and shear punch properties of filled and unfilled epoxy DLS 1832-1.

Material	Yield strength (MPa)	Modulus (GPa)	Failure strength (MPa)	Failure strain
Compression				
Unfilled	154	3.21	747	0.56
Filled	114	2.56	616	0.60
Tension				
Unfilled	NA	3.29	44	0.013
Filled	76	2.68	86	0.056
Shear punch				
Unfilled	74	0.99	80	0.08
Filled	58	0.84	66	0.13

The observed characteristic saw-tooth response of filled epoxy is the well-known type B crack growth behaviour in toughened epoxies, described by Garg and Mai (1988) as brittle unstable crack growth during which the crack proceeds in a stick-slip manner. The addition of 10% by weight core-shell particles to neat epoxy leads to a 22% decrease in shear punch yield strength, 15% decrease in modulus, 18% decrease in failure strength, and 63% increase in failure strain.
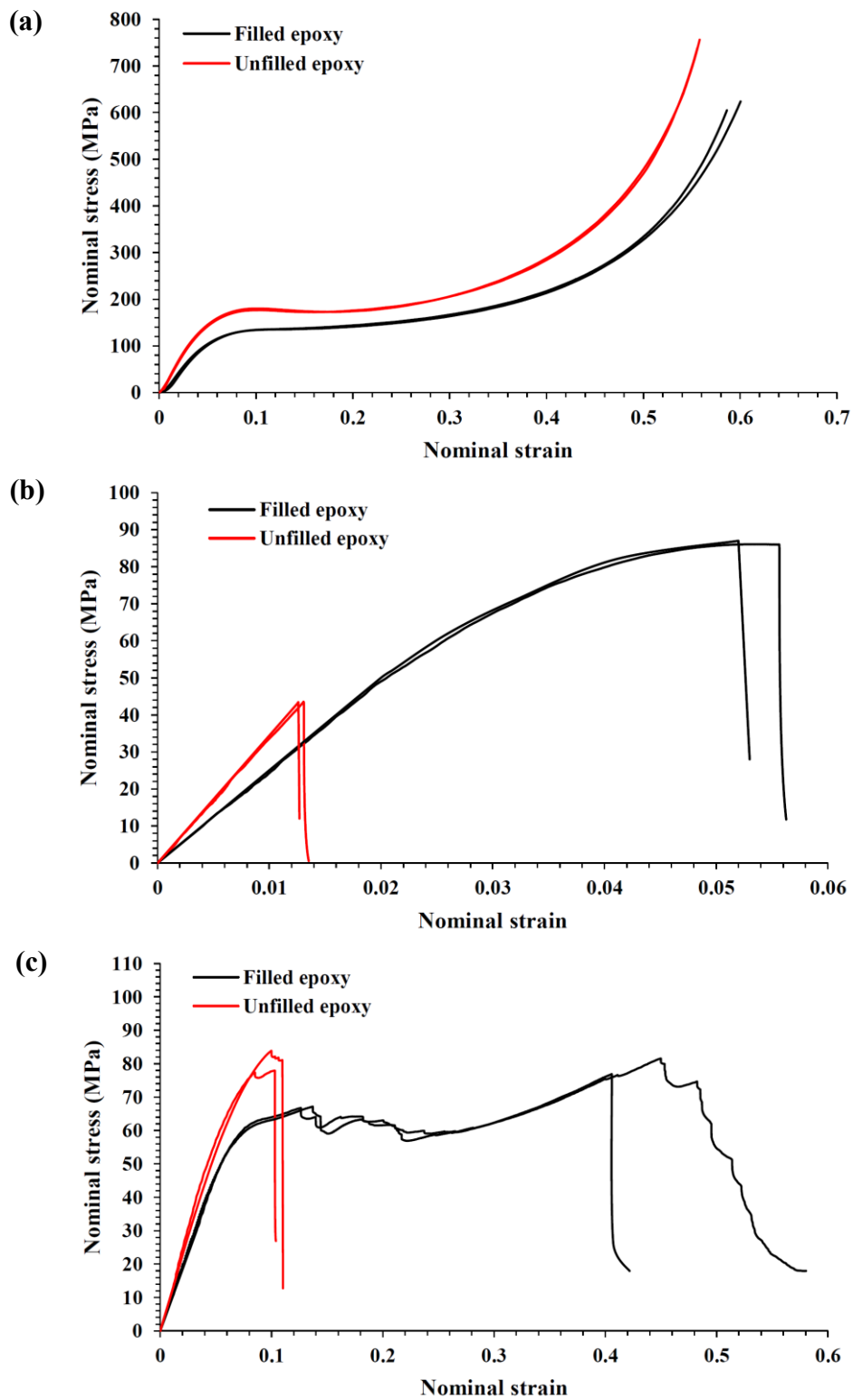
Figure 4.1 Comparison of quasi-static response of filled and unfilled epoxy DLS 1832-1;
(a) compression, (b) tension, and (c) shear punch.

107

4.2.1.2   Reaction induced phase separation

Nominal stress-strain curves for quasi-static compressive, tensile and shear punch response of toughened and untoughened epoxy 8552 are shown in Figure 4.2. Table 4.2 presents the quasi-static properties of toughened and untoughened epoxy under three loading cases.

Figure 4.2a presents the quasi-static compression behaviour of toughened and untoughened epoxy. The compressive nominal stress-strain curves show similar features to the filled and unfilled epoxy (Figure 4.1a); linear elastic response up to yield, then non-linear strain hardening up to a local maximum value of nominal stress, followed by strain softening up to a local minimum value of nominal stress, and lastly strain hardening up to compressive failure. Reaction induced phase separation based toughening of neat epoxy leads to a 14% decrease in compressive yield strength, 12% increase in compressive modulus, 46% increase in compressive failure strength, and 23% increase in the compressive failure strain.

The quasi-static tensile response of toughened and untoughened epoxy is presented in Figure 4.2b. The tensile nominal stress-strain curves of both toughened and untoughened epoxy indicate ductile behaviour, with linear elastic response up to yield, followed by non-linear response up to failure. Reaction induced phase separation based toughening of neat epoxy leads to a 21% decrease in tensile yield strength, 11% decrease in tensile modulus, 19% decrease in tensile failure strength, and 8% decrease in the tensile failure strain.

The quasi-static elastic moduli for both toughened and untoughened epoxy shows dependence on the loading condition (Table 4.2). The compressive and tensile yield strengths of toughened and untoughened epoxy are different, thereby indicating pressure dependent initial yield behaviour.

Figure 4.2c presents the quasi-static shear punch response of toughened and untoughened epoxy. The shear punch nominal stress-strain response of both toughened and untoughened epoxy is linear elastic up to failure, characteristic of brittle cracking. Reaction induced phase separation based toughening of neat epoxy leads to little or no change in shear punch modulus, 51% increase in shear punch failure strength, and 56% increase in shear punch failure strain.

Table 4.2 Quasi-static compression, tension and shear punch properties of toughened and untoughened epoxy 8552.

Material	Yield strength (MPa)	Modulus (GPa)	Failure strength (MPa)	Failure strain
Compression				
Untoughened	188	1.55	406	0.48
Toughened	161	1.73	592	0.59
Tension				
Untoughened	82	1.47	135	0.124
Toughened	65	1.31	109	0.114
Shear punch				
Untoughened	NA	0.61	57	0.094
Toughened	NA	0.59	86	0.147

4.2.2 Quasi-static initial yield and failure surface

The iterative numerical-experimental modelling approach developed in Chapter 3 is used to generate the quasi-static initial yield and failure surfaces for the four materials considered. A pressure dependent EDP model, with parameter $b = 2$ (parabolic shape of initial yield surface) was found to accurately predict the quasi-static shear punch response for all four materials tested. The revised parameter a, revised compressive yield strength and revised compressive modulus of the four epoxies investigated is presented in Table 4.3. The default flow potential eccentricity and zero dilation angle were selected to approximate associated flow.

Using the EDP material model parameters given in Table 4.3, the pressure dependent quasi-static initial yield surface is obtained for the four epoxy materials and is shown in Figures 4.3 and 4.4. The stress states at the point of initial yield within the specimens in FE analysis,

defined by the values of von Mises stress (σ_v), hydrostatic stress (σ_h) and stress triaxiality (η) for the three loading cases studied is marked on the initial yield surfaces (Figures 4.3 and 4.4) and is presented in Tables 4.4 and 4.5.

The FE analysis for the shear punch specimens indicates a complex stress state (including tensile, compressive and shear regimes) spanning a wide range of stress triaxialities within, and in the vicinity of, the gauge section. It should be noted that the value of η at initial yield in the gauge section deviates from the nominal value of $\eta = 0$ for pure shear. The FE model indicates that initial yield within the shear punch specimen takes place at the top surface directly in contact with the punch, and not at the centre of the gauge section. This observation reinforces the need to run FE simulations in parallel with the observed experimental results to correctly identify critical initial yield and failure points within the test specimens. It is insufficient to assume that the experimentally measured yield stress will correspond to conditions in the gauge section at the nominal value of stress triaxiality (Tables 4.4 and 4.5).

The elastic-plastic constitutive model is now applied to predict the stress state at the onset of failure in the test specimens for the four materials considered. Comparing the compressive, tensile and shear punch experimental responses with the corresponding FE results, candidates for the critical points at failure, and their states of stress, are identified. The state of stress and location of candidate failure points obtained from FE analysis is presented in Tables 4.4 and 4.5. A pressure dependent parabolic failure surface is fitted to the obtained critical failure points located at the centre of the gauge section for the compression and tensile loading cases as shown in Figures 4.3 and 4.4. The failure surface intersects the initial yield surface at a critical stress triaxiality (η^*). The critical stress triaxiality separates the two distinct regimes of failure; ductile regime ($\eta < \eta^*$) and brittle regime ($\eta > \eta^*$). It is observed from Figures 4.3 and 4.4 that for the shear punch loading case, the state of stress at the critical failure point directly under the punch on the top surface lies on the parabolic failure surface for all material types considered. Thus, for the ductile regime, the EDP model is found to predict both initial yield and failure initiation across the range of stress states.
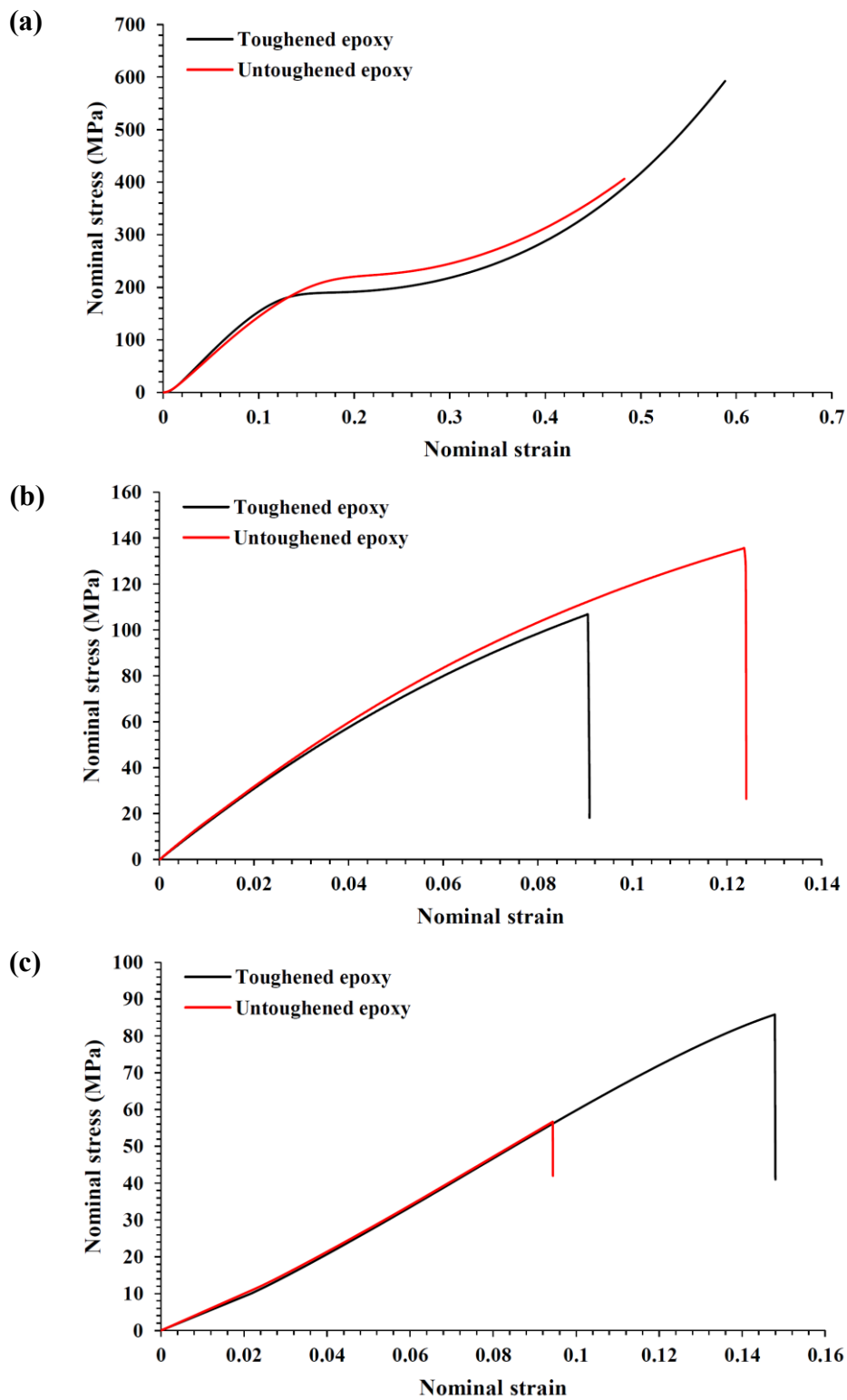
Figure 4.2 Comparison of quasi-static response of toughened and untoughened epoxy 8552; (a) compression, (b) tension, and (c) shear punch.

Table 4.3 Modelling parameters for quasi-static initial yield surface of four material types.

Material	a (/MPa)	Revised compressive yield strength (MPa)	Revised compressive modulus (GPa)
Unfilled epoxy	0.025	120	3.32
Filled epoxy	0.025	90	2.65
Untoughened epoxy	0.009	140	1.62
Toughened epoxy	0.009	115	1.81

From Figures 4.3 and 4.4, it is observed that both toughening strategies; incorporation of core-shell particles and reaction induced phase separation, increase the critical stress triaxiality of neat epoxy resin (Tables 4.4 and 4.5). The increase in critical stress triaxiality leads to a wider ductile failure regime ($\eta < \eta^*$) and narrower brittle failure regime ($\eta > \eta^*$), thus encouraging ductile failure and diminishing the likelihood of brittle failure under complex loading cases such as indentation and impact, potentially increasing the toughness, and in turn, the energy absorption capability of epoxy resin.
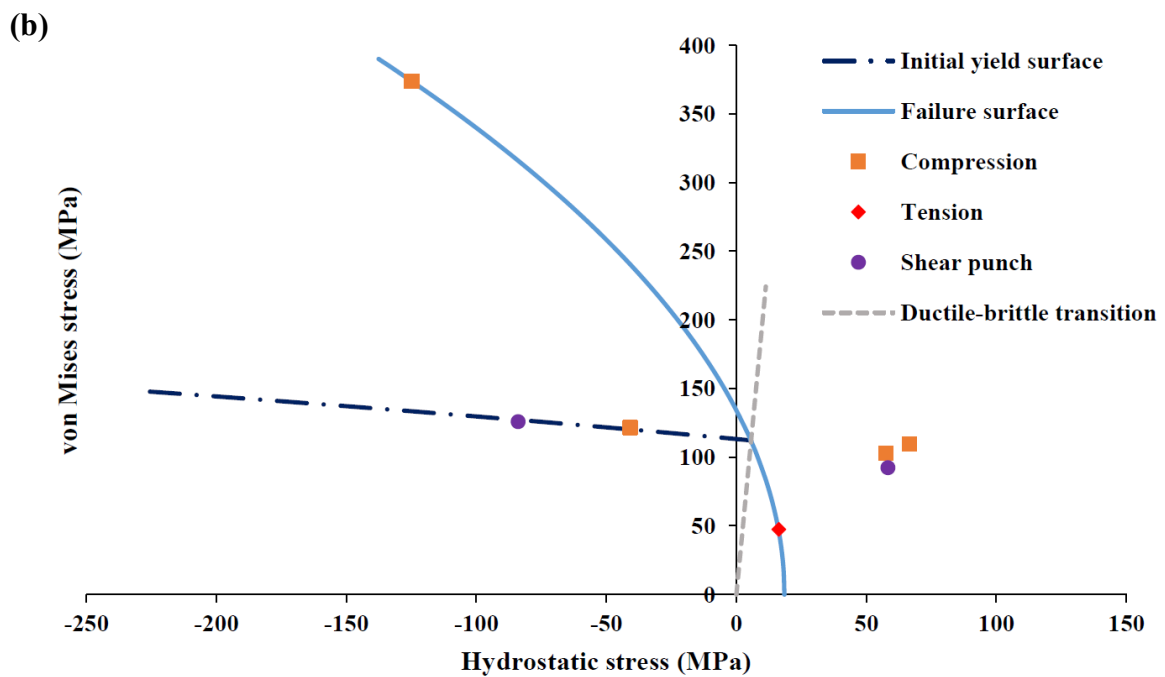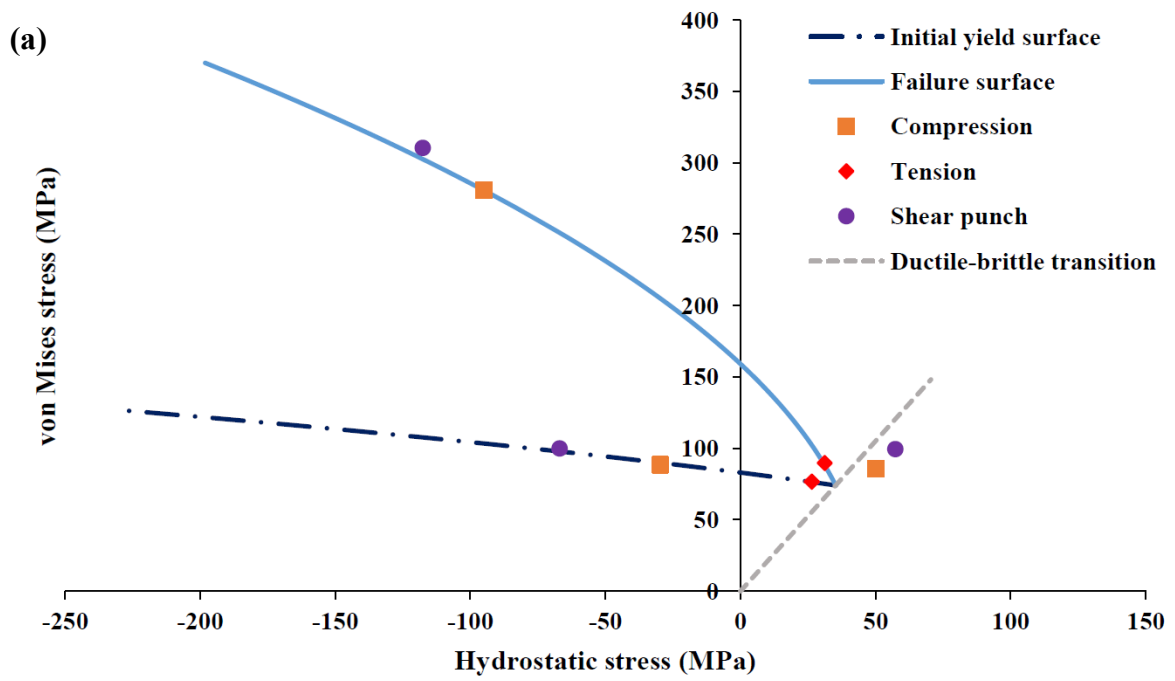
Figure 4.3 Quasi-static initial yield and failure surfaces of epoxy DLS 1832-1; (a) filled, and (b) unfilled.
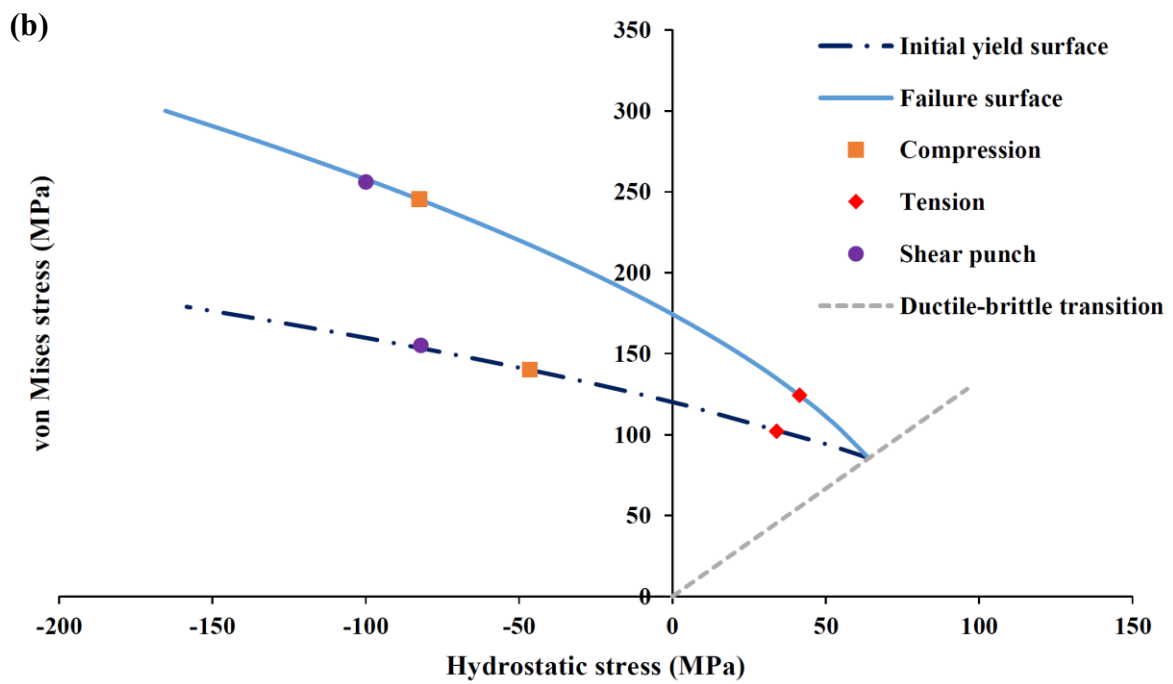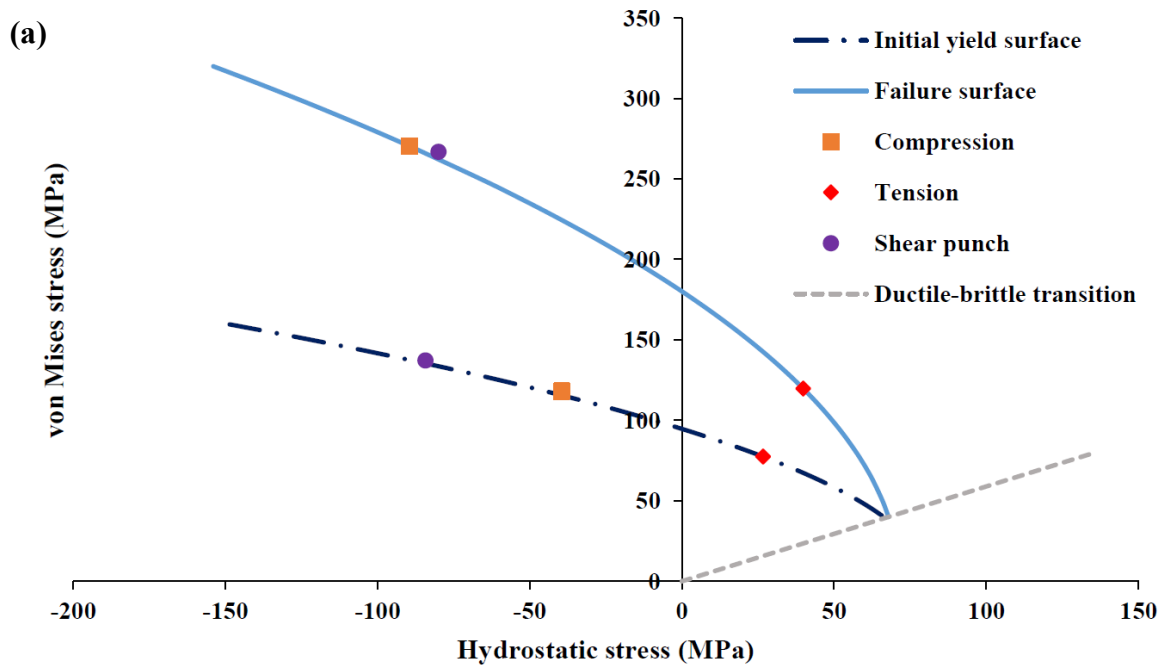
Figure 4.4 Quasi-static initial yield and failure surfaces for epoxy 8552; (a) toughened, and (b) untoughened.

Table 4.4 Stress state at initial yield and failure initiation obtained from FE simulations for candidate points within specimens for filled and unfilled epoxy DLS 1832-1.

Initial yield/Failure	Loading case	Location of yield/failure	σ_v (MPa)	σ_h (MPa)	η	Failure regime
Unfilled epoxy ($\eta^* = 0.05$)						
Initial yield	Compression	Centre of disk	121.6	-40.8	-0.34	NA
Initial yield	Shear punch	Top surface	126.1	-84.2	-0.67	NA
Failure	Compression	Centre of disk	372.0	-125.5	-0.34	Ductile
Failure	Compression	Edge of disk	102.9	57.4	0.56	Brittle
Failure	Compression	Edge of disk	109.7	66.6	0.61	Brittle
Failure	Tension	Gauge section	47.4	16.3	0.34	Brittle
Failure	Shear punch	Bottom surface	92.4	58.3	0.63	Brittle
Filled epoxy ($\eta^* = 0.48$)						
Initial yield	Compression	Centre of disk	88.4	-29.6	-0.33	NA
Initial yield	Tension	Gauge section	76.6	26.4	0.33	NA
Initial yield	Shear punch	Top surface	100.2	-67.1	-0.67	NA
Failure	Compression	Centre of disk	280.6	-94.8	-0.34	Ductile
Failure	Compression	Edge of disk	85.7	50.0	0.58	Brittle
Failure	Tension	Gauge section	89.7	31.1	0.35	Ductile
Failure	Shear punch	Top surface	310.5	-117.6	-0.38	Ductile
Failure	Shear punch	Bottom surface	99.4	57.3	0.58	Brittle

Table 4.5 Stress state at initial yield and failure initiation obtained from FE simulations for candidate points within specimens for toughened and untoughened epoxy 8552.

Initial yield/Failure	Loading case	Location of yield/failure	σ_v (MPa)	σ_h (MPa)	η	Failure regime
Untoughened epoxy ($\eta^* = 0.75$)						
Initial yield	Compression	Centre of disk	140.1	-46.5	-0.33	NA
Initial yield	Tension	Gauge section	102.1	34.0	0.33	NA
Initial yield	Shear punch	Top surface	155.3	-82.2	-0.53	NA
Failure	Compression	Centre of disk	245.3	-82.6	-0.34	Ductile
Failure	Tension	Gauge section	124.2	41.5	0.33	Ductile
Failure	Shear punch	Top surface	256.4	-100.1	-0.39	Ductile
Toughened epoxy ($\eta^* = 1.70$)						
Initial yield	Compression	Centre of disk	117.9	-39.5	-0.33	NA
Initial yield	Tension	Gauge section	77.5	26.7	0.33	NA
Initial yield	Shear punch	Top surface	137.2	-84.3	-0.61	NA
Failure	Compression	Centre of disk	270.5	-89.6	-0.33	Ductile
Failure	Tension	Gauge section	119.7	39.9	0.33	Ductile
Failure	Shear punch	Top surface	266.8	-80.0	-0.30	Ductile

4.3 Modelling strain rate dependence

Understanding strain rate sensitivity of epoxy is particularly important to accurately model the high strain rate and impact behaviour of carbon fibre reinforced epoxy composites. Epoxy is known to be highly sensitive to the applied strain rate. In this study, compression, tension and shear punch experiments are performed across a wide range of strain rates (10^{-3} to 10 /s) to investigate the strain rate sensitivity of the initial yield and failure surface of filled and unfilled epoxy.

4.3.1 Servo-hydraulic test setup

Disk-shaped compression test specimens and square plate specimens for shear punch tests (described in section 3.3) were machined from the as obtained square plates for higher strain rate tests. Tensile tests were conducted on dog-bone shaped specimens according to ASTM D638-14 (type V) (Figure 4.5). The gauge section was of length 9.53 mm and width 3.18 mm, with thickness of the specimens same as the supplied square plate samples (4.05 mm for filled epoxy and 4.5 mm for unfilled epoxy). Characterization tests were conducted over a wide range of strain rates, 10^{-3} to 10^{-1} /s on a screw-driven Instron machine, and 10^{-1} to 10 /s on a servo-hydraulic Instron machine. In order to achieve a constant strain rate during the loading of the specimen at higher strain rates using the servo-hydraulic Instron machine, a delaying mechanism was used to allow enough time for the machine to accelerate. The nominal stress was calculated from the Instron load cell measurements, and nominal strain was obtained using the crosshead displacement.

4.3.2 Higher strain rate test results

4.3.2.1 Compression tests

Compression tests were carried out on filled and unfilled epoxy specimens at strain rates of 10^{-3}, 10^{-2}, 1 and 10 /s. Nominal compressive stress-compressive strain plots for filled and unfilled epoxy indicate; the compressive modulus is insensitive to the applied strain rate, compressive yield strength increases with an increase in strain rate, and compressive failure

strain is inversely proportional to strain rate. Each compressive nominal stress-strain curve shows the same characteristics typical of the quasi-static test case; initial linear elastic response up to yield, followed by non-linear strain hardening up to a local maximum value of nominal stress, strain softening up to a local minimum value of nominal stress, immediately then followed by strain hardening up to compressive failure. The quasi-static compressive failure strength also increases with an increase in strain rate. Figure 4.6 presents a plot of revised compressive yield strength versus log (strain rate) for both filled and unfilled epoxy, with a linear least squares fit approximation used to model the strain rate sensitivity of the initial yield surface, assuming the shape of the initial yield surface remains unchanged. This approach has been used in several previous studies in literature to model the effect of strain rate on the deformation and damage response of epoxy (Chevalier et al., 2016; Morelle et al., 2017; Morin et al., 2010; Werner and Daniel, 2014).
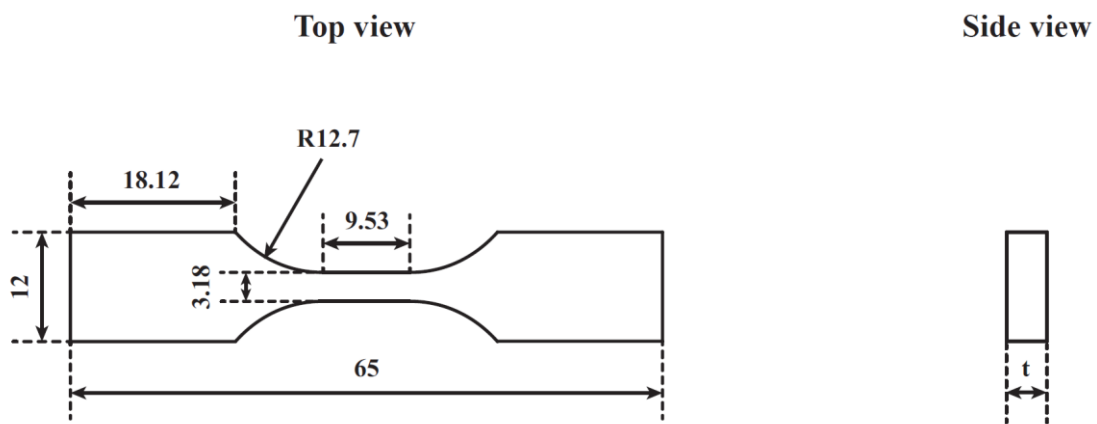
Figure 4.5 Tensile dog-bone specimens (ASTM Standard D638-14 type V) for higher strain rate testing on servo-hydraulic Instron test setup.
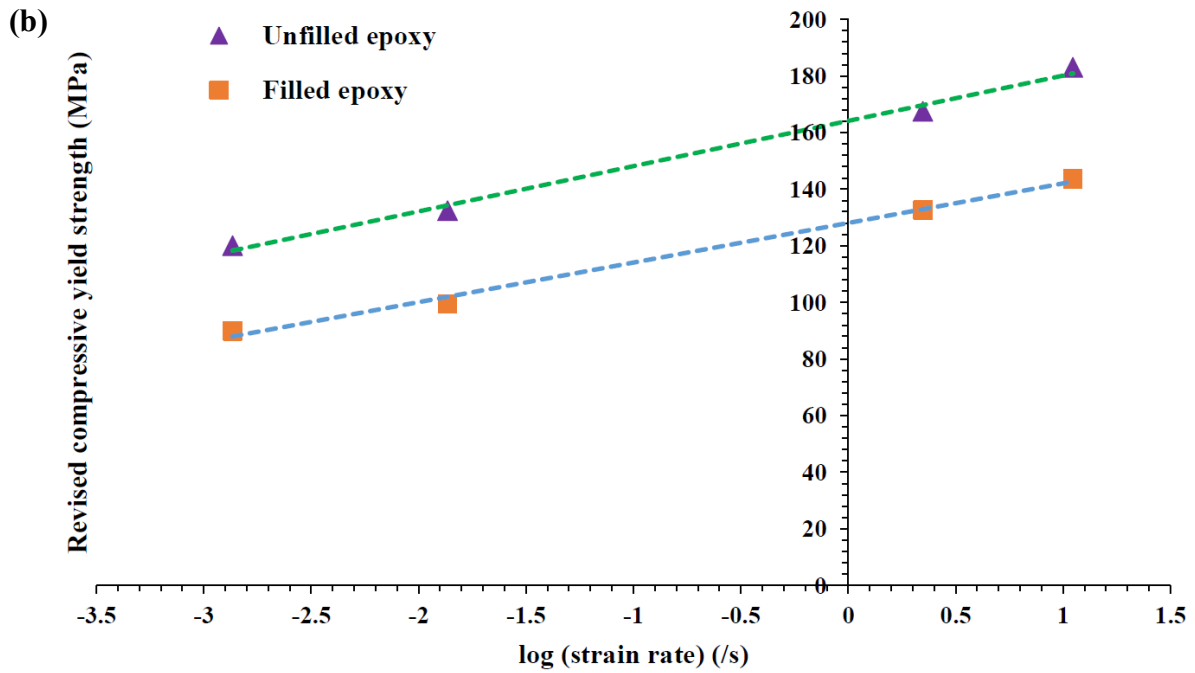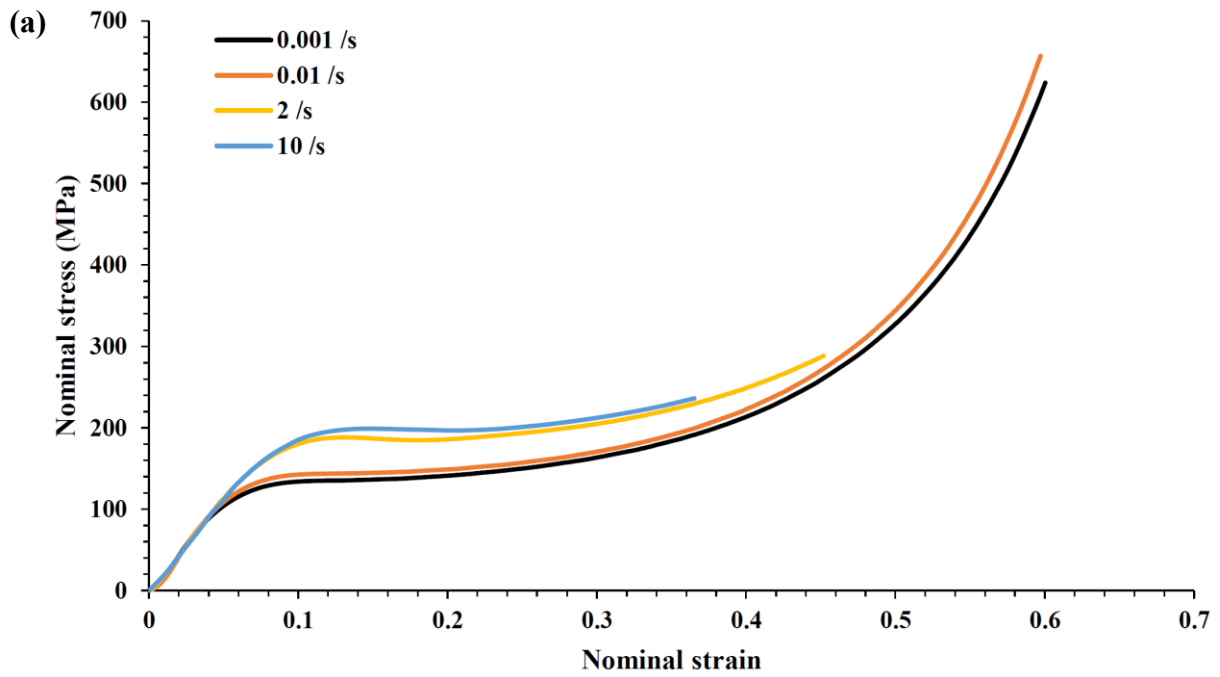
Figure 4.6 (a) Compressive response of filled epoxy DLS 1832-1 over a wide range of strain rates, (b) Revised compressive yield strength vs. log (strain rate) for filled and unfilled epoxy DLS 1832-1.

4.3.2.2   Tensile tests

Higher strain rate tensile experiments were carried out on filled and unfilled epoxy specimens at loading rates of 1, 10 and 50 mm/s, corresponding to strain rates of 0.1, 1 and 5 /s. Nominal tensile stress-tensile strain plots for filled and unfilled epoxy show that an increase in the applied strain rate is accompanied by decrease in the tensile failure strain, while the tensile modulus gradually increases. For unfilled epoxy, each stress-strain plot is characterised by a linear elastic response up to brittle failure. Tensile response of filled epoxy at different strain rates, shown in Figure 4.7, clearly illustrates the transition from ductile to brittle failure with an increase in the strain rate. At lower strain rates near the quasi-static range (10^{-3}-10^{-2} /s), the nominal stress-strain curve indicates ductile behaviour, with a linear elastic response up to yield, followed by a non-linear response up to failure. At higher loading rates (0.1-5 /s), the nominal stress-strain curve shows a linear elastic response up to failure, indicating brittle failure.
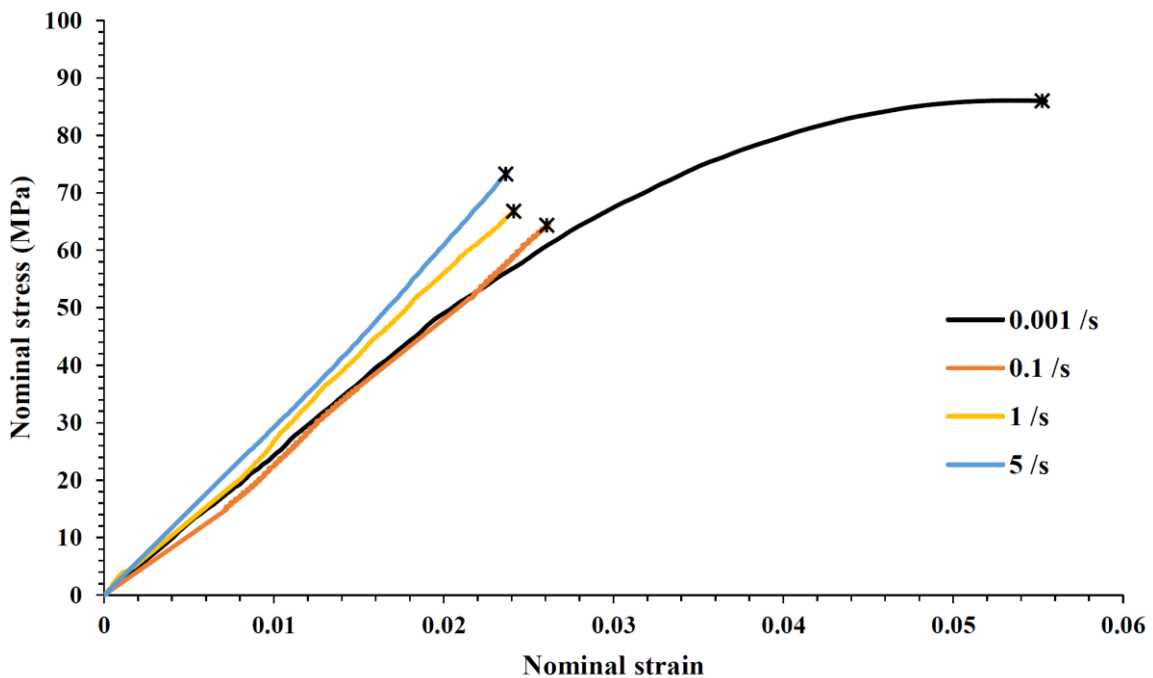
Figure 4.7 Tensile response of filled epoxy DLS 1832-1 over a wide range of strain rates.

4.3.2.3   Shear punch tests

Shear punch experiments were conducted on filled and unfilled epoxy specimens at strain rates of 10^{-3}, 10^{-2}, 0.1 and 1 /s. For unfilled epoxy, each shear punch stress-strain plot at higher strain rates is characterised by a linear elastic response up to brittle failure. Nominal stress-strain plots for unfilled epoxy show that an increase in the applied strain rate leads to a decrease in the failure strain, while the shear punch modulus increases.

The quasi-static shear punch nominal stress-strain response of filled epoxy is linear elastic up to yield, followed by a non-linear response up to brittle failure initiation, characterised by the presence of cracks at the periphery of the punch and a sudden drop in nominal stress. Brittle failure initiation is followed by a saw-tooth response at an approximately constant nominal stress value, indicating crack propagation within the shear punch specimen. This is followed by strain hardening up to final failure. Figure 4.8 illustrates the shear punch response of filled epoxy at different strain rates. The absence of the final strain hardening phase before final failure when the applied strain rate increases from 10^{-3} to 10^{-2} /s indicates a transition from ductile to brittle failure, consistent with the strain rate dependent tensile behaviour. An increase in strain rate increases the shear punch yield strength while decreasing the value of strain at failure initiation. The shear punch modulus does not change appreciably with an increase in strain rate.
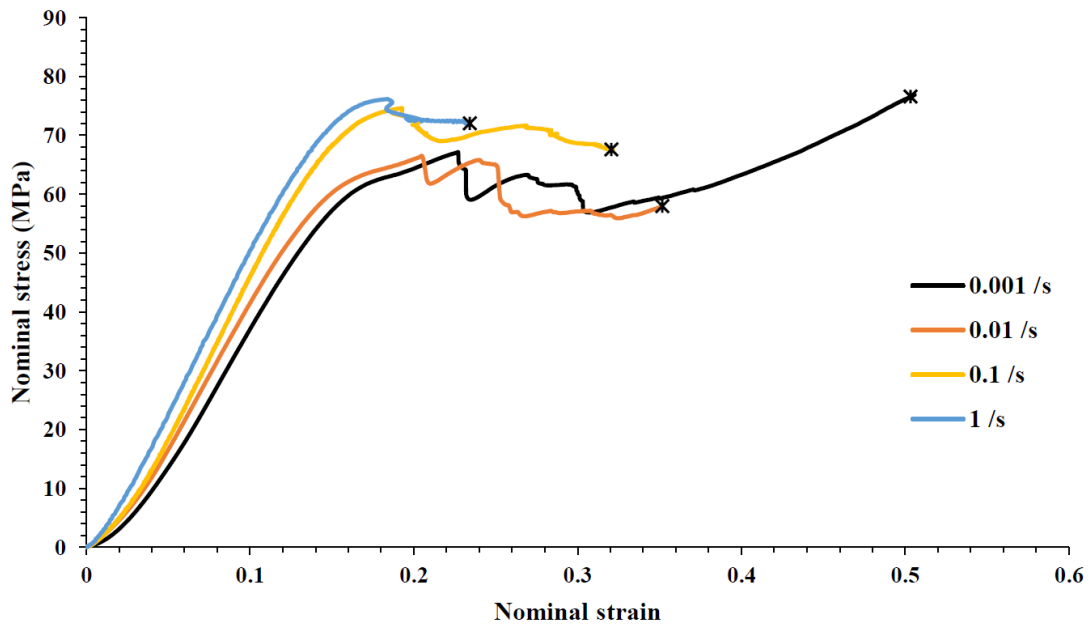
Figure 4.8 Shear punch response of filled epoxy DLS 1832-1 over a wide range of strain rates.

4.4   Strain rate dependent initial yield and failure surfaces

FE simulations are carried out in Abaqus/Explicit using a strain rate dependent EDP model to predict the high strain rate tensile and shear punch experimental response of filled and unfilled epoxy. Comparing the tensile and shear punch experimental response with the corresponding FE results, critical failure points are identified within the test specimens for each loading case. The state of stress and location of critical failure points for each of the three loading cases is obtained from FE analysis. The tensile dog-bone specimen fails at the gauge section at high strain rates. FE analysis for shear punch specimens indicate two locations of failure; one directly below the punch on the top surface of the specimen undergoing compressive loading, and the other at the bottom surface of the specimen with predominantly tensile loading. A stress state dependent parabolic failure surface is fitted to the obtained critical failure points for the tensile and shear punch loading cases. The initial yield and failure surfaces at quasi-static (QS) and higher strain rate (HSR) for both filled and unfilled epoxy is shown in Figure 4.9 to illustrate the effect of strain rate. Here, QS and HSR refer to strain rates of 10^{-3} and 1 /s, respectively. For both filled and unfilled epoxy,

the initial yield surface shifts upwards with an increase in strain rate while the failure surface shifts slightly downwards. The net result of the individual shifts in the initial yield and failure surface is that the critical stress triaxiality (η^*) decreases. For filled epoxy, η^* decreases from 0.48 to 0.09 when the strain rate is increased from QS (10^{-3} /s) to HSR (1 /s) (Figure 4.9a). η^* decreases from 0.05 to -0.07 when the strain rate is increased from QS (10^{-3} /s) to HSR (1 /s) for unfilled epoxy (Figure 4.9b). Thus, for both filled and unfilled epoxy, an increase in strain rate narrows the ductile failure regime, while simultaneously increasing the brittle failure regime. It should be noted that at both strain rates considered in Figure 4.9, the filled epoxy is less likely to fail in a brittle mode compared to the unfilled epoxy under complex loading cases such as indentation and impact, clearly illustrating the benefits of toughening neat epoxy to increase resistance to damage and energy absorption capability.

4.5 Conclusions

This study aims to systematically investigate the effect of strain rate and two toughening strategies on the stress state dependent initial yield and failure surface of epoxy. Addition of core-shell particles and reaction induced phase separation were the two toughening strategies considered. Quasi-static compression, tension and shear punch tests were carried out to span a wide range of stress triaxialities for four types of epoxy resins. The EDP model developed in section 3.4, by using FE analysis in parallel with the experimental results, was used to obtain the pressure dependent quasi-static initial yield and failure surfaces for the four materials investigated. The addition of core-shell particles to neat epoxy decreases its modulus and yield strength, while increasing its ductility. Reaction induced phase separation based toughening also leads to a reduction in yield strength of epoxy. Critical stress triaxialities were identified for each material type, and a consistent trend of increase in the ductile failure regime (due to an increase in critical stress triaxiality) is noted due to toughening of epoxy using both strategies considered in the present investigation.

In order to probe the strain rate sensitivity of epoxy, compression, tension and shear punch tests are carried out over a wide range of strain rates (10^{-3}-10 /s) for the filled and unfilled epoxy specimens. A linear fit of the experimental compressive yield strength vs log(strain

rate) data was used to model the strain rate sensitivity of the initial yield surface. A strain rate dependent EDP model thus obtained was used to identify candidate locations of failure for the tensile and shear punch loading case at higher rates of strain. Comparing the tensile and shear punch experimental response at higher strain rates with the corresponding FE results, critical failure points are identified within the test specimens for each loading case. The state of stress at the location of failure initiation is obtained from FE analysis for both the filled and unfilled specimens. A stress state dependent parabolic failure surface is fitted to the obtained critical failure points for the tensile and shear punch loading cases. Thus, the strain rate dependent parabolic failure surface is obtained for the two materials. For both filled and unfilled epoxy, the initial yield surface shifts upwards with an increase in strain rate while the failure surface shifts slightly downwards. The net result of the individual shifts in the initial yield and failure surface is that the critical stress triaxiality decreases. Thus, an increase in strain rate narrows the ductile failure regime, while simultaneously increasing the brittle failure regime. It should be noted that the filled epoxy is less likely to fail in a brittle mode compared to the unfilled epoxy under complex loading cases such as indentation and impact, clearly illustrating the benefits of toughening neat epoxy to increase resistance to damage and energy absorption capability.
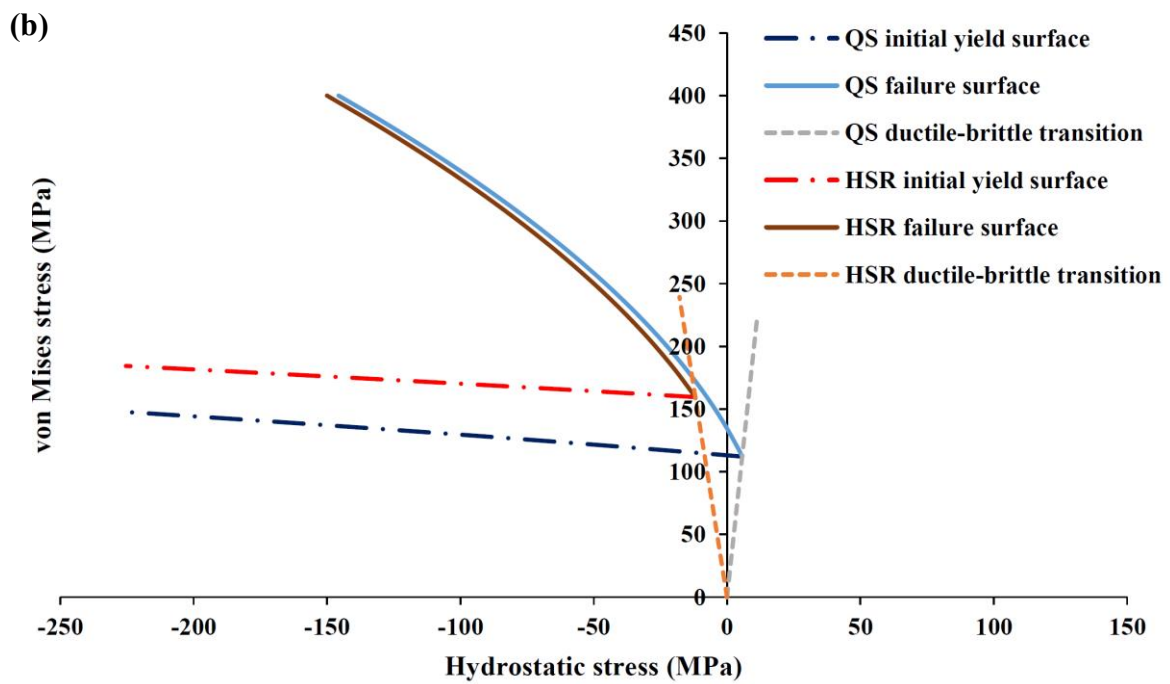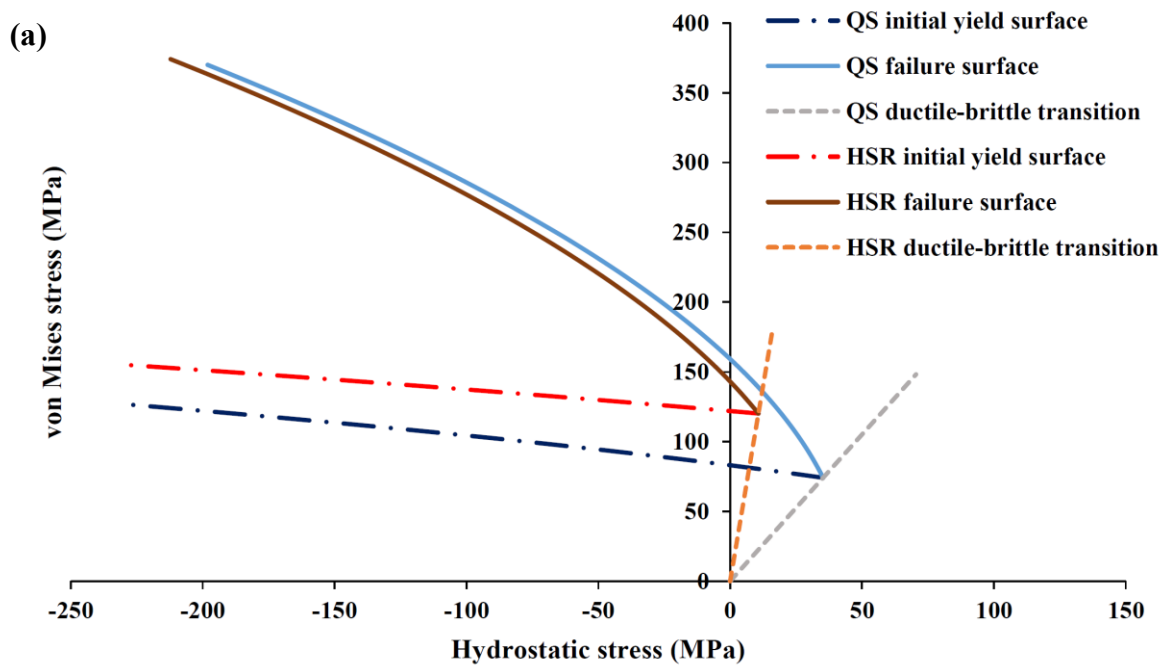
Figure 4.9 Strain rate dependent initial yield and failure surfaces for epoxy DLS 1832-1; (a) filled, and (b) unfilled.

Chapter 5   Impact perforation of carbon fibre reinforced epoxy composites

5.1   Introduction

In this chapter, experimental studies are conducted on the quasi-static indentation and ballistic impact perforation behaviour of plain weave carbon/epoxy composites to investigate the effect of toughening the epoxy matrix to improve resistance to indentation and impact. The values of energy absorbed during quasi-static and impact perforation for the composites are compared with the corresponding values for thin aluminium alloy AA 6082-T4 target plates investigated in Chapter 2. Additional quasi-static edge-clamped indentation studies are performed on carbon fibre reinforced epoxy composites using indenters with different tip geometries to assess the nose shape sensitivity of failure initiation in composite plates. A qualitative comparison of the indenter tip geometry and stress state dependence of damage in carbon/epoxy composites and thin ductile metal plates is carried out. Chapters 3 and 4 on the stress state and strain rate dependent yield and failure behaviour of epoxies toughened using two different strategies inform the qualitative discussion on the quasi-static indentation and impact perforation response of carbon fibre reinforced epoxy composites studied in this chapter.

Carbon fibre reinforced epoxy composites are known to be particularly susceptible to ballistic impact loading, with their perforation resistance and damage tolerance dependent on the failure properties of the epoxy matrix. One of the ways to enhance the energy absorption capability and, in turn, resistance to impact damage of carbon/epoxy composites is to increase the fracture toughness of epoxy resin by incorporation of toughening particles.

There are limited studies on the ballistic impact behaviour of fibre reinforced composites with toughened epoxy matrices (Laurenzi et al., 2013; Pandya et al., 2012; Pol et al., 2012; Rahman et al., 2013; Tehrani et al., 2013). These studies reported an enhancement in ballistic impact resistance of fibre reinforced composites with filled epoxy matrices on addition of toughening particles.

Understanding stress state dependence of failure for carbon fibre reinforced epoxy composites is essential to accurately predict their quasi-static and high strain rate perforation response for a wide range of projectile nose shapes. While there are several analytical studies on the ballistic impact behavior of fibre reinforced composites (Caprino et al., 2007; Cheeseman and Bogetti, 2003; López-Puente et al., 2007; Mohan and Velu, 2014; Morye et al., 2000; Naik et al., 2012, 2006, 2005; Pandya et al., 2015; Rajagopal and Naik, 2014; Shaktivesh et al., 2013), there are only a few investigations on projectile nose shape sensitivity of failure initiation in carbon fibre reinforced epoxy composites during ballistic impact (Ben-Dor et al., 2002; Ulven et al., 2003; Wen, 2000). There is a need to systematically characterize the quasi-static and impact perforation behavior of carbon fibre reinforced epoxy composites for different indenter/projectile tip geometries to accurately predict their ballistic impact characteristics over a wide range of stress states and strain rates.

The present study aims to investigate the effect of toughening the epoxy matrix as a part of plain weave carbon/epoxy composites, by the addition of core-shell particles, on their quasi-static indentation and ballistic impact perforation response. This study also aims to assess the nose shape sensitivity of the quasi-static edge-clamped indentation behaviour of carbon fibre reinforced epoxy composites using indenters with three different tip geometries; flat, intermediate and hemispherical. Two types of composites are characterised in this study; plain weave carbon fibre reinforced epoxy DLS 1832-1 (hereafter referred to as unfilled CFRE) and plain weave carbon fibre reinforced core-shell particle filled epoxy DLS 1832-1 (hereafter referred to as filled CFRE). Quasi-static compression, tension and edge-clamped indentation tests (flat-nosed indenter) are carried for both types of composites to evaluate the effectiveness of the toughening method adopted. Next, impact perforation experiments are performed on both filled and unfilled CFRE to compare their ballistic impact performance in terms of ballistic limit velocities, energy absorption capability and failure

mechanisms. The impact resistance of carbon/epoxy composites is compared with that of a 1 mm thick AA 6082-T4 target plate investigated in Chapter 2. Finally, quasi-static edge-clamped indentation experiments are conducted on unfilled CFRE using different indenter tip geometries to span a wide range of stress states at failure. The indenter nose shape sensitivity, and in turn, the stress state dependence of failure in case of carbon fibre composites is qualitatively assessed. The quasi-static perforation characteristics of thin ductile metal plates (Chapter 2) and carbon fibre reinforced epoxy composites are compared qualitatively, and similarities and differences in their stress state dependent fracture behaviour are discussed in the context of the stress state and strain rate dependent yield and failure response of filled and unfilled epoxies (Chapters 3 and 4).

5.2   Materials and quasi-static characterisation

Two types of composites were supplied by Hexcel Composites, UK in the form of square plates 130 mm x 130 mm:

(A) Plain weave carbon fibre reinforced epoxy DLS 1832-1 of thickness 4.5 ($\pm$0.1) mm, density 1540 kg/m^3 and Poisson's ratio 0.25.

(B) Plain weave carbon fibre reinforced epoxy DLS 1832-1, with the epoxy matrix filled with 10% by weight core-shell particles (outer diameter 100 nm), of thickness 4.4 ($\pm$0.1) mm, density 1540 kg/m^3 and Poisson's ratio 0.25.

The composite layups were symmetric and quasi-isotropic (in-plane isotropic). The layups were [0/90]$_S$, and the Poisson's ratio was provided by the supplier. These two materials were characterised by considering three tests; compression, tension, and edge-clamped indentation using a flat indenter. Repeat tests were conducted for each load case to obtain a consistent material response. The compression and tensile test setups are given in section 3.3, while the edge-clamped indentation setup is described in section 3.5. Tensile test specimens were machined as per ASTM Standard D3039-14 from the square plates at an orientation parallel to the weave direction. Since the composite layups are quasi-isotropic, in-plane anisotropy can be neglected. Compression tests were performed on circular disks of diameter 8 mm machined from the square plates with thickness equal to the plate

thickness. It should be noted that the tensile tests were in-plane, while the compression tests were out-of-plane. Quasi-static characterisation tests were conducted using a screw-driven Instron test machine at a strain rate of approximately 10^{-3} /s for both types of composites. The force was obtained from the load cell, and the crosshead displacement obtained was corrected for crosshead compliance for all three loading cases.

5.2.1 Compression and tensile test results

Nominal stress-strain curves for quasi-static compressive and tensile response of filled and unfilled CFRE are shown in Figures 5.1a and 5.1b, respectively. Multiple tests were performed for each loading case (not shown in the figure) to ensure good repeatability of the quasi-static material response. Table 5.1 presents the quasi-static properties of filled and unfilled CFRE under compressive and tensile loading.

Table 5.1 Quasi-static compressive and tensile properties of filled and unfilled CFRE.

Material	Yield strength (MPa)	Modulus (GPa)	Failure strength (MPa)	Failure strain
Compression				
Unfilled CFRE	NA	24.74	1104	0.046
Filled CFRE	NA	16.59	962	0.058
Tension				
Unfilled CFRE	NA	54.97	1017	0.019
Filled CFRE	981	42.61	1052	0.026

Figure 5.1a presents the quasi-static compression behaviour of filled and unfilled CFRE. For both types of composites, the compressive nominal stress-strain curve is linear up to compressive failure, with the absence of yield/strain hardening in the material response. This contrasts with the quasi-static compressive response of filled and unfilled epoxy DLS 1832-

130

1 investigated in Chapter 4, which is characterised by a linear elastic response up to yield, followed by non-linear strain hardening, strain softening and finally strain hardening up to failure. Toughening the epoxy matrix as part of the composite by adding 10% by weight core-shell particles leads to a 33% reduction in compressive modulus, 13% decrease in compressive failure strength, and 26% increase in the compressive failure strain.

The quasi-static tensile response of filled and unfilled CFRE is given in Figure 5.1b. The tensile nominal stress-strain curve of filled CFRE indicates ductile behaviour, with a linear elastic response up to yield, followed by a non-linear response up to failure. The corresponding plot for unfilled CFRE shows a linear elastic response up to failure, indicating brittle failure. These stress-strain plots are in good agreement qualitatively with those obtained for filled and unfilled epoxy DLS 1832-1 (Chapter 4). From Figure 5.1b and Table 5.1, it can be observed that addition of core-shell particles to the epoxy matrix in the carbon/epoxy composite results in a 22% decrease in tensile modulus, 3% increase in tensile failure strength, and 37% increase in failure strain.

The quasi-static compression and tensile moduli for both filled and unfilled CFRE are different, indicating out-of-plane anisotropy (Table 5.1).
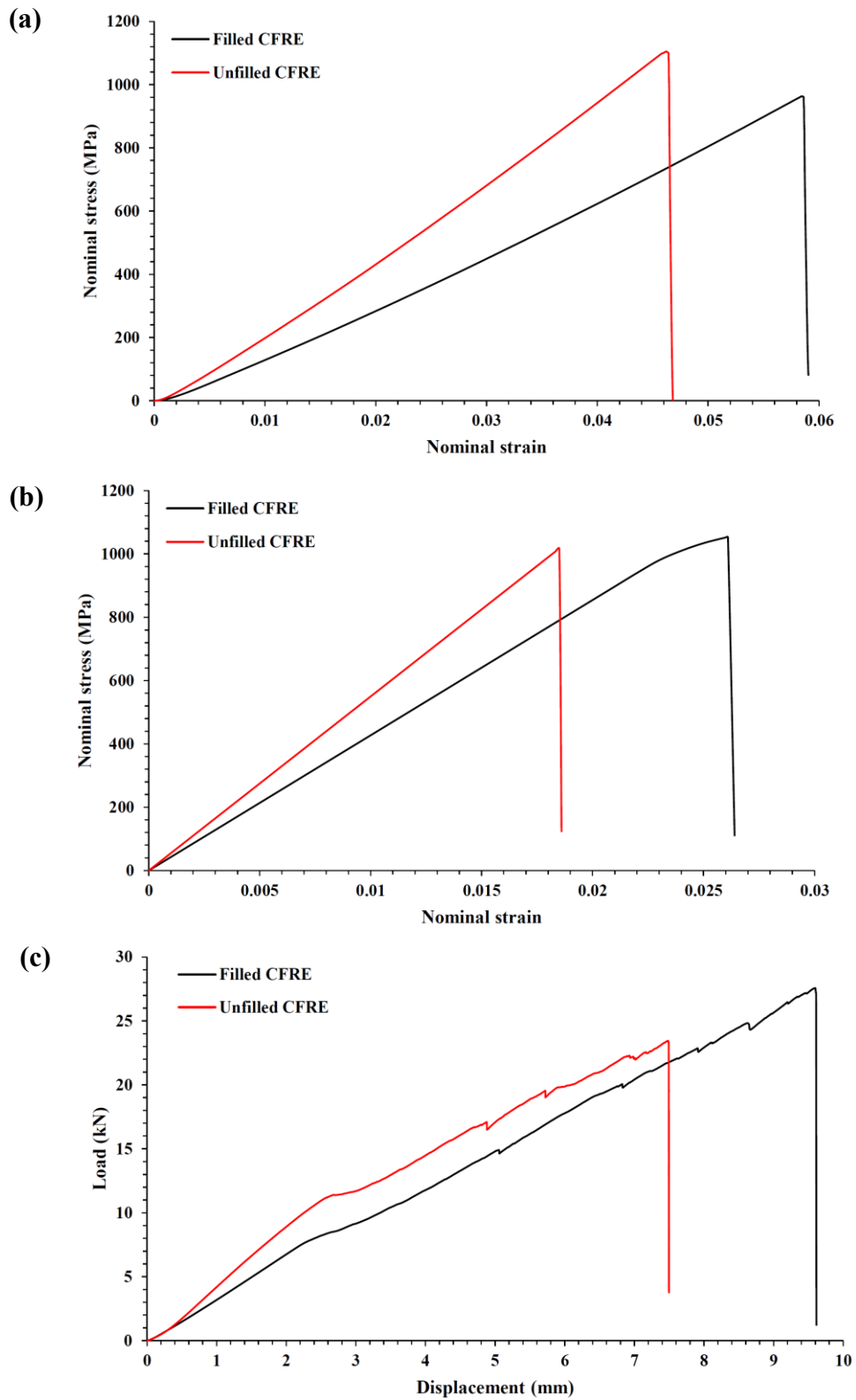
Figure 5.1 Comparison of experimental quasi-static response of filled and unfilled CFRE; (a) compression, (b) tension, and (c) edge-clamped indentation (flat indenter).

132

5.2.2 Edge-clamped indentation test results

The force-displacement curves measured during quasi-static edge-clamped indentation tests for a flat indenter nose shape are presented in Figure 5.1c. Multiple tests were conducted for each composite type (not shown in the figure) to ensure good repeatability of the response. The indenter force-displacements plots are characterised by an initial linear response up to failure initiation. This is followed by a reduction in the slope of the curve as failure propagates through the thickness of the carbon/epoxy composite plate. Sequential damage of the plain weave carbon fabric layers of the composite plate at regular intervals is observed, terminating in final fracture characterised by a large drop in the value of applied indenter force. Layer-by-layer failure is typical of carbon fibre reinforced epoxy composites, and is therefore distinct from the indentation response of filled and unfilled epoxy. Energy absorbed by the composite plate up to failure E_A during indentation is defined as the area under the indenter force-displacement curve. From Figure 5.1c, it can be observed that the initial slope of the indenter force-displacement curve is lower for the filled CFRE compared to the unfilled CFRE. However, a larger displacement at final fracture for the filled CFRE plate results in the absorption of 46% more energy up to failure. Thus, the energy absorption capability of plain weave carbon/epoxy composites during quasi-static perforation is enhanced due to toughening of the epoxy matrix by the addition of core-shell particles. A reduction in modulus along with an increase in ductility is also observed due to toughening of epoxy during quasi-static in-plane tensile and out-of-plane compression tests (Figures 5.1a and 5.1b). From previous experimental studies (Chapter 4), we know that the addition of core-shell particles to epoxy increases its ductility while also reducing its modulus during three different modes of loading; compression, tension and shear punch loads. The epoxy matrix within the composite is in a complex state of stress, presumably a combination of tensile, compressive and shear loads, during edge-clamped indentation of the composite plate. Therefore, we hypothesize that the increase in ductility of epoxy resin in different states of stress due to particle reinforcement leads to enhancement of the energy absorption capability of filled CFRE.

5.3 Impact response of plain weave carbon/epoxy composites: blunt indenter

5.3.1 Impact test setup

The ballistic impact test setup is identical to the one used to investigate the impact perforation behaviour of a thin AA 6082-T4 target in Chapter 2. The test specimens used consist of flat composite plates (both filled and unfilled) with a circular target area of diameter 100 mm fully clamped around the edge. Impact experiments were performed using flat-ended rigid mild steel projectiles with diameter 12.5 mm and mass 20.2 g. The projectiles were fired using a single stage gas gun with a barrel of internal diameter 12.7 mm. A high-speed camera (Vision Research Phantom V710) was used to capture the impact and residual velocities of the projectile during impact, as discussed in Chapter 2. Positive velocity was defined in the direction of initial impact.

5.3.2 Ballistic impact test results

Figure 5.2 presents a plot of residual velocity V_r versus impact velocity V_i for both filled and unfilled CFRE obtained by performing multiple ballistic impact experiments. At least six impact experiments were performed for each composite material. The values of lower and upper ballistic limit velocities were thus obtained for both types of composite targets. The energy absorbed by the target (E_A) during impact is calculated as:

$$E_A = \frac{1}{2} m_p (V_i^2 - V_r^2) \qquad (5.1)$$

where m_p is the mass of the projectile. Table 5.2 presents the quasi-static indentation and ballistic impact properties of filled and unfilled CFRE perforated by a flat indenter/projectile. The values of energy absorbed by the target during impact given in Table 5.2 are calculated based on upper ballistic limit velocity. The corresponding properties for a thin AA 6082-T4 target (Chapter 2) are provided for comparison.
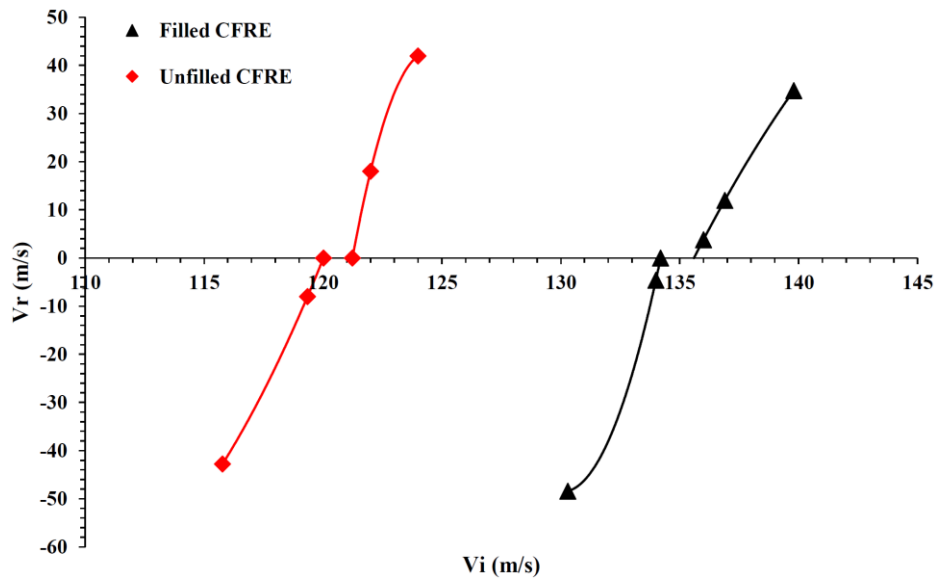
Figure 5.2 Residual velocity (V_r) versus incident velocity (V_i) for ballistic impact perforation of filled and unfilled CFRE by a flat-ended projectile.

Table 5.2 Quasi-static edge-clamped indentation and ballistic impact properties of different materials perforated by a flat indenter/projectile.

Material	Plate thickness, t (mm)	Lower ballistic limit (m/s)	Upper ballistic limit (m/s)	E_A (J)	$\overline{E_A}$ (Jm²/kg)
Quasi-static edge-clamped indentation					
AA 6082-T4	1	NA	NA	14.2	5.27
Unfilled CFRE	4.5	NA	NA	94.2	13.59
Filled CFRE	4.4	NA	NA	137.6	20.31
Ballistic impact					
AA 6082-T4	1	60.1	62.2	39.08*	14.47
Unfilled CFRE	4.5	120.0	121.2	148.36*	21.41
Filled CFRE	4.4	134.2	134.9	183.80*	27.12

*Values of E_A during impact are calculated based on upper ballistic limit velocity.

The values of energy absorbed by a thin aluminium alloy plate during quasi-static edge-clamped indentation (Mohagheghian et al., 2017b) and impact perforation (Chapter 4) by a flat indenter/projectile are obtained from previous studies.

Specific energy absorbed by the different materials, $\overline{E_A}$ is calculated as:

$$\overline{E_A} = \frac{E_A}{\rho t} \tag{5.2}$$

where, ρ and t denote density and thickness of the composite plate, respectively. $\overline{E_A}$ is the energy absorbed normalized by the target mass per unit area.

From Table 5.2, it is inferred that the specific energy absorbed during quasi-static indentation and ballistic impact perforation increases by 49% and 27%, respectively on incorporation of core-shell particles into epoxy matrix as part of the plain weave carbon/epoxy composite. Thus, toughening of the epoxy matrix in a carbon fibre reinforced epoxy composite is an effective way of increasing resistance to both quasi-static indentation and ballistic impact perforation. It can also be concluded that both types of carbon/epoxy composites have a significantly greater specific energy absorption capability compared to AA 6082-T4, with $\overline{E_A}$ for quasi-static perforation enhanced by 158% for unfilled CFRE and 285% for filled CFRE compared to the monolithic aluminium alloy plate. The increase in $\overline{E_A}$ during impact perforation for both composites compared to AA 6082-T4 (48% for unfilled CFRE and 87% for filled CFRE) is also substantial, but lower than that in case of quasi-static indentation. It may be noted that the trend in the ballistic impact properties of filled and unfilled CFRE can be inferred from the quasi-static edge-clamped indentation results.

Figure 5.3 illustrates damage patterns during ballistic impact by a flat projectile on the front (impact) and back (distal) surfaces of unfilled CFRE target plates at different incident projectile impact velocities. For incident projectile velocities below the lower ballistic limit (Figure 5.3a), crack propagation is seen on the impact surface along the weave directions of the carbon/epoxy composite target. No damage pattern is visible on the back surface of the target. At incident projectile velocities within the ballistic limit range of unfilled CFRE (between the lower and upper ballistic limits) shown in Figure 5.3b, the projectile is stuck

within the target plate. A plug of the same diameter as the projectile is ejected from the back of the target plate (not shown in the figure). The front face of the target indicates a similar damage pattern to the previous case (Figure 5.3a), with prominent cracks propagating radially outward from the periphery of the projectile in the contact zone along the warp and fill directions of the composite target. An examination of the distal surface of the target plate indicates sequential ply-by-ply shear plugging failure through the thickness of the unfilled CFRE plate along with significant delamination of the plain weave carbon fabric layers. For incident projectile impact velocities higher than the upper ballistic limit (Figure 5.3c), the damage patterns on the front and back surfaces of the target plate are qualitatively similar to the ones observed for incident velocities within the ballistic limit range (Figure 5.2b). However, more extensive delamination is observed at the distal surface at incident velocities higher than the upper ballistic limit (Figure 5.3c). Similar damage patterns during impact are observed for filled CFRE plates.

The failure mode and damage patterns during impact of filled and unfilled CFRE target plates struck by a flat-ended projectile are qualitatively similar to the ones obtained during quasi-static perforation using a flat indenter tip geometry. Failure takes place predominantly by shear plugging in both loading cases considered. Significant delamination is observed in the case of ballistic impact, while bulging at the back face of the plate with only partial delamination is seen during quasi-static indentation.
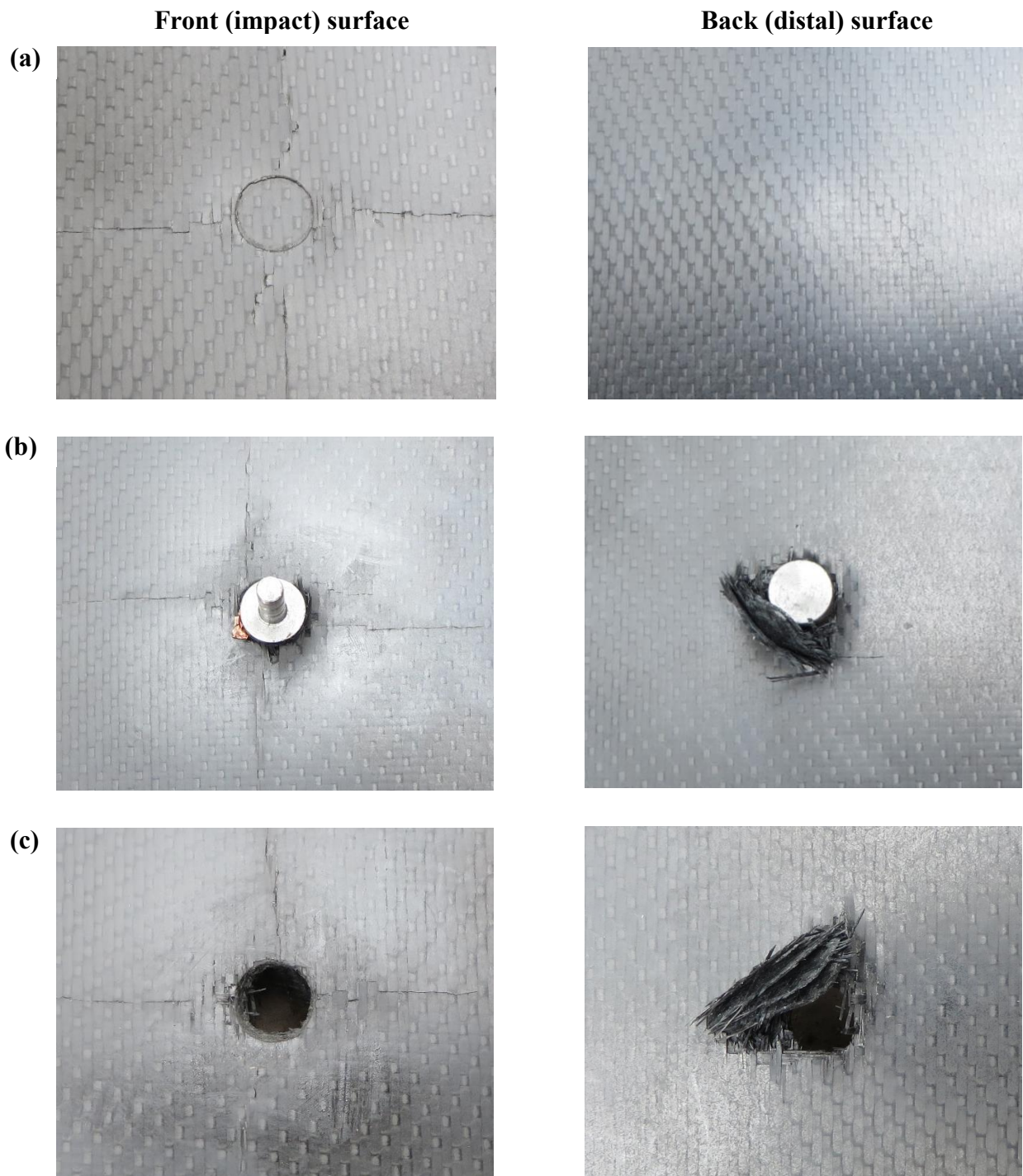
Figure 5.3 Photographs of damage patterns on the front and back surfaces of unfilled CFRE target plates during ballistic impact, with incident projectile impact velocities (a) below lower ballistic limit, (b) within the ballistic limit range and (c) above upper ballistic limit.

5.4 Indenter nose shape sensitivity of carbon/epoxy composites

Quasi-static edge-clamped indentation experiments are conducted on unfilled CFRE plates using three different indenter tip geometries to span a wide range of stress states at failure. Thus, indenter nose shape sensitivity, and in turn, stress state dependence of failure in case of carbon fibre reinforced epoxy composites is qualitatively assessed. Three indenter nose shapes are considered for the indentation tests; flat, intermediate ($R_f = 12 \, mm$) and hemispherical. Quasi-static indentation tests are conducted on unfilled CFRE plates using a screw-driven Instron test machine at a strain rate of approximately 10^{-3} /s for the different indenters. The indenter force is obtained from the load cell, and the crosshead displacement obtained is corrected for crosshead compliance for all three indenter tip geometries.

Figure 5.4 presents force-displacement curves measured during quasi-static edge-clamped indentation tests on unfilled CFRE plates using three different indenter nose shapes. The corresponding damage patterns on the front and back surfaces are presented in Figure 5.5. It can be observed that there is a transition in failure mode from shear plugging dominated failure for flat and intermediate indenter tip geometries to tensile failure (accompanied by petal formation and bending) for hemispherical indenters. Repeat tests were performed for each nose shape to ensure consistent material response. Indenter force-displacements plots are characterised by a linear response up to failure initiation, followed by a reduction in slope of the curve. As shear failure propagates through the thickness of the carbon/epoxy composite plate, sequential damage of the woven fabric layers at regular intervals is observed, terminating in final fracture characterised by a large drop in the value of applied indenter force. Table 5.3 presents the quasi-static edge-clamped indentation properties of unfilled CFRE plates perforated by indenters with three different nose shapes. The corresponding properties for a 1 mm thick AA 6082-T4 plate (Mohagheghian et al., 2017b) are provided for comparison. From Figure 5.4, it can be observed that the initial slope of the indenter force-displacement curve is highest for the flat-ended indenter, followed by the intermediate nose shape ($R_f = 12 \, mm$), and least for the hemispherical indenter. This trend is in agreement with the corresponding results for thin aluminium alloy plates investigated by Mohagheghian et al. (2017b). The displacement at final fracture increases as the frontal

139

nose radius of the indenter is changed from flat to intermediate. This results in an increase of 11% in the overall energy absorbed up to fracture for the intermediate nose shape compared to the flat-ended indenter. However, when the frontal nose radius of the indenter is further increased from $R_f = 12\ mm$ to $R_f = 6.25\ mm$ (hemispherical), the unfilled CFRE plate fails prematurely resulting in a significant decrease of 57% in the value of energy absorbed up to failure for the hemispherical indenter compared to the intermediate indenter nose shape. This trend in E_A for different indenter frontal nose radii for unfilled CFRE plates shown in Table 5.3 contrasts with the corresponding values for thin aluminium alloy AA 6082-T4 plates studied in Chapter 2.
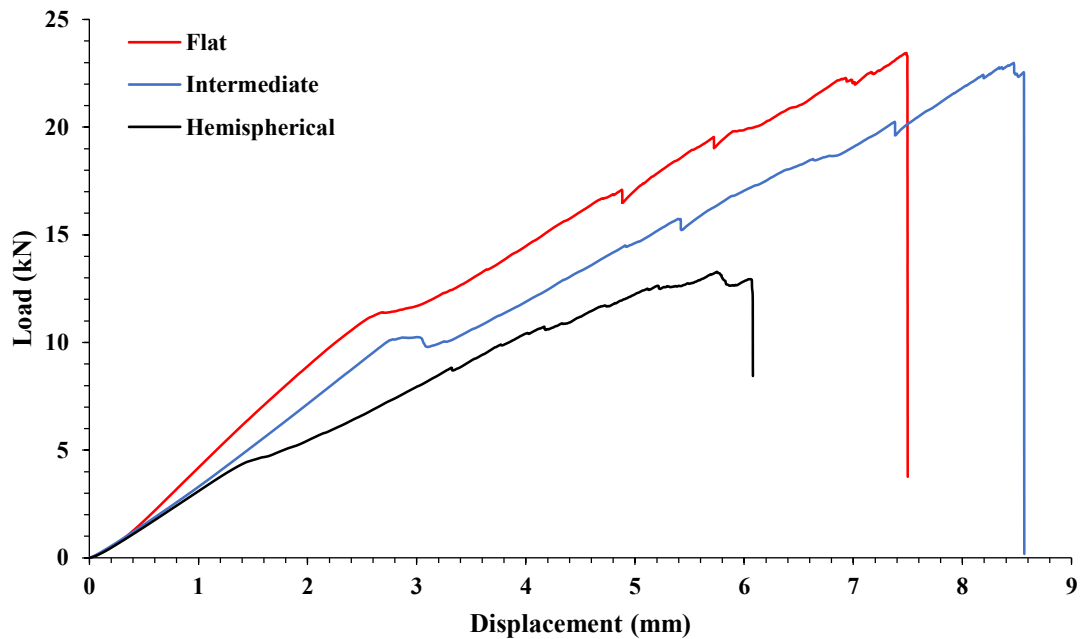
Figure 5.4 Experimental quasi-static edge-clamped indentation response of unfilled CFRE plates using indenters with different nose shapes.

Front surface   **Back surface**

(a)

(b)

(c)
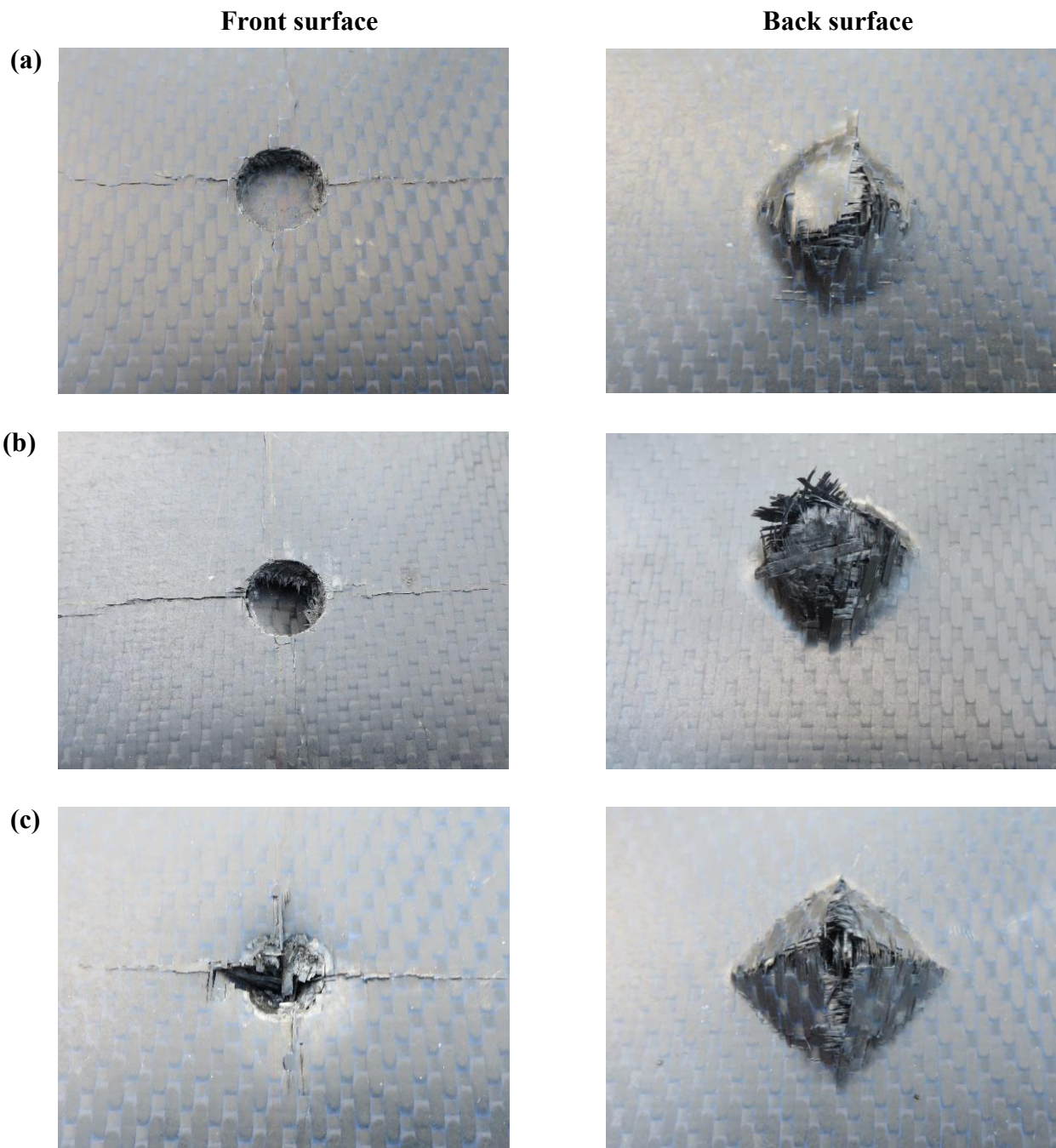
Figure 5.5 Photographs of damage patterns on the front and back surfaces of unfilled CFRE target plates during quasi-static edge-clamped indentation with different indenter nose shapes; (a) flat, (b) intermediate and (c) hemispherical.

Table 5.3 Quasi-static edge-clamped indentation properties of unfilled CFRE and AA 6082-T4 perforated by different indenter nose shapes.

Indenter nose shape	Peak indenter force (kN)	Displacement at failure (mm)	E_A (J)	$\overline{E_A}$ (Jm^2/kg)
Unfilled CFRE				
Flat	23.44	7.49	94.2	13.59
Intermediate	22.98	8.56	104.5	15.08
Hemispherical	13.19	6.07	44.6	6.44
Aluminium alloy 6082-T4				
Flat	4.06	7.66	14.2	5.27
Intermediate	6.45	13.52	37.4	13.85
Hemispherical	5.07	13.26	31.8	11.78

For quasi-static indentation tests using a flat indenter, the unfilled CFRE plates fail by shear plugging. A bulge is formed on the back face of the target and partial delamination of the woven fabric layers is observed at final fracture. A similar damage mode is observed for the intermediate indenter frontal nose radius. However, for the hemispherical indenter, petal formation and bending takes place at the back face of the carbon/epoxy composite plate at fracture, indicating predominantly tensile failure. Hence, a transition in failure mode from shear plugging to tensile fracture is experimentally observed, also seen for thin aluminium alloy plates investigated in Chapter 2. Based on the stress state dependent quasi-static yield and failure response of filled and unfilled epoxies studied in Chapters 3 and 4, we hypothesize that premature failure observed during quasi-static perforation of the unfilled CFRE plate by a hemispherical indenter is due to fracture in the brittle regime. When the carbon/epoxy composite is subjected to indentation loading, the epoxy matrix within the

composite is under a complex state of stress. Depending on the indenter nose shape, the epoxy matrix fails in the ductile or brittle failure regime. Shear-dominated failure of the epoxy matrix occurs at a value of stress triaxiality lower than the critical stress triaxiality (ductile failure regime), and therefore a larger value of failure strain is obtained for indenters with a nose shape close to flat. However, for hemispherical indenters, the epoxy matrix fails in the brittle failure regime, with a lower strain to failure. As a result, the energy absorbed by the unfilled CFRE target plate up to failure during quasi-static indentation is lower for a hemispherical indenter compared to the flat indenter nose shape. Further experiments are needed to completely span the full range of indenter nose shapes to validate this hypothesis. Numerical simulation studies of the carbon/epoxy composites using stress state dependent material models of the carbon fibres and epoxy matrix would be required to obtain the accurate stress state at the critical material point within the matrix at onset of failure.

5.5 Discussion

In their investigation on the quasi-static and impact perforation of polymer-metal bi-layer plates by a blunt indenter, Mohagheghian et al. (2017a) showed that using a frontal polymer layer increases the perforation resistance of the metal backing layer by changing the effective indenter nose shape. Thus, changing the effective indenter tip geometry is a viable strategy of enhancing the energy absorption capability of carbon fibre reinforced epoxy composites. Two different strategies for enhancing $\overline{E_A}$ are considered in the present study; changing the indenter nose shape, and addition of core-shell particles to the epoxy matrix. From Tables 5.2 and 5.3, it is inferred that the specific energy absorption capability of carbon/epoxy composite plates perforated by a flat indenter increases by 49% on incorporation of core-shell particles into the epoxy matrix. On the other hand, changing the indenter tip geometry increases the energy absorption capability of unfilled CFRE plates by up to 11%, for the range of projectile nose shapes considered. Thus, it can be concluded that toughening the epoxy matrix by adding 10% by weight core-shell particles is a more effective strategy compared to changing the indenter nose shape, to increase resistance to quasi-static indentation.

5.6   Conclusions

Experimental ballistic impact studies are performed on filled and unfilled CFRE plates to investigate the effect of toughening the epoxy matrix by the addition of core-shell particles. Enhancement in ballistic impact performance in terms of critical velocities and specific energy absorbed up to failure is obtained experimentally. Quasi-static edge-clamped indentation tests are carried out on unfilled CFRE plates using indenters with different tip geometries to assess the nose shape sensitivity and stress state dependence of failure for the composite material considered. The failure modes during quasi-static indentation and ballistic impact are observed. The quasi-static and impact perforation resistance of carbon/epoxy composites is compared with that of a 1 mm thick AA 6082-T4 target plate investigated in Chapter 2. The specific observations are:

- The initial slope of the indenter force-displacement curve is lower for the filled CFRE compared to the unfilled CFRE. However, a larger displacement at final fracture for the filled CFRE plate results in a 46% enhancement in E_A compared to unfilled CFRE.

- $\overline{E_A}$ during quasi-static indentation and ballistic impact perforation increases by 49% and 27%, respectively on incorporation of core-shell particles into epoxy matrix as part of the plain weave carbon/epoxy composite. Thus, toughening the epoxy matrix is an effective way of increasing resistance to both quasi-static indentation and ballistic impact perforation.

- Carbon/epoxy composites have a significantly greater $\overline{E_A}$ compared to AA 6082-T4, with $\overline{E_A}$ for quasi-static perforation enhanced by 158% for unfilled CFRE and 285% for filled CFRE compared to the monolithic aluminium alloy plate. $\overline{E_A}$ during impact perforation is increased by 48% for unfilled CFRE and 87% for filled CFRE compared to AA 6082-T4.

- The failure modes and damage patterns during impact of filled and unfilled CFRE target plates struck by a flat-ended projectile are qualitatively similar to those for quasi-static perforation using a flat indenter tip geometry. Failure takes place predominantly by shear plugging in both loading cases considered. Significant delamination is observed

in the case of ballistic impact, while bulging at the back face of the plate with only partial delamination is seen during quasi-static indentation.

- The variation in E_A for different indenter frontal nose radii for unfilled CFRE contrasts with the corresponding trend for thin aluminium alloy AA 6082-T4 plates. This is due to premature failure of the epoxy matrix by brittle fracture observed during quasi-static perforation of the unfilled CFRE plate by a hemispherical indenter. When the carbon/epoxy composite is subjected to indentation, the epoxy matrix is under a complex state of stress. Depending on the indenter nose shape, the epoxy matrix fails in the ductile or brittle failure regime. Shear-dominated failure of the epoxy matrix occurs at a value of stress triaxiality lower than the critical stress triaxiality i.e. in ductile failure regime, and therefore a larger values of failure strain are expected for indenters with a nose shape close to flat. However, for hemispherical indenters, the epoxy matrix fails in the brittle failure regime, with a lower strain to failure. As a result, the energy absorbed by the unfilled CFRE target plate up to failure during quasi-static indentation is lower for a hemispherical indenter compared to the flat indenter nose shape.

- $\overline{E_A}$ of carbon/epoxy composite plates perforated by a flat indenter increases by 49% on incorporation of core-shell particles into the epoxy matrix. On the other hand, changing the indenter tip geometry increases $\overline{E_A}$ of unfilled CFRE plates by up to 11%, for the range of projectile nose shapes considered. Thus, it can be concluded that toughening the epoxy matrix by adding 10% by weight core-shell particles is a more effective strategy compared to changing the indenter nose shape, to increase resistance to quasi-static perforation.

Chapter 6   Conclusions and future work

6.1   Conclusions

As described in section 1.2, the objectives of this thesis were: (i) to understand the influence of the projectile nose shape on the impact energy absorption and perforation resistance of thin ductile aluminium alloy plates, (ii) to systematically probe and model phenomenologically the stress state and strain rate dependent initial yield and failure response of epoxy resin, and to investigate the effect of reinforcing epoxy by introducing different toughening strategies on the failure response, (iii) to explore the influence of microstructural modifications within the epoxy matrix on the quasi-static and impact perforation characteristics of carbon fibre reinforced epoxy composites. The first objective was tackled in Chapter 2 by studying the impact behavior of thin ductile aluminium alloy plates using projectiles with different tip geometries to induce a wide range of stress states. The second objective was addressed in Chapters 3 and 4 by systematically characterizing and modelling the failure behavior of epoxy resin. Two different toughening strategies were investigated; addition of core-shell particles and reaction induced phase separation based toughening. The final objective was treated in Chapter 5 by conducting experiments on the quasi-static indentation and impact perforation behavior of carbon fibre reinforced epoxy composites. The conclusions drawn through Chapters 2 to 5 are summarized in the following sections. This chapter ends with suggestions for future work.

6.1.1 Impact response of thin aluminium alloy plates

- Four distinct stages of perforation are observed in the numerical predictions; initial damage, complete damage, lower ballistic limit and upper ballistic limit.

- Energy absorbed by the thin ductile metal target is significantly influenced by the nose shape of the projectile. Energy absorbed by the target is the highest for a projectile nose shape intermediate between flat and hemispherical. There exists an optimum projectile nose shape for which energy absorbed by the target is maximised.

- A sharper peak in energy absorbed by the target is obtained for projectiles with variation in R_f compared to projectiles with variation in R_c. The global maximum energy absorbed by the target is for the case of the projectile with $R_f = 9\ mm$.

- There is a need to include strain rate dependent plasticity and failure in the FE material model to better predict the ballistic impact behaviour.

- Numerical predictions based on the modified Mohr-Coulomb and Johnson-Cook failure criteria are compared with experimental results to assess their suitability in predicting stress state dependent ductile fracture. The Johnson-Cook model cannot accurately predict the transition in failure mode during impact perforation. The strain rate dependent modified Mohr-Coulomb failure model is most suitable for predicting ductile fracture during impact.

- Discrepancies between experimental and numerical results for E_A using the MMC failure model for projectile nose shapes close to flat can be attributed to premature failure in the FE simulations arising from limited calibration tests used to define the MMC failure surface in stress space. There is a need to perform additional calibration tests at negative stress triaxialities to improve the accuracy of FE predictions for these cases.

6.1.2 Prediction of failure initiation in core-shell particle filled epoxy

- An iterative numerical-experimental approach is necessary to obtain the stress state dependent initial yield and failure surfaces for filled epoxy.

- Quasi-static indentation tests with three different indenter nose shapes and two boundary conditions are performed to further probe the predicted regimes of response under more complex load cases. A good agreement is obtained between the experimental results and the FE analysis using the material model developed. Careful consideration of the boundary compliance and effect of variation in plate thickness is essential to accurately predict the quasi-static indentation response.

- Two distinct regimes of failure are identified for filled epoxy, with a transition from ductile failure ($\eta < 0.48$) to brittle failure ($\eta > 0.48$) at a critical stress triaxiality. For the ductile regime, the pressure dependent exponential Drucker-Prager model is found to predict both initial yield and failure initiation across the range of stress states. In the brittle failure regime, a maximum principal stress failure criterion with a weak dependence on Lode angle is suitable for predicting failure.

6.1.3 Effect of strain rate and toughening strategies on failure initiation in epoxy

- The addition of core-shell particles to neat epoxy decreases its modulus and yield strength, while increasing its ductility. Reaction induced phase separation based toughening also leads to a reduction in yield strength of epoxy.

- Critical stress triaxialities are identified for each material type, and a widening of the ductile failure regime due to an increase in critical stress triaxiality is observed on toughening epoxy using both strategies considered.

- For both filled and unfilled epoxy, the initial yield surface shifts upwards with an increase in strain rate while the failure surface shifts slightly downwards. Thus, an increase in strain rate narrows the ductile failure regime due to a decrease in the critical stress triaxiality, while simultaneously increasing the brittle failure regime.

- Filled epoxy is less likely to fail in a brittle mode compared to the unfilled epoxy under complex loading cases such as indentation and impact, clearly illustrating the benefits of toughening neat epoxy to increase resistance to damage and energy absorption capability.

6.1.4 Impact perforation of carbon fibre reinforced epoxy composites

- The initial slope of the quasi-static indenter force-displacement curve is lower for the filled CFRE compared to the unfilled CFRE. However, a larger displacement at final fracture for the filled CFRE plate results in a 46% enhancement in E_A compared to unfilled CFRE. We know that the addition of core-shell particles to epoxy increases its ductility while also reducing its modulus during three different modes of loading; compression, tension and shear punch loads (Chapter 4). The epoxy matrix within the composite is in a complex state of stress, presumably a combination of tensile, compressive and shear loads, during edge-clamped indentation of the composite plate. Therefore, we hypothesize that the increase in ductility of epoxy resin in different states of stress due to particle reinforcement leads to enhancement of the energy absorption capability of filled CFRE.

- $\overline{E_A}$ during quasi-static indentation and ballistic impact perforation increases by 49% and 27%, respectively on incorporation of core-shell particles into epoxy matrix as part of the plain weave carbon/epoxy composite. Thus, toughening the epoxy matrix is an effective way of increasing resistance to both quasi-static indentation and ballistic impact perforation.

- Carbon/epoxy composites have a significantly greater $\overline{E_A}$ compared to AA 6082-T4, with $\overline{E_A}$ for quasi-static perforation enhanced by 158% for unfilled CFRE and 285% for filled CFRE compared to the monolithic aluminium alloy plate. $\overline{E_A}$ during impact perforation is increased by 48% for unfilled CFRE and 87% for filled CFRE compared to AA 6082-T4.

- The failure modes and damage patterns during impact of filled and unfilled CFRE target plates struck by a flat-ended projectile are qualitatively similar to those for quasi-static perforation using a flat indenter tip geometry. Failure takes place predominantly by

shear plugging in both loading cases considered. Significant delamination is observed in the case of ballistic impact, while bulging at the back face of the plate with only partial delamination is seen during quasi-static indentation.

- The variation in E_A for different indenter frontal nose radii for unfilled CFRE contrasts with the corresponding trend for thin aluminium alloy AA 6082-T4 plates. This is due to premature failure of the epoxy matrix by brittle fracture observed during quasi-static perforation of the unfilled CFRE plate by a hemispherical indenter.

- When the carbon/epoxy composite is subjected to indentation, the epoxy matrix is under a complex state of stress. Depending on the indenter nose shape, the epoxy matrix fails in the ductile or brittle failure regime. Shear-dominated failure of the epoxy matrix occurs at a value of stress triaxiality lower than the critical stress triaxiality i.e. in ductile failure regime, and therefore a larger values of failure strain are expected for indenters with a nose shape close to flat. However, for hemispherical indenters, the epoxy matrix fails in the brittle failure regime, with a lower strain to failure. As a result, the energy absorbed by the unfilled CFRE target plate up to failure during quasi-static indentation is lower for a hemispherical indenter compared to the flat indenter nose shape.

- $\overline{E_A}$ of carbon/epoxy composite plates perforated by a flat indenter increases by 49% on incorporation of core-shell particles into the epoxy matrix. On the other hand, changing the indenter tip geometry increases $\overline{E_A}$ of unfilled CFRE plates by up to 11%, for the range of projectile nose shapes considered. Thus, it can be concluded that toughening the epoxy matrix by adding 10% by weight core-shell particles is a more effective strategy compared to changing the indenter nose shape, to increase resistance to quasi-static perforation.

6.2   Future work

The following recommendations are made for future work:

6.2.1   Impact response of thin aluminium alloy plates

The FE calculations in Chapter 2 are applicable to impact loading conditions up to fracture for the thin ductile metal plate. Further development of the FE model with a stress state dependent yield criterion, including the effect of coupling stress triaxiality and Lode parameter, is needed to accurately capture the impact perforation behavior. Including thermo-mechanical coupling in the FE model is also essential in order to better predict the response under ballistic impact loading.

6.2.2   Prediction of failure initiation in core-shell particle filled epoxy

The FE model developed in Chapter 3 based on an iterative numerical-experimental approach to predict initial yield and failure of epoxy does not consider the influence of the Lode parameter on the material behaviour. This is in large part due to a limitation in the number of characterization techniques (applicable only to ductile metals) in literature to fully explore the complete range of possible stress states for polymers. There is a need to develop a novel test methodology to systematically probe the stress space at failure initiation, by inducing different combinations of stress triaxiality and Lode parameter, for polymeric materials in order to capture their mechanical behavior.

6.2.3   Effect of strain rate and toughening strategies on failure initiation in epoxy

Thermal softening due to adiabatic heating can have a strong influence in the mechanical response of epoxies especially during deformation at high strain rate and impact perforation. Further investigation is needed into the process of heat generation under complex states of stress at higher strain rates, as encountered during impact. Ideally the temperature rise should be measured directly during dynamic deformation, e.g. split-Hopkinson bar experiment, as

well as projectile impact experiments using high speed thermal imaging. This will provide insight into energy absorbed by heat generation during dynamic loading of epoxy.

Additional studies on the influence of microstructural modifications in epoxy on its failure behaviour are required. Toughened epoxies with fillers of different particle size and weight fractions should be tested to explore the influence of the full range of filler parameters on the failure response.

6.2.4 Impact perforation of carbon fibre reinforced epoxy composites

Impact experiments are performed using a flat-ended projectile on both filled and unfilled CFRE to obtain the ballistic limit velocities and energy absorption capability (Chapter 5). Further ballistic impact tests on both types of composite targets using different projectile tip geometries are needed to span the entire range of projectile nose shapes. Similarly, in Chapter 5, quasi-static edge-clamped indentation tests are performed on unfilled CFRE using three different indenter tip geometries. Further quasi-static perforation experiments with different indenter nose shapes should be performed to validate the hypothesis presented in Chapter 5. Lastly, numerical studies of the carbon/epoxy composites need to be performed using stress state dependent material models of the carbon fibres and epoxy matrix to obtain accurate predictions of the stress state at critical material points within the matrix at onset of failure for both quasi-static indentation and impact loads.

Chapter 7 Appendix A: Quasi-static perforation response of thin aluminium alloy plates

The results presented in Appendix A are from a previous study on predicting the quasi-static perforation response of thin aluminium alloy plates (Mohagheghian et al., 2017b). This section summarizes the quasi-static characterisation methodology and finite element model development presented by Mohagheghian et al. (2017b).

7.1 Quasi-static characterisation

7.1.1 Calibration of anisotropy and post-necking behaviour

Beese et al. (2010) showed the importance of including anisotropy in the plasticity model in predicting the indentation response of aluminium alloy sheets. Using the same experimental method, Mohagheghian et al. (2017b) measured the anisotropy of AA 6082-T4 sheets by performing quasi-static tensile tests (ASTM Standard E8/E8M) on dog-bone specimens machined with orientations parallel, perpendicular and at 45° to the rolling direction. The tensile tests were performed using an Instron screw driven test machine at a crosshead speed of 0.9 mm/min, corresponding to a nominal strain rate of approximately 5×10^{-4} /s. The force and displacement were obtained from the Instron load cell and a laser extensometer, respectively. In-plane strains, parallel and perpendicular to the loading direction, were measured using digital image correlation, by monitoring the deformation in the gauge section of the dog-bone specimens. The quasi-static tensile results in the three orientations are shown in Figure A.1. It can be observed that the in-plane anisotropy of the material is negligible. In order to calculate the out-of-plane anisotropy, Mohagheghian et al. (2017b)

used Lankford's r-value approach to calibrate Hill's yield surface (Hill, 1948).

The Hill yield surface for anisotropic materials is as follows:

$$f(\sigma) = \sqrt{F(\sigma_{22} - \sigma_{33})^2 + G(\sigma_{33} - \sigma_{11})^2 + H(\sigma_{11} - \sigma_{22})^2 + 2L\sigma_{23}{}^2 + 2M\sigma_{31}{}^2 + 2N\sigma_{12}{}^2} \quad (7.1)$$

where, σ refers to stress and F, G, H, L, M and N are material constants. Subscripts 1 and 2 indicate orthogonal in-plane directions while subscript 3 indicates through thickness direction. The tensile tests performed were assumed to be in a state of plane stress. Therefore, only four constants, F, G, H and N needed to be calibrated. The values of these constants are related to R_{11}, R_{22}, R_{33} and R_{12}, which are the ratios of stress components to the reference yield stress, by the following equations:

$$F = \frac{1}{2}\left(\frac{1}{R_{22}^2} + \frac{1}{R_{33}^2} - \frac{1}{R_{11}^2}\right)$$

$$G = \frac{1}{2}\left(\frac{1}{R_{33}^2} + \frac{1}{R_{11}^2} - \frac{1}{R_{22}^2}\right)$$

$$H = \frac{1}{2}\left(\frac{1}{R_{11}^2} + \frac{1}{R_{22}^2} - \frac{1}{R_{33}^2}\right) \tag{7.2}$$

$$N = \frac{3}{2R_{12}^2}$$

The values of R_{11}, R_{22}, R_{33} and R_{12} for AA 6082-T4, obtained from Lankford's r values and used to define the Hill yield surface are presented in Table A.1.

Table 7.1 Measured anisotropy constants for AA 6082-T4 used to define the Hill yield surface (Mohagheghian, 2013; Mohagheghian et al., 2017b).

R_{11}	R_{22}	R_{33}	R_{12}	R_{13}	R_{23}
1	1.01	0.876	1.01	1	1
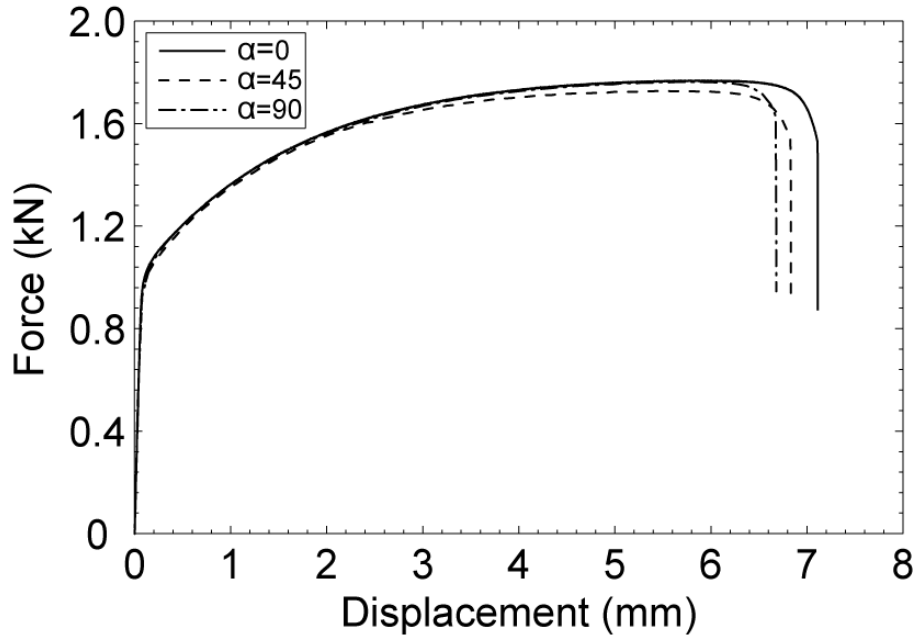
Figure 7.1 Quasi-static uniaxial tensile response of AA 6082-T4 in three different orientations (α) relative to the rolling direction (Mohagheghian et al., 2017b).

The post-necking strain hardening behaviour was assumed to follow a power law relationship at large plastic strains given by:

$$\bar{\sigma} = A(\varepsilon_0 + \bar{\varepsilon}_p)^n \qquad (7.3)$$

where, $\bar{\sigma}$ and $\bar{\varepsilon}_p$ denote equivalent stress and equivalent plastic strain, respectively. A, ε_0 and n are constant coefficients obtained by fitting the power law relationship with experimental data, the values of which are presented in Table A.2.

Table 7.2 Coefficients of power law isotropic hardening for AA 6082-T4 (Mohagheghian et al., 2017b).

A	n	ε_0
480	0.0027	0.19

157

7.1.2 Quasi-static failure model

Mohagheghian et al. (2017b) used the MMC model to predict ductile fracture during quasi-static perforation of thin aluminium alloy plates. In the MMC model, the onset of failure is taken to occur when the damage indicator D becomes equal to 1 (Bai and Wierzbicki, 2008a). Assuming that the stress triaxiality and Lode angle are constant throughout deformation, and excluding the dependence of the stress triaxiality and Lode angle on the generalized hardening rule proposed by Bai and Wierzbicki (2008), the MMC model reduces to:

$$\bar{\varepsilon}_f = \left\{ \frac{A}{c_2} \times \left[\sqrt{\frac{1 + c_1{}^2}{3}} \cos\left(\frac{\bar{\theta}\pi}{6}\right) + c_1 \left(\eta + \frac{1}{3} \sin\left(\frac{\bar{\theta}\pi}{6}\right) \right) \right] \right\}^{\frac{1}{n}} \tag{7.4}$$

where, $\bar{\varepsilon}_f$ is the effective plastic strain at the point of fracture, η is stress triaxiality and $\bar{\theta}$ is the normalised Lode angle. c_1 and c_2 are calibration parameters obtained from experimental data and numerical simulations.

Since η and $\bar{\theta}$ are not constant during deformation in several loading cases, average values of stress triaxiality, η_{avg} and normalised Lode angle, $\bar{\theta}_{avg}$ over the equivalent plastic strain range up to the point of fracture were used for calibration (Bai and Wierzbicki, 2009; Wierzbicki et al., 2005).

Mohagheghian et al. (2017b) performed two types of characterisation experiments to obtain effective plastic strain at fracture under two different states of stress; tensile tests on dog-bone specimens (Figure A.1) and notched specimens. Notched specimens identical to those used by Beese et al. (2010) with a thickness of 1 mm were used. The tensile tests on notched specimens were conducted on an Instron test machine at a crosshead speed of 0.72 mm/min, corresponding to a nominal strain rate of approximately 5×10^{-4} /s, same as in the case of the dog-bone specimens. The force and displacement were obtained from the Instron load cell and a laser extensometer, respectively.

Next, a combination of experimental and numerical approaches was used to obtain the

fracture strain as well as averaged values of η and $\bar{\theta}$ at the critical material point, used subsequently to calibrate the MMC failure model. Measuring the fracture strain directly from characterization tests was found to be challenging since experimental techniques such as DIC, while allowing local measurement of strain, could not predict the location of failure accurately if ductile fracture were to occur through the thickness of the specimen.

3D FE analysis of the calibration tests was performed using an elastic plastic material model, with the Hill anisotropic yield surface, defined in Equations A.1 and A.2 and Table A.1. The elastic modulus and Poisson's ratio was 70 GPa and 0.33, respectively. The FE model did not include any failure criterion, and was used to obtain the stress state and deformation at the critical point within the specimens corresponding to the point at which failure was seen to occur in the experiments. Mohagheghian et al. (2017b) also considered the effects of mesh sensitivity and metal anisotropy on the post-necking and failure response for the numerical analysis of the two calibration tests. The fracture conditions for the dog-bone and notched specimens are presented in Table A.3.

After fitting the surface defining the failure strain in the stress triaxiality-Lode parameter space (Equation A.4) to the calibration data points given in Table A.3, the calibration parameters obtained are $c_1 = 0.003$ and $c_2 = 231.96$.

Table 7.3 Fracture conditions for dog-bone and notched specimens (Mohagheghian et al., 2017b).

Test	$\bar{\varepsilon}_f$	η_{avg}	$\bar{\theta}_{avg}$
Tensile (dog-bone)	0.63	0.398	0.856
Tensile (notched)	0.50	0.507	0.451

7.2 3D model development

Mohagheghian et al. (2017b) investigated the effect of boundary conditions, anisotropy and friction on the quasi-static edge-clamped indentation response of AA 6082-T4. They simulated a 3D quarter plate model using Abaqus/Standard perforated with a hemispherical indenter. To assess boundary compliance, the clamping conditions were simulated in detail. A quarter plate was modelled with symmetry boundary conditions applied along the free edges. The circular test area, the region of plate under the clamping ring and the retaining bolts were included in the model. The retaining bolts were modelled as cylindrical rigid pins, with frictionless contact defined between the bolts and the plate. The mesh in regions of the plate close the indenter was refined until the simulation results became insensitive to the size of the mesh on further refinement. Coulomb friction with a coefficient of friction of 0.25 was used between the indenter and the plate, based on a typical value for dynamic friction coefficient between steel and aluminium based on literature. An elastic plastic material model with the Hill anisotropic yield surface (Section A.1) and the MMC failure model was used for the plate.

7.2.1 Effect of boundary compliance

Two cases were considered to investigate the influence of the boundary conditions; (a) fully clamped boundary with all degrees of freedom at the edge of the plate constrained to be zero, and (b) compliant boundary, with only the vertical degrees of freedom at the plate edge constrained to be zero. For the compliant boundary condition, the nodes at were free to translate in the horizontal plane, only constrained by the retaining pins. This condition represented frictionless contact between the clamping ring and the plate. Mohagheghian et al. (2017b) concluded that boundary compliance needs to be included for a good match of the FE results with the experiment. Further investigations into the effect of material anisotropy and coefficient of friction on the numerical quasi-static edge-clamped indentation response were carried out. They observed that introducing anisotropy reduced the slope of the force-displacement curve, and was essential to provide a close match with the

experiment. The numerical results were less sensitive to the coefficient of friction, with a value of 0.25 providing the best results.

7.2.2 2D axisymmetric model

Mohagheghian et al. (2017b) developed a 2D axisymmetric FE model using Abaqus/Explicit to reduce computational costs and possibly provide higher mesh refinement than the 3D FE model, especially for indenters with higher local curvatures. Axisymmetric continuum elements were used to discretise the thin aluminium alloy plate and the indenter was modelled using rigid elements. Most of the plate was meshed with four elements through the thickness, with local mesh refinement under the indenter corner. The local mesh refinement was optimised separately for each indenter geometry. As in the 3D model, in-plane anisotropy was neglected. The MMC failure model was implemented, and the FE calculation stopped when failure initiation ($D = 1$) occurred at any point within the specimen. The MMC failure locus was implemented in Abaqus in tabular form. Compliant boundary condition was considered in the axisymmetric model by introducing a one-dimensional non-linear spring at the plate edge, which only allowed horizontal translation of the edge. The spring response was considered to be bilinear and calibrated such that the 2D FE simulation result matched well with the experiment for a hemispherical indenter. The indenter tip geometries used in the 2D FE model were the same as those for the experimental investigation (Figure 2.3). For the flat indenter, a small corner radius of 0.1 mm was introduced to remove the stress singularity at the sharp corner.

References

(Gama) Haque, B.Z., Harrington, J.L., Gillespie Jr, J.W., 2012. Multi-hit ballistic impact on S-2 glass/SC15 thick-section composites: finite element analyses. J. Strain Anal. Eng. Des. 47, 495–512. doi:10.1177/0309324712456823

Abdulhamid, H., Kolopp, A., Bouvet, C., Rivallant, S., 2013. Experimental and numerical study of AA5086-H111 aluminum plates subjected to impact. Int. J. Impact Eng. 51, 1–12. doi:10.1016/j.ijimpeng.2012.06.011

Abu Talib, A.R., Abbud, L.H., Ali, A., Mustapha, F., 2012. Ballistic impact performance of Kevlar-29 and Al2O3 powder/epoxy targets under high velocity impact. Mater. Des. 35, 12–19. doi:10.1016/j.matdes.2011.08.045

Akbari, B., Bagheri, R., 2007. Deformation mechanism of epoxy/clay nanocomposite. Eur. Polym. J. 43, 782–788. doi:10.1016/j.eurpolymj.2006.11.028

Alcock, B., Cabrera, N.O., Barkoula, N.-M., Wang, Z., Peijs, T., 2008. The effect of temperature and strain rate on the impact performance of recyclable all-polypropylene composites. Compos. Part B Eng. 39, 537–547. doi:10.1016/j.compositesb.2007.03.003

Alhazov, D., Zussman, E., 2012. Study of the energy absorption capabilities of laminated glass using carbon nanotubes. Compos. Sci. Technol. 72, 681–687. doi:10.1016/j.compscitech.2012.01.016

Argento, A., Kim, W., Lee, E.C., Harris, A.M., Mielewski, D.F., 2011. Rate dependencies and energy absorption characteristics of nanoreinforced, biofiber, and microcellular polymer composites. Polym. Compos. 32, 1423–1429. doi:10.1002/pc

Asp, L.E., Berglund, L.A., Gudmundson, P., 1995. Effects of a composite-like stress state on the fracture of epoxies. Compos. Sci. Technol. 53, 27–37. doi:10.1016/0266-3538(94)00075-1

Asp, L.E., Berglund, L.A., Talreja, R., 1996a. Prediction of Matrix-Initiated Transvere Failure in Polymer Composites. Compos. Sci. Technol. 56, 1089–1097.

Asp, L.E., Berglund, L.A., Talreja, R., 1996b. A criterion for crack initiation in glassy polymers subjected to a composite-like stress state. Compos. Sci. Technol. 56, 1291–1301. doi:10.1016/S0266-3538(96)00090-5

Atkins, A.G., Afzal Khan, M., Liu, J.H., 1998. Necking and radial cracking around perforations in thin sheets at normal incidence. Int. J. Impact Eng. 21, 521–539.

Awerbuch, J., Bodner, S.R., 1977. An Investigation of Oblique Perforation of Metallic Plates by Projectiles.

Exp. Mech. 17, 147–153.

Ayatollahi, M.R., Shadlou, S., Shokrieh, M.M., 2011. Mixed mode brittle fracture in epoxy/multi-walled carbon nanotube nanocomposites. Eng. Fract. Mech. 78, 2620–2632. doi:10.1016/j.engfracmech.2011.06.021

Backman, M.E., Goldsmith, W., 1978. The mechanics of penetration of projectiles into targets. Int. J. Eng. Sci. 16, 1–99.

Bai, Y., Wierzbicki, T., 2009. Application of extended Mohr–Coulomb criterion to ductile fracture. Int. J. Fract. 161, 1–20. doi:10.1007/s10704-009-9422-8

Bai, Y., Wierzbicki, T., 2008a. A new model of metal plasticity and fracture with pressure and Lode dependence. Int. J. Plast. 24, 1071–1096. doi:10.1016/j.ijplas.2007.09.004

Bai, Y., Wierzbicki, T., 2008b. A new model of metal plasticity and fracture with pressure and Lode dependence. Int. J. Plast. 24, 1071–1096. doi:10.1016/j.ijplas.2007.09.004

Bain, E.D., Knorr, D.B., Richardson, A.D., Masser, K.A., Yu, J., Lenhart, J.L., 2016. Failure processes governing high-rate impact resistance of epoxy resins filled with core???shell rubber nanoparticles. J. Mater. Sci. 51, 2347–2370. doi:10.1007/s10853-015-9544-5

Bandyopadhyay, S., 1990. Review of the microscopic and macroscopic aspects of fracture of unmodified and modified epoxy resins. Mater. Sci. Eng. A 125, 157–184. doi:10.1016/0921-5093(90)90167-2

Bao, Y., Wierzbicki, T., 2004. On fracture locus in the equivalent strain and stress triaxiality space. Int. J. Mech. Sci. 46, 81–98. doi:10.1016/j.ijmecsci.2004.02.006

Bardella, L., Belleri, A., 2011. Two features of the uniaxial compression of a glassy epoxy resin: the yield stress rate-dependence and the volumetric instability. Mech. Time-Dependent Mater. 15, 255–275. doi:10.1007/s11043-010-9131-8

Barsoum, I., Faleskog, J., 2007. Rupture mechanisms in combined tension and shear—Experiments. Int. J. Solids Struct. 44, 1768–1786. doi:10.1016/j.ijsolstr.2006.09.031

Battistella, M., Cascione, M., Fiedler, B., Wichmann, M.H.G., Quaresimin, M., Schulte, K., 2008. Fracture behaviour of fumed silica/epoxy nanocomposites. Compos. Part A Appl. Sci. Manuf. 39, 1851–1858. doi:10.1016/j.compositesa.2008.09.010

Becu, L., Maazouz, A., Sautereau, H., Gerard, J.F., 1997. Fracture behavior of epoxy polymers modified with core-shell rubber particles. J. Appl. Polym. Sci. 65, 2419–2431. doi:10.1002/(SICI)1097-4628(19970919)65:12<2419::AID-APP14>3.0.CO;2-W

Beese, A.M., Luo, M., Li, Y., Bai, Y., Wierzbicki, T., 2010. Partially coupled anisotropic fracture model for aluminum sheets. Eng. Fract. Mech. 77, 1128–1152. doi:10.1016/j.engfracmech.2010.02.024

Beissel, S.R., Holmquist, T.J., Johnson, G.R., 2012. Influence of the third invariant in the ballistic impact of silicon carbide. Int. J Impact Eng. 45, 52-59.

Ben-Dor, G., Dubinsky, A., Elperin, T., 2002. A model for predicting penetration and perforation of FRP laminates by 3-D impactors. Compos. Struct. 56, 243–248. doi:10.1016/S0263-8223(02)00009-0

Boeing Report, 2006. Aero - Boeing 787 from the ground up.

Borvik, T., Hopperstad, O.S., Langseth, M., Malo, K.A., 2003. Effect of target thickness in blunt projectile penetration of Weldox 460 E steel plates. Int. J. Impact Eng. 28, 413–464.

Buitrago, B.L., Santiuste, C., Sánchez-Sáez, S., Barbero, E., Navarro, C., 2010. Modelling of composite sandwich structures with honeycomb core subjected to high-velocity impact. Compos. Struct. 92, 2090–2096. doi:10.1016/j.compstruct.2009.10.013

Caprino, G., Lopresto, V., Santoro, D., 2007. Ballistic impact behaviour of stitched graphite/epoxy laminates. Compos. Sci. Technol. 67, 325–335. doi:10.1016/j.compscitech.2006.04.015

Carolan, D., Ivankovic, A., Kinloch, A.J., Sprenger, S., Taylor, A.C., 2016. Toughening of epoxy-based hybrid nanocomposites. Polym. (United Kingdom) 97, 179–190. doi:10.1016/j.polymer.2016.05.007

Cheeseman, B.A., Bogetti, T.A., 2003. Ballistic impact into fabric and compliant composite laminates. Compos. Struct. 61, 161–173. doi:10.1016/S0263-8223(03)00029-1

Chen, C., Justice, R.S., Schaefer, D.W., Baur, J.W., 2008. Highly dispersed nanosilica–epoxy resins with enhanced mechanical properties. Polymer (Guildf). 49, 3805–3815. doi:10.1016/j.polymer.2008.06.023

Chen, W., Lu, F., Cheng, M., 2002. Tension and compression tests of two polymers under quasi-static and dynamic loading. Polym. Test. 21, 113–121. doi:10.1016/S0142-9418(01)00055-1

Chen, W., Zhou, B., 1998. Constitutive behavior of Epon 828/T-403 at various strain rates. Mech. Time-Dependent Mater. 2, 103–111.

Chen, X., Zhou, Y., Wells, G., 2014. Numerical and experimental investigations into ballistic performance of hybrid fabric panels. Compos. Part B Eng. 58, 35–42. doi:10.1016/j.compositesb.2013.10.019

Chen, Y., Clausen, A.H., Hopperstad, O.S., Langseth, M., 2009. Stress–strain behaviour of aluminium alloys at a wide range of strain rates. Int. J. Solids Struct. 46, 3825–3835. doi:10.1016/j.ijsolstr.2009.07.013

Chen, Y., Pang, B., Zheng, W., Peng, K., 2013. Experimental investigation on normal and oblique ballistic

impact behavior of fiber metal laminates. J. Reinf. Plast. Compos. 32, 1769–1778. doi:10.1177/0731684413498434

Chevalier, J., Morelle, X.P., Bailly, C., Camanho, P.P., Pardoen, T., Lani, F., 2016. Micro-mechanics based pressure dependent failure model for highly cross-linked epoxy resins. Eng. Fract. Mech. 158, 1–12. doi:10.1016/j.engfracmech.2016.02.039

Coleman, J.N., Khan, U., Blau, W.J., Gun'ko, Y.K., 2006a. Small but strong: A review of the mechanical properties of carbon nanotube–polymer composites. Carbon N. Y. 44, 1624–1652. doi:10.1016/j.carbon.2006.02.038

Coleman, J.N., Khan, U., Gun'ko, Y.K., 2006b. Mechanical reinforcement of polymers using carbon nanotubes. Adv. Mater. 18, 689–706. doi:10.1002/adma.200501851

Cook, W.D., Mayr, A.E., Edward, G.H., 1998. Yielding behaviour in model epoxy thermosets — II. Temperature dependence. Polymer (Guildf). 39, 3725–3733. doi:10.1016/S0032-3861(97)10335-4

Corbett, G.G., Reid, S.R., Johnson, W., 1996. Impact loading of plates and shells by free-flying projectiles: A review. Int. J. Impact Eng. 18, 141–230.

Corran, R.S.J., Ruiz, C., Shadbolt, P.J., 1983a. On the design of containment shields. Comput. Struct. 16, 563–572.

Corran, R.S.J., Shadbolt, P.J., Ruiz, C., 1983b. Impact loading of plates - an experimental investigation. Int. J. Impact Eng. 1, 3–22.

Crouch, I.G., Baxter, B.J., Woodward, R.L., 1990. Empirical tests of a model for thin plate perforation. Int. J. Impact Eng. 9, 19–33.

Dalmas, D., Guerra, C., Scheibert, J., Bonamy, D., 2013. Damage mechanisms in the dynamic fracture of nominally brittle polymers. Int. J. Fract. 184, 93–111. doi:10.1007/s10704-013-9839-y

Day, R.J., Lovell, P.A., Wazzan, A.A., 2001. Toughened carbon/epoxy composites made by using core/shell particles. Compos. Sci. Technol. 61, 41–56. doi:10.1016/S0266-3538(00)00169-X

Deng, S., Ye, L., 2006. Fracture behaviours of nano-silica modified epoxies at elevated temperatures. Key Eng. Mater. 312, 243–250. doi:10.4028/www.scientific.net/KEM.312.243

Dittanet, P., Pearson, R.A., 2012. Effect of silica nanoparticle size on toughening mechanisms of filled epoxy. Polymer (Guildf). 53, 1890–1905. doi:10.1016/j.polymer.2012.02.052

Dorogoy, A., Karp, B., Rittel, D., 2011. A Shear Compression Disk Specimen with Controlled Stress Triaxiality Under Quasi-Static Loading. Exp. Mech. 51, 1545–1557. doi:10.1007/s11340-012-9630-4

Duan, Y., Keefe, M., Bogetti, T.A., Cheeseman, B.A., 2005. Modeling the role of friction during ballistic impact of a high-strength plain-weave fabric. Compos. Struct. 68, 331–337. doi:10.1016/j.compstruct.2004.03.026

EADS Report, 2006. Taking the lead: A350XWB presentation.

El-Magd, E., Abouridouane, M., 2006. Characterization, modelling and simulation of deformation and fracture behaviour of the light-weight wrought alloys under high strain rate loading. Int. J. Impact Eng. 32, 741–758. doi:10.1016/j.ijimpeng.2005.03.008

Feli, S., Namdari Pour, M.H., 2012. An analytical model for composite sandwich panels with honeycomb core subjected to high-velocity impact. Compos. Part B Eng. 43, 2439–2447. doi:10.1016/j.compositesb.2011.11.028

Fereidoon, A., Rajabpour, M., Hemmatian, H., 2013. Fracture analysis of epoxy/SWCNT nanocomposite based on global–local finite element model. Compos. Part B Eng. 54, 400–408. doi:10.1016/j.compositesb.2013.05.020

Fiedler, B., Hojo, M., Ochiai, S., Schulte, K., Ando, M., 2001. Failure behavior of an epoxy matrix under different kinds of static loading. Compos. Sci. Technol. 61, 1615–1624. doi:10.1016/S0266-3538(01)00057-4

Gama, B.A., Gillespie Jr, J.W., 2011. Finite element modeling of impact, damage evolution and penetration of thick-section composites. Int. J. Impact Eng. 38, 181–197. doi:10.1016/j.ijimpeng.2010.11.001

Gama, B.A., Gillespie Jr, J.W., 2008. Punch shear based penetration model of ballistic impact of thick-section composites. Compos. Struct. 86, 356–369. doi:10.1016/j.compstruct.2007.11.001

Gao, X., Jensen, R.E., McKnight, S.H., Gillespie Jr, J.W., 2011. Effect of colloidal silica on the strength and energy absorption of glass fiber/epoxy interphases. Compos. Part A Appl. Sci. Manuf. 42, 1738–1747. doi:10.1016/j.compositesa.2011.07.029

Gao, X., Kim, J., 2006. Modeling of ductile fracture: Significance of void coalescence. Int. J. Solids Struct. 43, 6277–6293. doi:10.1016/j.ijsolstr.2005.08.008

Garg, A.C., Mai, Y.W., 1988. Failure mechanisms in toughened epoxy resins-A review. Compos. Sci. Technol. 31, 179–223. doi:10.1016/0266-3538(88)90009-7

Garg, M., Mulliken, A.D., Boyce, M.C., 2008. Temperature rise in polymeric materials during high rate deformation. J. Appl. Mech. 75, 11009. doi:10.1115/1.2745388

Ghorbel, E., 2008. A viscoplastic constitutive model for polymeric materials. Int. J. Plast. 24, 2032–2058.

doi:10.1016/j.ijplas.2008.01.003

Ghosh, S.K., Travis, F.W., 1979. An investigation into the static and dynamic piercing of diaphragms. Int. J. Mech. Sci. 21, 1–22.

Gilioli, A., Manes, A., Giglio, M., Wierzbicki, T., 2015. Predicting ballistic impact failure of aluminium 6061-T6 with the rate-independent Bao-Wierzbicki fracture model. Int. J. Impact Eng. 76, 207–220. doi:10.1016/j.ijimpeng.2014.10.004

Glaskova, T., Aniskevich, K., Borisova, A., 2013. Modeling of creep for multiwall carbon nanotube/epoxy nanocomposite. J. Appl. Polym. Sci. 129, 3314–3324. doi:10.1002/app.39067

Gojny, F.H., Wichmann, M.H.G., Fiedler, B., Schulte, K., 2005. Influence of different carbon nanotubes on the mechanical properties of epoxy matrix composites – A comparative study. Compos. Sci. Technol. 65, 2300–2313. doi:10.1016/j.compscitech.2005.04.021

Gómez-del Río, T., Rodríguez, J., Pearson, R.A., 2014. Compressive properties of nanoparticle modified epoxy resin at different strain rates. Compos. Part B Eng. 57, 173–179. doi:10.1016/j.compositesb.2013.10.002

Gower, H.L., Cronin, D.S., Plumtree, A., 2008. Ballistic impact response of laminated composite panels. Int. J. Impact Eng. 35, 1000–1008. doi:10.1016/j.ijimpeng.2007.07.007

Gruben, G., Hopperstad, O.S., Børvik, T., 2012. Evaluation of uncoupled ductile fracture criteria for the dual-phase steel Docol 600DL. Int. J. Mech. Sci. 62, 133–146. doi:10.1016/j.ijmecsci.2012.06.009

Gu, B., Li, Y., 2005. Ballistic perforation of conically cylindrical steel projectile into three-dimensional braided composites. AIAA J. 43, 426–434. doi:10.2514/1.11729

Gu, B., Xu, J., 2004. Finite element calculation of 4-step 3-dimensional braided composite under ballistic perforation. Compos. Part B Eng. 35, 291–297. doi:10.1016/j.compositesb.2004.01.001

Guo, Y., Li, Y., 2007. Quasi-static/dynamic response of SiO2–epoxy nanocomposites. Mater. Sci. Eng. A 458, 330–335. doi:10.1016/j.msea.2007.02.011

Gupta, N.K., Iqbal, M.A., Sekhon, G.S., 2008. Effect of projectile nose shape, impact velocity and target thickness on the deformation behavior of layered plates. Int. J. Impact Eng. 35, 37–60. doi:10.1016/j.ijimpeng.2006.11.004

Gupta, N.K., Iqbal, M.A., Sekhon, G.S., 2007. Effect of projectile nose shape, impact velocity and target thickness on deformation behavior of aluminum plates. Int. J. Solids Struct. 44, 3411–3439. doi:10.1016/j.ijsolstr.2006.09.034

Gupta, N.K., Iqbal, M.A., Sekhon, G.S., 2006. Experimental and numerical studies on the behavior of thin aluminum plates subjected to impact by blunt- and hemispherical-nosed projectiles. Int. J. Impact Eng. 32, 1921–1944. doi:10.1016/j.ijimpeng.2005.06.007

Gupta, P.K., Iqbal, M.A., Mohammad, Z., 2016. Energy dissipation in plastic deformation of thin aluminum targets subjected to projectile impact. Int. J. Impact Eng. 0, 1–12. doi:10.1016/j.ijimpeng.2017.05.008

Gupta, P.K., Iqbal, M.A., Mohammad, Z., Baqi, A., Gupta, N.K., 2017. Energy absorption in thin metallic targets subjected to oblique projectile impact: A numerical study. Thin-Walled Struct. 1–10. doi:10.1016/j.tws.2017.08.005

Gurusideswar, S., Velmurugan, R., 2014. Strain rate sensitivity of glass/epoxy composites with nanofillers. Mater. Des. 60, 468–478. doi:10.1016/j.matdes.2014.03.065

Ha-Minh, C., Imad, A., Boussu, F., Kanit, T., 2013. On analytical modelling to predict of the ballistic impact behaviour of textile multi-layer woven fabric. Compos. Struct. 99, 462–476. doi:10.1016/j.compstruct.2012.10.011

Haijun, X., Lulu, L., Guangtao, C., Na, Z., Yiming, F., Weirong, H., 2013. Impact response and damage evolution of triaxial braided carbon/epoxy composites. Part I: Ballistic impact testing. Text. Res. J. 83, 1703–1716. doi:10.1177/0040517512474363

Hao, S.J., Cui, L.S., Wang, Y.D., Jiang, D.Q., Yu, C., Jiang, J., Brown, D.E., Ren, Y., 2011. The ultrahigh mechanical energy-absorption capability evidenced in a high-strength NbTi/NiTi nanocomposite. Appl. Phys. Lett. 99, 24102. doi:10.1063/1.3610562

Hazell, P.J., Appleby-Thomas, G., 2009. A study on the energy dissipation of several different CFRP-based targets completely penetrated by a high velocity projectile. Compos. Struct. 91, 103–109. doi:10.1016/j.compstruct.2009.04.036

Hill, R., 1948. A theory of the yielding and plastic flow of anisotropic metals. Proc. R. Soc. A Math. Phys. Eng. Sci. 193, 281–297.

Hoo Fatt, M.S., Lin, C., Revilock Jr, D.M., Hopkins, D.A., 2003. Ballistic impact of GLARE fiber–metal laminates. Compos. Struct. 61, 73–88. doi:10.1016/S0263-8223(03)00036-9

Hosur, M. V, Mohammed, A.A., Zainuddin, S., Jeelani, S., 2008. Impact performance of nanophased foam core sandwich composites. Mater. Sci. Eng. A 498, 100–109. doi:10.1016/j.msea.2007.11.156

Hou, J.P., Ruiz, C., Trojanowski, A., 2000. Torsion tests of thermosetting resins at impact strain rate and under quasi-static loading. Mater. Sci. Eng. A 283, 181–188. doi:10.1016/S0921-5093(00)00725-5

169

Hou, W., Zhu, F., Lu, G., Fang, D.-N., 2010. Ballistic impact experiments of metallic sandwich panels with aluminium foam core. Int. J. Impact Eng. 37, 1045–1055. doi:10.1016/j.ijimpeng.2010.03.006

Hsieh, T.H., Kinloch, A.J., Taylor, A.C., Kinloch, I.A., 2011. The effect of carbon nanotubes on the fracture toughness and fatigue performance of a thermosetting epoxy polymer. J. Mater. Sci. 46, 7525–7535. doi:10.1007/s10853-011-5724-0

Hu, Y., Xia, Z., Ellyin, F., 2003. Deformation behavior of an epoxy resin subject to multiaxial loadings. Part I: Experimental investigations. Polym. Eng. Sci. 43, 721–733.

Hu, Z., Arefin, M.R.H., Yan, X., Fan, Q.H., 2014. Mechanical property characterization of carbon nanotube modified polymeric nanocomposites by computer modeling. Compos. Part B Eng. 56, 100–108. doi:10.1016/j.compositesb.2013.08.052

Iqbal, M.A., Gupta, G., Diwakar, A., Gupta, N.K., 2010. Effect of projectile nose shape on the ballistic resistance of ductile targets. Eur. J. Mech. - A/Solids 29, 683–694. doi:10.1016/j.euromechsol.2010.02.002

Iqbal, M.A., Gupta, N.K., 2011. Ballistic limit of single and layered aluminium plates. Strain 47, 205–219. doi:10.1111/j.1475-1305.2008.00601.x

Iqbal, M.A., Gupta, P.K., Deore, V.S., Tak, S.K., Tiwari, G., Gupta, N.K., 2012. Effect of target span and configuration on the ballistic limit. Int. J. Impact Eng. 42, 11–24. doi:10.1016/j.ijimpeng.2011.10.004

Iqbal, M.A., Khan, S.H., Ansari, R., Gupta, N.K., 2013. Experimental and numerical studies of double-nosed projectile impact on aluminum plates. Int. J. Impact Eng. 54, 232–245. doi:10.1016/j.ijimpeng.2012.11.007

Iqbal, M.A., Tiwari, G., Gupta, P.K., 2016. Energy dissipation in thin metallic shells under projectile impact. Eur. J. Mech. A/Solids 59, 37–57. doi:10.1016/j.euromechsol.2016.03.004

Iqbal, M.A., Tiwari, G., Gupta, P.K., Bhargava, P., 2015. Ballistic performance and energy absorption characteristics of thin aluminium plates. Int. J. Impact Eng. 77, 1–15. doi:10.1016/j.ijimpeng.2014.10.011

Ivañez, I., Santiuste, C., Barbero, E., Sanchez-Saez, S., 2011. Numerical modelling of foam-cored sandwich plates under high-velocity impact. Compos. Struct. 93, 2392–2399. doi:10.1016/j.compstruct.2011.03.028

Johnsen, B.B., Kinloch, A.J., Mohammed, R.D., Taylor, A.C., Sprenger, S., 2007. Toughening mechanisms of nanoparticle-modified epoxy polymers. Polymer (Guildf). 48, 530–541. doi:10.1016/j.polymer.2006.11.038

Johnson, G.R., Cook, W.H., 1985. Fracture characteristics of three metals subjected to various strains, strain rates, temperatures and pressures. Eng. Fract. Mech. 21, 31–48.

Jordan, J.L., Foley, J.R., Siviour, C.R., 2008. Mechanical properties of Epon 826/DEA epoxy. Mech. Time-Dependent Mater. 12, 249–272. doi:10.1007/s11043-008-9061-x

Kanchanomai, C., Rattananon, S., Soni, M., 2005. Effects of loading rate on fracture behavior and mechanism of thermoset epoxy resin. Polym. Test. 24, 886–892. doi:10.1016/j.polymertesting.2005.06.006

Karp, B., Dorogoy, A., Rittel, D., 2013. A Shear Compression Disk Specimen with Controlled Stress Triaxiality Under Dynamic Loading. Exp. Mech. 53, 243–253. doi:10.1007/s11340-012-9630-4

Kinloch, A.J., Masania, K., Taylor, A.C., Sprenger, S., Egan, D., 2007. The fracture of glass-fibre-reinforced epoxy composites using nanoparticle-modified matrices. J. Mater. Sci. 43, 1151–1154. doi:10.1007/s10853-007-2390-3

Knorr Jr, D.B., Yu, J.H., Richardson, A.D., Hindenlang, M.D., McAninch, I.M., La Scala, J.J., Lenhart, J.L., 2012. Glass transition dependence of ultrahigh strain rate response in amine cured epoxy resins. Polymer (Guildf). 53, 5917–5923. doi:10.1016/j.polymer.2012.09.058

Kody, R.S., Lesser, A.J., 1999. Yield behavior and energy absorbing characteristics of rubber-modified epoxies subjected to biaxial stress states. Polym. Compos. 20, 250–259. doi:10.1002/pc.10352

Kody, R.S., Lesser, A.J., 1997. Deformation and yield of epoxy networks in constrained states of stress. J. Mater. Sci. 32, 5637–5643.

Kpenyigba, K.M., Jankowiak, T., Rusinek, A., Pesci, R., 2013. Influence of projectile shape on dynamic behavior of steel sheet subjected to impact and perforation. Thin-Walled Struct. 65, 93–104. doi:10.1016/j.tws.2013.01.003

Kpenyigba, K.M., Jankowiak, T., Rusinek, A., Pesci, R., Wang, B., 2015. Effect of projectile nose shape on ballistic resistance of interstitial-free steel sheets. Int. J. Impact Eng. 79, 83–94. doi:10.1016/j.ijimpeng.2014.10.007

Landkof, B., Goldsmith, W., 1985. Petalling of thin, metallic plates during penetration by cylindro-conical projectiles. Int. J. Solids Struct. 21, 245–266.

Langseth, M., Larsen, P.K., 1994. Dropped objects' plugging capacity of aluminium alloy plates. Int. J. Impact Eng. 15, 225–241.

Larsson, F., 1997. Damage tolerance of a stitched carbon/epoxy laminate. Compos. Part A Appl. Sci. Manuf. 28, 923–934. doi:10.1016/S1359-835X(97)00063-8

Laurenzi, S., Pastore, R., Giannini, G., Marchetti, M., 2013. Experimental study of impact resistance in multi-walled carbon nanotube reinforced epoxy. Compos. Struct. 99, 62–68. doi:10.1016/j.compstruct.2012.12.002

Lee, O.S., Kim, M.S., 2003. Dynamic material property characterization by using split Hopkinson pressure bar (SHPB) technique. Nucl. Eng. Des. 226, 119–125. doi:10.1016/S0029-5493(03)00189-4

Lee, Y.-W., Woertz, J.C., Wierzbicki, T., 2004. Fracture prediction of thin plates under hemi-spherical punch with calibration and experimental verification. Int. J. Mech. Sci. 46, 751–781. doi:10.1016/j.ijmecsci.2004.05.004

Lee, Y.S., Wetzel, E.D., Wagner, N.J., 2003. The ballistic impact characteristics of Kevlar woven fabrics impregnated with a colloidal shear thickening fluid. J. Mater. Sci. 38, 2825–2833.

Lemanski, S.L., Petrinic, N., Nurick, G.N., 2013. Experimental characterisation of aluminium 6082 at varying temperature and strain rate. Strain 49, 147–157. doi:10.1111/str.12022

Leppin, S., Woodward, R.L., 1986. Perforation mechanisms in thin titanium alloy targets. Int. J. Impact Eng. 4, 107–115.

Lesser, A.J., Kody, R.S., 1997. A generalized model for the yield behavior of epoxy networks in multiaxial stress states. J. Polym. Sci. Part B Polym. Phys. 35, 1611–1619. doi:10.1002/(SICI)1099-0488(19970730)35:10<1611::AID-POLB13>3.0.CO;2-D

Levy, N., Goldsmith, W., 1984. Normal impact and perforation of thin plates by hemispherically-tipped projectiles - II. Experimental results. Int. J. Impact Eng. 2, 299–324.

Li, C., Strachan, A., 2011. Molecular dynamics predictions of thermal and mechanical properties of thermoset polymer EPON862/DETDA. Polymer (Guildf). 52, 2920–2928. doi:10.1016/j.polymer.2011.04.041

Li, Y., Luo, M., Gerlach, J., Wierzbicki, T., 2010. Prediction of shear-induced fracture in sheet metal forming. J. Mater. Process. Technol. 210, 1858–1869. doi:10.1016/j.jmatprotec.2010.06.021

Liang, Y.-M., Liechti, K.M., 1996. On the large deformation and localization behavior of an epoxy resin under multiaxial stress states. Int. J. Solids Struct. 33, 1479–1500. doi:10.1016/0020-7683(95)00105-0

Lin, K.F., Shieh, Y.D., 1998. Core-shell particles designed for toughening the epoxy resins. II. Core-shell-particle-toughened epoxy resins. J. Appl. Polym. Sci. 70, 2313–2322. doi:10.1002/(SICI)1097-4628(19981219)70:12<2313::AID-APP2>3.0.CO;2-P

Littell, J.D., Ruggeri, C.R., Goldberg, R.K., Roberts, G.D., Arnold, W.A., Binienda, W.K., 2008. Measurement of epoxy resin tension, compression, and shear stress–strain curves over a wide range of strain rates

using small test specimens. J. Aerosp. Eng. 21, 162–173. doi:10.1061/(ASCE)0893-1321(2008)21:3(162)

Liu, D., Stronge, W.J., 2000. Ballistic limit of metal plates struck by blunt deformable missiles: experiments. Int. J. Solids Struct. 37, 1403–1423.

Liu, S., Fan, X., He, C., 2016. Improving the fracture toughness of epoxy with nanosilica-rubber core-shell nanoparticles. Compos. Sci. Technol. 125, 132–140. doi:10.1016/j.compscitech.2016.01.009

López-Puente, J., Zaera, R., Navarro, C., 2008. Experimental and numerical analysis of normal and oblique ballistic impacts on thin carbon/epoxy woven laminates. Compos. Part A Appl. Sci. Manuf. 39, 374–387. doi:10.1016/j.compositesa.2007.10.004

López-Puente, J., Zaera, R., Navarro, C., 2007. An analytical model for high velocity impacts on thin CFRPs woven laminated plates. Int. J. Solids Struct. 44, 2837–2851. doi:10.1016/j.ijsolstr.2006.08.022

Lu, H., Tan, G., Chen, W., 2001. Modeling of constitutive behavior for Epon 828/T-403 at high strain rates. Mech. Time-Dependent Mater. 5, 119–130.

Lulu, L., Haijun, X., Na, Z., Guangtao, C., Yiming, F., Weirong, H., 2013. Impact response and damage evolution of triaxial braided carbon/epoxy composites. Part II: finite element analysis. Text. Res. J. 83, 1821–1835. doi:10.1177/0040517512474364

Luo, M., Wierzbicki, T., 2010. Numerical failure analysis of a stretch-bending test on dual-phase steel sheets using a phenomenological fracture model. Int. J. Solids Struct. 47, 3084–3102. doi:10.1016/j.ijsolstr.2010.07.010

Martinez-Rubi, Y., Ashrafi, B., Guan, J., Kingston, C., Johnston, A., Simard, B., Mirjalili, V., Hubert, P., Deng, L., Young, R.J., 2011. Toughening of epoxy matrices with reduced single-walled carbon nanotubes. ACS Appl. Mater. Interfaces 3, 2309–2317. doi:10.1021/am200523z

Mayr, A.E., Cook, W.D., Edward, G.H., 1998. Yielding behaviour in model epoxy thermosets — I. Effect of strain rate and composition. Polymer (Guildf). 39, 3719–3724. doi:10.1016/S0032-3861(97)10334-2

Mirjalili, V., Hubert, P., 2010. Modelling of the carbon nanotube bridging effect on the toughening of polymers and experimental verification. Compos. Sci. Technol. 70, 1537–1543. doi:10.1016/j.compscitech.2010.05.016

Miwa, M., Takeno, A., Yamazaki, H., Watanabe, A., 1995. Strain rate and temperature dependence of shear properties of epoxy resin. J. Mater. Sci. 30, 1760–1765. doi:10.1007/BF00351607

Mohagheghian, I., 2013b. Impact response of polymers and polymer nanocomposites. University of

Cambridge.

Mohagheghian, I., McShane, G.J., Stronge, W.J., 2017a. Quasi-static and impact perforation of polymer-metal bi-layer plates by a blunt indenter. Thin-Walled Struct. 117, 35–48. doi:10.1016/j.tws.2017.03.036

Mohagheghian, I., McShane, G.J., Stronge, W.J., 2016. Impact perforation of polymer-metal laminates: Projectile nose shape sensitivity. Int. J. Solids Struct. 88–89, 337–353. doi:10.1016/j.ijsolstr.2016.01.010

Mohagheghian, I., McShane, G.J., Stronge, W.J., 2015. Impact perforation of monolithic polyethylene plates: Projectile nose shape dependence. Int. J. Impact Eng. 80, 162–176. doi:10.1016/j.ijimpeng.2015.02.002

Mohagheghian, I., McShane, G.J., Stronge, W.J., 2011. Impact response of polyethylene nanocomposites. Procedia Eng. 10, 704–709. doi:10.1016/j.proeng.2011.04.117

Mohagheghian, I., Stronge, W.J., McShane, G.J., 2017b. Predicting indenter nose shape sensitivity for quasi-static perforation of thin metallic plates. Eur. J. Mech. A/Solids 61, 134–150. doi:10.1016/j.euromechsol.2016.09.004

Mohan, S., Velu, S., 2014. Ballistic impact behaviour of unidirectional fibre reinforced composites. Int. J. Impact Eng. 63, 164–176. doi:10.1016/j.ijimpeng.2013.07.008

Morelle, X.P., Chevalier, J., Bailly, C., Pardoen, T., Lani, F., 2017. Mechanical characterization and modeling of the deformation and failure of the highly crosslinked RTM6 epoxy resin. Mech. Time-Dependent Mater. 1–36. doi:10.1007/s11043-016-9336-6

Morin, D., Haugou, G., Bennani, B., Lauro, F., 2010. Identification of a new failure criterion for toughened epoxy adhesive. Eng. Fract. Mech. 77, 3481–3500. doi:10.1016/j.engfracmech.2010.09.016

Morye, S.S., Hine, P.J., Duckett, R.A., Carr, D.J., Ward, I.M., 2000. Modelling of the energy absorption by polymer composites upon ballistic impact. Compos. Sci. Technol. 60, 2631–2642. doi:10.1016/S0266-3538(00)00139-1

Muhi, R.J., Najim, F., de Moura, M.F.S.F., 2009. The effect of hybridization on the GFRP behavior under high velocity impact. Compos. Part B Eng. 40, 798–803. doi:10.1016/j.compositesb.2009.08.002

Mulliken, A.D., Boyce, M.C., 2006. Mechanics of the rate-dependent elastic–plastic deformation of glassy polymers from low to high strain rates. Int. J. Solids Struct. 43, 1331–1356. doi:10.1016/j.ijsolstr.2005.04.016

Nahshon, K., Hutchinson, J.W., 2008. Modification of the Gurson Model for shear failure. Eur. J. Mech. - A/Solids 27, 1–17. doi:10.1016/j.euromechsol.2007.08.002

Naik, N.K., Doshi, A. V, 2008. Ballistic impact behaviour of thick composites: Parametric studies. Compos.

174

Struct. 82, 447–464. doi:10.1016/j.compstruct.2007.01.025

Naik, N.K., Doshi, A. V, 2005. Ballistic impact behavior of thick composites: Analytical formulation. AIAA J. 43, 1525–1536.

Naik, N.K., Gadipatri, R., Thoram, N.M., Kavala, V.R., Ch, V., 2010. Shear properties of epoxy under high strain rate loading. Polym. Eng. Sci. 50, 780–788. doi:10.1002/pen

Naik, N.K., Kumar, S., Ratnaveer, D., Joshi, M., Akella, K., 2012. An energy-based model for ballistic impact analysis of ceramic-composite armors. Int. J. Damage Mech. 22, 145–187. doi:10.1177/1056789511435346

Naik, N.K., Pandya, K.S., Kavala, V.R., Zhang, W., Koratkar, N.A., 2014a. High-strain rate compressive behavior of multi-walled carbon nanotube dispersed thermoset epoxy resin. J. Compos. Mater. doi:10.1177/0021998314527329

Naik, N.K., Pandya, K.S., Kavala, V.R., Zhang, W., Koratkar, N.A., 2014b. Alumina nanoparticle filled epoxy resin: High strain rate compressive behavior. Polym. Eng. Sci. doi:10.1002/pen

Naik, N.K., Shankar, P.J., Kavala, V.R., Ravikumar, G., Pothnis, J.R., Arya, H., 2011. High strain rate mechanical behavior of epoxy under compressive loading: Experimental and modeling studies. Mater. Sci. Eng. A 528, 846–854. doi:10.1016/j.msea.2010.10.099

Naik, N.K., Shrirao, P., 2004. Composite structures under ballistic impact. Compos. Struct. 66, 579–590. doi:10.1016/j.compstruct.2004.05.006

Naik, N.K., Shrirao, P., Reddy, B.C.K., 2006. Ballistic impact behaviour of woven fabric composites: Formulation. Int. J. Impact Eng. 32, 1521–1552. doi:10.1016/j.ijimpeng.2005.01.004

Naik, N.K., Shrirao, P., Reddy, B.C.K., 2005. Ballistic impact behaviour of woven fabric composites: Parametric studies. Mater. Sci. Eng. A 412, 104–116. doi:10.1016/j.msea.2005.08.019

Nicholas, T., 1981. Tensile testing of materials at high rates of strain. Exp. Mech. 21, 177–185. doi:10.1007/BF02326644

Palomby, C., Stronge, W.J., 1988. Blunt missile perforation of thin plates and shells by discing. Int. J. Impact Eng. 7, 85–100.

Pandya, K.S., Akella, K., Joshi, M., Naik, N.K., 2012. Ballistic impact behavior of carbon nanotube and nanosilica dispersed resin and composites. J. Appl. Phys. 112, 113522. doi:10.1063/1.4769750

Pandya, K.S., Dharmane, L., Pothnis, J.R., Ravikumar, G., Naik, N.K., 2012. Stress wave attenuation in composites during ballistic impact. Polym. Test. 31, 261–266.

doi:10.1016/j.polymertesting.2011.11.006

Pandya, K.S., Kumar, C.V.S., Nair, N.S., Patil, P.S., Naik, N.K., 2015. Analytical and experimental studies on ballistic impact behavior of 2D woven fabric composites. Int. J. Damage Mech. 24. doi:10.1177/1056789514531440

Pandya, K.S., Naik, N.K., 2016. Nanoparticle dispersed resins and composites under quasi-static loading: Shear plugging behavior. Polym. Compos. 37. doi:10.1002/pc.23539

Pandya, K.S., Naik, N.K., 2015a. Analytical and experimental studies on ballistic impact behavior of carbon nanotube dispersed resin. Int. J. Impact Eng. 76. doi:10.1016/j.ijimpeng.2014.09.003

Pandya, K.S., Naik, N.K., 2015b. Energy absorption capability of carbon nanotubes dispersed in resins under compressive high strain rate loading. Compos. Part B Eng. 72. doi:10.1016/j.compositesb.2014.11.026

Pandya, K.S., Pothnis, J.R., Ravikumar, G., Naik, N.K., 2013. Ballistic impact behavior of hybrid composites. Mater. Des. 44, 128–135. doi:10.1016/j.matdes.2012.07.044

Pandya, K.S., Sesha Kumar, C. V, Nair, N.S., Patil, P.S., Naik, N.K., 2014. Analytical and experimental studies on ballistic impact behavior of 2D woven fabric composites. Int. J. Damage Mech. doi:10.1177/1056789514531440

Pandya, K.S., Veerraju, C., Naik, N.K., 2011. Hybrid composites made of carbon and glass woven fabrics under quasi-static loading. Mater. Des. 32, 4094–4099. doi:10.1016/j.matdes.2011.03.003

Petel, O.E., Ouellet, S., Loiseau, J., Marr, B.J., Frost, D.L., Higgins, A.J., 2013. The effect of particle strength on the ballistic resistance of shear thickening fluids. Appl. Phys. Lett. 102, 64103. doi:10.1063/1.4791785

Pol, M.H., Liaghat, G.H., Hajiarazi, F., 2012. Effect of nanoclay on ballistic behavior of woven fabric composites: Experimental investigation. J. Compos. Mater. 47, 1563–1573. doi:10.1177/0021998312449768

Pothnis, J.R., Perla, Y., Arya, H., Naik, N.K., 2011. High strain rate tensile behavior of aluminum alloy 7075 T651 and IS 2062 mild steel. J. Eng. Mater. Technol. 133, 21026. doi:10.1115/1.4003113

Pothnis, J.R., Ravikumar, G., Joshi, M., Akella, K., Kumar, S., Naik, N.K., 2012. High strain rate compressive behavior of epoxy LY 556: Radial constraint effect. Mater. Sci. Eng. A 538, 210–218. doi:10.1016/j.msea.2012.01.032

Raguraman, M., Jagadeesh, G., Deb, A., Barton, D.C., 2010. Experimental and Numerical Investigation of the Behavior of Aluminium Plates Upon Ballistic Impact. Exp. Tech. 34, 49–60. doi:10.1111/j.1747-

1567.2009.00559.x

Rahman, M., Hosur, M., Zainuddin, S., Vaidya, U., Tauhid, A., Kumar, A., Trovillion, J., Jeelani, S., 2013. Effects of amino-functionalized MWCNTs on ballistic impact performance of E-glass/epoxy composites using a spherical projectile. Int. J. Impact Eng. 57, 108–118. doi:10.1016/j.ijimpeng.2013.01.011

Rajagopal, A., Naik, N.K., 2014. Oblique ballistic impact behavior of composites. Int. J. Damage Mech. 23, 453–482. doi:10.1177/1056789513499268

Ravi-Chandar, K., 1998. Dynamic fracture of nominally brittle materials. Int. J. Fract. 90, 83–102.

Recht, R.F., Ipson, T.W., 1963. Ballistic perforation dynamics. J. Appl. Mech. 30(3), 384-390.

Rice, J.R., Tracey, D.M., 1969. On the ductile enlargement of voids in triaxial stress fields. J. Mech. Phys. Solids 17, 201–217.

Rodríguez-Millán, M., Vaz-Romero, A., Rusinek, A., Rodríguez-Martínez, J.A., Arias, A., 2014. Experimental Study on the Perforation Process of 5754-H111 and 6082-T6 Aluminium Plates Subjected to Normal Impact by Conical, Hemispherical and Blunt Projectiles. Exp. Mech. 54, 729–742. doi:10.1007/s11340-013-9829-z

Roy, P.K., Ullas, A. V, Chaudhary, S., Mangla, V., Sharma, P., Kumar, D., Rajagopal, C., 2013. Effect of SBA-15 on the energy absorption characteristics of epoxy resin for blast mitigation applications. Iran. Polym. J. 22, 709–719. doi:10.1007/s13726-013-0169-8

Seidt, J.D., Michael Pereira, J., Gilat, A., Revilock, D.M., Nandwana, K., 2013. Ballistic impact of anisotropic 2024 aluminum sheet and plate. Int. J. Impact Eng. 62, 27–34. doi:10.1016/j.ijimpeng.2013.06.001

Senthil, K., Iqbal, M.A., Arindam, B., Mittal, R., Gupta, N.K., 2016. Ballistic resistance of 2024 aluminium plates against hemispherical, sphere and blunt nose projectiles. Thin-Walled Struct. 1–12. doi:10.1016/j.tws.2017.02.028

Sevkat, E., Liaw, B., Delale, F., Raju, B.B., 2009. A combined experimental and numerical approach to study ballistic impact response of S2-glass fiber/toughened epoxy composite beams. Compos. Sci. Technol. 69, 965–982. doi:10.1016/j.compscitech.2009.01.001

Seyed Yaghoubi, A., Liaw, B., 2013. Effect of lay-up orientation on ballistic impact behaviors of GLARE 5 FML beams. Int. J. Impact Eng. 54, 138–148. doi:10.1016/j.ijimpeng.2012.10.007

Shadlou, S., Alishahi, E., Ayatollahi, M.R., 2013. Fracture behavior of epoxy nanocomposites reinforced with different carbon nano-reinforcements. Compos. Struct. 95, 577–581. doi:10.1016/j.compstruct.2012.08.002

177

Shaktivesh, S., Nair, N.S., Sesha Kumar, C. V, Naik, N.K., 2013. Ballistic impact performance of composite targets. Mater. Des. 51, 833–846. doi:10.1016/j.matdes.2013.04.093

Silva, M.A.G., Cismaşiu, C., Chiorean, C.G., 2005. Numerical simulation of ballistic impact on composite laminates. Int. J. Impact Eng. 31, 289–306. doi:10.1016/j.ijimpeng.2004.01.011

Singh, S., Srivastava, V.K., Prakash, R., 2013. Characterisation of multi-walled carbon nanotube reinforced epoxy resin composites. Mater. Sci. Technol. 29, 1–5. doi:10.1179/1743284713Y.0000000288

Song, B., Chen, W., Montgomery, S.T., Forrestal, M.J., 2009. Mechanical response of an alumina-filled epoxy at various strain rates. J. Compos. Mater. 43, 1519–1536. doi:10.1177/0021998308337741

Srivastava, I., Koratkar, N., 2010. Fatigue and fracture toughness of epoxy nanocomposites. JOM 62, 50–57.

Staab, G.H., Gilat, A., 1991. A Direct Tension Split Hopkinson Bar for High Strain Rate Testing. Exp. Mech. 31, 232–235. doi:10.1007/BF02326065

Sue, H.J., 1992. Craze-like damage in a core-shell rubber-modified epoxy system. J. Mater. Sci. 27, 3098–3107. doi:10.1007/BF01154125

Sun, L., Gibson, R.F., Gordaninejad, F., 2011. Multiscale analysis of stiffness and fracture of nanoparticle-reinforced composites using micromechanics and global–local finite element models. Eng. Fract. Mech. 78, 2645–2662. doi:10.1016/j.engfracmech.2011.07.002

Sun, L., Gibson, R.F., Gordaninejad, F., Suhr, J., 2009. Energy absorption capability of nanocomposites: A review. Compos. Sci. Technol. 69, 2392–2409. doi:10.1016/j.compscitech.2009.06.020

Tang, L.-C., Zhang, H., Han, J.-H., Wu, X.-P., Zhang, Z., 2011. Fracture mechanisms of epoxy filled with ozone functionalized multi-wall carbon nanotubes. Compos. Sci. Technol. 72, 7–13. doi:10.1016/j.compscitech.2011.07.016

Tay, T.E., Ang, H.G., Shim, V.P.W., 1995. An empirical strain rate-dependent constitutive relationship for glass-fibre reinforced epoxy and pure epoxy. Compos. Struct. 33, 201–210. doi:10.1016/0263-8223(95)00116-6

Tehrani, M., Boroujeni, A.Y., Hartman, T.B., Haugh, T.P., Case, S.W., Al-Haik, M.S., 2013. Mechanical characterization and impact damage assessment of a woven carbon fiber reinforced carbon nanotube–epoxy composite. Compos. Sci. Technol. 75, 42–48. doi:10.1016/j.compscitech.2012.12.005

Tehrani, M., Safdari, M., Al-Haik, M.S., 2011. Nanocharacterization of creep behavior of multiwall carbon nanotubes/epoxy nanocomposite. Int. J. Plast. 27, 887–901. doi:10.1016/j.ijplas.2010.10.005

Teng, X., Wierzbicki, T., 2006. Evaluation of six fracture models in high velocity perforation. Eng. Fract.

Mech. 73, 1653–1678. doi:10.1016/j.engfracmech.2006.01.009

Teng, X., Wierzbicki, T., 2005a. Transition of failure modes in round-nosed mass-to-beam impact. Eur. J. Mech. - A/Solids 24, 857–876. doi:10.1016/j.euromechsol.2005.04.001

Teng, X., Wierzbicki, T., 2005b. Numerical study on crack propagation in high velocity perforation. Comput. Struct. 83, 989–1004. doi:10.1016/j.compstruc.2004.12.001

Thitsartarn, W., Fan, X., Sun, Y., Yeo, J.C.C., Yuan, D., He, C., 2015. Simultaneous enhancement of strength and toughness of epoxy using POSS-Rubber core-shell nanoparticles. Compos. Sci. Technol. 118, 63–71. doi:10.1016/j.compscitech.2015.06.011

Thostenson, E.T., Ren, Z., Chou, T.-W., 2001. Advances in the science and technology of carbon nanotubes and their composites: a review. Compos. Sci. Technol. 61, 1899–1912. doi:10.1016/S0266-3538(01)00094-X

Timoshenko, S., Woinowsky-Krieger, S., 1959. Thoery of Plates and Shells.

Tiwari, G., Iqbal, M.A., Gupta, P.K., Gupta, N.K., 2014. The ballistic resistance of thin aluminium plates with varying degrees of fixity along the circumference. Int. J. Impact Eng. 74, 46–56. doi:10.1016/j.ijimpeng.2014.01.007

Trojanowski, A., Ruiz, C., Harding, J., 1997. Thermomechanical properties of polymers at high rates of strain. J. Phys. IV 7, 447–452.

Tsai, J.-L., Cheng, Y.-L., 2008. Investigating nanoparticle effect on the mode I fracture toughness of glass/epoxy composites. Adv. Mater. Res. 47–50, 1153–1156. doi:10.4028/www.scientific.net/AMR.47-50.1153

Udatha, P., Sesha Kumar, C. V, Nair, N.S., Naik, N.K., 2012. High velocity impact performance of three-dimensional woven composites. J. Strain Anal. Eng. Des. 47, 419–431. doi:10.1177/0309324712448578

Ulven, C., Vaidya, U.K., Hosur, M. V, 2003. Effect of projectile shape during ballistic perforation of VARTM carbon/epoxy composite panels. Compos. Struct. 61, 143–150. doi:10.1016/S0263-8223(03)00037-0

Vijayan, V., Hegde, S., Gupta, N.K., 2016. Deformation and ballistic performance of conical aluminum projectiles impacting thin aluminum targets: Influence of apex angle. Int. J. Impact Eng. 0. doi:10.1016/j.ijimpeng.2017.05.009

Wambua, P., Vangrimde, B., Lomov, S., Verpoest, I., 2007. The response of natural fibre composites to ballistic impact by fragment simulating projectiles. Compos. Struct. 77, 232–240. doi:10.1016/j.compstruct.2005.07.006

Wang, Z., Liu, F., Liang, W., Zhou, L., 2013. Nanoscale analysis of tensile properties and fracture of nanoreinforced epoxy polymer using micromechanics. J. Reinf. Plast. Compos. 32, 1224–1233. doi:10.1177/0731684413486848

Watson, J., Serrano, J., 2010. Composite materials for wind blades. windsystemsmag.com

Wen, H.M., 2000. Predicting the penetration and perforation of FRP laminates struck normally by projectiles with different nose shapes. Compos. Struct. 49, 321–329. doi:10.1016/S0263-8223(00)00064-7

Werner, B.T., Daniel, I.M., 2014. Characterization and modeling of polymeric matrix under multi-axial static and dynamic loading. Compos. Sci. Technol. 102, 113–119. doi:10.1016/j.compscitech.2014.07.025

Wetzel, B., Haupert, F., Zhang, M.Q., 2003. Epoxy nanocomposites with high mechanical and tribological performance. Compos. Sci. Technol. 63, 2055–2067. doi:10.1016/S0266-3538(03)00115-5

Wetzel, B., Rosso, P., Haupert, F., Friedrich, K., 2006. Epoxy nanocomposites – fracture and toughening mechanisms. Eng. Fract. Mech. 73, 2375–2398. doi:10.1016/j.engfracmech.2006.05.018

Wierzbicki, T., 1999. Petalling of plates under explosive and impact loading. Int. J. Impact Eng. 22, 935–954.

Wierzbicki, T., Bao, Y., Lee, Y.-W., Bai, Y., 2005. Calibration and evaluation of seven fracture models. Int. J. Mech. Sci. 47, 719–743. doi:10.1016/j.ijmecsci.2005.03.003

Wright, S.C., Fleck, N.A., Stronge, W.J., 1993. Ballistic impact of polycarbonate - An experimental investigation. Int. J. Impact Eng. 13(1), 1-20.

Wu, X.-F., Ghoshal, G., Kartashov, M., Aslan, Z., Turner, J.A., Dzenis, Y.A., 2008. Experimental characterization of the impact-damage tolerance of a cross-ply graphite-fiber/epoxy laminate. Polym. Compos. 29, 534–543. doi:10.1002/pc

Xia, Z., Hu, Y., Ellyin, F., 2003. Deformation behavior of an epoxy resin subject to multiaxial loadings. Part II: Constitutive modeling and predictions. Polym. Eng. Sci. 43, 734–748.

Xue, L., 2007. Damage accumulation and fracture initiation in uncracked ductile solids subject to triaxial loading. Int. J. Solids Struct. 44, 5163–5181. doi:10.1016/j.ijsolstr.2006.12.026

Yamamoto, N., John Hart, A., Garcia, E.J., Wicks, S.S., Duong, H.M., Slocum, A.H., Wardle, B.L., 2009. High-yield growth and morphology control of aligned carbon nanotubes on ceramic fibres for multifunctional enhancement of structural composites. Carbon 47, 551-560.

Yao, X.F., Yeh, H.Y., Zhou, D., Zhang, Y.H., 2005. The structural characterization and properties of SiO2-epoxy nanocomposites. J. Compos. Mater. 40, 371–381. doi:10.1177/0021998305055193

Yao, X.F., Zhou, D., Yeh, H.Y., 2008. Macro/microscopic fracture characterizations of SiO2/epoxy nanocomposites. Aerosp. Sci. Technol. 12, 223–230. doi:10.1016/j.ast.2007.03.005

Ye, Y., Chen, H., Wu, J., Ye, L., 2007. High impact strength epoxy nanocomposites with natural nanotubes. Polymer (Guildf). 48, 6426–6433. doi:10.1016/j.polymer.2007.08.035

Yibo, P., Gang, W., Tianxing, Z., Shangfeng, P., Yiming, R., 2013. Dynamic mechanical behaviors of 6082-t6 aluminum alloy. Adv. Mech. Eng. 2013, 1–9. doi:10.1155/2013/878016

Yungwirth, C.J., 2006. Ballistic response of pyramidal lattice truss structures. University of Virginia.

Zamani, M.M., Fereidoon, A., Sabet, A., 2012. Multi-walled carbon nanotube-filled polypropylene nanocomposites: high velocity impact response and mechanical properties. Iran. Polym. J. 21, 887–894. doi:10.1007/s13726-012-0097-z

Zamanian, M., Mortezaei, M., Salehnia, B., Jam, J.E., 2013. Fracture toughness of epoxy polymer modified with nanosilica particles: Particle size effect. Eng. Fract. Mech. 97, 193–206. doi:10.1016/j.engfracmech.2012.10.027

Zappalorto, M., Salviato, M., Quaresimin, M., 2011. Influence of the interphase zone on the nanoparticle debonding stress. Compos. Sci. Technol. 72, 49–55. doi:10.1016/j.compscitech.2011.09.016

Zappalorto, M., Salviato, M., Quaresimin, M., 2011. Assessment of debonding-induced toughening in nanocomposites. Procedia Eng. 10, 2973–2978. doi:10.1016/j.proeng.2011.04.493

Zhang, H., Tang, L.-C., Zhang, Z., Friedrich, K., Sprenger, S., 2008. Fracture behaviours of in situ silica nanoparticle-filled epoxy at different temperatures. Polymer (Guildf). 49, 3816–3825. doi:10.1016/j.polymer.2008.06.040

Zhao, Y., Schiraldi, D.A., 2005. Thermal and mechanical properties of polyhedral oligomeric silsesquioxane (POSS)/polycarbonate composites. Polymer (Guildf). 46, 11640–11647. doi:10.1016/j.polymer.2005.09.070

Zhou, J., Hayden, M., Gao, X., 2013. An investigation of the strain rate and temperature effects on the plastic flow stress and ductile failure strain of aluminum alloys 5083-H116, 6082-T6 and a 5183 weld metal. Proc. Inst. Mech. Eng. Part C J. Mech. Eng. Sci. 227, 883–895. doi:10.1177/0954406212450962